ENTRAINMENT, CHEMISTRY, AND STRUCTURE OF FIRE PLUMES

Thesis by

Stephen James Toner

In Partial Fulfillment of the
Requirements for the Degree of
Doctor of Philosophy

California Institute of Technology
Pasadena, California

1987

Submitted October 2, 1986

© 1986

Stephen James Toner

All Rights Reserved

in memory of my father

Acknowledgements

My most sincere appreciation goes to my advisor, Professor E.E. Zukoski, for his valuable discussions and suggestions during the course of this work. In addition, discussions with Professors T. Kubota, F.E. Marble, and R.H. Sabersky were both enlightening and encouraging.

The second part of this work was conducted with Dr. R. Miake-Lye of GALCIT, and his contributions are gratefully acknowledged.

Thanks are certainly due my fellow graduate students in Mechanical Engineering; in particular, Mr. T. Sobota for his many valuable suggestions, and Mr. J. Morehart for his critical reading of this report.

My wife, Ritsuko, deserves special thanks for her unselfish support and encouragement, and for putting my work before hers. Thanks to my parents for their encouragement and guidance.

Finally, I would like acknowledge the personal financial support of the Exxon Teaching Fellowship. This research was supported by the U.S. Department of Commerce, National Bureau of Standards, Center for Fire Research through Grant no. 60NANB5D0562 and by the Gas Research Institute through Grant no. 5083-260-0878.

Abstract

In Part 1, the entrainment in the lowest regions of buoyant fire plumes burning from an environment of quiescent fresh air (lower layer) across an interface into an environment of hot combustion products (upper layer) is investigated. Measurements using 20 to 200 kW natural gas flames formed above a 0.19 m diameter burner show that the entrained mass flux is nearly linear with distance from the fire source and essentially independent of the fuel flow rate. Comparison with previous results suggests that this linear dependence is valid over a wide range of conditions, but that the magnitude of the entrainment near the burner is influenced by the initial buoyancy of the plume.

The chemistry of the products in the upper layer is also investigated. Over the ranges studied, the composition was a function of the upper-layer equivalence ratio only, and independent of the temperature of the upper layer or the residence time of the gas in it. For fuel-lean fires the product composition suggests that the fuel reaction is nearly complete, in contrast to fuel-rich fires where some of the stable intermediates are found to "freeze out" of the reaction prior to completion.

The experimental method is extended to entrainment measurements on steady, axisymmetric, fully turbulent jet diffusion flames of hydrogen in air. In the momentum-dominated regions of the flame, the nondimensional mass flux used to characterize this regime is found to be constant as expected. The transition between momentum-dominated and buoyancy-dominated regions is also observed.

In Part 2, a novel diagnostic technique, which makes use of laser light scattered by soot particles, was used in an effort to identify flame sheets within a natural gas diffusion flame. Soot particles, inherently created and consumed

in the flame, were used as the scattering medium, which obviated the need for externally supplied seed material. Since no foreign material was added to the flame, the current technique can be considered truly nonintrusive. The soot distribution within a large buoyant natural gas diffusion flame is argued to be a reasonable marker for the presence of a diffusion flame. Measurements made in 47.4 to 190 kW natural gas flames stabilized on a 0.5 m diameter burner show that when soot is present within the outer boundary of the flame, it is observed as thin sheets, which become narrower in regions where the average strain rate is estimated to be greater. The structure of the soot distribution suggests that the combustion occurs along sheets of diffusion flamelets that are highly wrinkled and convoluted. Furthermore, they are distributed fairly uniformly within the volume of the flame, based on images of the associated soot, and occupy about 40 to 60% of the volume.

Contents

List of Figures

Part 1

List of Tables

List of Symbols

Symbol	Description
a_i	mole fraction of the ith fuel component
A_C, A_H, A_O, A_N	coefficients in the conservation of atoms equations (defined in **2.8**)
A_i	area of the chromatogram peak of the ith sample component
b	characteristic jet radius
b_i'	mole fraction of the ith component of dry air
b_i	mole fraction of the ith component of air
B_C, B_H, B_O, B_N	coefficients in the conservation of atoms equations (defined in **2.9**)
c_1	ratio of the oxygen response factor to the argon response factor
c_f	speed of sound in the jet fluid
c_∞	speed of sound in the ambient fluid
$c_{p\infty}$	specific heat of the ambient fluid at constant pressure
D_0	burner diameter
D_s	effective source diameter
f_i	chromatographic response factor for the ith sample component
g	acceleration due to gravity
H	arbitrary entrainment measurement plane
ΔH_i°	heat of formation per mole of the ith component
ΔH_r°	heat of reaction per mole of fuel
ΔH_s°	heat of stoichiometric reaction per mole of fuel
I	number of moles of air per mole of fuel in the reaction

I_s	number of moles of air per mole of fuel in a stoichiometric reaction
J	jet vertical momentum flux
J_0	jet initial vertical momentum flux
L	flame height
$\dot{m}$	jet mass flux
$\dot{m}_e$	entrainment mass flux
$\dot{m}_f$	fuel mass flux
$\dot{m}_i$	mass flow rate across the interface due to mixing
M_∞	molecular weight of the ambient fluid
M_f	molecular weight of the fuel
N_p	total number of moles in the product per mole of fuel
p	ambient pressure
p_v	vapor pressure of water in air
p_v'	saturated vapor pressure of water at a given temperature
$\dot{Q}$	heat release rate of the fuel
r	radial coordinate
t	time
$\overline{T}$	average temperature in the jet
T_∞	ambient temperature
T_d	ambient dry-bulb temperature
T_w	ambient wet-bulb temperature
u	axial velocity
$\overline{u}$	average axial velocity in the jet
u_0	average velocity at the burner exit
u_s	effective source velocity

v	radial velocity
W_1	mass fraction of fuel in a stoichiometric mixture
x_i	moles of ith product component per mole fuel
$\hat{x}_i$	moles of ith product component per mole fuel in a stoichiometric reaction
y_i	moles of ith product component divided by the moles of nitrogen gas in the product
Y_C, Y_H, Y_O, Y_N	coefficients in the conservation of atoms equations (defined in **2.10**)
$\mathrm{Y_i}$	mole fraction of the ith product component
z	axial coordinate
z_0	effective origin offset
δ	characteristic thickness of a shear layer
Δ	length of the intermittent flame region
θ	angular circumferential coordinate
μ_f	fuel dynamic viscosity
μ_∞	ambient fluid dynamic viscosity
$\overline{\mu}$	average dynamic viscosity in the jet
ν_f	fuel kinematic viscosity
ρ	density
ρ_∞	ambient fluid density
$\overline{\rho}$	average density in the jet

Dimensionless Coefficients and Parameters

C_1	mass entrainment coefficient for a momentum-dominated jet
C_2	momentum-growth coefficient
C_3	momentum-growth coefficient for a buoyancy-dominated jet

C_4	mass entrainment coefficient for a buoyancy-dominated jet
C_L	flame length coefficient
M_A	jet exit Mach number with respect to the ambient fluid sonic speed
M_C	convective Mach number
M_H	jet exit Mach number with respect to the fuel sonic speed
Q^*	flame heat-addition parameter
$\mathrm{Re_f}$	Reynolds number based on actual burner exit conditions
$\mathrm{Re_s}$	effective source Reynolds number
$\mathrm{Re_L}$	overall flame-zone Reynolds number
$\mathrm{Ri_f}$	Richardson number based on actual burner exit conditions
$\mathrm{Ri_s}$	effective source Richardson number
β^2	ambient fluid density divided by the density of the products of a stoichiometric reaction at the adiabatic flame temperature
ξ	nondimensional streamwise coordinate
ξ_L	nondimensional streamwise coordinate at the flame tip
ϕ	equivalence ratio (fuel-to-air ratio divided by the stoichiometric fuel-to air ratio)

Part 1

Entrainment and Chemistry of Buoyant Fire Plumes and Turbulent Jet Flames

Chapter 1

Introduction

The spread of fires through buildings is a complex phenomenon enveloping a number of scientific disciplines. Complex chemical processes, heat transfer, and fluid dynamics are all intimately interwoven in the physics describing the phenomenon. Recently, in an attempt to understand the flow of hot and potentially flammable gases through structures, a two-layer model has been developed, the basic assumption being that each compartment or room of the structure is composed of two homogeneous gas volumes or layers, the upper or ceiling layer containing the hot, buoyant gases, and the lower layer containing the cooler gases (Zukoski, 1978; Emmons, 1978). This model forms the basis for the current investigation.

As a fire begins to burn near the floor of a room, it entrains fresh air and produces a plume of hot buoyant gases that rise to the ceiling and spread out to form an upper layer. In essence, the plume pumps mass from the lower layer to the upper layer, changing its chemical composition and thermal energy in the process. When the fire is small, the plume is composed mostly of air. As the fire continues to burn, more mass reaches the ceiling layer and the layer thickens. Any vents or openings adjacent to the ceiling layer can cause material from this layer to "spill over" into other compartments while also allowing fresh air to enter the room from this or other openings. The danger from the spread of these hot gases is due to toxicity as well as to pyrolysis and possible subsequent ignition of fuel items located adjacent to the hot gases.

A different and potentially more dangerous scenario is presented when the fire plume is unable to entrain enough fresh air to completely burn all the fuel in the flame. This can occur when the flame is quite large or when the upper layer has thickened sufficiently to limit the area of the plume adjacent to fresh

air. In this case, combustible material builds up in the upper layer and can be spread throughout the structure. This could lead to the dangerous phenomenon of flashover if it ignites and spreads the fire throughout the room and possibly into other compartments.

The entire process is quite complicated, and modelling it properly depends strongly upon having reliable information to model each of its component processes adequately. In the past decade the fire plume itself has received a great deal of attention. Of particular interest were the entrainment rates of the plume and the global chemistry. Although a significant amount of work on entrainment in turbulent plumes was done before this period, most of it dealt with the far field, i.e., in regions far from the source where the temperature and density differ little from the ambient (Schmidt, 1941; Morton et al., 1956). Clearly, this is not applicable to room fires where the flame size is usually a significant fraction of the room height. For these cases, it is necessary to study entrainment in regions of high heat release and immediately downstream. A number of these studies (McCaffrey, 1979; Cox and Chitty, 1980; McCaffrey and Cox, 1982) have used local point measurements of mean axial velocity and mean density (or temperature), the product of which was then integrated to determine the plume mass flux. This technique has two inherent difficulties. First, small errors in the velocity or density measurements near the outer edges of the plume will be magnified when integrated over a large region. Also, defining the local vertical mass flux as the product of the local mean values of axial velocity and density ignores the correlation between fluctuations of the axial velocity and the density. This can cause significant errors since buoyancy is the driving force of the flow. A number of investigators have avoided these difficulties by making direct measurements of the plume entrainment. Cetegen (1982) measured the entrainment for plumes

that had entrained enough fresh air to be fuel-lean. As mentioned above, a more dangerous situation occurs when the plume is fuel-rich.

Beyler (1983) and Lim (1984) made measurements in plumes that were fuel-rich. In Beyler's investigation, the upper layer was not well mixed and the interface between the layers was not well defined. Although the experimental technique gave measurements of the entrainment, the distance over which this entrainment occurred was ambiguous. Lim's experiment had a much clearer interface and a well-mixed upper layer, but the instrumentation and technique used yielded results with relatively large uncertainties.

The purpose of the current investigation is the measurement of entrainment and resulting global chemistry from flames burning through the lower layer and into the upper layer. Since the material in the upper layer is vitiated, a flame burning into this layer entrains fresh air only over a limited fraction of its length. Entrainment in the lowest regions of the flame then becomes quite important and the resulting limited fresh air supply can significantly affect the global chemistry of the fire.

As an aside to this work, the experimental technique was modified in order to study entrainment in free turbulent jet diffusion flames from the momentum-dominated to the buoyancy-dominated regimes. This technique allowed a more direct measurement of the entrainment than the point-measurement technique employed by Becker and Yamazaki (1978) in developing their comprehensive model of the fully turbulent jet diffusion flame.

This report describes measurements of plume entrainment by axisymmetric buoyant diffusion flames burning through a region of fresh air into a region of combustion products. Measurements of the resulting chemical composition of

the upper layer are also presented. The fuel used was natural gas and diffusion flames from 20 to 200 kW were formed above a 0.19 m diameter burner. The interface between the upper and lower layer was maintained at a constant height of between 0.01 and 0.23 m above the burner surface. The initial Reynolds number of the fuel, based on the burner diameter, varied from 150 to 1500, while the initial Richardson number was in the range of 10^{-1} to 10. In addition, measurements of entrainment and flame height from fully turbulent jet diffusion flames are presented. Hydrogen flames from a 4.25 mm diameter nozzle were used in this part of the work and had heat release rates from 45 to 120 kW and effective source Reynolds and Richardson numbers on the order of 25,000 and 10^{-7}, respectively.

Chapters 2 and 3 concern the work on buoyant fire plumes, while the study of turbulent jet diffusion flames is presented in Chapter 4.

The experimental technique used for entrainment and upper layer chemistry measurements is described in Chapter 2. By allowing the chemical composition in a well-mixed upper layer to reach steady state, we were able to measure this composition and to determine from these measurements the entrainment of lower-layer fresh air into the plume. The chemical analysis of the various species in the hot upper layer was performed using a gas chromatograph with multiple-column switching.

The measurements of near-field plume entrainment and upper layer chemistry are presented in Chapter 3. It is found that the plume entrainment near the burner is nearly linear with the length of the entrainment region and essentially independent of the fuel flow rate. Comparing the results with other entrainment results (Cetegen, 1982; Beyler, 1983), we found that the initial buoyancy of the plume and the resulting large structures formed directly above the burner surface

appear to have a significant effect on the entrainment in the near field. The results of chemical analysis of the upper layer are also presented in this chapter. For lean fires, the reaction is essentially complete and the excess air simply dilutes the products of combustion, while for rich fires, oxidation of various chemical intermediates appears to "freeze" before completion, leading to excess hydrogen and highly toxic amounts of carbon monoxide.

The entrainment and flame height measurements for fully turbulent jet diffusions flames are presented in Chapter 4. There appear to be two entrainment regimes separated by a transition region. The momentum-dominated regime has a constant nondimensional plume mass flux. In the current experiments, this constant value was determined to be substantially larger than that measured by Becker and Yamazaki (1978). In the buoyancy-dominated regime, the nondimensional plume mass flux increased with the nondimensional streamwise length, as expected from dimensional and similarity arguments. Flame height measurements are also presented.

The calculations required for reduction of the natural gas flame data and the uncertainty analysis are detailed in Appendix A, and the tabulated results are presented in Appendix B.

Chapter 2

Experimental Technique

The present investigation is concerned with the entrainment and chemistry of buoyant fire plumes burning from an environment of quiescent fresh air across an interface into an environment of hot combustion products as shown in figure (2.1). This two-environment approach follows the current models of room fires in which the room is assumed to consist of two homogeneous gas volumes or layers, the upper or ceiling layer containing the hot-buoyant products of the fire, and the lower or floor layer containing the cooler gases. In this way the current investigation models the chemistry and entrainment of room fires when the fire plume itself burns across the floor layer and plunges into the ceiling layer.

2.1 Plume Entrainment Measurement Technique

In recent years, direct measurements of jet and plume entrainment have been used to avoid the difficulties inherent with integrating point measurements, especially at the outer edges of the plume or jet where small errors in velocity or density measurements can prove fatal (Ricou and Spalding, 1961; Becker and Yamazaki, 1978; Cox and Chitty, 1980; McCaffrey, 1979). These direct methods have worked on the principle of dividing the axial extent of the jet or plume into two distinct sections and measuring the entrainment over one of these sections. In this same way, the current experiment used the two-layer model of fire-involved rooms to divide the entraining region. Fresh air was allowed to be entrained only over a certain axial region of the flame. Above this, the flame products from a well-stirred upper layer were re-entrained. By maintaining the interface at a given location and allowing the chemical composition of the upper layer to reach steady state, we were able to measure the composition and then calculate the entrainment of fresh air into the plume.

The concept is shown schematically in figure (2.2). Fuel is delivered to the plume at a flowrate $\dot{m}_f$. As it burns, it entrains a mass of air, $\dot{m}_e$, from below the interface. This air is heated and chemically changed as it reacts with the fuel and is transported via buoyancy across the interface to the upper layer where it remains in this stably stratified, well-mixed region. The total mass flow of the plume to the upper layer is then $\dot{m}_f + \dot{m}_e$. In addition, air enters the upper layer at a rate $\dot{m}_i$ due to mixing along the interface separating the two layers. Because this interface is stably stratified, we would expect that this mixing entrainment would be small. In fact, using smoke to visualize the flow along the interface, we observed no mixing and so the entrainment, $\dot{m}_i$, was assumed to be negligible.

The method used to measure the entrainment mass flux was similar to that used by Cetegen (1982) and Lim (1984). Measuring the composition of the gas in a well-mixed upper layer allows calculation of the ratio, $\dot{m}_e/\dot{m}_f$.

2.1.1 Chemistry Equations

The buoyant plume was produced by a natural gas diffusion flame in air. The chemical composition of natural gas is represented as

$$a_1 CH_4 + a_2 C_2H_6 + a_3 C_3H_8 + a_4 N_2 + a_5 CO_2 \,, \tag{2.1}$$

where the a_i are the mole fractions determined by an analysis of the gas by the Southern California Gas Company. The composition varies only slightly from week to week and a typical representation is given in Table **2.1**.

The chemical composition of dry air was taken as

$$b_1' O_2 + b_2' N_2 + b_4' CO_2 + b_5' Ar \,, \tag{2.2}$$

where the constants b_i' were given by their standard values ($b_1' = 0.2095$, $b_2' = 0.7809$, $b_4' = 0.0003$, $b_5' = 0.0093$) or were measured. In addition, the vapor

pressure of water in laboratory air was calculated by using a polynomial fit to the Smithsonian vapor pressure data (Smithsonian Inst., 1939). We calculated the vapor pressure for the wet-bulb temperature and then corrected it to atmospheric conditions, using the dry-bulb temperature and laboratory barometric pressure. The vapor pressure was then divided by the laboratory pressure to give the mole fraction of water vapor in air. The chemical composition air is then given by

$$b_1O_2 + b_2N_2 + b_3H_2O + b_4CO_2 + b_5Ar\,, \tag{2.3}$$

where

$$b_i = (1 - b_3)b_i', \qquad i = 1, 2, 4, 5\,. \tag{2.4}$$

The combustion reaction of 1 mole of natural gas and I moles of air can then be represented as

$$\begin{aligned} &a_1CH_4 + a_2C_2H_6 + a_3C_3H_8 + a_4N_2 + a_5CO_2 \\ &+I(b_1O_2 + b_2N_2 + b_3H_2O + b_4CO_2 + b_5Ar) \Rightarrow \\ &x_1H_2 + x_2O_2 + x_3N_2 + x_4CH_4 + x_5CO + x_6CO_2 + x_7H_2O \\ &+x_8C_8H(s) + x_9C_2H_2 + x_{10}C_2H_4 + x_{11}C_2H_6 + x_{12}Ar\,, \end{aligned} \tag{2.5}$$

where the selected products are a liberal list of products obtained for reactions of natural gas and air. Soot is represented by the empirical formula $C_8H(s)$ (Glassman, 1977). In this equation there are thirteen unknowns (I, x_1, x_2, ..., x_{12}).

The unknowns in **2.5** can be evaluated by using the five conservation-of-atoms equations for C, H, O, N, and Ar, as well as determining, through gas analysis, independent relationships between the various x_i. If eight such relationships are found, the equations can be solved.

2.1.1.1 Conservation of atoms

The five equations for conservation of atoms can be written as

$$a_1 + 2a_2 + 3a_3 + a_5 + Ib_4 = x_4 + x_5 + x_6 + 8x_8 + 2x_9 + 2x_{10} + 2x_{11} \quad (2.6a)$$

$$2a_1 + 3a_2 + 4a_3 + Ib_3 = x_1 + 2x_4 + x_7 + \tfrac{1}{2}x_8 + x_9 + 2x_{10} + 3x_{11} \quad (2.6b)$$

$$2a_5 + I(2b_1 + b_3 + 2b_4) = 2x_2 + x_5 + 2x_6 + x_7 \quad (2.6c)$$

$$a_4 + Ib_2 = x_3 \quad (2.6d)$$

$$Ib_5 = x_{12}\,. \quad (2.6e)$$

For reasons dealing with the gas analysis technique, which will become clear later, **2.6c** and **2.6e** were combined and the equations were rewritten as

$$-B_C I + Y_C x_3 + 8x_8 = A_C \quad (2.7a)$$

$$x_7 - B_H I + Y_H x_3 + \tfrac{1}{2}x_8 = A_H \quad (2.7b)$$

$$x_7 - B_O I + Y_O x_3 = A_O \quad (2.7c)$$

$$-B_N I + Y_N x_3 = A_N\,, \quad (2.7d)$$

where

$$A_C = a_1 + 2a_2 + 3a_3 + a_5 \quad (2.8a)$$

$$A_H = 2a_1 + 3a_2 + 4a_3 \quad (2.8b)$$

$$A_O = 2a_5 \quad (2.8c)$$

$$A_N = a_4 \quad (2.8d)$$

$$B_C = b_4 \quad (2.9a)$$

$$B_H = b_3 \quad (2.9b)$$

$$B_O = 2(b_1 + c_1 b_5) + b_3 + 2b_4 \quad (2.9c)$$

$$B_N = b_2 \quad (2.9d)$$

$$Y_C = y_4 + y_5 + y_6 + 2y_9 + 2y_{10} + 2y_{11} \tag{2.10a}$$

$$Y_H = y_1 + 2y_4 + y_9 + 2y_{10} + 3y_{11} \tag{2.10b}$$

$$Y_O = 2(y_2 + c_1 y_{12}) + y_5 + 2y_6 \tag{2.10c}$$

$$Y_N = 1\,, \tag{2.10d}$$

and each of the y_i is defined as

$$y_i = x_i / x_3\,, \tag{2.11}$$

and c_1 is a determined constant that will be described in detail later. All of the y_i in **2.10** can be determined from the gas analysis, as will be shown later, with the exception of y_2 and y_{12}. However, for a certain value of c_1, the quantity $y_2 + c_1 y_{12}$ can also be determined. Because of this, all the coefficients in **2.8**, **2.9**, and **2.10** are determinable. So **2.7** becomes a set of four linear equations with four unknowns and can be solved. The solution and the uncertainty analysis are given in Appendix A.

The original method of solving the conservation-of-atoms equations, **2.6**, was to measure y_7 in addition to the other y_i shown in **2.10**. Then the quantity $x_7 = y_7 x_3$ in **2.7** is absorbed into Y_H and Y_O, and the set of equations becomes the overconstrained set of four equations in three unknowns. This created no problem, however, since the coefficients are not exact numbers but rather are measured quantities with experimental uncertainties. This method of solving **2.7** yielded satisfactory solutions for I, x_3, and x_8; however, the measured values of y_7 for water vapor had an uncertainty much larger than that for any of the other measured quantities. Since the problem was originally overconstrained, the value of x_7 was determined by neglecting the measured values of y_7 and solving the deterministic system shown in **2.7**. Indeed, the variability of the calculated

quantity, x_7, was less than that obtained through direct measurements, since the quantities used to determine x_7 were measured with a high degree of precision.

Once I has been calculated, the entrainment mass flux can be calculated from

$$\dot{m}_e = \frac{\mathrm{M}_\infty}{\mathrm{M}_\mathrm{f}} I \dot{m}_f \,, \tag{2.12}$$

where M_∞ and M_f are the molecular weights of air and fuel, respectively.

2.2 Upper Layer Chemistry Analysis

Once the entrainment has been calculated along with the mole quantities x_3, x_7, and x_8, y_7 and y_8 can be found from **2.11**. Such is not the case, however, for y_2 and y_{12}, since x_2 and x_{12} are not known. But x_{12} can be calculated from **2.6e** and then using **2.11**, x_2 can be calculated from

$$x_2 = x_3(y_2 + c_1 y_{12}) - c_1 x_{12} \tag{2.13}$$

so that y_2 and y_{12} can be determined. Once all the y_i are determined, the mole fractions of the sample can be calculated as

$$\mathrm{Y}_i = \frac{y_i}{\sum_{k=1}^{12} y_k} \,. \tag{2.14}$$

2.2.1 Standard Heat of Reaction

Once the composition of the products in **2.5** has been determined, the standard heat of reaction can be determined per mole of natural gas. The heat of formation for natural gas is

$$\Delta H^\circ_{n.g.} = a_1 \Delta H^\circ_{\mathrm{CH_4}} + a_2 \Delta H^\circ_{\mathrm{C_2H_4}} + a_3 \Delta H^\circ_{\mathrm{C_3H_8}} + a_4 \Delta H^\circ_{\mathrm{N_2}} + a_5 \Delta H^\circ_{\mathrm{CO_2}} \tag{2.15}$$

and for air is

$$\Delta H^\circ_{air} = b_1 \Delta H^\circ_{\mathrm{O_2}} + b_2 \Delta H^\circ_{\mathrm{N_2}} + b_3 \Delta H^\circ_{\mathrm{H_2O}} + b_4 \Delta H^\circ_{\mathrm{CO_2}} + b_5 \Delta H^\circ_{\mathrm{Ar}} \,. \tag{2.16}$$

Likewise, for the products, the heat of formation per mole is

$$\Delta H_p^\circ = \sum_{k=1}^{12} \mathrm{Y}_k \Delta H_k^\circ \,, \tag{2.17}$$

where ΔH_k° is the standard heat of formation for the kth component of the product. Therefore, for the reaction shown in **2.5**, the heat of reaction at standard conditions is

$$\Delta H_r^\circ = N_p \Delta H_p^\circ - I \Delta H_{air}^\circ - \Delta H_{n.g.}^\circ \,, \tag{2.18}$$

where N_p is the number of moles of product for the reaction.

2.3 Stoichiometry and Equivalence Ratio

For the stoichiometric reaction of natural gas and air, **2.5** simpifies to

$$\begin{aligned} &a_1\mathrm{CH_4} + a_2\mathrm{C_2H_6} + a_3\mathrm{C_3H_8} + a_4\mathrm{N_2} + a_5\mathrm{CO_2} \\ &+ I_s(b_1\mathrm{O_2} + b_2\mathrm{N_2} + b_3\mathrm{H_2O} + b_4\mathrm{CO_2} + b_5\mathrm{Ar}) \Rightarrow \\ &\hat{x}_3\mathrm{N_2} + \hat{x}_6\mathrm{CO_2} + \hat{x}_7\mathrm{H_2O} + \hat{x}_{12}\mathrm{Ar} \end{aligned} \,, \tag{2.19}$$

where I_s is the number of moles of air required for the complete combustion of one mole of fuel. The equations of conservation of atoms can now be simplified to

$$a_1 + 2a_2 + 3a_3 + a_5 + I_s b_4 = \hat{x}_6 \tag{2.20a}$$

$$2a_1 + 3a_2 + 4a_3 + I_s b_3 = \hat{x}_7 \tag{2.20b}$$

$$2a_5 + I_s(2b_1 + b_3 + 2b_4) = 2\hat{x}_6 + \hat{x}_7 \tag{2.20c}$$

$$a_4 + I_s b_2 = \hat{x}_3 \tag{2.20d}$$

$$I_s b_5 = \hat{x}_{12} \,. \tag{2.20e}$$

Solving for I_s gives

$$I_s = (4a_1 + 7a_2 + 10a_3)/2b_1 \,. \tag{2.21}$$

In addition, the mole quantities for the stoichiometric reaction, and hence the mole fractions, can be obtained.

Once I_s is calculated, the equivalence ratio for any reaction can be simply determined by

$$\phi = I_s/I \,. \tag{2.22}$$

As with the calculations in other sections, the uncertainty analysis for the calculations in this section is given in detail in Appendix A.

2.4 Gas-Analysis Technique

Up to now, the assumption has been made that we could measure the quantities y_1, y_4, y_5, y_6, y_9, y_{10}, y_{11}, and the sum $y_2 + c_1 y_{12}$ for a known constant c_1. The goal of the gas-analysis system, which will be discussed presently, was to measure these.

The system consisted of a Hewlett-Packard HP 5890A Gas Chromatograph with an HP 3392A Integrator and an HP 19405A Sampler/Event Controller. The process of gas chromatography is a combination of art and science, which is described in detail elsewhere (McNair and Bonelli, 1968; Thompson, 1977). Briefly, gas-solid chromatography works on the principle that as a gas sample mixture is carried by an inert gas through a column packed with active solids, such as molecular sieves or porous polymers, the different components of the gas mixture will be adsorbed or retained by the solids at different rates. The sample-gas components are separated in this manner and carried by the inert gas to a detector/recorder, which indicates the presence and measures the amount of the component in the column effluent. The separation process is a strong function

of the carrier gas used and its flow rate, the column size and length, the solids used, and the column temperature. All of these must be considered to provide proper analysis of the gas sample to be tested.

The gas chromatography system is shown schematically in figure (2.3) and consists of:

1. a carrier gas supply;
2. a sample inlet system;
3. a column and switching system;
4. a temperature-controlled oven;
5. a detector/recorder system.

2.4.1 Gas-Analysis System Design

The first step in designing the system was to identify the components to be measured and their quantities. These are shown in Table **2.2**. Many of these chemical components impose some limitation on the choices available for the system components.

2.4.1.1 Detector and recorder

The most common types of detectors and those considered for this analysis were the flame ionization detector (FID) and the thermal conductivity detector (TCD). The FID measures the conductivity of the column effluent flowing in a hydrogen-air flame. The effluent is mixed with the hydrogen. Ions produced by the sample component flowing through the flame change the conductivity of the flame and are thus measured. Difficulties with this detector occur when the components produce little or no response. Such components include hydrogen, nitrogen, carbon monoxide, carbon dioxide, water vapor, and oxygen, making

the FID impractical for our case.

The TCD detects the difference in thermal conductivity between the column effluent and a reference flow of carrier gas alone. The thermal conductivity is determined by measuring the resistance of a heated tungsten-alloy filament in the flow using a Wheatstone bridge. The thermal conductivity of a gas determines its ability to conduct heat away from the filament, changing its temperature and thus its resistance.

The TCD was selected for use in the present work. Oxygen in the sample can cause oxidation of the TCD filament if its temperature is high enough and sufficient oxygen is present in the sample. This was avoided by reducing the sample volume and maintaining a relatively low filament temperature. In addition, the TCD filament, a tungsten-rhenium alloy, had a chemically passivated surface to protect against oxidation.

The recorder was the HP 3392A Integrator, which accepted the TCD voltage and detected and integrated the peaks in the signal caused by the change in thermal conductivity as a sample component was eluted. The integrator was capable of plotting the signal, detecting and identifying the peaks, and integrating the areas, all with a high degree of accuracy. In addition, calibrations were computed, and comparisons with the calibrations allowed the integrator to report the sample quantities directly. Combined with the controller and chromatograph, the integrator allowed the whole run to be automated insuring reproducibility.

2.4.1.2 Carrier gas

The carrier gas was chosen with the following requirements in mind:

1. It must be inert with the sample.
2. It must be compatible with the TCD.

3. It must minimize diffusion of the sample components.

The carrier gases most commonly used are hydrogen, helium, nitrogen, and argon. Since hydrogen, nitrogen, and argon are components of the sample gas, they would be unsuitable as carrier gases. Also, hydrogen causes obvious difficulties if it enters the hot detector in the presence of oxygen. Since the TCD responds to any gas whose thermal conductivity is different from that of the carrier gas, helium is compatible with the detector. Because the thermal conductivity of helium is much higher than that for all the components in the sample except hydrogen, the response to a mixture of helium and one of these components was easily measured and was in fact a linear combination of the thermal conductivities of helium and the component. Although helium does not have a high molecular weight to minimize diffusion, it was the preferred carrier gas and was selected for use because of its high thermal conductivity, which allowed greater sensitivity in measurements of the heavier gases.

The use of helium as the carrier gas did create some problems. First, the diffusivity of hydrogen in helium is so large that elution times for hydrogen were required to be short in order to minimize the diffusion. The second problem was more serious. The thermal conductivity of a helium-hydrogen mixture has been measured by Hansen et al. (1964) and is shown qualitatively in figure (2.4). The thermal conductivity initially drops with increasing amounts of hydrogen to a minimum at 13% mole fraction hydrogen. Not only is the response curve nonlinear, but, for a given thermal coductivity, it is double-valued! This is clearly unacceptable and makes quantitative determinations of hydrogen suspect. Reliable results can be obtained, however, if the hydrogen concentration is large enough to be measured by the detector (larger than the minimum detectable quantity, MDQ), but small enough that the hydrogen concentration in helium

is well below the concentration of minimum thermal conductivity. Indeed, in this range the thermal conductivity is nearly linear with hydrogen concentration. Thus, when hydrogen is in the sample, it is required to choose a sample size small enough to guarantee that the hydrogen quantity in the sample is in the desired range. A 0.1 cc sample size was determined to provide good response for hydrogen samples in the range from 0.05% to 40% mole fraction.

2.4.1.3 Sample inlet system

The most precise method of introducing the gas sample into the system is through a gas-sample valve with a sample loop as shown in figure (2.5). The valve is a 6-port rotary valve (Valco Series HP). In the off position, the sample is allowed to flow freely through the sample loop to purge the loop and introduce the sample. At the same time, the carrier gas flows directly from its source to the column. When the valve is switched to the on position, the carrier gas flushes the sample from the loop into the column, while the sample stream itself is isolated. Because of water vapor in the sample, it was necessary to heat the valve and sample loop in a controlled compartment at 80°C to prevent condensation.

2.4.1.4 Column selection and switching

The testing requirements of the system created some unique problems. There is no single column that will separate all the desired components in a reasonable time. In fact, some of the sample components can actually reduce the performance of some of the most typical packing solids used. To alleviate these problems a multicolumn system and switching valves were used. Design of the system required an analysis of the various separations desired.

Since hydrogen is often the most difficult component to quantify, it was considered first. The sample volume and carrier gas selections were discussed

above and determined to be sufficient. Separation of hydrogen and air (or other components) can be accomplished with a molecular sieve, silica gel, or porous polymer, although, in the case of the porous polymer, retention times would be prohibitively long for some of the other components, if the column was long enough to separate the hydrogen. Separation of oxygen or argon from nitrogen requires the use of a molecular sieve, preferably MS 5A, which would also allow satisfactory separation of hydrogen, methane, carbon monoxide, and ethane. The only difficulty in the separation of these so-called "light gases" on MS 5A is the separation of argon and oxygen, which are not separated on these columns without the use of subambient temperatures and/or long columns, both of which make quantification difficult. Since neither of these options was desirable, it was determined to allow argon and oxygen to elute together.

The unsaturated C_2 hydrocarbons and carbon dioxide do not elute satisfactorily from MS 5A columns, which must therefore be protected from these sample constituents. This required the use of a valve-switching system as shown in figure (2.6) to isolate and bypass the MS 5A column, while the C_2 hydrocarbons and carbon dioxide elute from a different column. In this arrangement the "light gases" are eluted quickly from the first column (a porous polymer) and enter the second column, the MS 5A column, which is then isolated (simply storing its contents while the "heavy gases" elute from the first column). Then the MS 5A column is again put in-line and the previously stored gases continue their separation and elution. Since storing the light gases can cause the hydrogen peak to diffuse, resulting in a loss of resolution of the peak, it is preferable to elute the hydrogen from the MS 5A before isolating this column to elute the "heavy gases." This juggling of elution times is an art and is accomplished through adjustments to column lengths, column temperatures, valve switching times, and

carrier gas flowrates.

Separation of the C_2 hydrocarbons and carbon dioxide is easily accomplished with any of a number of the porous polymer columns. These columns also separate water which deactivates the MS 5A column.

Water vapor tends to give unreliable measurements with the use of polymer columns when low concentration are present. Although this problem was minimized by using a very polar porous polymer, Porapak T, the results for water were determined to be less reliable than desired. For that reason, the peak obtained for water was neglected in the calculations.

Methane is separated by both the Porapak T and the MS 5A. Separating methane sufficiently from air in the Porapak T column, however, requires a long column, which is undesirable because this would greatly increase the length of time necessary for water vapor, the slowest component, to elute.

2.4.2 Final Design

The final conceptual design is shown in figure (2.7). After the testing of various samples to determine retention times as a function of column temperature and length, the following design was chosen as suitable:

1. The first column was $6' \times 1/8''$ stainless steel tubing with 80/100 mesh size Porapak T.
2. The second column was $8' \times 1/8''$ stainless steel tubing with 80/100 mesh size washed molecular sieve 5A.
3. The carrier gas, helium, had a flowrate of 20.0 cc/min.
4. The columns were maintained at 80°C for the first 13.00 minutes. This would allow all the components except water vapor to be eluted. Then to

speed up the elution of water vapor, the temperature of the controlled oven was increased at a rate of 20°C per minute to a final temperature of 120°C. It was held at this temperature until the water vapor eluted completely.

The history of the sample component elution is shown schematically in figure (2.8). Initially, the entire sample is introduced into the Porapak T column, which is in series with the MS 5A column (figure (2.8a)). The "light" gases (hydrogen, oxygen, nitrogen, argon, carbon monoxide) flow through the Porapak T column together while the "heavy" gases (methane, carbon dioxide, ethylene, ethane, acetylene, and water vapor) are retained by the column in respectively increasing degrees. The methane is retained a small amount so that it is only slightly behind the "light" gases as shown in figure (2.8b). The "light" gases and methane are carried into the MS 5A column and begin separating in the order of hydrogen, oxygen plus argon, nitrogen, methane, and carbon monoxide (figure (2.8c)). (Note that the methane, which enters the MS 5A column after the carbon monoxide, actually passes the carbon monoxide in this column.) The hydroden peak elutes from the column at 1.70 minutes, and at 1.90 minutes the MS 5A column is isolated and bypassed with the oxygen plus argon, nitrogen, methane, and carbon monoxide stored within, as shown in figure (2.8d). For the next four minutes, carbon dioxide, ethylene, ethane, and acetylene are eluted directly from the Porapak T column at 2.57, 2.73, 2.97, and 5.14 minutes, respectively (figure (2.8e)). Only water vapor remains in the Porapak T column as the MS 5A column is switched back in line at 5.90 minutes (figure (2.8f)), causing the previously stored gases to elute in the order oxygen plus argon, nitrogen, methane, and carbon monoxide at 6.57, 7.44, 9.28, and 11.56 minutes, respectively, as shown in figure (2.8g). After these peaks are completed, at 13.00 minutes, the flow is again switched to the Porapak T and the oven temperature

is increased (figure (2.8h)), allowing the water vapor peak to be eluted at 22.9 minutes.

2.4.3 Gas Chromatograph Calibration Technique

Quantitative measurements in gas chromatography are based on the assumption that as a component is eluted and the TCD signal produces its peak, the "amount" of the measured component is directly proportional to the area of its peak. This is true if the concentration is linear with the detector response. For the small sample volume used in this analysis, linearity was a sound assumption.

The method of calibration used is called "area normalization" and is a technique that is relatively insensitive to the size of the sample injected from one run to the next. The relationship for this technique is represented as

$$\mathrm{Y}_i = \frac{f_i A_i}{\sum_{k=1}^{n} f_k A_k}, \tag{2.23}$$

where Y_i is the mole fraction of the ith component in the sample, A_i its measured area, and f_i its response factor. If a known sample is input, **2.23** can be solved to determine the f_i.

This method was used for the sample shown in Table **2.3**, and the response factors, f_i, were determined for methane, carbon dioxide, carbon monoxide, hydrogen, oxygen, and nitrogen. The calibration was repeated a number of times to test repeatability and to measure uncertainties.

Calibration for the C_2 hydrocarbons were carried out in a similar fashion with a different calibration standard (which also contained nitrogen) in order to determine the f_i for ethylene, ethane, and acetylene (given the previous response factor for nitrogen).

The response factor for argon was not determined from calibration but rather

was taken from the standard results of Dietz (1967).

Finally, water vapor was calibrated in air using saturated conditions and condensing at a controlled temperature to produce a known content of water vapor in air. More than twenty such tests were run to guarantee linearity and repeatability. However, after careful analysis of the data, it became obvious that the uncertainties in the water vapor determinations were larger than the uncertainties that could be obtained by simply calculating the quantity of water vapor from **2.7**.

The calibrations varied only slightly over several months of testing, and these effects were taken into account.

2.4.4 Determination of y_i

From **2.11** and **2.23**, we find that the y_i are given by

$$y_i = \frac{f_i A_i}{f_3 A_3}, \qquad i = 1,4,5,6,7,9,10,11\,. \tag{2.24}$$

Also, the area under the oxygen plus argon peak is represented as

$$A_{2+12} = \frac{\mathrm{Y}_2}{f_2} + \frac{\mathrm{Y}_{12}}{f_{12}}\,. \tag{2.25}$$

Therefore,

$$\begin{aligned} \frac{f_2 A_{2+12}}{f_3 A_3} &= \frac{\mathrm{Y}_2}{\mathrm{Y}_3} + \frac{f_2}{f_{12}}\frac{\mathrm{Y}_{12}}{\mathrm{Y}_3} \\ &= y_2 + \frac{f_2}{f_{12}} y_{12}\,. \end{aligned} \tag{2.26}$$

So if c_1 is chosen as

$$c_1 = f_2/f_{12}\,, \tag{2.27}$$

then

$$y_2 + c_1 y_{12} = \frac{f_2 A_{2+12}}{f_3 A_3}\,, \tag{2.28}$$

and all the quantities desired of the gas analysis have been calculated. Each of these quantities has an uncertainty, which is calculated in detail in Appendix A.

2.5 Chemical Equilibrium Calculation

Proper modelling of the chemistry could be performed with a chemical kinetics code and flow modelling, but would be prohibitively difficult. Only if the flow was laminar and steady would such an analysis be feasible. Therefore, in an attempt to obtain what might be considered a zeroth-order approximation of the chemistry, calculations were made of the chemical equilibrium compositions of the combustion process as a function of the equivalence ratio. The computations were carried out with the CHEMKIN (Kee et al., 1980) interpreter and used a computation scheme developed by Sandia National Laboratory, Livermore, and modelled after the Stanford Equilibrium Code developed by Reynolds (1986). This code calculates the equilibrium composition of a reacting ideal gas mixture for fixed atomic composition, temperature, and pressure based on values of the species' Gibb functions provided by the user.

The code was used in two different modes. First, computations of equilibrium conditions at constant pressure and enthalpy, the latter evaluated from the input temperature and species mole fractions, returned an adiabatic flame temperature and the equilibrium chemical composition at this temperature. This is clearly an unrealistic estimate of the actual conditions but does provide a limiting case. More realistic estimates were obtained using a scheme that calculates the equilibrium state at a given temperature, pressure, and atomic population. These calculations can be expected to roughly model a reaction that quenches after having been "completed" at the given calculation temperature. In this respect, the calculations help approximate the temperature at which a given chemical constituent "freezes" in the reaction process. It must be emphasized,

however, that this is indeed a crude representation of the actual physics and chemistry of the problem.

2.6 Fire and Gas Sampling Experimental Facilities

The burner and hood assembly are the same as those used by Cetegen (1982) and are shown in figure (2.9). The well-mixed upper layer was produced by a 1.2 m cube, open on the bottom, placed over the flame at a given distance above the burner surface, the distance adjustable using a hoist/pulley mechanism. As the plume delivered material to the box, the box filled until gas spilled out from the bottom edges. The plume was then able to entrain fresh air only up to the interface, while the gas in the box was re-entrained into the upper layer region of the plume and mixed in this way. The entire process was allowed to run for more than 30 minutes to guarantee that the process had reached steady state. The location of the interface between the two layers was determined by the use of a shadowgraph technique.

A 0.19 m diameter burner was used to deliver natural gas fuel to the flame. The fuel passed through a 5 cm deep porous bed of 6.3 mm diameter spherical glass beads whose surface was made flat and flush with the outer metal edges of the burner. The sides of the burner were vertical and extended to the floor 70 cm below the burner surface. The fuel flow rate was measured using a Merriam laminar flowmeter and a Barocel differential pressure transducer connected to a Datametrics electronic manometer.

The entire burner and cube assembly was located in the center of a 2.4 m square area enclosed on the sides by a double layer of aluminum screen used to reduce the strength of flow disturbances present in the laboratory air. The screens were 2.4 m high and above them was a large hood, which removed exhaust

gases from the laboratory.

The sample was withdrawn through a 9.5 mm diameter stainless steel tube inserted into the upper layer at various depths, although the standard location was 90 cm above the interface and hence about 30 cm below the top of the box. The top of the probe drew in the sample through two areas of 1.5 cm^2, each separated by a distance of 5 cm. An aspirated chromel-alumel thermocouple was placed at the entrance of the probe and was shielded from any external radiation. The probe was placed at various heights in the box, although chemical analysis of samples removed at different probe heights showed only very slight variance with height. This differs with the observations of Beyler (1983) and suggests that the technique used in the current experiment allowed better mixing of the upper layer.

Gas samples withdrawn by the probe were transported by 6.4 mm copper tubing to a fiberglass prefilter and a 0.1 μm particle filter used to remove soot. The samples were then transported again by copper tube to the gas chromatograph sample-inlet valve. The tubes and filter were heated to 65°C to prevent water vapor from condensing. The residence time of the gas in the hot sections of the probe before reaching the constant temperature tubing was less than one second.

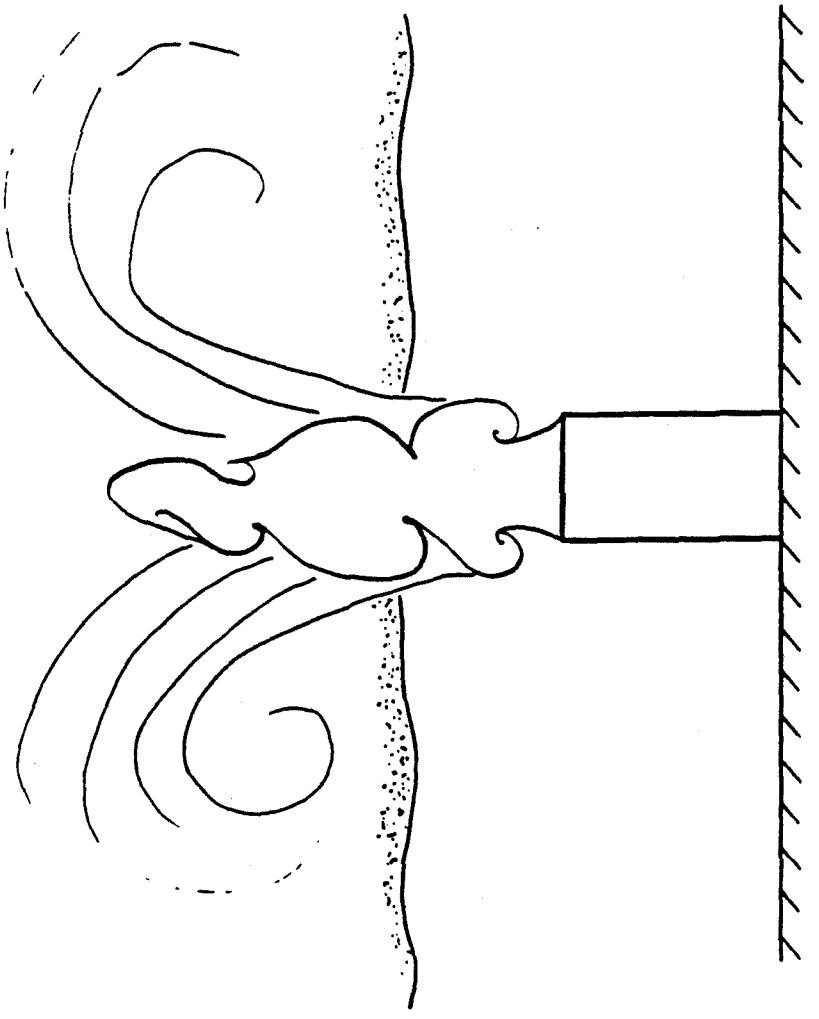

Figure (2.1) Fire Plume in a two-layer environment.

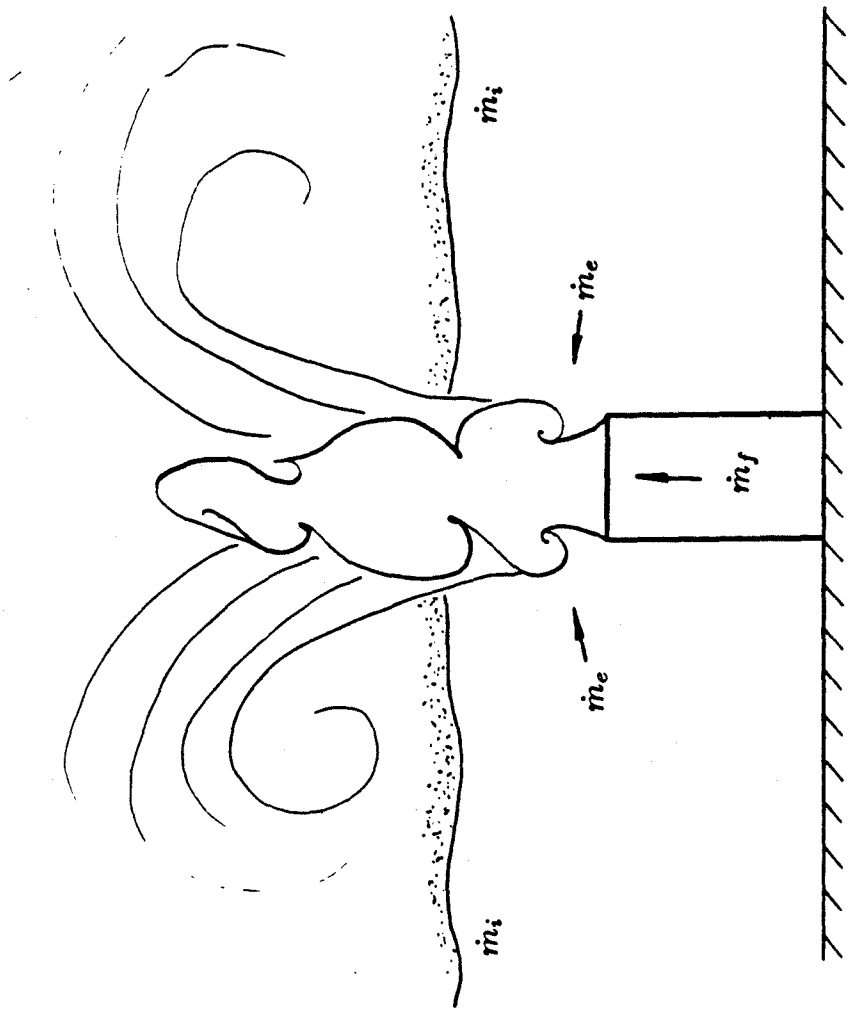

Figure (2.2) Mass flux contributions to the ceiling layer.

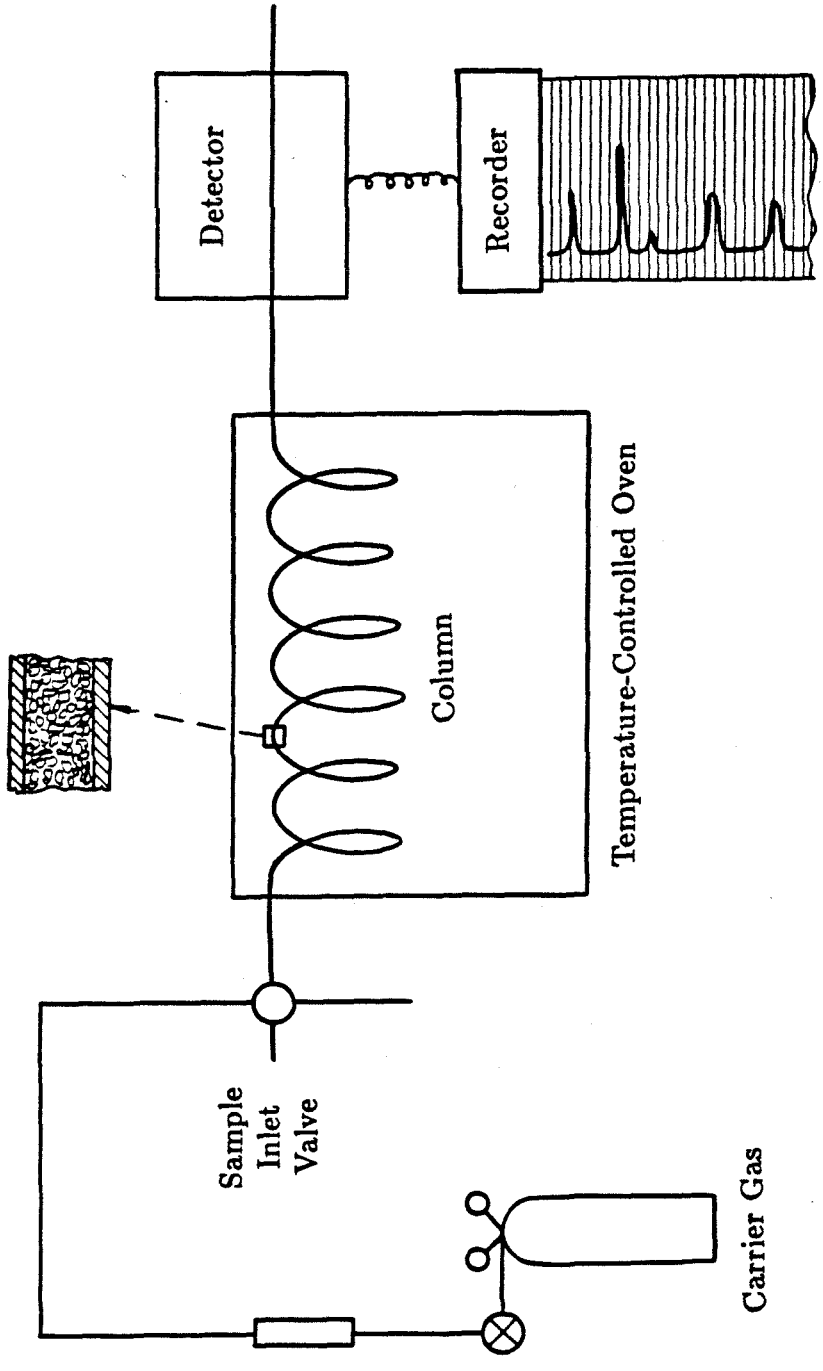

Figure (2.3) Basic gas chromatography system.

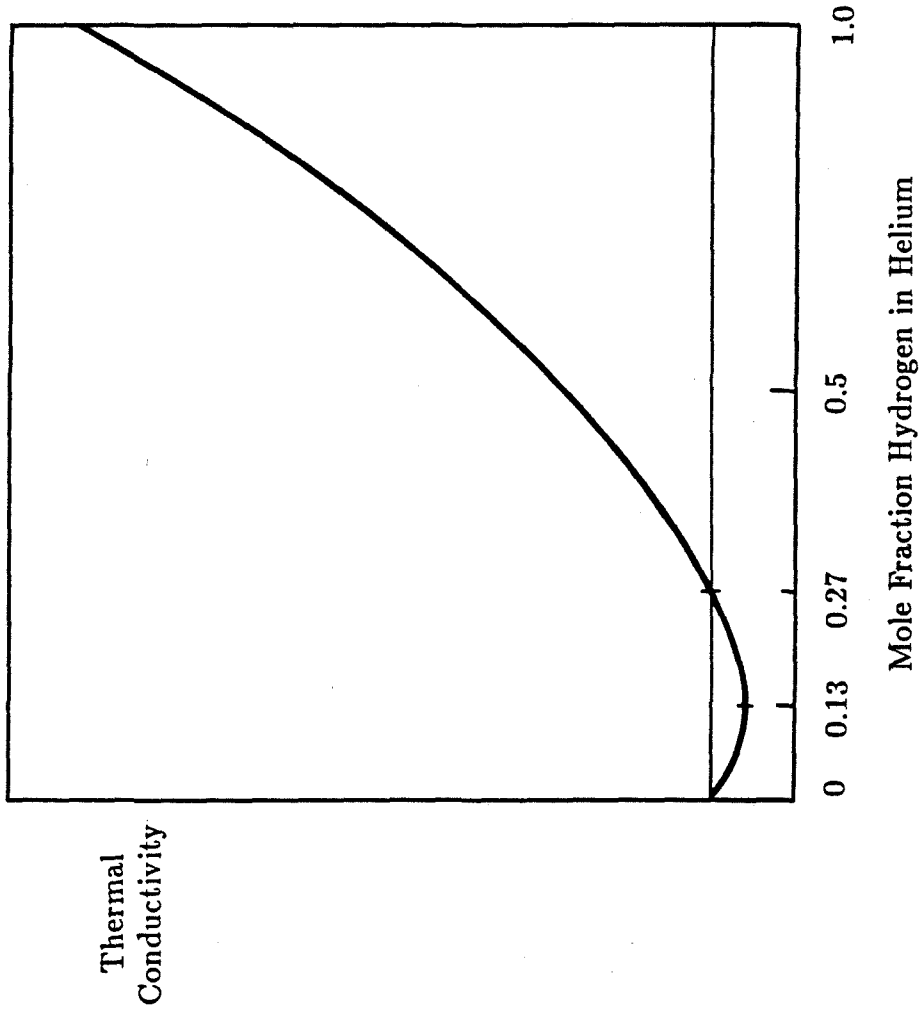

Figure (2.4) Thermal conductivity of a hydrogen-helium mixture.

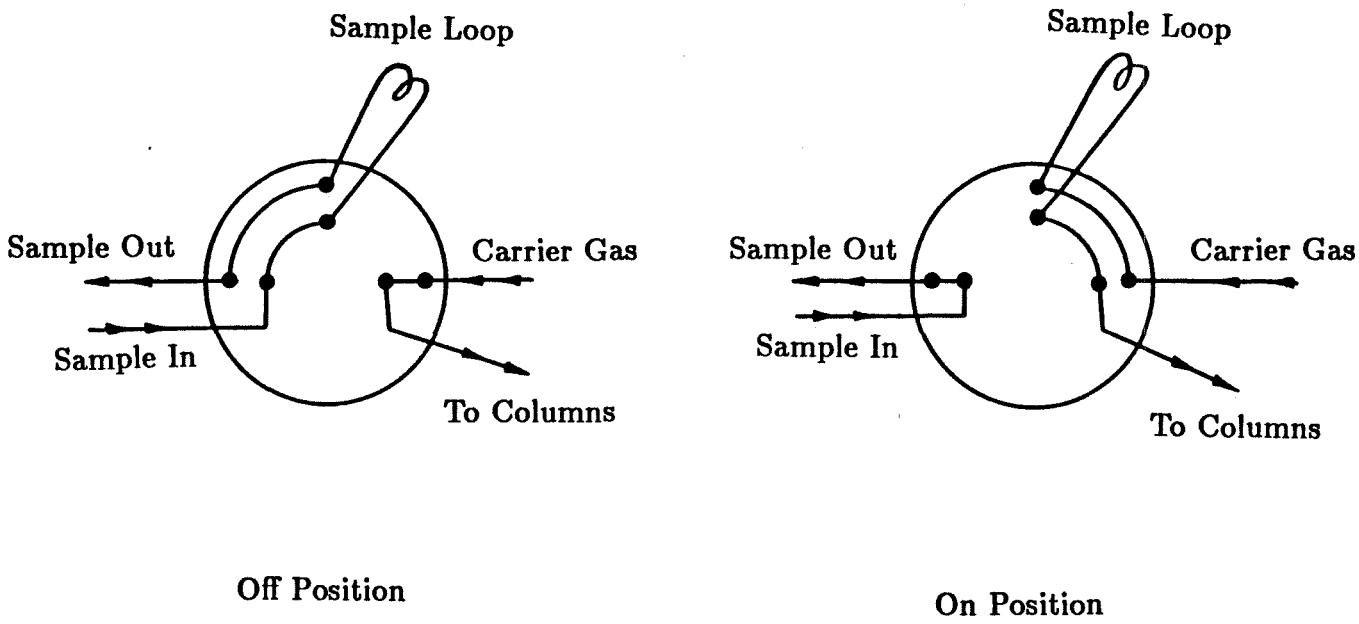

Figure (2.5) Gas sample valve system.

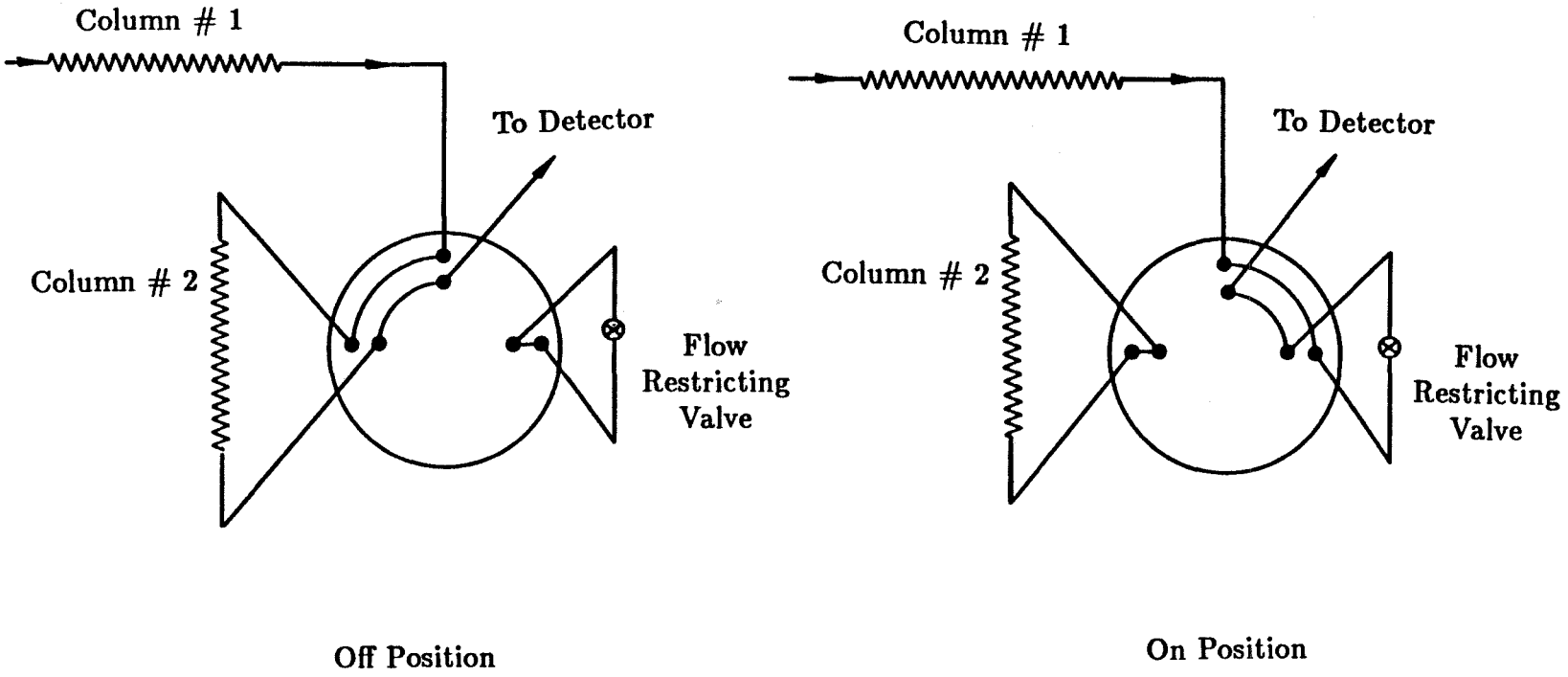

Figure (2.6) Series/bypass switching valve system.

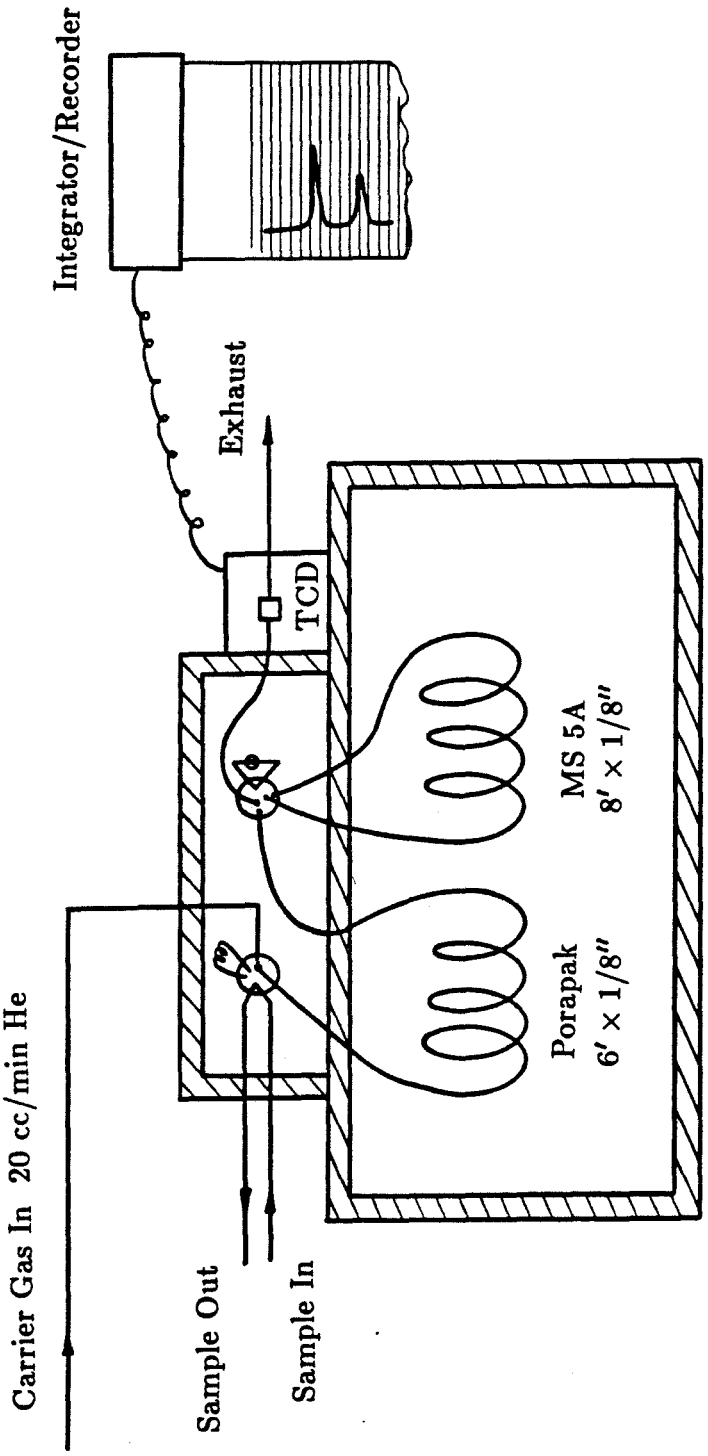

Figure (2.7) Gas chromatography system final design.

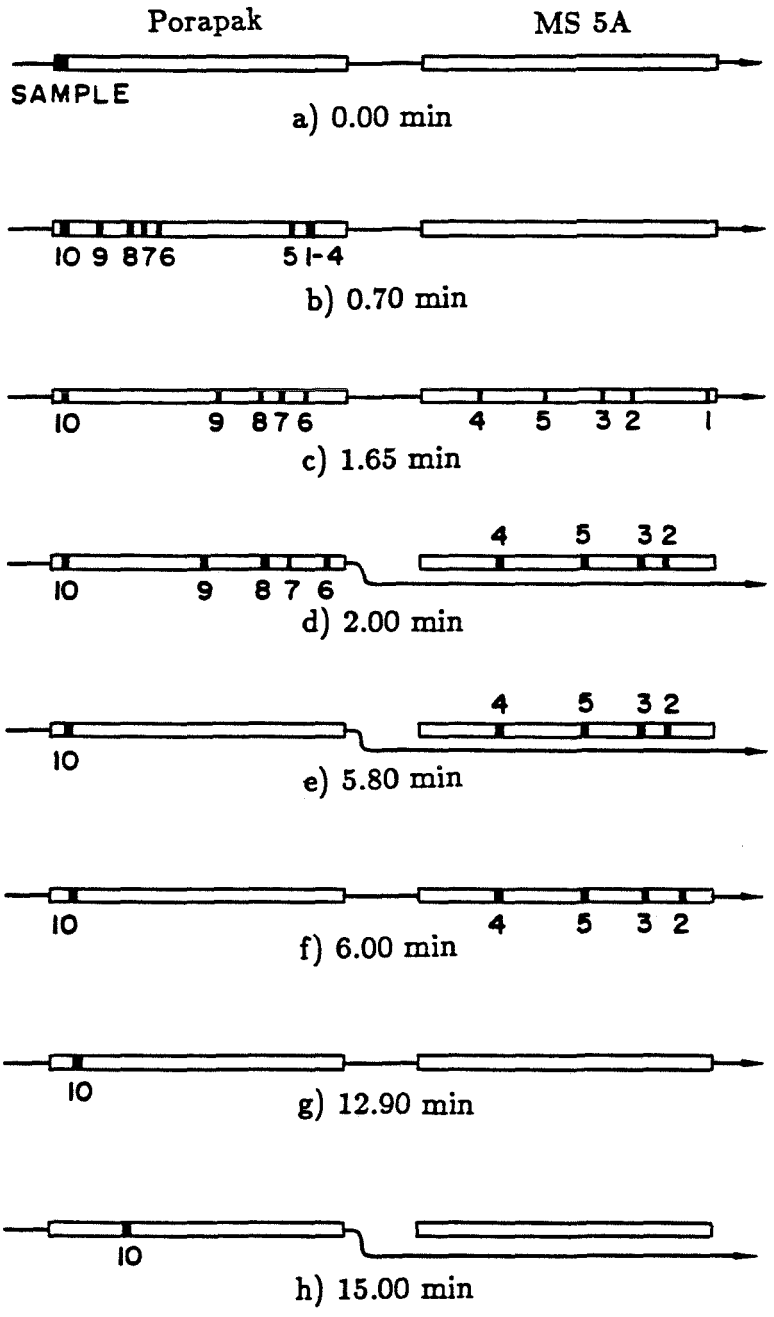

1: H_2
2: O_2
3: N_2
4: CO
5: CH_4
6: CO_2
7: C_2H_4
8: C_2H_6
9: C_2H_2
10: H_2O

Figure (2.8) History of the sample component elutions.

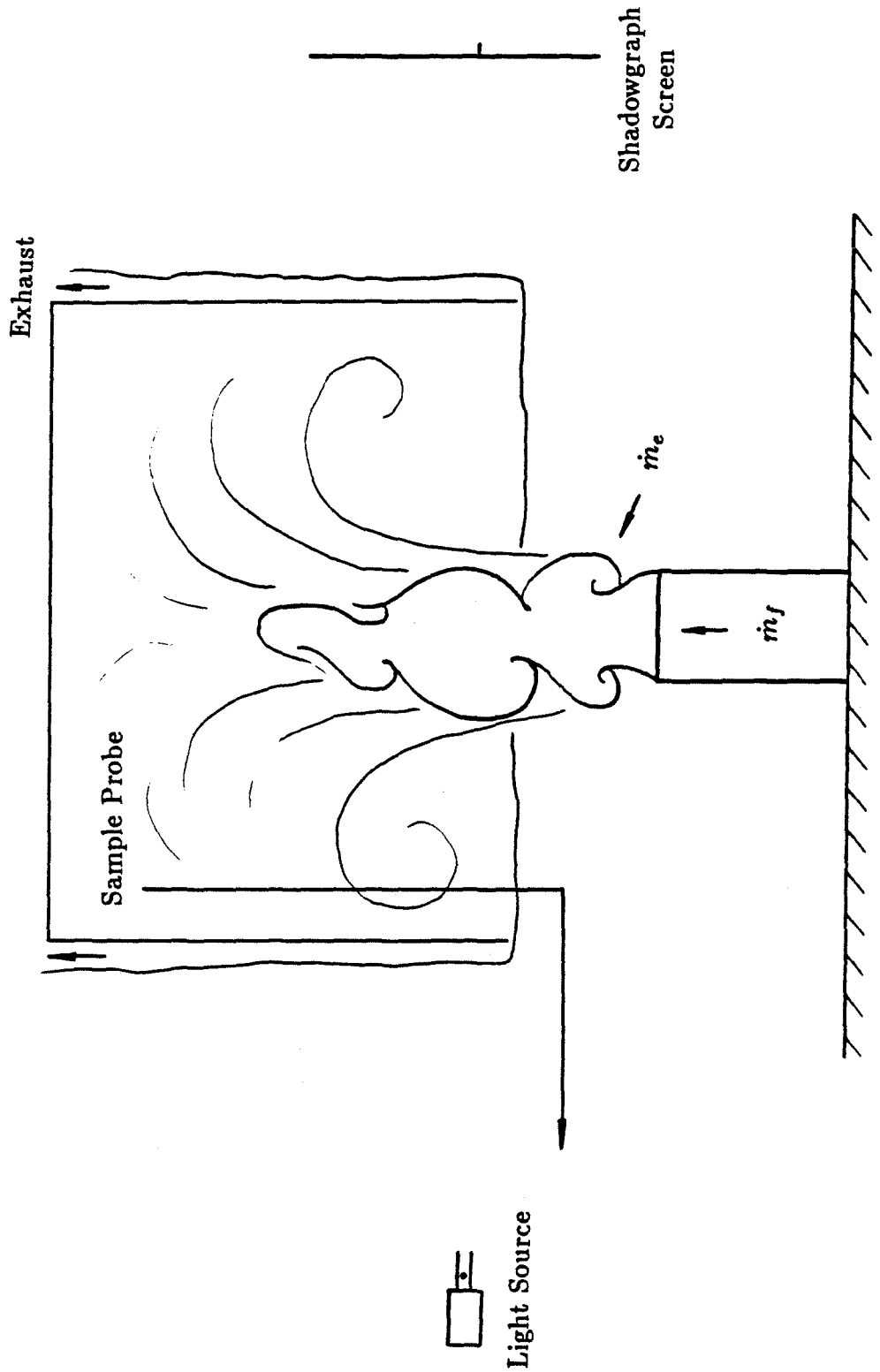

Figure (2.9) Burner and hood assembly.

Table 2.1. Typical Natural Gas Composition

molecular weight 17.51
heating value 35.3 kJ/ℓ
dynamic viscosity 108.9 μP

	Mole Fractions		
methane	0.9201	hexanes +	0.0005
ethane	0.0422	isobutane	0.0010
propane	0.0104	n-butane	0.0016
nitrogen	0.0159	isopentane	0.0004
carbon dioxide	0.0076	n-pentane	0.0004

Table 2.2. Design Gas Sample Mixture

	Mole Fractions		
argon	0–1%	carbon monoxide	0–3%
methane	0–10%	hydrogen	0–5%
oxygen	0–20%	ethane	0–1%
water vapor	3–20%	ethylene	0–1%
nitrogen	50–80%	acetylene	0–1%
carbon dioxide	1–10%		

Table 2.3. Calibration Gas Composition

Mole Fractions (+/- 2% relative)			
Sample 1		Sample 2	
methane	2.029%	carbon monoxide	1.001%
carbon monoxide	0.965%	carbon dioxide	0.999%
carbon dioxide	5.46%	acetylene	1.001%
hydrogen	1.124%	ethylene	0.999%
oxygen	1.963%	ethane	0.999%
nitrogen	balance	methane	1.001
		nitrogen	balance

Chapter 3

Experimental Results

The entrainment and chemistry of natural gas fire plumes in a two-layer environment were studied here through chemical analysis of the ceiling layer. Results were obtained for upper-layer interfaces close to the burner surface and for combustion ranging from quite lean ($\phi = 0.2$) to quite rich ($\phi = 2.2$).

3.1 Entrainment Results

3.1.1 Definition of Entrainment

Before presenting the results, it is necessary to discuss what is meant by entrainment, how it is measured in the present investigation, and how it has been defined and measured in other investigations. Entrainment here is defined quite simply as the total plume vertical mass flux at a given vertical location minus the fuel flow rate, that is,

$$\dot{m}_e(z) = \dot{m}(z) - \dot{m}_f \,, \tag{3.1}$$

where $\dot{m}$ is the total plume mass flux and is defined as

$$\dot{m}(z) = \int_0^{2\pi} \int_0^{\infty} \overline{\rho(r,z,\theta)\, u(r,z,\theta)}\, r\, dr\, d\theta \,. \tag{3.2}$$

This is the standard definition of entrainment and it merits some discussion. In general, if the source of mass, momentum, and/or buoyancy is flush with the floor as shown in figure (3.1a), then by conservation of mass

$$\dot{m}_e(z) = -\lim_{r\to\infty} \int_0^z \rho(r,z)\, v(r,z)\, 2\,\pi\, r\, dz \,, \tag{3.3}$$

where the density and velocity have been assumed to be axisymmetric at large r, and the entrainment is seen to vanish at $z = 0$. Such is not the case, however, in the present work where the source is located in free space, i.e., away from a floor

or walls. In this case, due to the flux of mass through the bottom of the control volume in figure (3.1b), **3.3** no longer accurately defines the entrainment, and even at the origin ($z = 0$), the entrainment is not necessarily zero.

The measurement of the entrainment through chemical analysis of the ceiling layer in a two-layer experiment comes, in fact, from a direct measurement of the quantity given in **3.2**. (Actually, this is not quite correct since the two layers do not extend to infinity in the radial direction, but the layers certainly extend to a large enough radius that any vertical mass flux outside this region is negligible.) Any mass crossing the plane $z = H$ in figure (3.1b) enters the ceiling layer and is well mixed with the other contents of the upper layer. Indeed, if this were not the case, that is, if mass were able to cross the $z = H$ plane and not enter the layer, then it would eventually be required to backflow below $z = H$ and therefore its pathline would lead to both positive and negative contributions in **3.2** that would exactly cancel out. Therefore, measuring the quantity of mass entering the upper layer is a direct and correct measurement of the plume mass flux at the height $z = H$, where H is the location of the plane asymptotic to the bottom of the ceiling layer at large radii, if: 1. the upper layer extends to a radius large enough that the vertical mass flux outside this radius is negligible, and 2. the mass flux of lower layer air across the interface due to molecular diffusion is small. Both of these are reasonable assumptions in the present work.

3.1.1.1 Different plume configurations

An important point that must be made about the current work is that it is a study of fire plume entrainment in a two-layer environment with the source located in unbounded space. Specifically, the entrainment of fresh air from the lower layer that is subsequently deposited in the upper layer is measured. This is not necessarily equivalent to the entrainment of a plume in a uniform environment

or a plume propagating from a floor. To clarify these distinctions, the four different cases are shown along with a far-field streamline cartoon in figure (3.2).

The most studied case of a turbulent plume is that discharging into a uniform environment, as shown in figures (3.2a) and (3.2b). In modelling the irrotational flow outside of the turbulent regions of the plume, the use of a line of sinks along the plume centerline has proven to be valuable (Lippisch, 1958; Taylor, 1958). For a plume discharging from a wall, the resulting image sinks induce a far-field flow with streamlines similar to those shown in figure (3.2a). The unbounded plume in a uniform environment (figure 3.2b) is quite different. Here the sink line has no image and the streamlines are observed to be, at least qualitatively, parabolic.

Adding a two layer environment to these cases can lead to significantly different observations, as shown in figures (3.2c) and (3.2d). Using gases to study the plume, we find the pressure gradient effect of the environment negligible for laboratory scale experiments. However, effects due to the difference in density between the two layers must be kept in mind. Mak (1985) studied this effect for negatively buoyant salt-water jets. His conclusions, however, can be applied to buoyant gas jets and imply that when the average density of the plume is less than 0.8 times the upper-layer density, the entire plume penetrates the interface without leaving its edges behind in the lower layer, even though the density of the plume is distributed in such a way that its value near the edges of the plume is greater than the upper-layer density. In the extreme case of a cool plume trying to enter the upper layer, a significant portion of the plume may be unable to cross the interface, resulting in the formation of jets of cool gas spreading radially outward along the interface (Cooper, 1983). In the present investigation, however, due to the large difference between the plume temperature

and the temperature of the upper layer, the plume essentially entered the upper layer unaffected by the density change.

Although the far-field streamlines in the above case might be affected by the presence of an upper layer, the entrainment is not appreciably changed since the significantly affected streamlines are far from the plume centerline and thus represent quite small velocities. Therefore, if the streamlines in regions of non-negligible velocity are effectively unchanged by the upper layer, then the results obtained from the two-layer experiment would be applicable to cases of uniform environment. Visual observations of the fire plume with smoke marking of the streaklines suggested that the effect of the upper layer was small in the present work, but the magnitude of the effect was not clearly determined.

3.1.2 Plume Entrainment Measurements

The entrainment mass flux was determined by our using the technique described in Chapter 2. Values were obtained for interface heights of 0.01, 0.05, 0.10, 0.15, and 0.23 m above the burner surface and for various heat release rates ranging from 12 to 135 kW. Inlet Reynolds numbers for the fuel, based on the burner diameter, ranged from 150 to 1500, while inlet Richardson numbers varied from 10^{-1} to 10. Residence times of the gas in the upper layer varied from 25 seconds to over 4 minutes.

The location of the interface appeared quite distinct, probably due to a well-mixed upper layer and the local stability of the upper layer. As discussed by Zukoski (1985), material added to the layer can produce either a well-mixed layer or a continuously stratified layer depending on the details of the flow. In the present case, measurements of gas chemistry at various heights in the box showed the effect of probe height in the box to be minimal. That is, the upper

layer appeared to be quite well mixed.

The interface was located by the use of a shadowgraph system to determine the level of the upper layer at a position far enough from the plume centerline for the plume vertical velocity to be negligible. The interface was unsteady and possessed low-frequency internal waves with amplitudes less than 2 cm.

The entrainment results are presented in three different ways. Figure (3.3) presents the entrained mass flux versus the fuel flow rate. Lines of constant equivalence ratio are also shown, where the equivalence ratio is defined as the fuel-to-air ratio divided by the stoichiometric fuel-to-air ratio. For a given interface height, the entrained mass flux is nearly independent of the fuel flow rate. Only for small fires ($\dot{m}_f < 0.5$ g/s) is there any apparent dependence on fuel flow rate. The entrained mass flow rate decreases with decreasing fuel flow rate, but even this effect is quite small and is, in fact, observed only at distances of 5 cm or more from the burner surface.

Up to this point, the flames along with their resulting plumes have been discussed as if belonging to a single regime; and, for the most part, flames arising in accidental fires are of a single type (Zukoski, 1985). The whole flame is essentially buoyancy controlled and the flame has a length that is independent of the source diameter and depends primarily on the heat release rate. The flame shape is that of an unsteady, but well-defined, column. The behavior of the flame can be characterized by a dimensionless heat release parameter, Q^*, which Zukoski (1975) has defined as

$$Q^* = \frac{\dot{Q}}{\rho_\infty c_{p\infty} T_\infty \sqrt{g D_0} D_0^2}, \tag{3.4}$$

where $\dot{Q}$ is the heat release rate of the fire, and ρ_∞, $c_{p\infty}$, and T_∞ are the density, specific heat at constant pressure, and temperature of the ambient fluid, g is the

acceleration of gravity, and D_0 is the burner diameter. For flames in the regime described above, Q^* is between about 1 and 500. For smaller heat release rates (or larger source diameters), a transition occurs for Q^* less than about 1. In this regime, the flame breaks up into a number of independent flamelets.

The small dependence of the entrainment on the fuel flow rate (and hence the heat release rate) can now be explained in light of the flow regimes discussed above. For a fuel mass flow rate of less than 0.5 g/s, the dimensionless heat release rate, Q^*, is less than 1.5. Thus, it is quite possible that the results for $\dot{m}_f < 0.5$ g/s correspond to a different flame regime than those for the higher flow rate flames. It is interesting to note that for $z = 1$ cm and for all but the lowest fuel flow rate tested at $z = 5$ cm, the effect of a different flame regime is not seen. This implies that, nearest the burner surface, the effect of the fuel flow rate is negligible, a conclusion also suggested from visual observations of this region.

The entrained mass flow rate is next presented as a function of the equivalence ratio in figure (3.4). Here, there appears to be a small dependence on the equivalence ratio; however, this can be explained rather as a dependence on Q^*.

The entrained mass flux depends most strongly on the length of the region over which fresh air can be entrained, i.e., the height of the interface above the burner. Figure (3.5) presents the entrained mass flow rate as a function of the interface height. This shows that the entrainment increases with increasing burner-to-interface height.

As mentioned above, for some of the fires studied (those with $Q^* < 1.5$ and at least 5 cm from the burner surface) there is a small effect of fuel flow rate on entrainment. The data points for these fires are neglected and the results are

given again in figure (3.6) as entrainment mass flux versus interface height, where this time there is no noticeable dependence on fuel flow rate. From this figure, it appears that the entrainment is nearly linear for $z < 10$ cm and again for $z > 10$ cm. Others have proposed various functional relationships between $\dot{m}_e$ and z, most of these being of the form $\dot{m}_e \sim z^n$ where $0.75 \leq n \leq 1.25$. Indeed, for $z > 10$ cm, this form agrees with the current results. That dependence should not be expected to hold very near the burner surface, however, since the entrainment for $z = 0$ will not necessarily vanish. The current results suggest that the entrained mass flux was, in fact, nonzero at the burner surface. This was also suggested by interface distortion near the fire plume. Although distortion in the interface and the uncertainty in locating it precisely might be partially responsible for this observation, the deviation was too large to be completely accounted for in this manner. The complete results are given in Appendix B.

An effective origin is often used in studying fully turbulent jets and plumes in order to clarify deviations in measurements due to the initial conditions at the source. In the present case, however, since the very near field was of primary interest, this was determined not to be of value. Visually observing the fire plumes, we saw that the behavior very near the burner, i.e., less than one-half diameter from the burner surface, was different from that observed farther downstream. Near the burner surface, a cylindrical flame sheet pinches in periodically toward the burner centerline. Farther downstream, large puffing structures dominate the flowfield. Because of these two distinct regions, different entrainment behavior should be expected for each region and, in fact, was observed.

Uncertainties in the determination of entrainment were calculated to be 3% or less for the fuel-rich fires, which is the approximate magnitude of the scatter in this data. For the fuel-lean fires, the uncertainty ranged from 3 to 10%, although

the precision for these data seems to be good. The measurement of the interface height seemed to be valid within 1 cm for $z \leq 10$ cm and to within 2 cm for $z \geq 15$ cm. The equations for these calculations are given in Appendix A.

3.1.2.1 Effect of the soot chemical representation

Soot was represented in the above calculations as C_8H, a representation presented by Glassman (1977). This corresponds to a mass fraction of nearly 99% for carbon. The sensitivity of the results to this assumption was tested by determining the entrainment in cases where soot was assumed to be represented by $C_{16}H$ and C_4H. In neither of these cases did the entrainment results change by more than 1%.

3.1.2.2 Effect of the probe location

Typically, the probe was placed in the upper layer at a distance of 90 cm from the bottom of the upper layer (30 cm below the top of the box). Tests of the uniformity of the upper layer were conducted by our moving the probe to 10 and 50 cm above the interface, as shown in figure (3.7). With the probe at 50 cm above the interface, the entrainment results varied by less than 3% from the results obtained with the probe at its standard measurement position. With the probe at 10 cm above the interface, the entrainment results were calculated to change by about 5% from the results obtained with the probe at its standard measurement position.

3.1.3 Comparison to Previous Results and Discussion

The current entrainment results were compared to the results of Cetegen (1982) (also in Cetegen et al., 1984), Beyler (1983) (also in Beyler, 1986), and Lim (1984). Cetegen measured entrainment in fuel-lean fires and proposed a theoretical model that, over the initial regions of the flame, entrained mass flux increases

as $z^{3/4}$. Figure (3.8) presents Cetegen's data (and a theoretically based fit to the data) along with the data (and data fit) for the current investigation. It appears that the 3/4-power model fits the Cetegen data no better than the linear fit with the present data. In addition, the current data deviate from the 3/4-power model. At least over the initial regions of the flame, the linear fit appears to represent the current data *and* the data of Cetegen and Lim quite well.

Beyler ran experiments with propane, propene, and several alcohols as fuels and proposed correlations based on the propane results. These correlations also represented the propene data quite well. Beyler determined the entrainment by measuring the mass flow rate of gas removed from near the top of the upper layer in order to maintain the interface at a fixed location. Because the gas was removed from the top of the upper layer, the upper layer in Beyler's experiments was not well mixed and the definition of an interface was obscure. Two different interface definitions were proposed and these differed in locating the interface by as much as 8 cm in some cases. In fact, the interface thickness was approximately 10 cm, based on the depth of the region over which 80% of the change in measured quantities between the two layers occurred. For each of these interface definitions, a data correlation was given that was proportional to $z^{1.2}$ or $z^{1.25}$. These two correlations are shown along with the current data in figure (3.9). The magnitude of the entrainment measured by Beyler over a given axial extent of the plume was much lower than that determined in the present experiments.

Beyler's propene results correlated well with the propane results, but the methanol results did not fit the propane models. In fact, the entrainment rates for the methanol fires were much higher than the propane and propene results.

As mentioned above, the results of Beyler were significantly lower than the current results, which we presume might be related to the initial buoyancy of

the fuel. Beyler used propane, which has a molecular weight of 44.10, for the majority of his tests. In addition, his burner was water-cooled. Because of this, the fuel was initially negatively buoyant and, rather than pinching in toward the burner centerline, the fuel would bulge radially outward. We can only guess what effects this might have, but it appears in the present experiments that the first few centimeters adjacent to the burner are the most significant in the production of the large puffing structures that characterize these flames. These structures strongly influence the entrainment in the initial regions of these flames. In an initially negatively buoyant flame, the "pinching in" process might occur farther downstream after the fuel has been heated. In essence, the virtual origin of the plume would be farther downstream, possibly as much as a diameter or two above the burner. Further evidence for this possible effect comes from the results of Beyler's methanol tests. This lower molecular weight (32.04) fuel was burned in a pool, and was thereby at above ambient temperatures. It is safe to assume that due to the elevated temperature, the fuel was initially buoyant. Beyler noted that not only was the entrainment higher with this fuel, but also that the flame structure was different, the methanol flame having "particularly large flame structures." In the present invesigation, the natural gas had a molecular weight of 17.51, and the burner surface was estimated to be between 400 and 600° K so that this fuel was initially very buoyant. Considering Beyler's propane data fit in figure (3.9), if the virtual origin was one diameter above the burner surface, we would find the data curve downstream of this point to be nearly linear, albeit with a different slope than observed for the current experiments.

3.2 Upper Layer Chemistry

Some of the most profound dangers of fires within structures are the result of the chemical composition of the plume gases entering the upper layer. Toxic gases

and combustible gases are often transported via the plume to the upper layer, where they can spread and possibly ignite. The most dangerous of the toxicants is carbon monoxide, which is fatal for quantities greater than 1% in one minute exposure time (Parker and West, 1973). The composition of gases transported by the fire plume was analyzed by measuring the chemistry of the upper layer above the plume after the layer chemistry and temperature were allowed to reach steady state by permitting gas to exit the well-mixed upper layer at the same rate as plume gas entered the layer. While in real fires the fuel chemistry is different and the process is transient, it is hoped that the current results for natural gas fuel will provide some understanding of actual fire-plume chemistry with a limited oxygen supply, a scenario which is common to fires within structures.

3.2.1 Chemical Species Measurements

Using the technique described in Chapter 2, we measured the chemistry of the combustion products in the upper layer for the same flame and interface conditions used to obtain the entrainment results. In addition, once the entrainment and the equivalence ratio had been determined, the chemical equilibrium composition of the reactants was computed at constant temperature and pressure. Figures (3.10) to (3.16) give the equilibrium mole fractions of the major stable species (O_2, N_2, H_2O, CO_2, CO, CH_4, and H_2) as a function of the equivalence ratio for various equilibrium temperatures. For fuel-lean fires, the equilibrium composition is independent of temperature and is simply the composition of the completed stoichiometric reaction plus excess air. Similarly, for fuel-rich fires the composition of the completed stoichiometric reaction plus excess fuel is approximated by the equilibrium composition at the lowest temperature shown (since at these temperatures little hydrogen or carbon monoxide is present under chemical equilibrium conditions). The actual temperatures observed in the upper layer

during testing are given in figure (3.17) as a function of equivalence ratio for the various interface heights tested and they range from 490 to 870° K.

Figures (3.18) to (3.24) give the actual mole fractions of the major stable species as a function of equivalence ratio. Several interesting observations can be made that might allow the extension of the current chemistry results to actual room fire models. First, the chemical composition of the upper layer depends on the stoichiometry of the layer gases and is independent of the temperature in the layer, although the temperature of this layer varies substantially, as shown in figure (3.17). It is also independent of the fuel flow rate, the residence time of the gas in the upper layer, or the location of the interface. The independence of the interface height (and hence temperature—see figure (3.17)) on the chemistry is particularly marked for the carbon monoxide mole fraction measurements in figure (3.22). These results also suggest that the chemical reaction is quenched at a temperature above 870° K.

The amounts of hydrogen, carbon monoxide, and methane in the upper layer compare quite well with the early results of Cetegen (1982) and Lim (1984). They also agree with the more extensive results of Beyler (1983) for hydrocarbon fuels, despite several major differences in the apparatus and technique. These include burner size, fuels used (Beyler ran extensive tests with propane in addition to a limited number of tests with a variety of other fuels), burner geometry and surface temperature, residence time in the upper layer, and upper layer homogeneity. Perhaps the difference in the upper layer is the most significant. In Beyler's experiments, the upper layer was stratified; therefore, even after a rich flame reached this layer there was still some oxygen available to the plume, especially near the interface region. This was not the case in the current experiments where once the fire plume crossed the distinct interface, if the process was fuel-

rich, the upper layer was depleted of oxygen. The only oxygen then available for combustion was that carried in the plume itself. Yet despite these major differences, the composition of the gas delivered by the plume to the upper layer appears to depend exclusively on the equivalence ratio of the combustion process. Non-hydrocarbon fuels used by Beyler, such as alcohols, did give substantially different results. However, this was probably due to the presence of oxygen and CO radicals in the fuel molecule itself.

3.2.2 Discussion of the Chemical Species Measurements

In the presence of sufficient air, the fuel reacts nearly completely while the excess air simply dilutes the products of combustion. This is especially clear from figures (3.18), (3.23), and (3.24). Oxygen concentration declines almost linearly from $\phi = 0$ to $\phi = 0.9$, while over this range neither methane nor hydrogen is detected. Near the stoichiometric mixture ratio, small amounts of oxygen are measured.

The carbon from the fuel is partitioned between carbon monoxide and carbon dioxide for lean fires. For $\phi < 0.5$, no significant carbon monoxide is present and the reaction of fuel is essentially complete, but for $0.5 < \phi < 1.0$, carbon monoxide was measured in the presence of oxygen. This indicates that the oxidation of carbon monoxide is incomplete. This is not surprising since the oxidation of carbon monoxide is a relatively slow reaction. Other investigators (Cetegen, 1982; Beyler, 1983; Lim, 1984) have made similar observations.

The results for $\phi > 1$ are more difficult to explain. Figure (3.18) shows that oxygen is absent as expected. In figure (3.21), the amount of carbon dioxide is less than the value predicted from chemical equilibrium computations at all the temperatures computed. Again, because the reaction producing carbon dioxide

is relatively slow, the results seem to suggest that the reaction stops before completion, as the reactants cool.

Figure (3.23) shows that the amount of methane appears to increase almost linearly with equivalence ratio over the range of fuel-rich fires studied. This is as expected, if it were assumed that the excess fuel remained as methane, a condition modelled by the equilibrium composition at the lower temperatures. However, while the mole fraction of methane is nearly linear, it is less than predicted if all the excess fuel remained as methane. This is attributed to the presence of hydrogen and carbon monoxide, as seen in figures (3.23) and (3.24). Hydrogen and carbon monoxide appear to freeze out before being oxidized.

As discussed in Chapter 2, the chemical equilibrium calculations give a crude approximation of the temperature at which the various chemical constituents freeze out of the complete reaction. When we compare the data shown in figures (3.18) to (3.24) to the chemical equilibrium calculation results shown in figures (3.10) to (3.16), the equilibrium results can be tested as a model for the actual product composition. For $\phi < 0.7$, the equilibrium results characterize the measurements quite well, while over the range $0.7 < \phi < 1.0$, deviations in the two appear to be limited to an excess in the amount of carbon monoxide measured along with a corresponding deficit in the amount of carbon dioxide measured.

The dependence of the equilibrium results for $\phi > 1$ on temperature makes the measurements in this region more difficult to analyze. Oxygen measurements appear to be modelled by the equilibrium calculations quite well except for small amounts of oxygen ($\sim$ 1% mole fraction) measured for some of the slightly rich ($1 < \phi < 1.5$) fires. Nitrogen, methane, and water vapor measurements are characterized well by the equilibrium calculations at constant temperatures between about 500 and 750° K. Carbon monoxide, carbon dioxide, and hydrogen are more

difficult to correlate. Equilibrium hydrogen and carbon monoxide mole fractions are strong functions of temperature, the hydrogen measurements falling between the equilibrium curves at 550 and 600° K, and the carbon monoxide measurements between the curves at 750 and 800° K. For both of these components, over the temperature difference between the curves cited, the calculations vary by about a factor of two. Finally, carbon dioxide was measured in quantities that are about 2% mole fraction less than expected from equilibrium calculations.

Relying on these correlations, we might find it appealing to attempt to model the measurements with equilibrium calculations between about 600 and 750° K. This would, however, be in conflict with the point made earlier that the measured composition was independent of upper layer temperature up to nearly 900° K. So if any reactions freeze, they must do so at higher temperatures.

The determination of the quantity of carbon monoxide produced by a fire still remains as an unsolved problem. Clearly, equilibrium calculations do not effectively model the experimental measurements. A number of models have been proposed (Bilger and Stårner, 1983; Peters, 1984; Liew et al., 1984; Vachon and Champion, 1986) that use limited equilibrium or reaction processes; however, none of these can be applied adequately to the current experiments.

It should be noted that although the C_2 hydrocarbons were measured, they were only present for rich flames and then only in very small amounts. The ratio of ethane-to-methane in the product under fuel-rich conditions was much smaller than the ethane-to-methane ratio in the fuel.

Combustion at the interface, a phenomenon that may be associated with some types of flashover, was observed at most of the interface heights studied. The approximate fuel flow rates for flashover at various interface heights are

symbolized by the open circles in figure (3.3). Beyler (1983) proposed a model for predicting the equivalence ratio for layer-burning which, using the current experimental conditions, gave equivalence ratios between 2.6 and 2.7.

3.2.3 Actual Heat of Reaction

The standard heat of reaction per mole of fuel was calculated for each of the experiments, using the actual measurements of product composition. The ratio of this actual heat of reaction, ΔH_r°, to the heat of reaction for the complete (stoichiometric) reaction, ΔH_s°, is given as a function of equivalence ratio in figure (3.25). Also shown in this figure is a theoretical maximum for this ratio. For fuel-lean fires, all of the fuel can, theoretically, be expected to react completely so that the ratio $\Delta H_r^\circ / \Delta H_s^\circ$ has a maximum value of one in this region. For fuel-rich fires, only $1/\phi$ of the fuel can, theoretically, be expected to react due to the deficiency of oxygen. Thus, in this range, the maximum value expected for $\Delta H_r^\circ / \Delta H_s^\circ$ is $1/\phi$. The actual heat of reaction appears to be consistently about 90% of the theoretically expected value.

These results suggest that for fire models, the heat release for $\phi \leq 1$ should be $0.9\dot{m}_f \Delta H_s^\circ$, and for $\phi > 1$ the proper estimate is $0.9\dot{m}_f \Delta H_s^\circ / \phi$, where ϕ is the equivalence ratio for the upper layer. These results are in agreement with the idea that the heat release can be calculated from the assumptions that for fuel-lean mixtures 90% of the fuel in the plume is consumed, and that for fuel-rich mixtures 90% of the oxygen in the plume is consumed.

As noted above, for fuel-lean fires the uncertainty in the results was larger than for fuel-rich fires. This is the probable cause of the scatter in the results for $\phi < 1$.

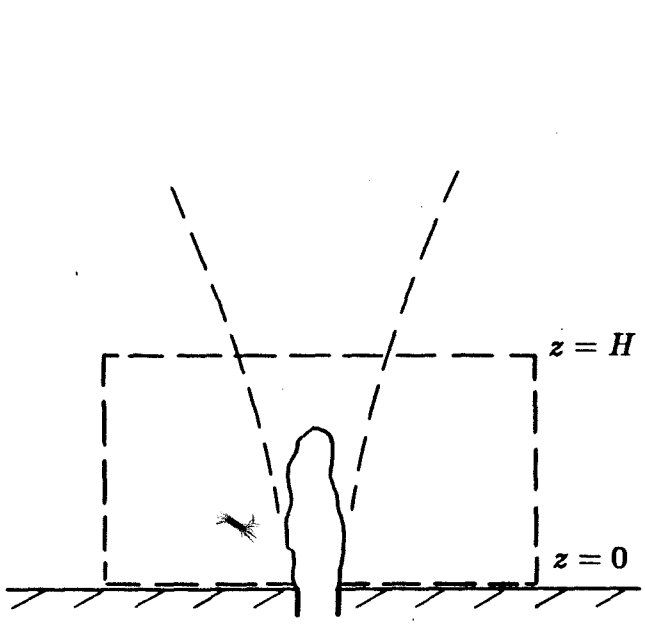

a) Source located at floor

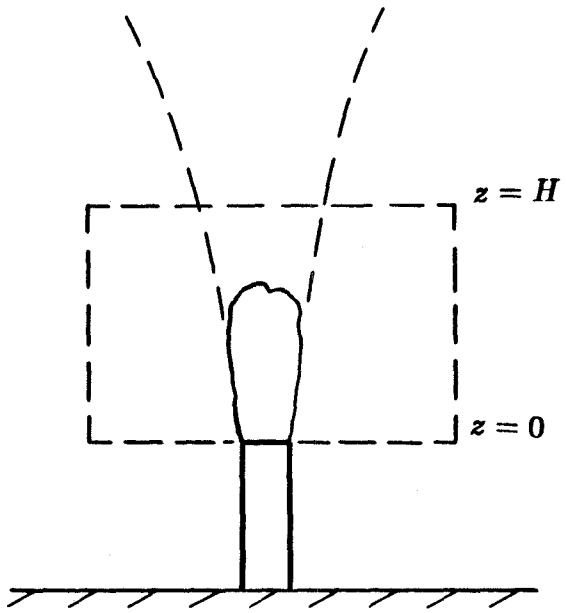

b) Source located away from floor

Figure (3.1) Comparison of bounded and unbounded plume sources.

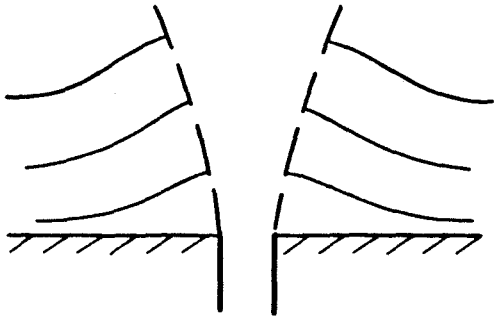

a) Bounded source in a uniform environment

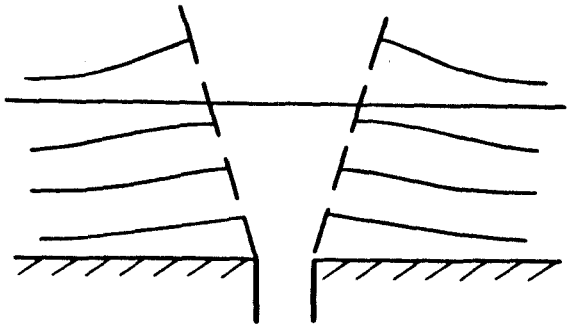

c) Bounded source in a two-layer environment

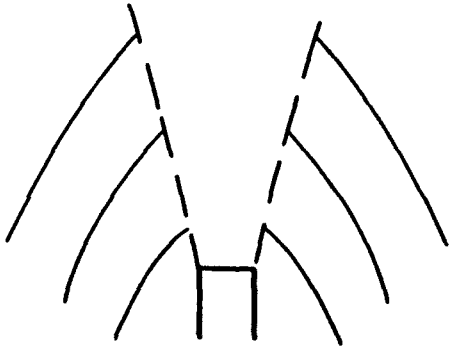

b) Unbounded source in a uniform environment

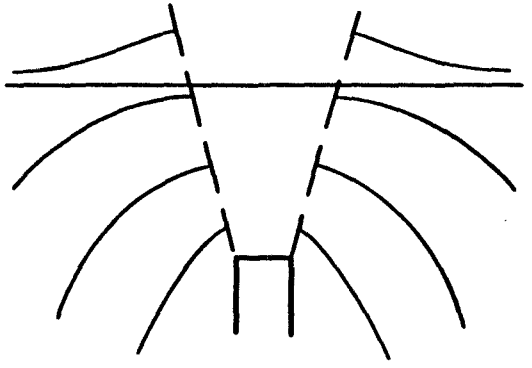

d) Unbounded source in a two-layer environment

Figure (3.2) Far-field streamline cartoons for bounded and unbounded sources in uniform and two-layer environments.

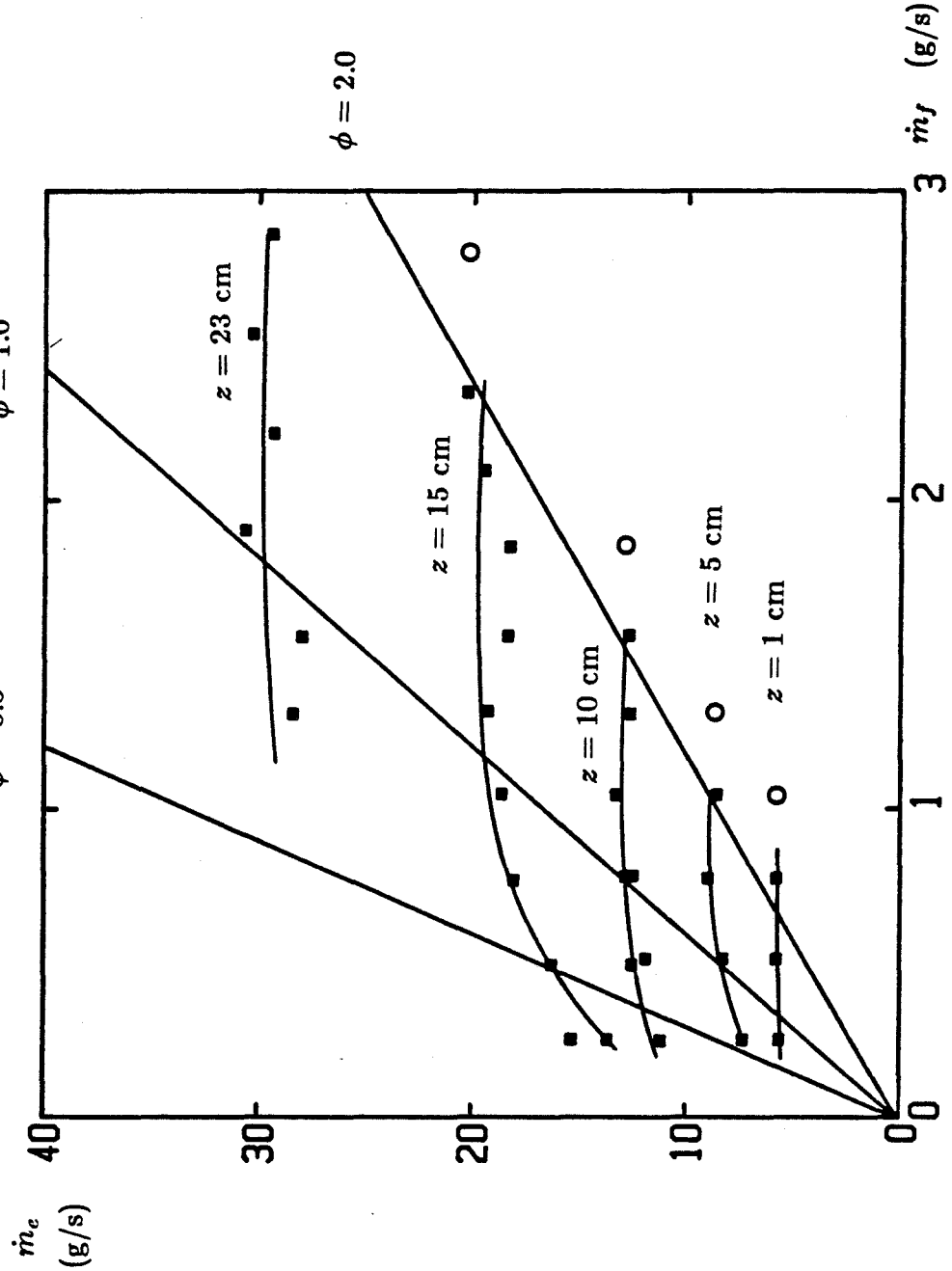

Figure (3.3) Entrained mass flow rate as a function of fuel mass flow rate for various interface heights, with constant equivalence ratio and flashover conditions shown.

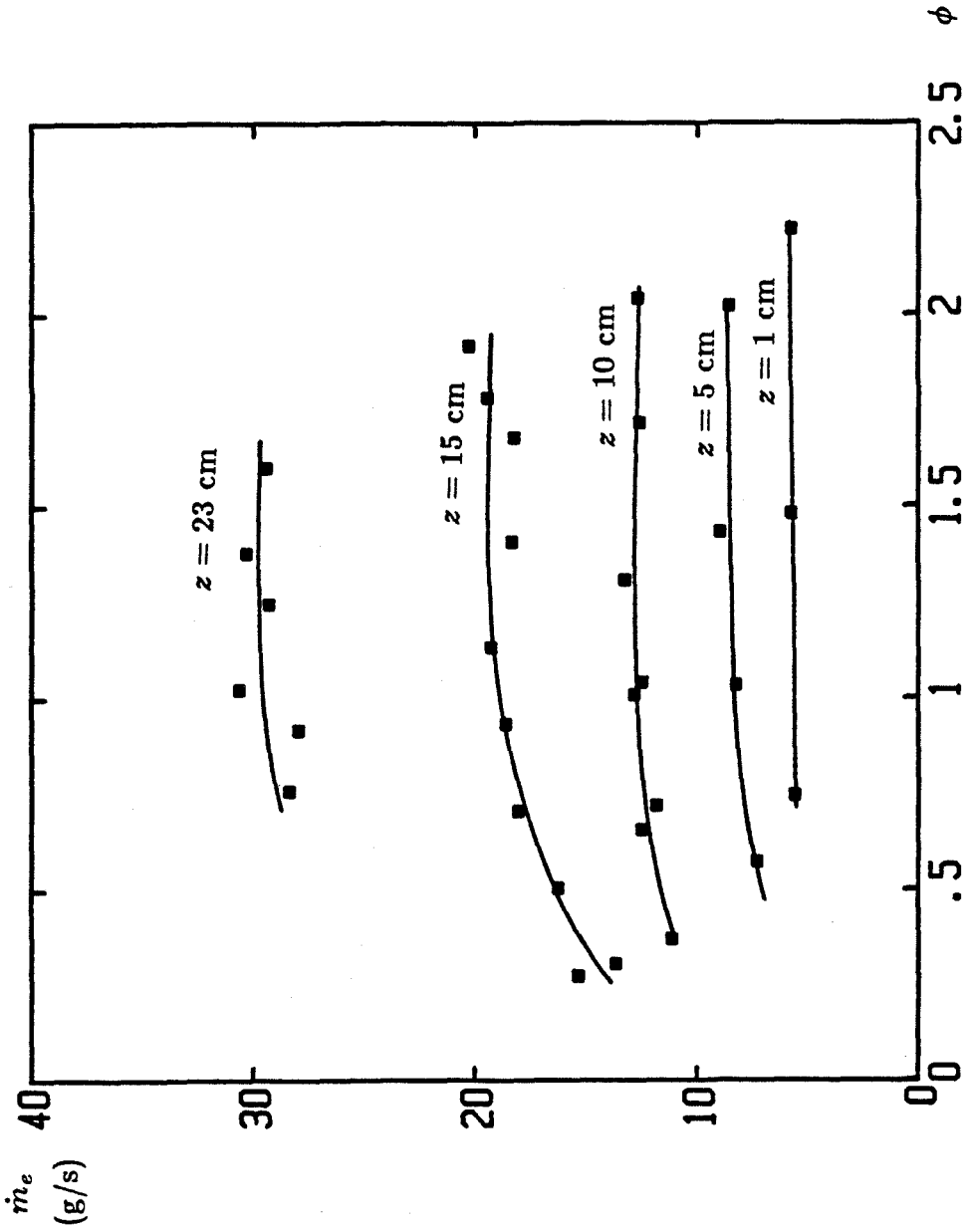

Figure (3.4) Entrained mass flow rate as a function of equivalence ratio for various interface heights.

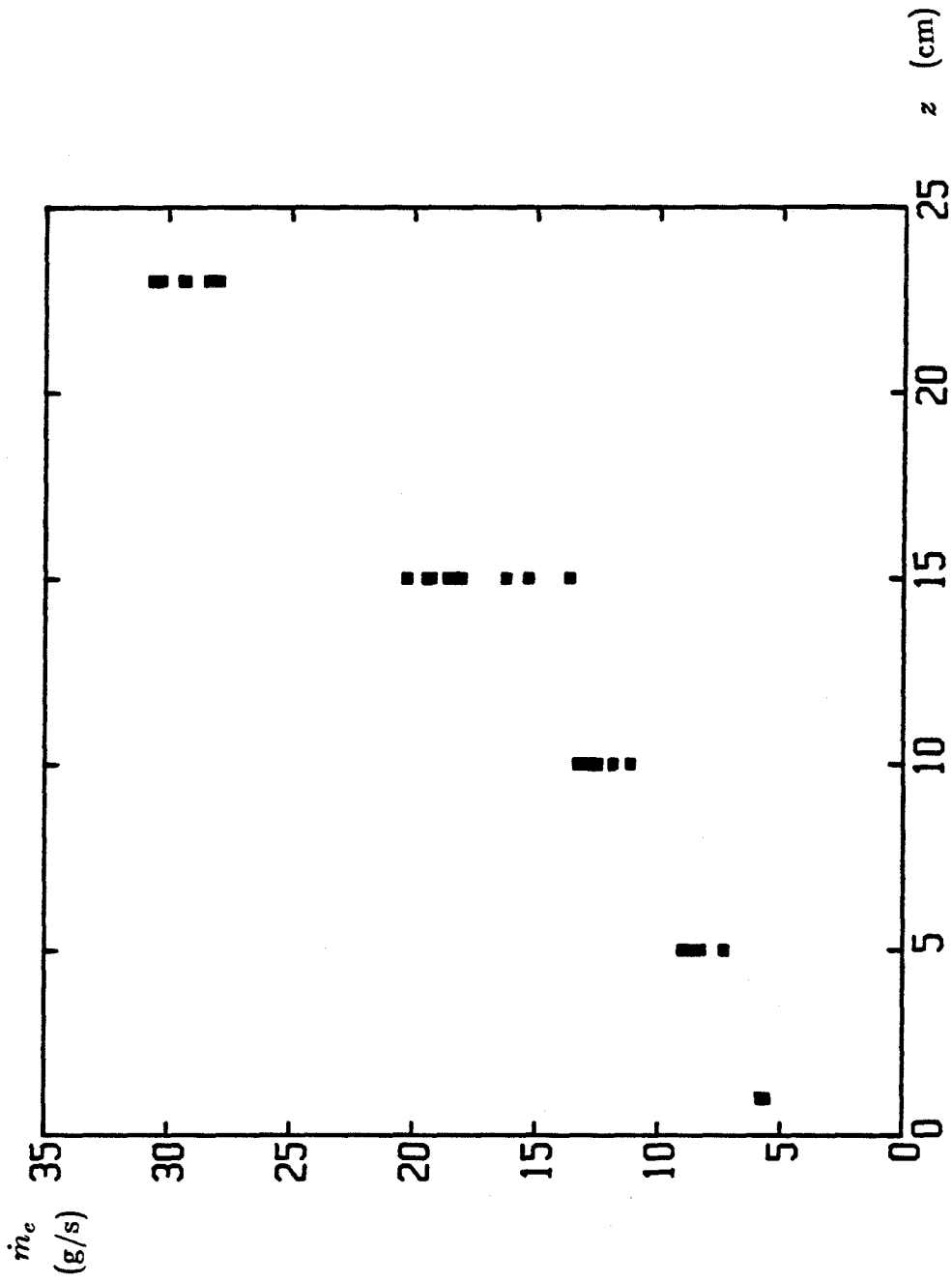

Figure (3.5) Entrained mass flow rate as a function of interface height.

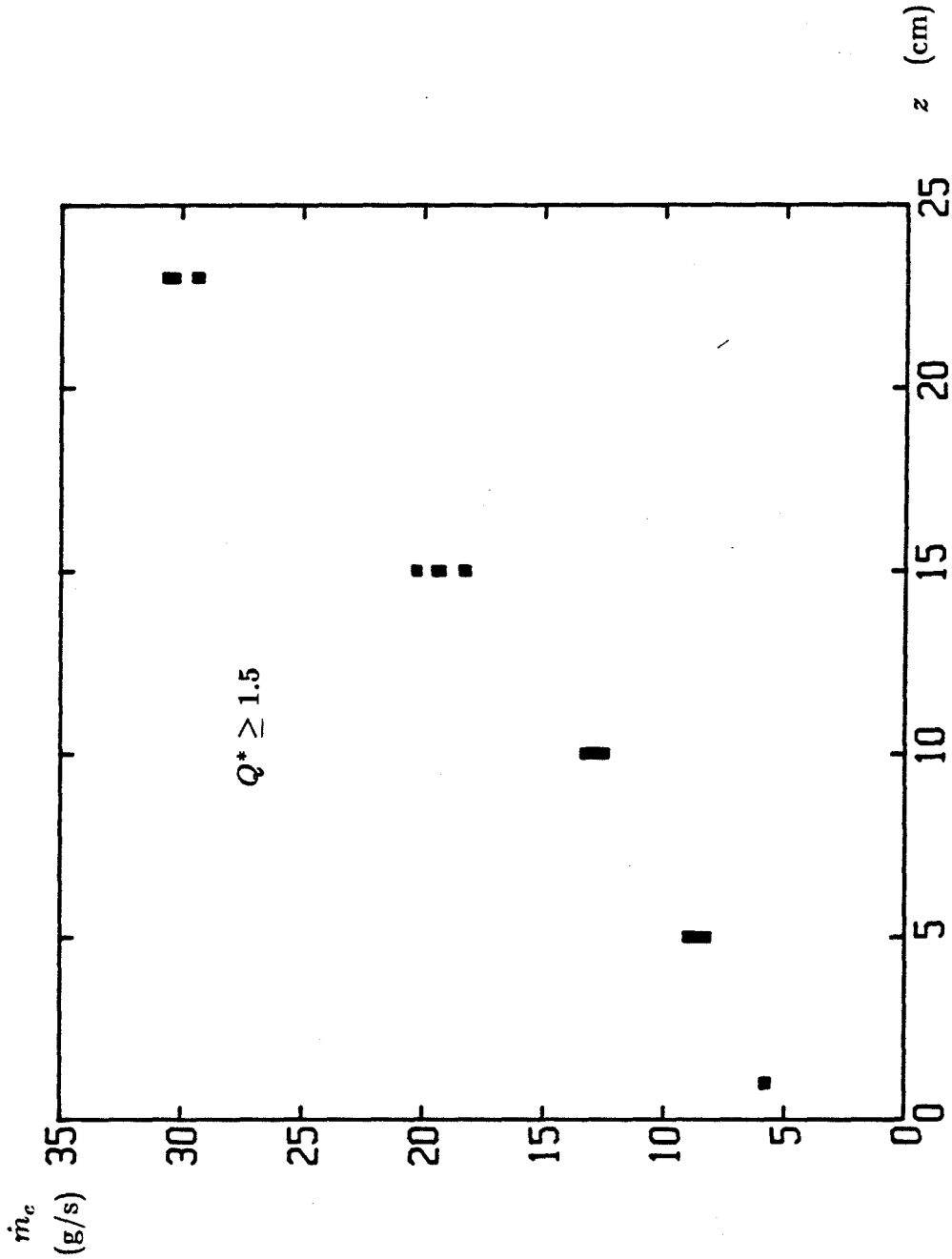

Figure (3.6) Entrained mass flow rate as a function of interface height for heat-addition parameter greater than or equal to 1.5.

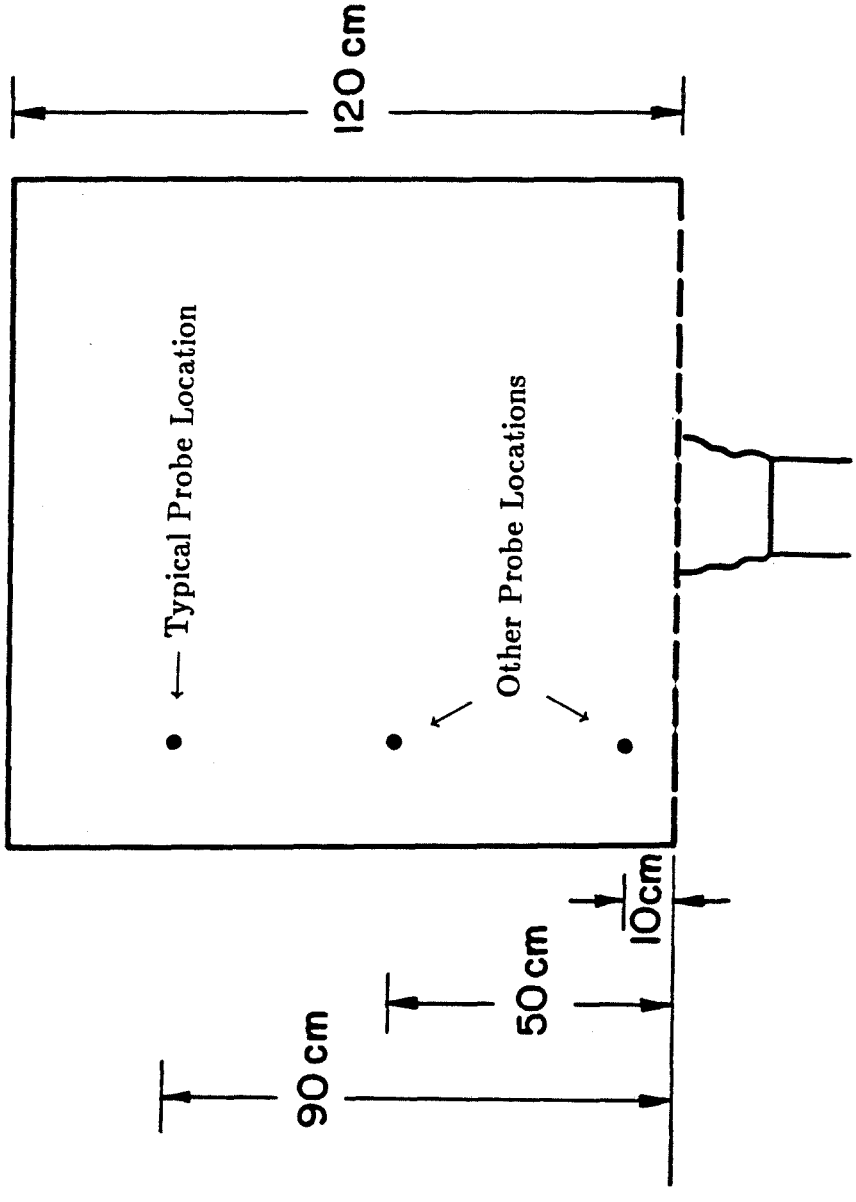

Figure (3.7) Gas sampling probe location.

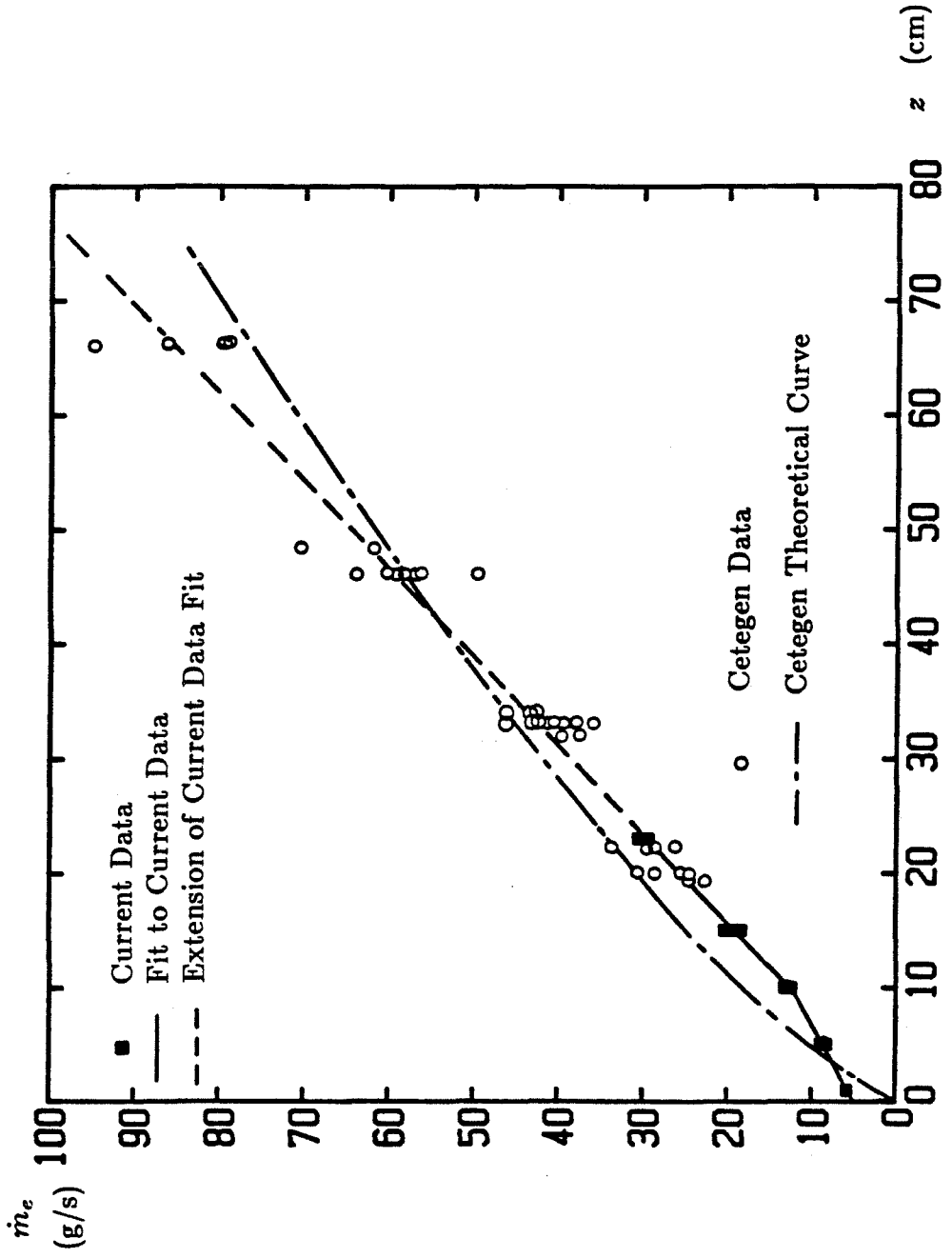

Figure (3.8) Comparison of entrained mass flow rate versus interface with Cetegen (1982).

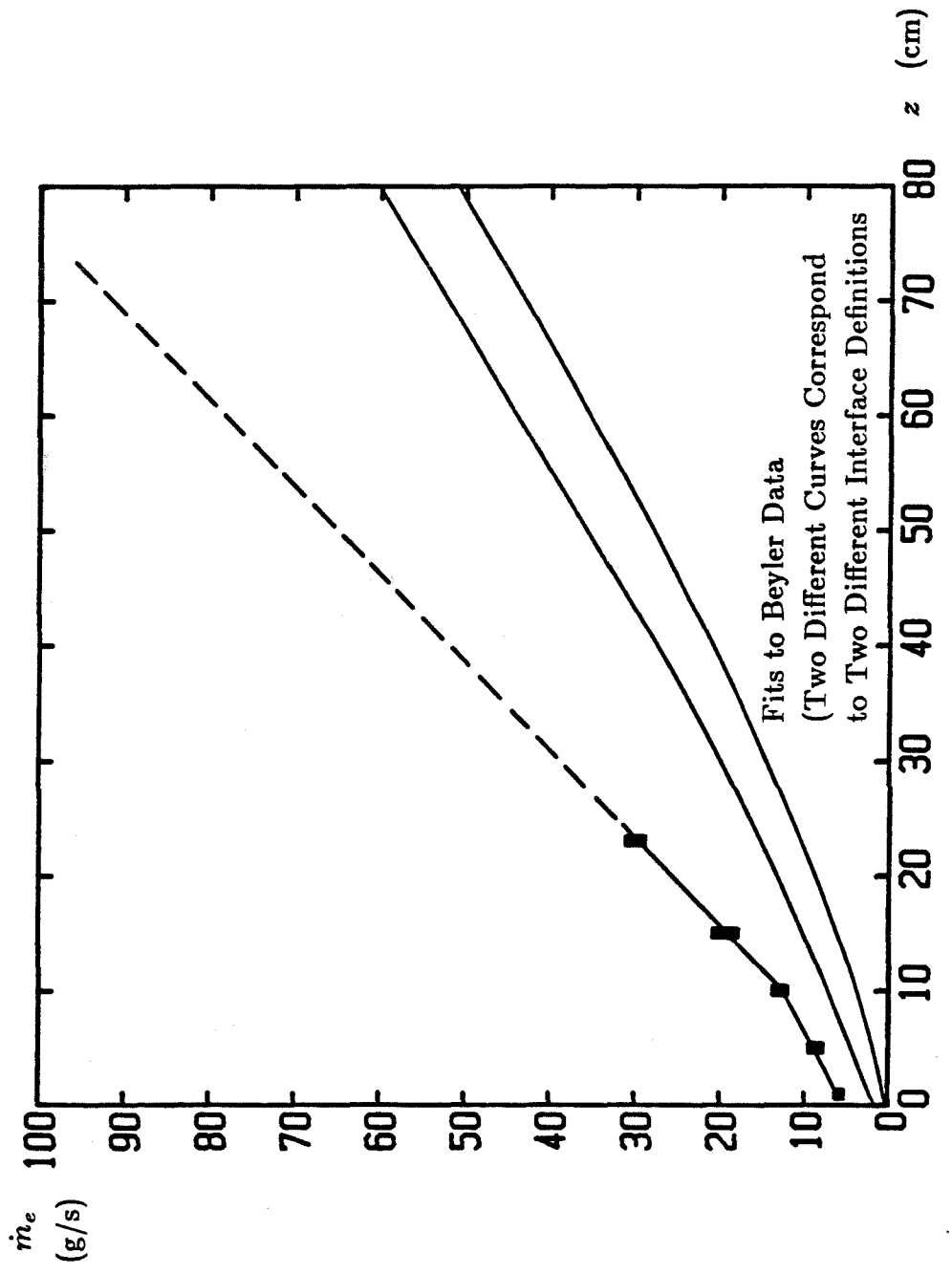

Figure (3.9) Comparison of entrained mass flow rate versus interface with Beyler (1983).

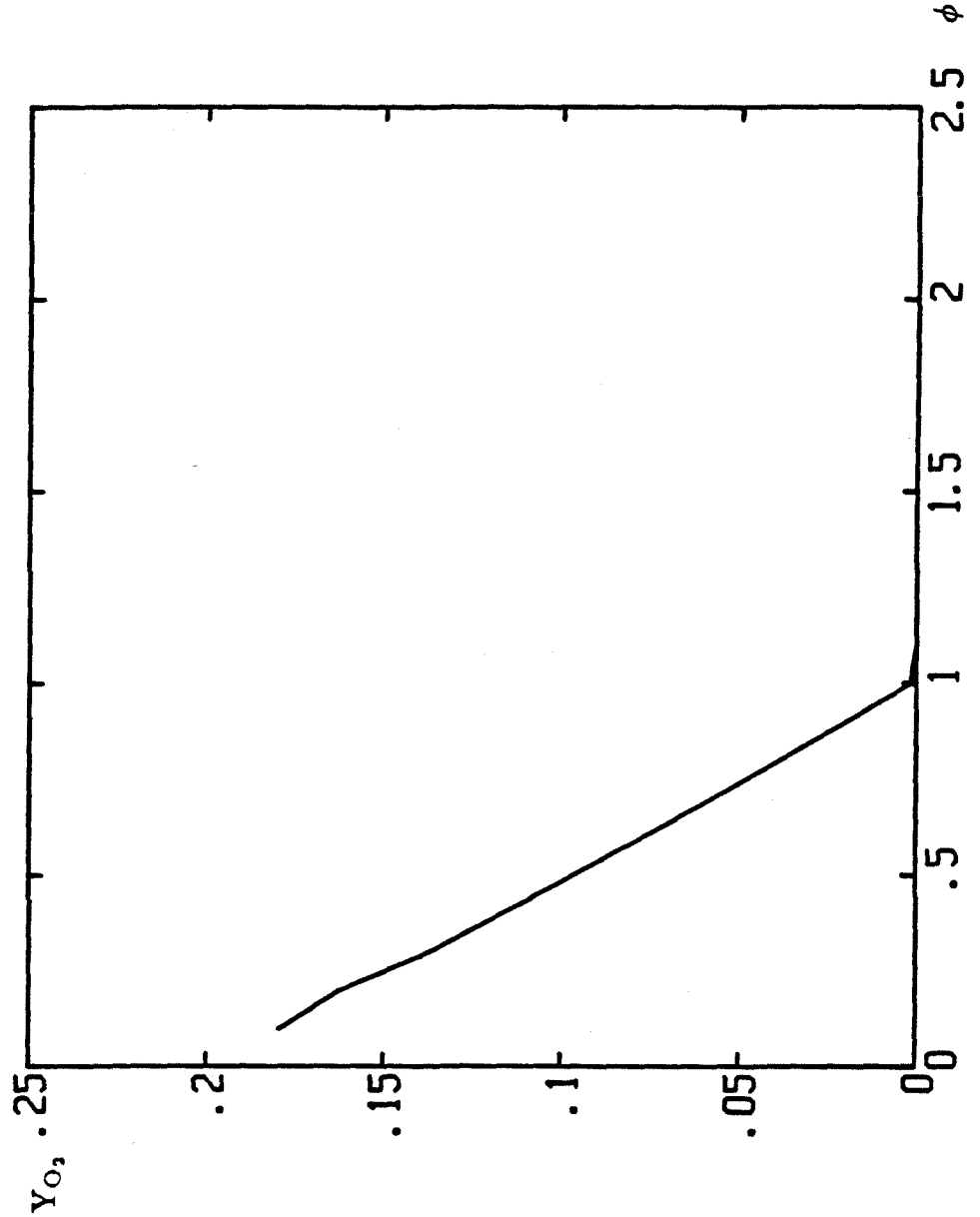

Figure (3.10) Chemical equilibrium mole fraction of oxygen as a function of equivalence ratio.

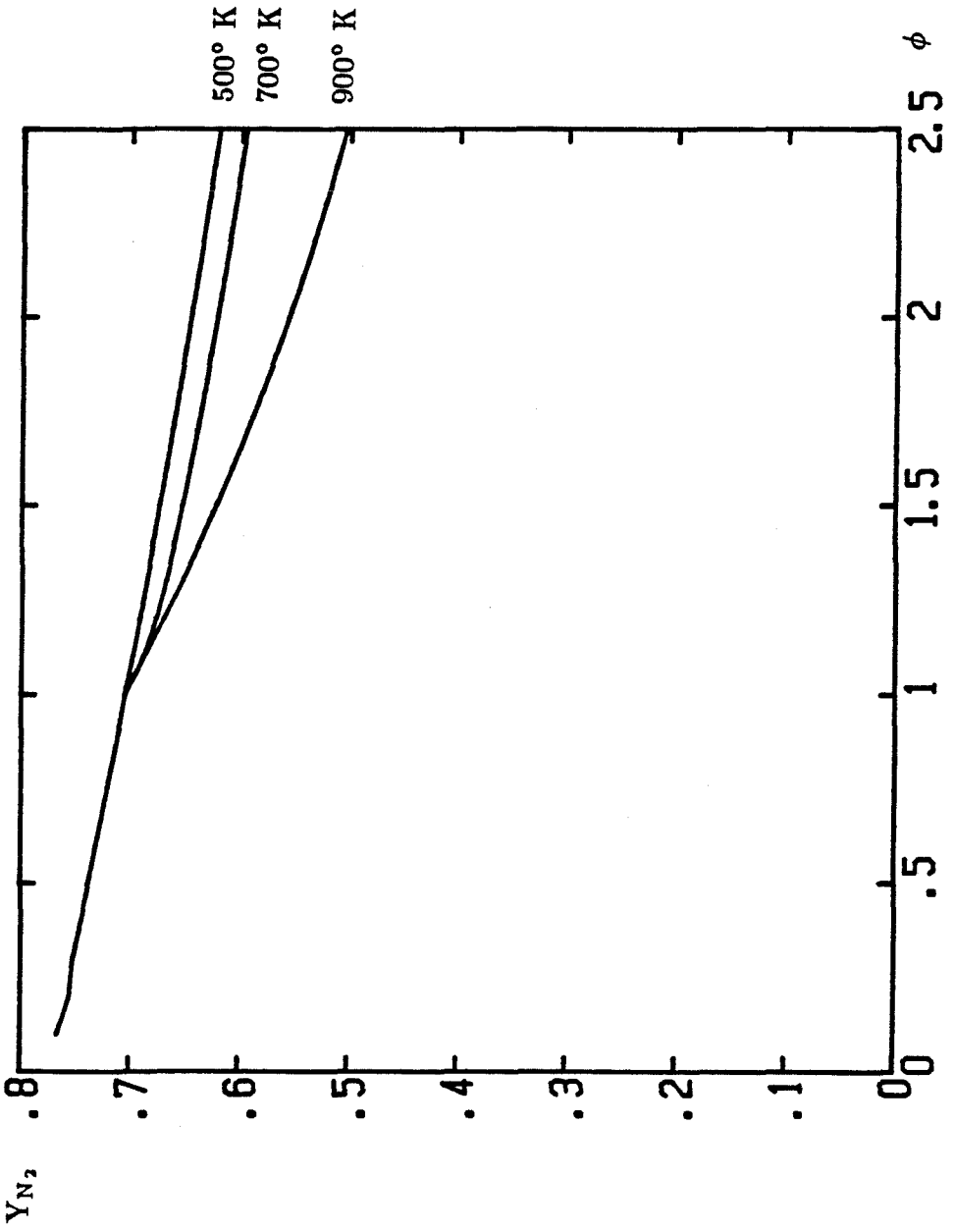

Figure (3.11) Chemical equilibrium mole fraction of nitrogen as a function of equivalence ratio.

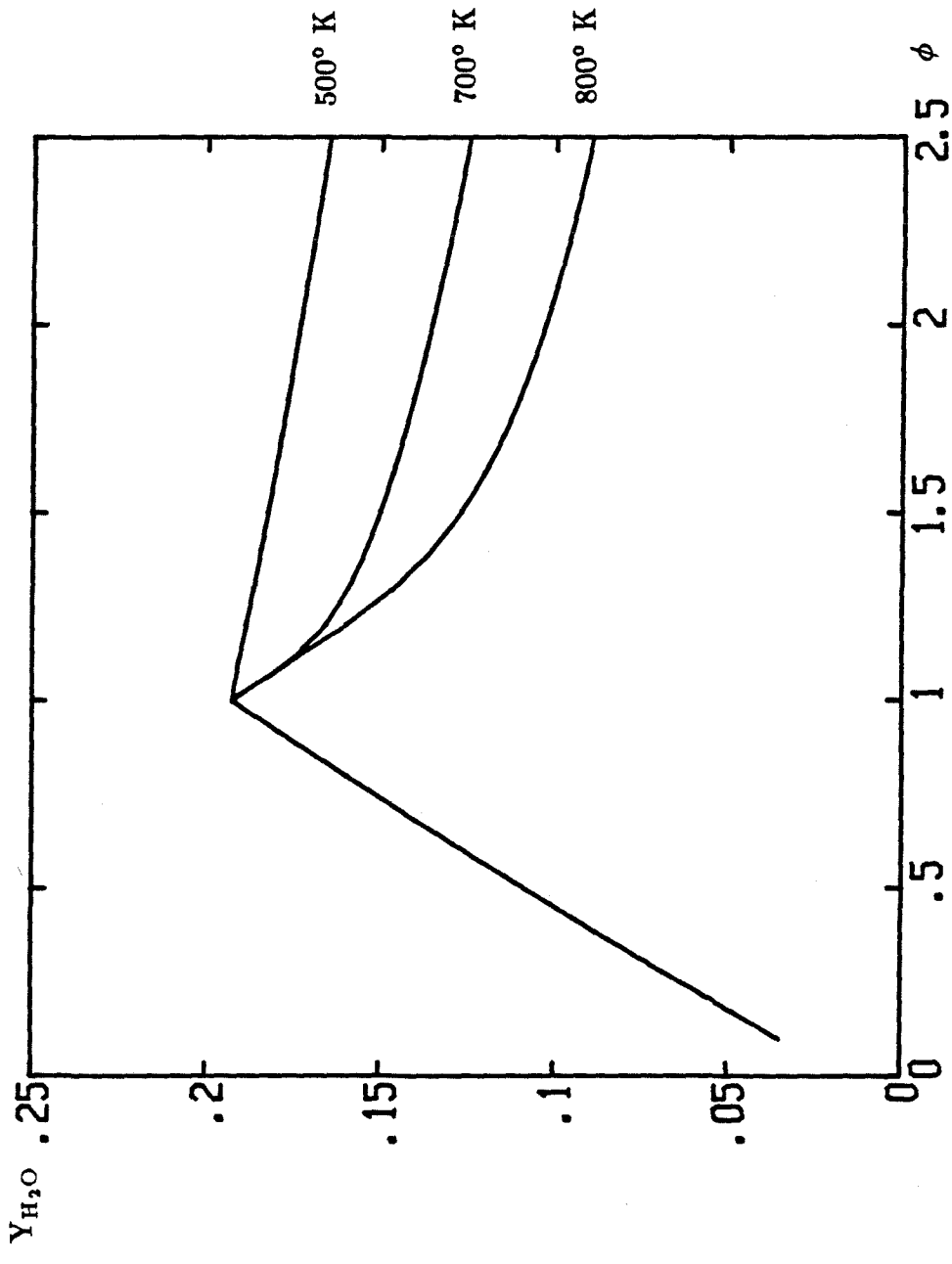

Figure (3.12) Chemical equilibrium mole fraction of water vapor as a function of equivalence ratio.

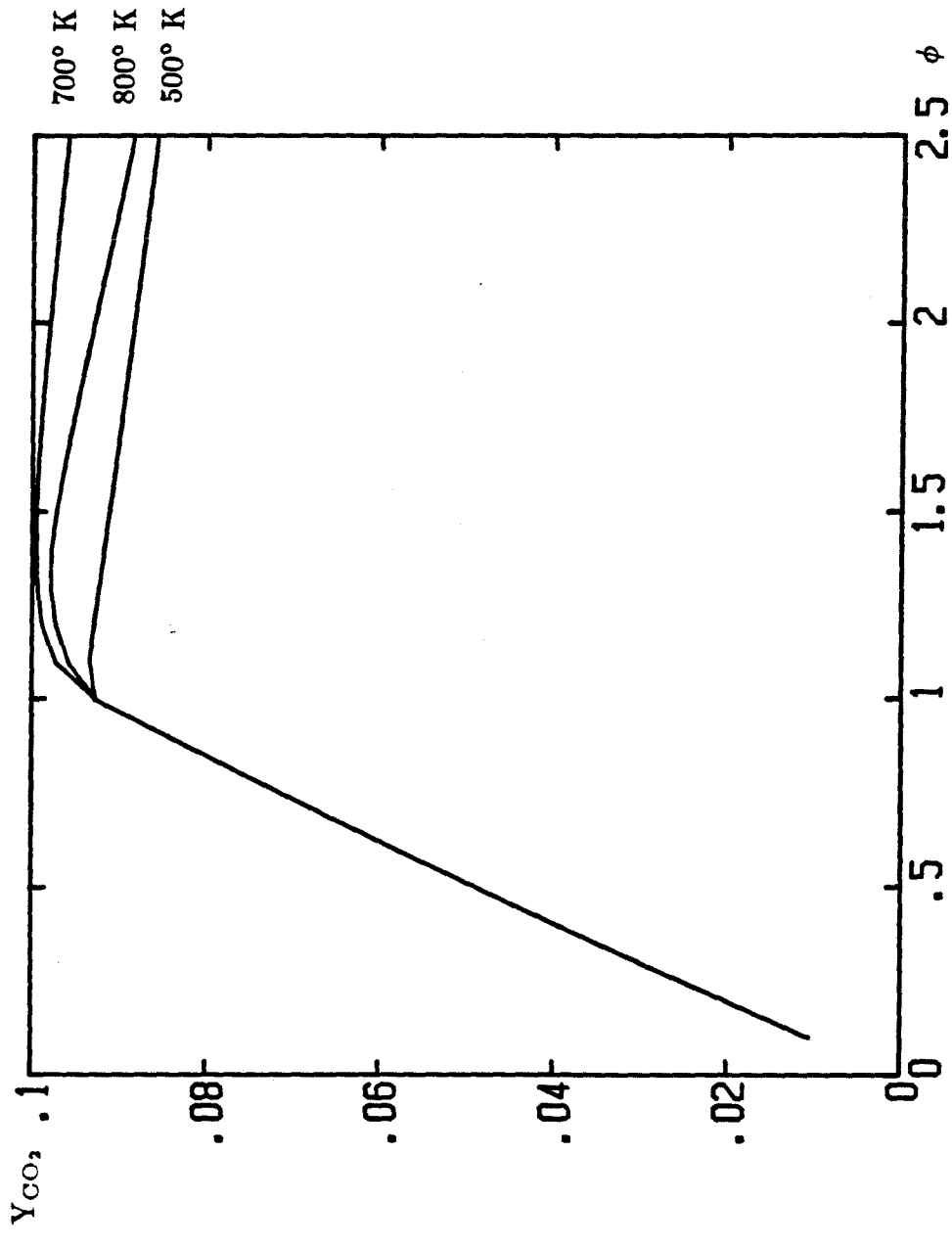

Figure (3.13) Chemical equilibrium mole fraction of carbon dioxide as a function of equivalence ratio.

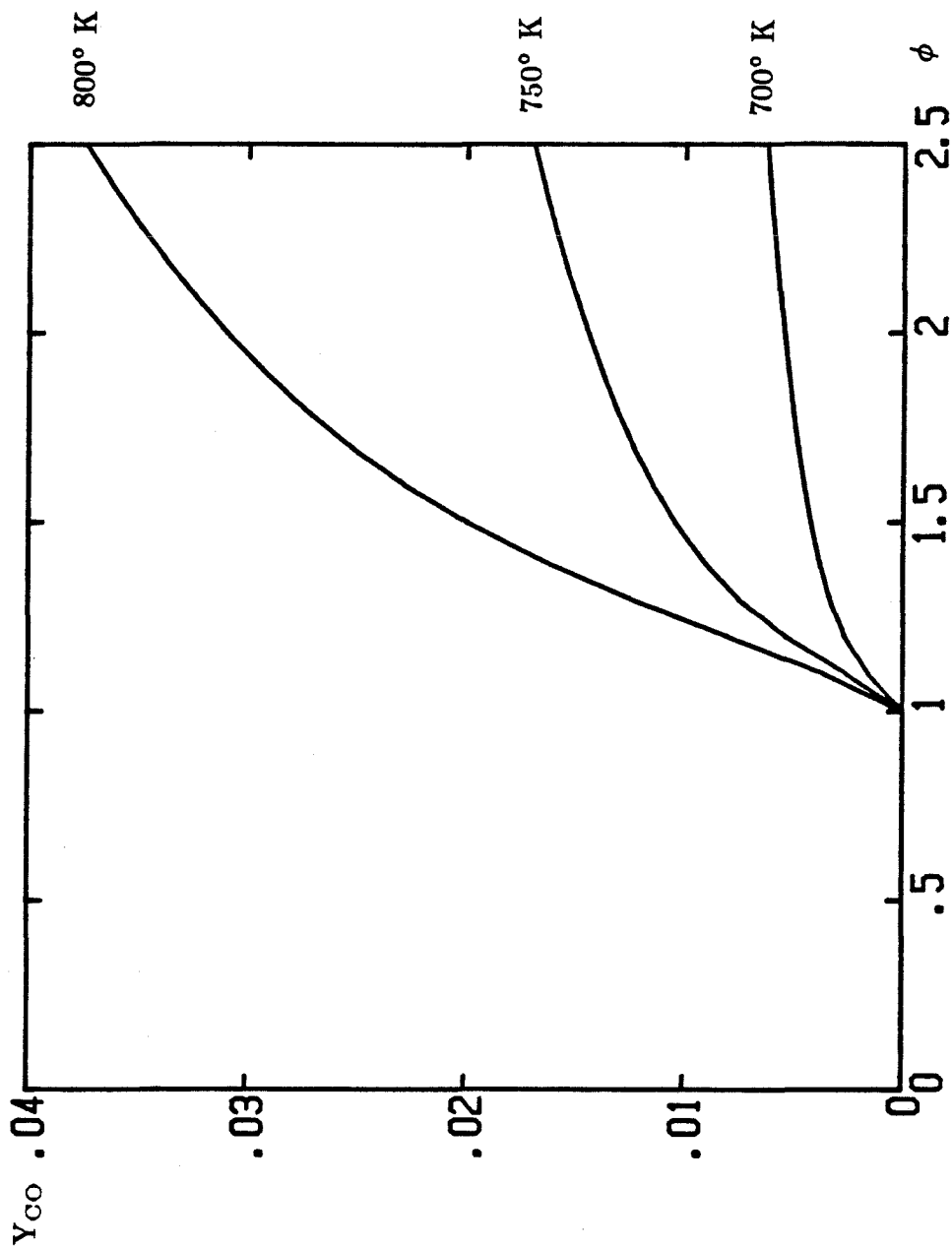

Figure (3.14) Chemical equilibrium mole fraction of carbon monoxide as a function of equivalence ratio.

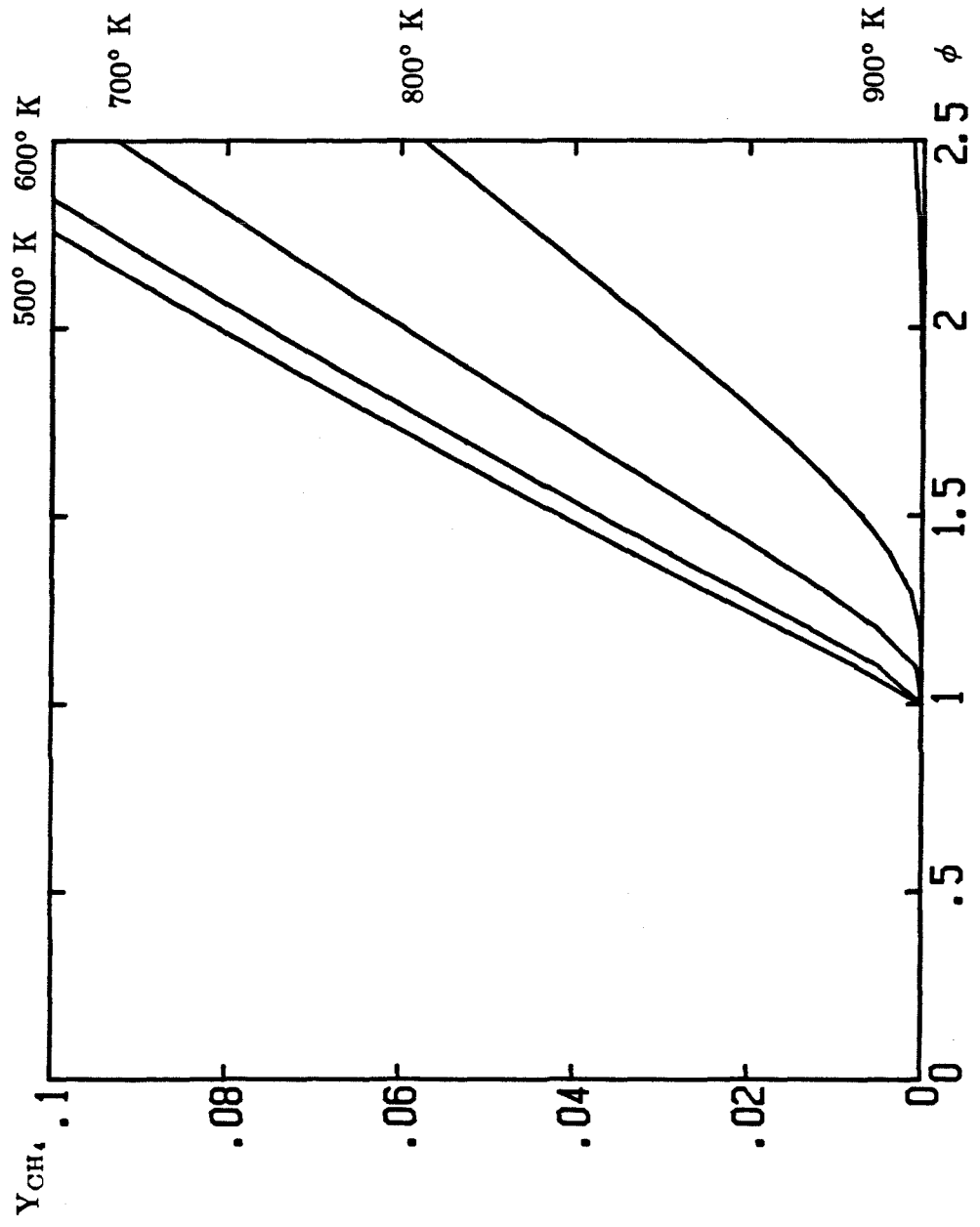

Figure (3.15) Chemical equilibrium mole fraction of methane as a function of equivalence ratio.

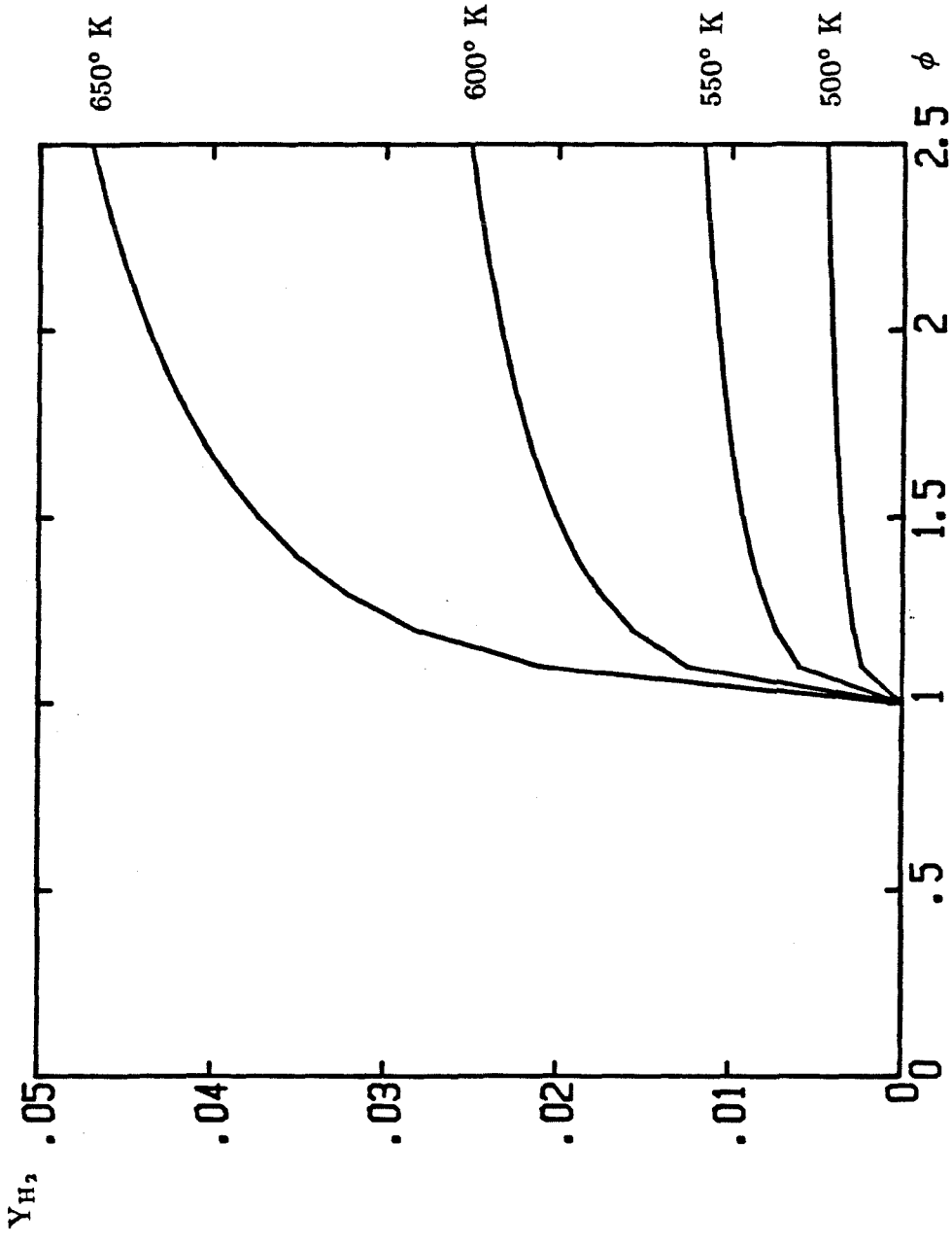

Figure (3.16) Chemical equilibrium mole fraction of hydrogen as a function of equivalence ratio.

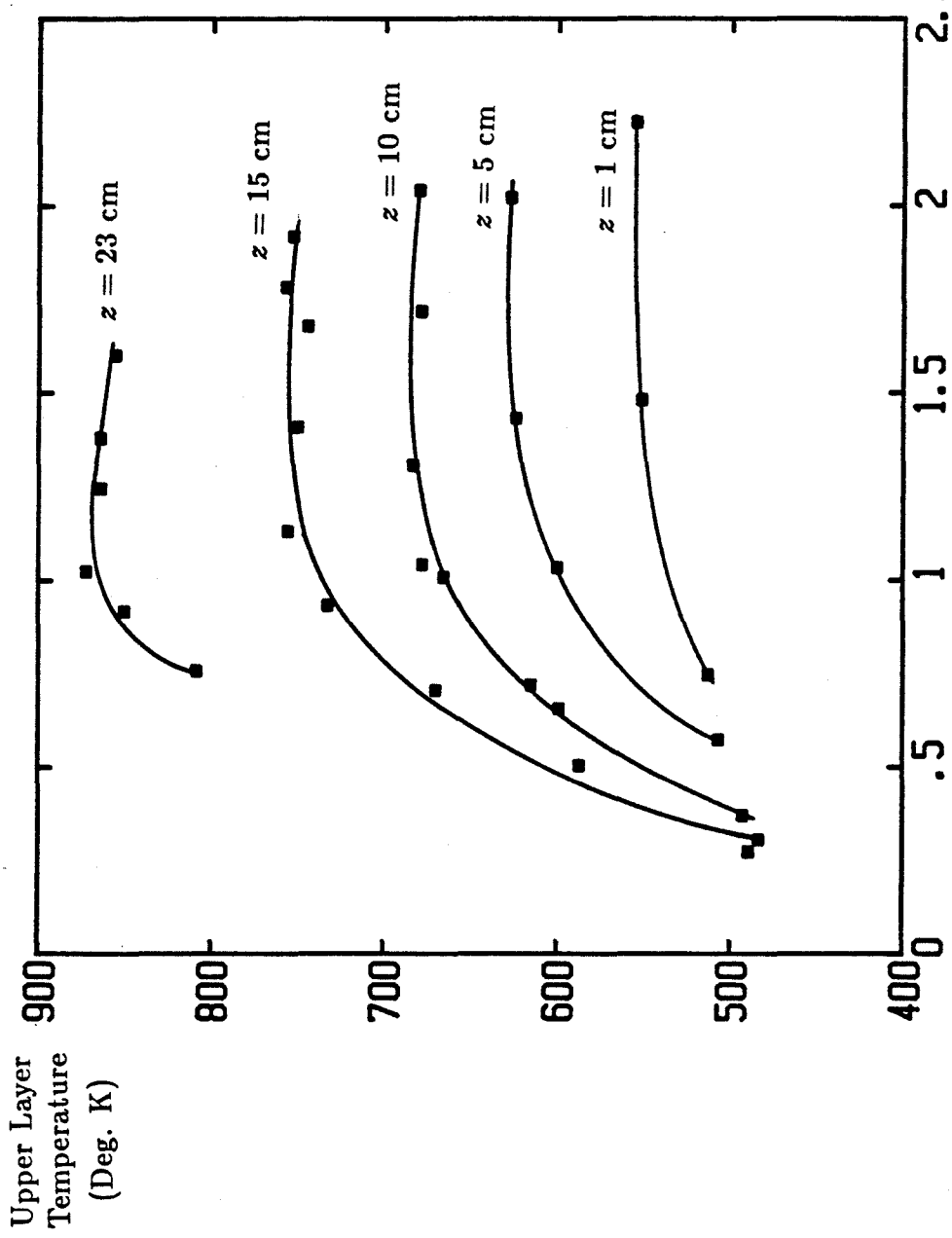

Figure (3.17) Upper layer temperatures as a function of equivalence ratio for various interface heights.

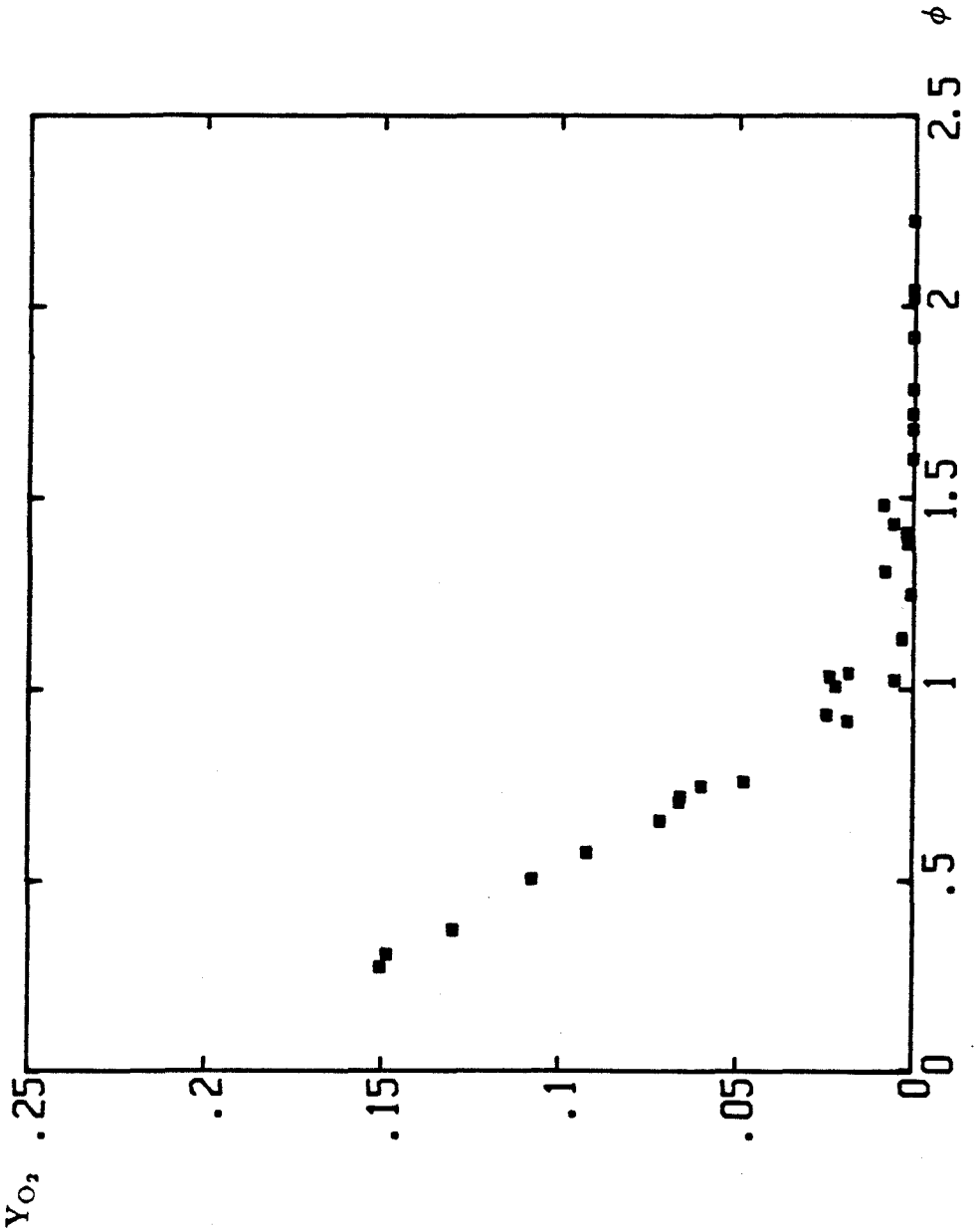

Figure (3.18) Oxygen mole fraction data as a function of equivalence ratio.

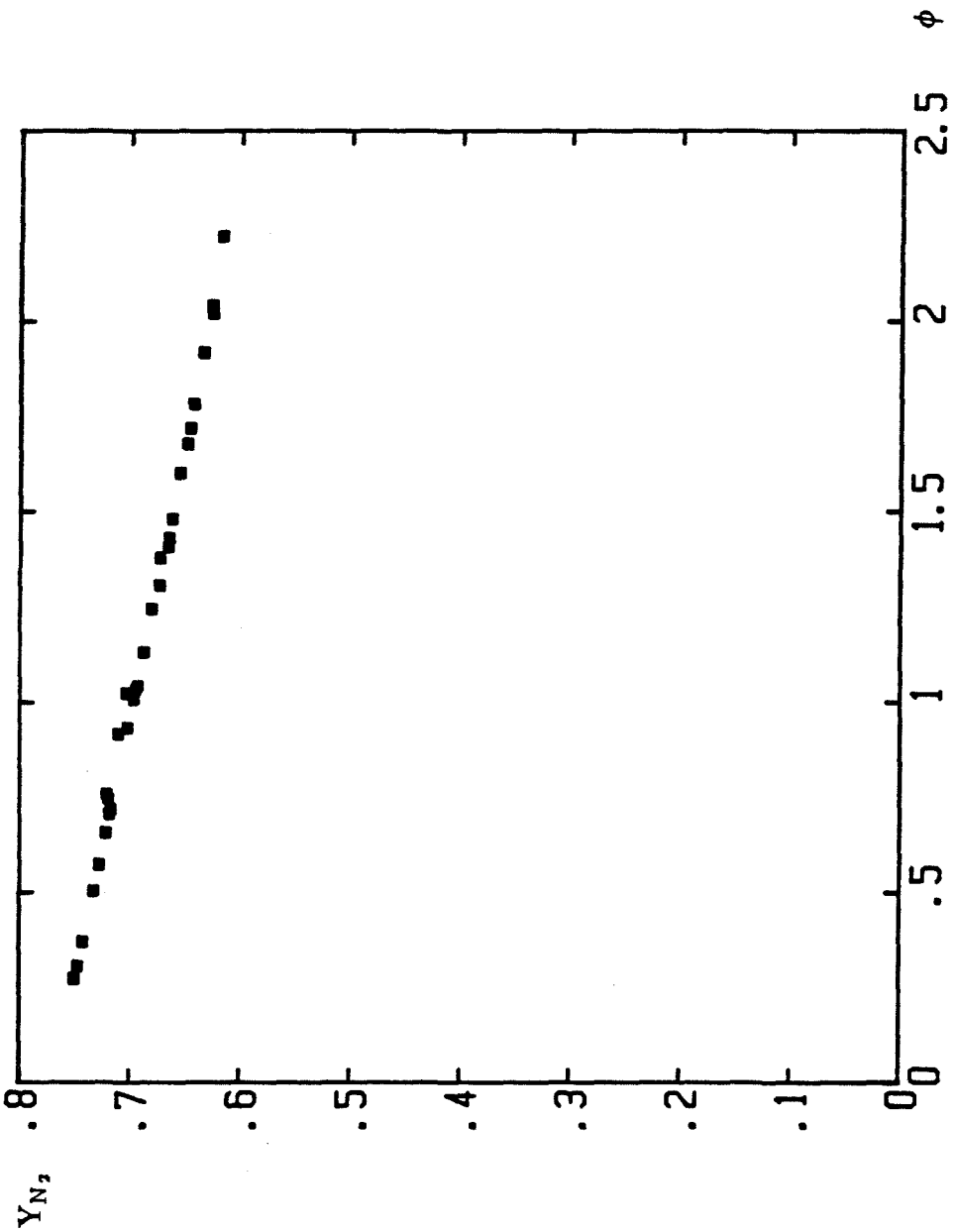

Figure (3.19) Nitrogen mole fraction data as a function of equivalence ratio.

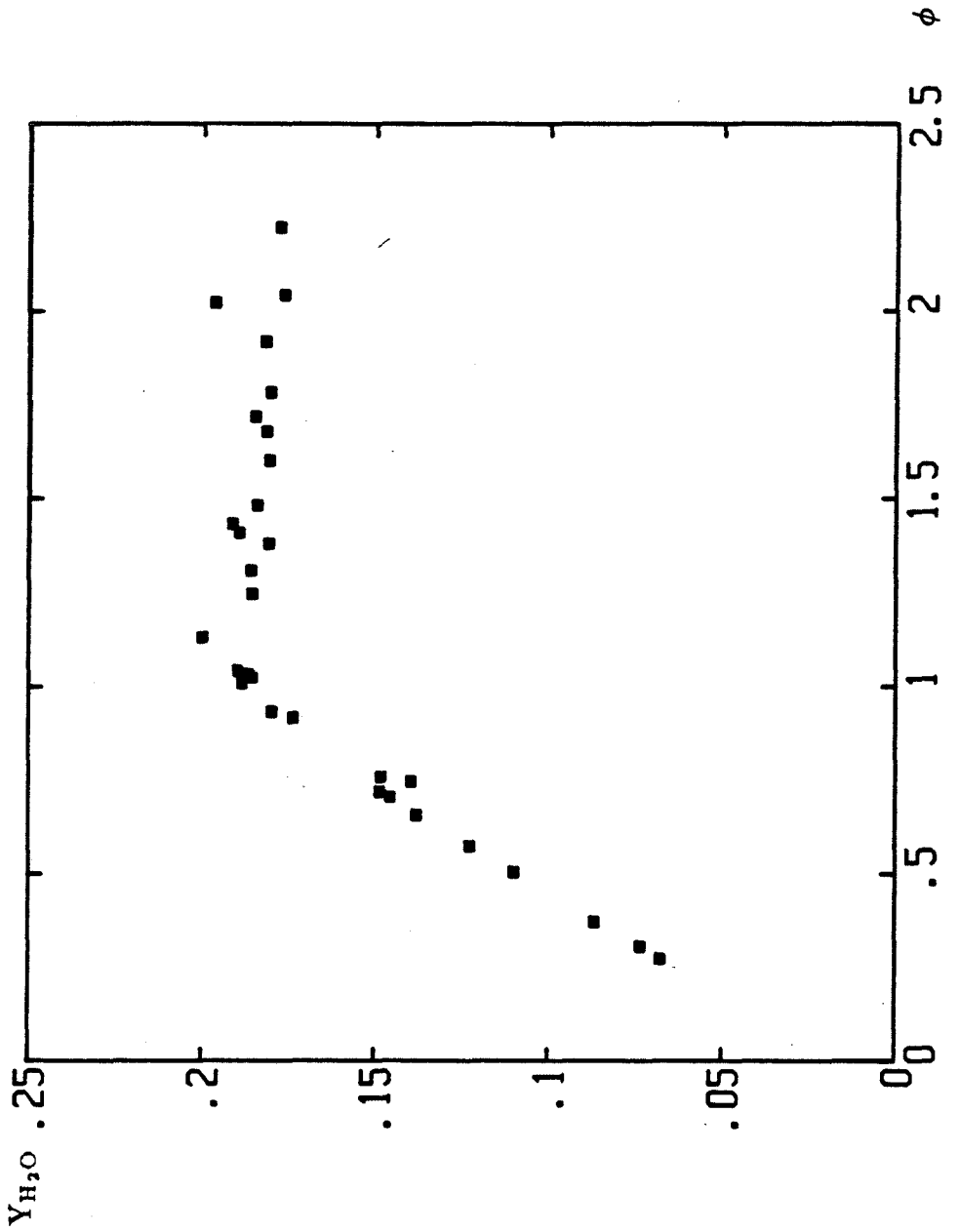

Figure (3.20) Water vapor mole fraction data as a function of equivalence ratio.

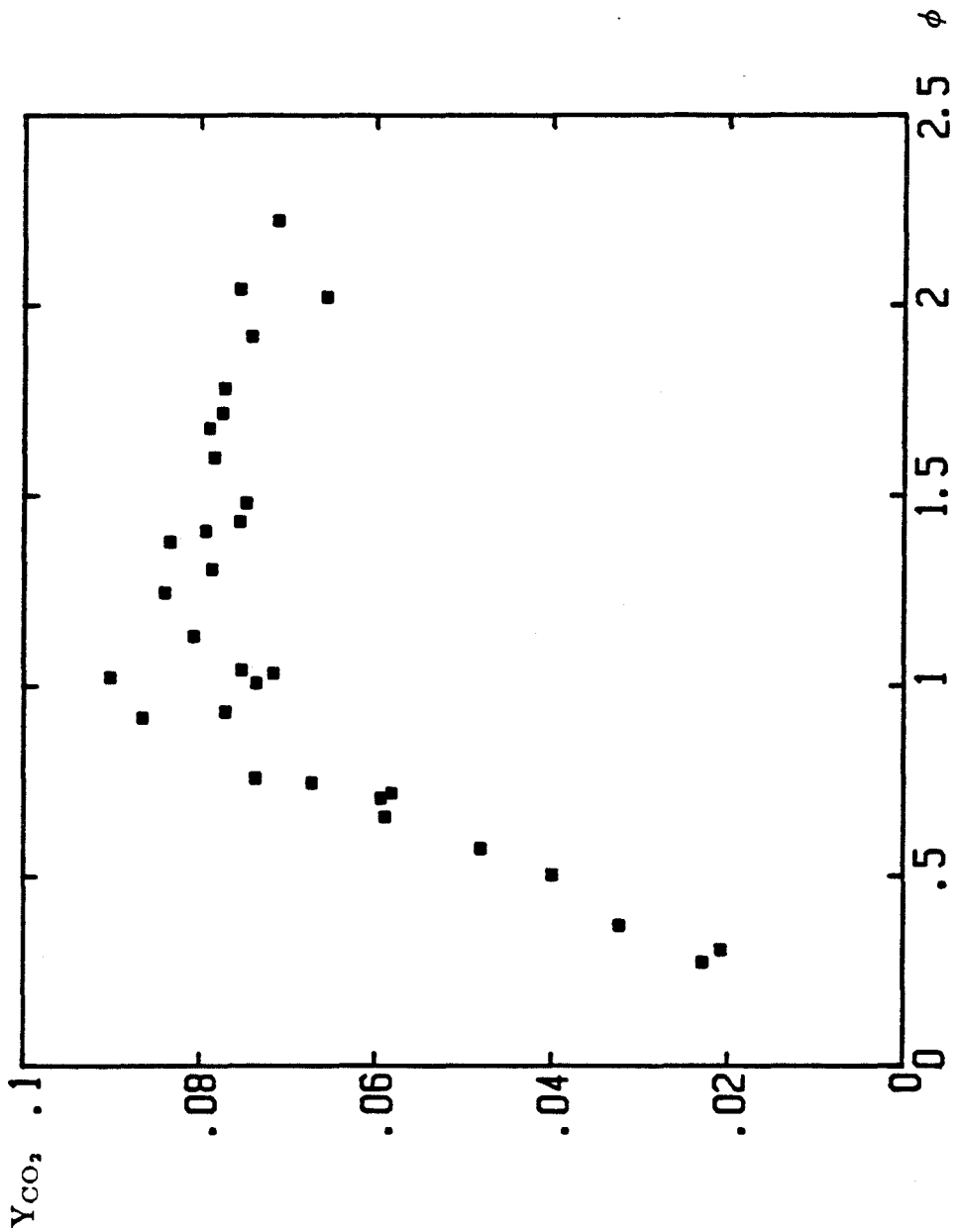

Figure (3.21) Carbon dioxide mole fraction data as a function of equivalence ratio.

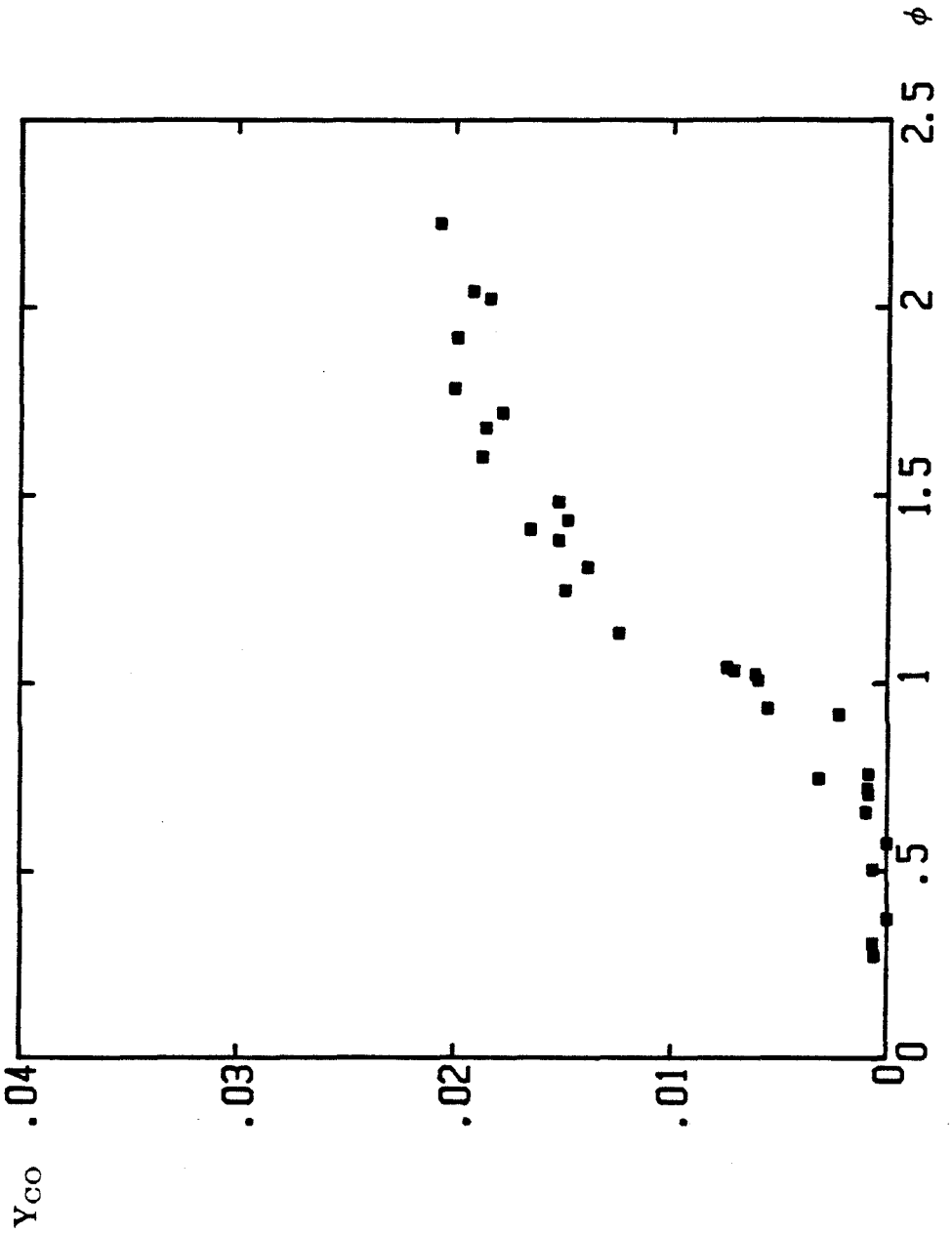

Figure (3.22) Carbon monoxide mole fraction data as a function of equivalence ratio.

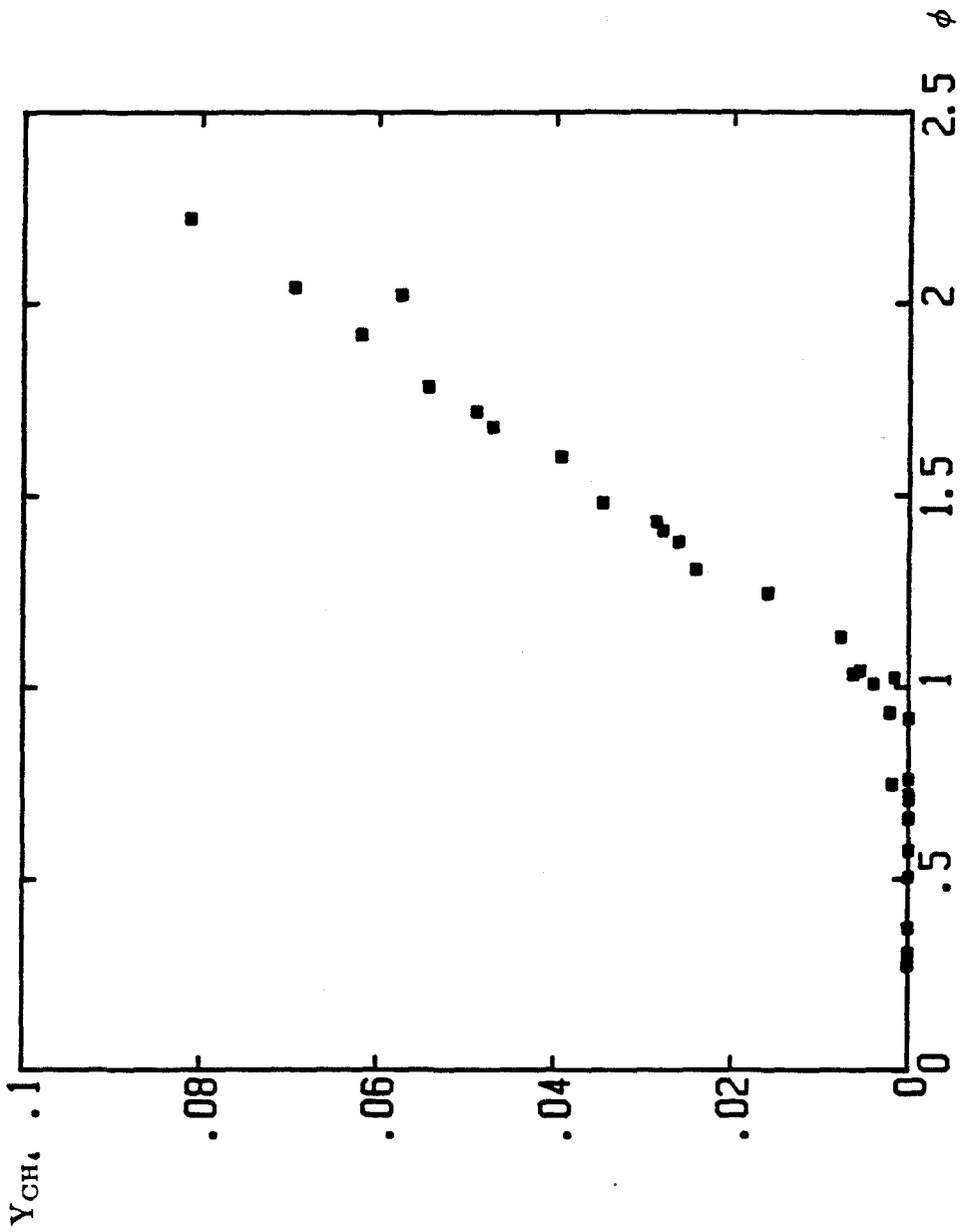

Figure (3.23) Methane mole fraction data as a function of equivalence ratio.

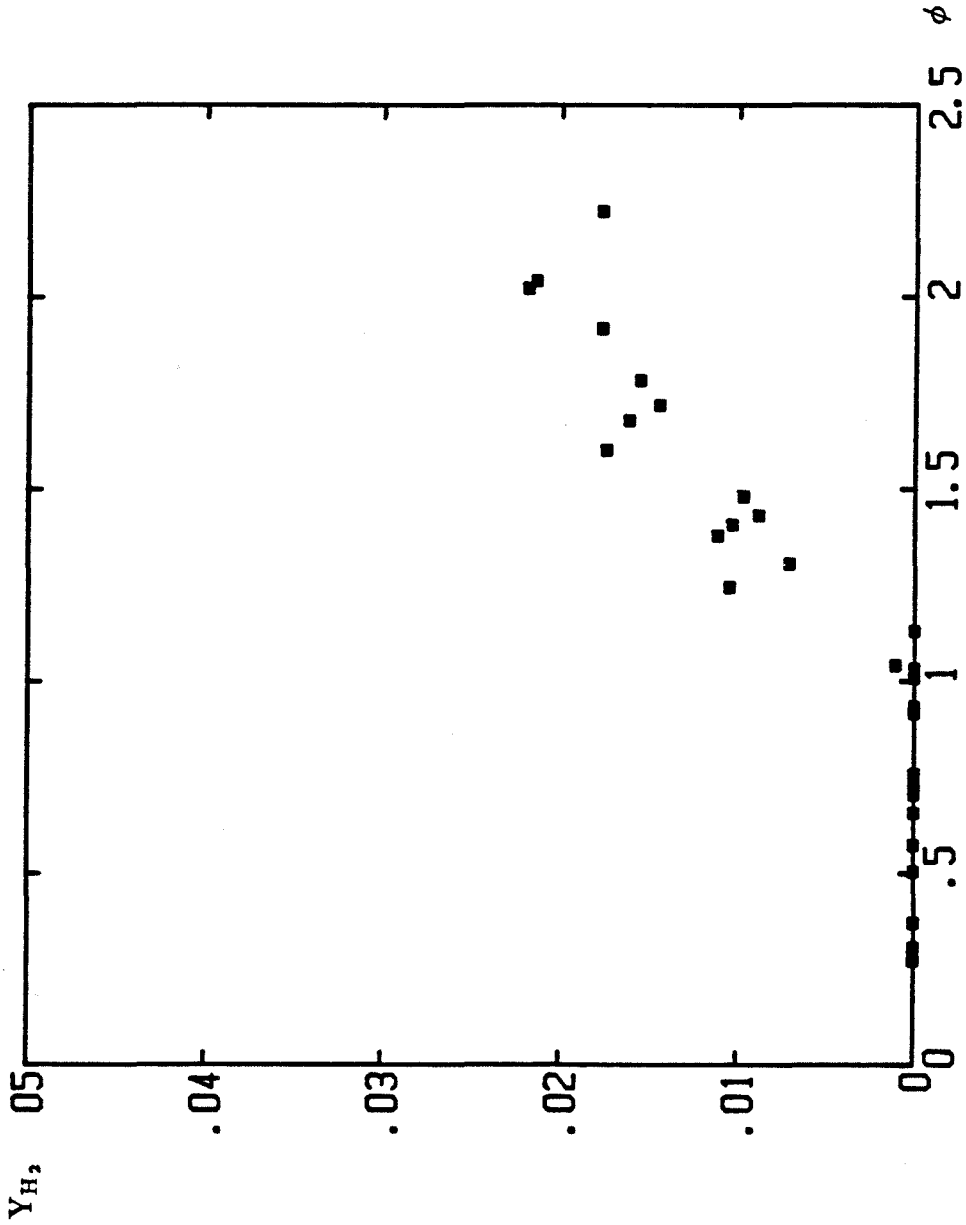

Figure (3.24) Hydrogen mole fraction data as a function of equivalence ratio.

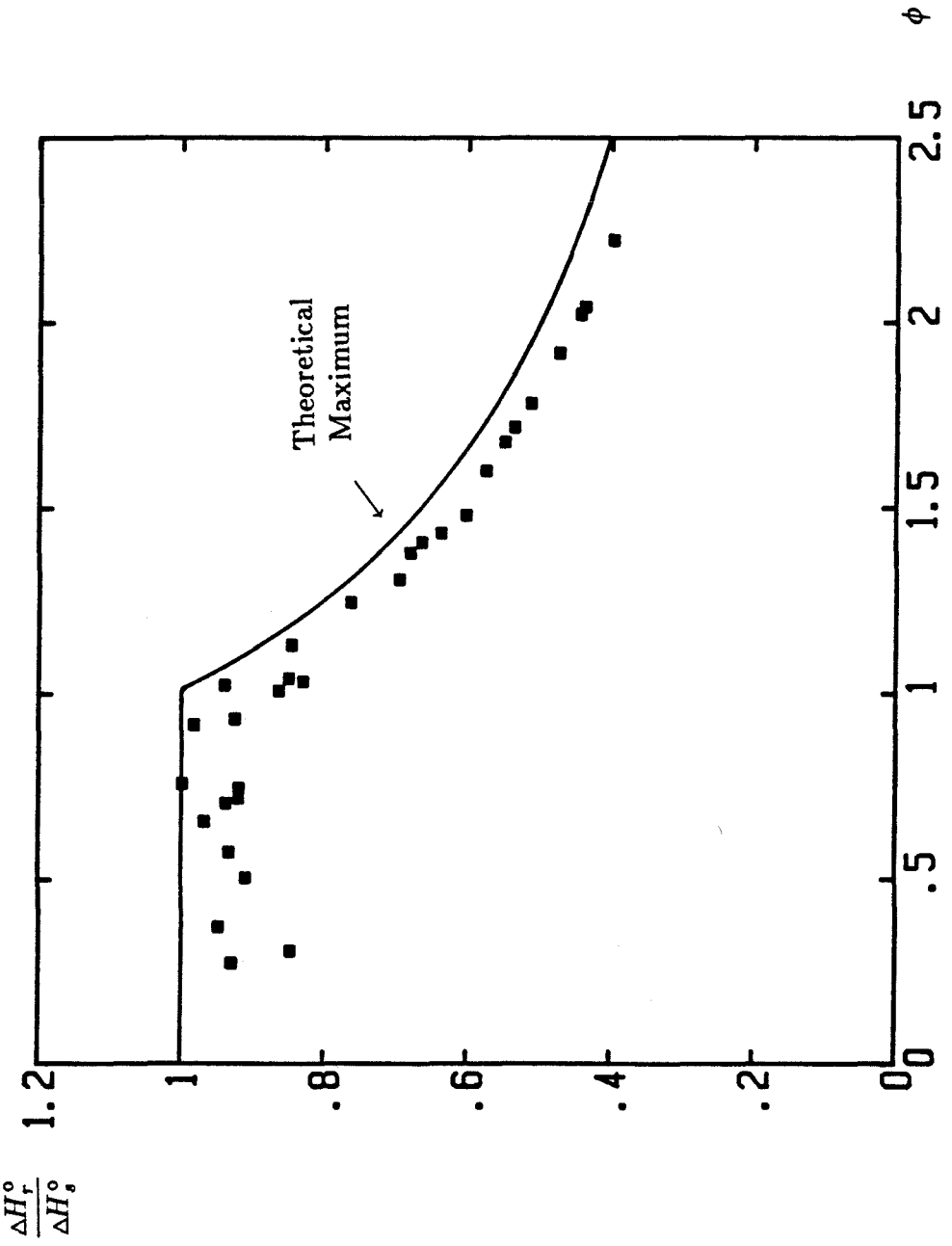

Figure (3.25) Ratio of measured heat of reaction to stoichiometric heat of reaction as a function of equivalence ratio.

Chapter 4

Entrainment in Fully Turbulent Jet Diffusion Flames

The technique used to determine entrainment is not limited to use on buoyant diffusion flames. As an extension of the work on near-field entrainment from buoyant diffusion flames, the technique was modified in order to measure entrainment in vertical, free-turbulent jet diffusion flames where momentum was important. This technique allowed a more direct measurement of the entrainment than the point-measurement technique employed by Becker and Yamazaki (1978) in developing their comprehensive model of the turbulent jet diffusion flame. Flame heights were also studied for comparison with previous results.

4.1 Experimental Technique

The two-layer technique used to measure the entrainment rates of turbulent hydrogen flames burning in air was a modification of the technique described in detail in Chapter 2. The concept is shown again in figure (4.1). Fuel is delivered to the jet flame at a flow rate $\dot{m}_f$. As it burns, it entrains a mass of air, $\dot{m}_e$, from below the interface. This air is heated and chemically altered as it reacts with the fuel and is transported in the plume to the upper layer where it remains in this stably stratified, well-mixed region. The major difference in the new technique was a simplification of the chemistry resulting from the use of hydrogen as the fuel. The reaction of 1 mole of hydrogen and I moles of air can be represented as

$$\begin{aligned} &H_2 + I(b_1 O_2 + b_2 N_2 + b_3 H_2O + b_4 CO_2 + b_5 Ar) \Rightarrow \\ &x_1 H_2 + x_2 O_2 + x_3 N_2 + x_4 CO_2 + x_5 H_2O + x_6 Ar\,, \end{aligned} \tag{4.1}$$

where air has been represented as

$$b_1 O_2 + b_2 N_2 + b_3 H_2O + b_4 CO_2 + b_5 Ar\,. \tag{4.2}$$

The selected products are a list of the products obtained from reactions of hydrogen and air at atmospheric conditions. In **4.1**, there are seven unknowns $(I, x_1, x_2, \ldots, x_6)$.

The unknowns in **4.1** can be evaluated by using the five conservation-of-atoms equations for C, H, O, N, and Ar, as well as by determining, through gas analysis, independent relationship between the various x_i.

The five conservation-of-atoms equations can be written as

$$Ib_4 = x_4 \tag{4.3a}$$

$$1 + Ib_3 = x_1 + x_5 \tag{4.3b}$$

$$I(b_1 + \tfrac{1}{2}b_3 + b_4 + c_1 b_5) = (x_2 + c_1 x_6) + x_4 + \tfrac{1}{2}x_5 \tag{4.3c}$$

$$Ib_2 = x_3\,, \tag{4.3d}$$

where the equations for argon and oxygen have been combined in order to accommodate the gas analysis technique. **4.3a**, **4.3b**, **4.3c**, and **4.3d** can be combined to get

$$\begin{aligned} I(b_1 + c_1 b_5) - \tfrac{1}{2} &= (x_2 + c_1 x_6) - \tfrac{1}{2}x_1 \\ &= [(y_2 + c_1 y_6) - \tfrac{1}{2}y_1]Ib_2\,, \end{aligned} \tag{4.4}$$

where $y_i = x_i/x_3$. Solving for I gives

$$I = \frac{1}{2\{b_1 + c_1 b_5 + [\frac{1}{2}y_1 - (y_2 + c_1 y_6)]b_2\}}\,. \tag{4.5}$$

Therefore, if the quantities $y_2 + c_1 y_6$ and y_1 can be measured for some constant c_1, then I can be determined and hence $\dot{m}_e/\dot{m}_f$ can be calculated from

$$\frac{\dot{m}_e}{\dot{m}_f} = \frac{\mathrm{M}_\infty}{\mathrm{M}_\mathrm{f}}\, I\,, \tag{4.6}$$

where M_∞ and M_f are the molecular weights of air and hydrogen, respectively.

4.1.1 Gas Analysis Technique

The gas analysis system was the same as that described in Chapter 2 except that, in this case, only the molecular sieve column was installed. This was possible because only hydrogen, nitrogen, and oxygen plus argon measurements were required. Calibrations were used to determine the response factors for the various components, and choosing c_1 as

$$c_1 = f_2/f_6 \tag{4.7}$$

allowed the required quantities, $y_2 + c_1 y_6$ and y_1, to be determined.

4.1.2 Burner and Gas Sampling Facilities

The hood and gas sampling assembly were similar to those described in Chapter 2. Since soot is not created by a hydrogen flame, no filtering of the sample gas was required. Also, since water vapor in the sample was not measured, the water was condensed out of the sample gas with an ice bath.

The burner used is shown in figure (4.2). The burner nozzle was a long-radius flow nozzle used to measure the fuel flow rate and had a throat diameter of 4.25 mm. Temperature and static pressure were measured in the large-diameter chamber upstream of the nozzle and an appropriate discharge coefficient was used to determine the actual flow rate (ASME, 1971).

4.2 Entrainment Results

The entrainment of turbulent, hydrogen jet diffusion flames was studied from regimes theorized to be momentum-dominated to those thought to be bouyancy-dominated. As discussed in Chapter 3, the distinctions between jets in a two-layer environment and those in a uniform environment must be kept in mind. In the present case, however, the discrepancy between these two cases appears to be quite small.

4.2.1 Free Turbulent Axisymmetric Flame Theory

Dimensional arguments and self-similarity have proven quite useful in developing a mature theory of fully turbulent jets and flames in the far field (Thring and Newby, 1952; Ricou and Spalding, 1961; Becker and Yamazaki, 1978; Dahm, 1985). The plume mass flux can be characterized by

$$\frac{d\dot{m}}{dz} = C_1(\pi\rho_\infty J/4)^{1/2}, \tag{4.8}$$

where C_1 is a constant and J is the local momentum flux of the jet. The constant, C_1, is not universal since its value for momentum-dominated flow is different from its buoyancy-dominated flow value. Also, Becker and Yamazaki (1978) argue that an average plume density, $\bar{\rho}$, would be the proper scaling density in **4.8**. For simplicity, however, **4.8** is the equation used for characterizing the plume mass flux. This equation can be analyzed in the limits of the momentum-dominated and buoyancy-dominated regimes.

The effect of buoyancy depends on the relative importance of the buoyancy force with respect to the initial momentum flux in the flow. Near the flame source, the momentum with which the fuel is injected may be so large that buoyancy forces are unimportant over a certain region of the flame. In this region the momentum flux, J, will be close to its initial values, J_0, and flow characteristics, such as entrainment rates, will be those of a momentum-dominated jet with no influence of buoyancy. In this case, **4.8** becomes

$$\dot{m} = C_1(4\rho_\infty J_0/\pi)^{1/2} z\,. \tag{4.9}$$

An effective source velocity and diameter can be defined by

$$u_s = \frac{J_0}{\dot{m}_f} \tag{4.10}$$

and

$$D_s = \left(\frac{4J_0}{\pi\rho_\infty u_s^2}\right)^{1/2} . \tag{4.11}$$

From these definitions, the effective diameter is seen to be equivalent to the diameter of a jet of fluid with density ρ_∞ and velocity u_s providing the momentum flux J_0. For a jet with a top-hat velocity profile, $u_s \rightarrow u_0$ and $D_s \rightarrow D_0\sqrt{\rho_0/\rho_\infty}$, where u_0, D_0, and ρ_0 refer to actual source conditions. A nondimensional mass flux can then be obtained from **4.9** as

$$\frac{\dot{m}D_s}{\dot{m}_f z} = C_1 \tag{4.12}$$

and is constant in the momentum-dominated case.

The behavior of the mass flux for the buoyancy-dominated case is quite different. The effect of buoyancy on these flames is determined by the ratio of the buoyancy force to the initial momentum flux. The buoyancy force can be scaled as $\rho_\infty g z^3$ if we assume that the spreading rates of these jets are linear. This representation also assumes that the density of the jet fluid is much smaller than the density of the ambient fluid. (This assumption appears to be valid in the region of high heat release. A more suitable scaling factor, however, would use $\rho_\infty - \bar{\rho}$, where $\bar{\rho}$ is an average plume density.) The ratio of buoyancy force on the plume to initial momentum flux can then be scaled by the local Richardson number, $\pi\rho_\infty g z^3/4J_0$, and the cube root of this provides a convenient nondimensional streamwise coordinate (Becker and Yamazaki, 1978),

$$\xi \equiv (\pi\rho_\infty g/4J_0)^{1/3} z \equiv \mathrm{Ri}_s{}^{1/3}\frac{z}{D_s} , \tag{4.13}$$

where

$$\mathrm{Ri}_s \equiv \pi\rho_\infty g D_s^3/4J_0 \equiv \frac{gD_s}{u_s^2} . \tag{4.14}$$

From this determination, $\xi \rightarrow 0$ corresponds to momentum-dominated flow and $\xi \rightarrow \infty$ corresponds to buoyancy-dominated flow. Becker and Yamazaki have

observed in their entrainment measurements that the transition between these regimes occurs between $\xi = 1$ and $\xi = 2.5$.

When buoyancy is important, a vertical momentum balance gives

$$\frac{dJ}{dz} = C_2 \pi \rho_\infty g z^2 , \tag{4.15}$$

which can be integrated to obtain

$$\frac{J}{J_0} = C_3 \xi^3 + 1 . \tag{4.16}$$

Then when $C_3 \xi^3$ is large compared to 1,

$$\frac{J}{J_0} = C_3 \xi^3 . \tag{4.17}$$

Substituting this into **4.8** yields an equation for the nondimensional mass flux

$$\frac{\dot{m} D_s}{\dot{m}_f z} = C_4 \xi^{3/2} , \tag{4.18}$$

and thus the nondimensional mass flux is linear with $\xi^{3/2}$. Again, the assumption that $\rho_\infty - \bar{\rho} \approx \rho_\infty$ has been made in **4.15** in order to obtain the $m \sim z^{5/2}$ dependence. This technique is the technique used by Becker and Yamazaki. The same $z^{5/2}$-dependence has been theorized by Cetegen et al. (1982), who extended the plume entrainment techniques of Schmidt (1941) and Morton et al. (1956) by allowing for a large, but constant, difference between the plume temperature and the ambient temperature, and by Delichatsios and Orloff (1984), using strictly dimensional arguments.

It is interesting to note that the only assumption that was made in the above analysis, relating to jet flames as compared to plumes in general, is the assumption that $\rho_\infty - \bar{\rho} \approx \rho_\infty$. This assumption is valid in the heat-release regions of the flame and possibly for short distances downstream from the flame tip.

4.2.2 Turbulence Parameters

To this point, the assumption has been made that the flames under discussion are fully turbulent. This suggests the need for some characteristic Reynolds number to signify the ratio of inertial forces to viscous forces. Becker and Liang (1978) argue that two such parameters are valuable. The effective source Reynolds number, defined by

$$\mathrm{Re}_s \equiv \frac{u_s D_s}{\nu_\infty}, \tag{4.19}$$

where ν_∞ is the kinematic viscosity of the ambient fluid, is a characteristic source ratio. The flame jet as a whole is characterized by the overall flame-zone Reynolds number, defined as

$$\mathrm{Re}_L \equiv \frac{14\beta\dot{m}_f}{\mu_\infty W_1 L}, \tag{4.20}$$

where L is the flame height, W_1 is the mass fraction of the source material in a stoichiometric mixture with the ambient fluid ($W_1 = 0.0283$ for hydrogen in air), and β is a density ratio ($\beta = 3.07$ for hydrogen in air). The overall flame-zone Reynolds number was derived from the intermediate definition $\mathrm{Re} \equiv 2\dot{m}/\pi\bar{\mu}b$, where b is the characteristic radius of the jet and $\bar{\mu}$ is the average dynamic viscosity in the jet, assuming a linear spreading rate and a stoichiometric fuel-air mixture at the flame height, i.e., $\dot{m} \approx \dot{m}_f/W_1$ at $z = L$. Also, the viscosity of the ambient fluid is used rather than an average viscosity, $\bar{\mu}$. The constant was chosen so that in the case of a momentum-dominated flame, the two Reynolds numbers, Re_s and Re_L, would be equal.

While the effective source Reynolds number is a valuable parameter, it neglects temperature effects on the jet density and dynamic viscosity. Actual turbulence effects can be characterized by the ratio of the jet momentum flux, J, to the jet viscous force, $\bar{\mu}\bar{u}\delta$, where $\bar{u}$ is the characteristic jet velocity, and δ is the characteristic shear-layer thickness. The characteristic jet velocity, $\bar{u}$, can be

scaled by

$$\bar{u} = (J/\bar{\rho}\delta^2)^{1/2}, \tag{4.21}$$

so that the Reynolds ratio goes as

$$\begin{aligned} \mathrm{Re} &= \frac{(\bar{\rho}J)^{1/2}}{\bar{\mu}} \\ &= \left(\frac{\bar{\rho}}{\rho_\infty}\right)^{1/2}\left(\frac{\mu_\infty}{\bar{\mu}}\right)\mathrm{Re}_s\,. \end{aligned} \tag{4.22}$$

Since the dynamic viscosity scales as $T^{1/2}$ (Reid et al. (1977)) and density as T^{-1}, the actual inertial-to-viscous ratio scales as $T_\infty/\bar{T}$ times the effective source Reynolds number, Re_s.

It is interesting to note that for the jet of uniform velocity issuing into a fluid of similar density, the effective source Reynolds number simplifies to the standard jet Reynolds number. If the densities of the jet and the ambient fluid are not initially equal, then the ratio of inertial forces to viscous forces is not initially Re_s in the momentum-dominated case. Since the jet entrains large amounts of ambient fluid over a relatively short distance, however, the ratio approaches Re_s quickly.

A convincing set of experiments does not yet exist for characterizing the transition to turbulent flow in flame jets in an unambiguous manner. However, Becker and Liang (1978) suggest that the transition occurs for Re_s in the range of 2000 to 5000. This suggestion was based on the flame-height measurements of Blinov and Khudiakov (1957). Dahm (1985) and Weddell (in Hottel, 1953) also found that for reactions in fuel jets, the flow was turbulent for Re_s greater than 3000 or 4000.

4.2.3 Compressibility Parameters

Compressibility effects in the flames were of concern and were characterized by

three Mach numbers. The first of these, M_H, is the Mach number of the jet based on actual nozzle exit conditions. This varied from 0.2 to 0.7. Since the jet entrains significant amounts of air quickly, the Mach number of the jet with respect to the sonic speed in air, M_A, was also calculated and this varied from 0.75 to 2.6. Neither of these, however, clearly represents the initial physics of the problem. Initially, the jet of essentially uniform velocity exits into the quiescent air environment. A shear layer develops between these two and determines the initial stability and mixing of the jet. In investigating the effects of Mach number on these processes, Papamoschou and Roshko (1986) proposed that the convective Mach number should be used to characterize the flow. This convective Mach number, M_C, of the fuel and air streams is based on velocities of the streams with respect to a frame moving with the organized large structures on the interface. (The convective Mach number was equivalent for each stream in the present investigation.) The velocity of these structures is inferred by requiring the total pressure of the streams with respect to the structures to be equal. For equal specific heat ratios between the two streams, this definition of Mach number can be written quite simply as $M_C = u_0/(c_f + c_\infty)$, where u_0 is the mean jet velocity at the source, and c_f and c_∞ are the sonic velocities for each stream. In the present experiments, it varied from 0.2 to 0.6. In this range, Papamoschou and Roshko found that the thickness of the shear layer changes less than 25% from incompressible results. In the present results, therefore, we do not expect that compressibility effects were large along the edges of the jet.

Compressibility effects near the centerline of the jet were analyzed by determining how many diameters downstream from the burner the jet required before the centerline velocities were lower than the speed of sound in air. Assuming a shear-layer flow at the nozzle exit and modelling the downstream flow using the

results of Albertson et al. (1950), we calculated the compressibility effects to be limited to, at most, the first 8 diameters downstream from the jet source. Since all the measurements were taken at more than 40 diameters from the source, this result also suggests that compressibility effects were small.

4.2.4 Experimental Results

Entrainment was measured using 45 to 120 kW hydrogen flames burning in air. The effective source Reynolds number ranged from 25,000 to 50,000 and the source Richardson numbers, Ri_s, varied from 10^{-8} to 10^{-7}. Entrainment was measured over the range of nondimensional streamwise lengths, ξ, from 0.5 to 2.5, and the effective nozzle diameter was about 1.1 mm. The results are presented in Table **4.1**.

Figure (4.3) shows nondimensional plume mass flux versus nondimensional streamwise location. This figure also presents a fit to the data of Becker and Yamazaki (1978) along with the constant value of nondimensional plume mass flux determined by Ricou and Spaulding (1961) for regions where the jet density nearly reaches the ambient density, which is not the case in the region of combustion.

The results show the trends expected from the analysis presented above. For $\xi^{3/2} < 1.3$, the nondimensional mass flux appears to have reached the constant value expected for momentum-dominated flows as given in **4.12**. Here $C_1 = 0.24$. Ricou and Spaulding found $C_1 = 0.32$ for their isothermal plumes, while Becker and Yamazaki found $C_1 = 0.16$ for their hydrogen-stabilized propane flames. It should be pointed out that Becker and Yamazaki questioned the accuracy of their results due to their experimental technique, which was based on the use of a pitot probe and uncorrected thermocouple to infer point measurements

of density and velocity. The mass flux in their measurements was evaluated numerically from the product of these measurements. In addition to the large errors inherent in integrating point measurements near the outer edges of the jet, this technique also neglects the fluctuation-correlation term, which Papanicolaou (1984) found led to errors as large as 25%.

For $\xi^{3/2} > 1.3$, the nondimensional mass flux appears to be in a state of transition. The results are shown again on a linear scale in figure (4.4). The dashed lines in this figure are the fits to the results of Becker and Yamazaki. Note that the buoyancy-dominated representation of their data goes through the origin (no virtual-origin offset) and yields $C_4 = 0.08$. For the present results either the transition is not yet complete or a significant virtual-origin offset exists.

For the buoyancy-dominated case, **4.18** can be rewritten in the more useful form

$$\dot{m} = \tfrac{\pi}{4} C_4 \rho_\infty \sqrt{g} z^{5/2} . \tag{4.23}$$

Here, the plume mass flux is independent of the fuel mass flux. In the current results, even at the largest axial distance, there was a 25% variation in the measured values of C_4 (see Table **4.1**). It is assumed that the plume had not yet fully reached the buoyancy-dominated region. Furthermore, if the deviations from the behavior expected from **4.18** were due to a virtual-origin offset, then **4.23** might be written as

$$\dot{m}^{2/5} = \left(\tfrac{\pi}{4} C_4 \rho_\infty \sqrt{g}\right)^{2/5} (z - z_0) , \tag{4.24}$$

and plotting $\dot{m}^{2/5}$ as a function of z would determine the value of the virtual-origin offset, z_0. This plot is shown in figure (4.5) and is inconclusive, again suggesting that the buoyancy-dominated regime had not been fully reached. Another point worthy of consideration is that the flames corresponding to the largest

values of ξ measured had lengths lower than the interface heights. However, since the interfaces in these experiments were less than 20% of the flame height from the mean flame height, the assumption that $\rho_\infty - \bar{\rho} \approx \rho_\infty$ is still valid, and so **4.15** will still hold.

Since the data in figure (4.4) are still in the transition regime, it can only be used to obtain an upper bound for C_4. If we use the data for the largest value of ξ, the current results give $C_4 \leq 0.105$. Other measurements of entrainment are provided by Delichatsios and Orloff (1984) and Cetegen et al. (1984). Delachatsios and Orloff (1984) measured the entrainment using propane flames and a Ricou-Spalding type apparatus, and determined that $C_4 = 0.04$. Cetegen et al. (1984) measured the entrainment in flames that were formed above large diameter burners and found that over the turbulent range of these flames $C_4 = 0.10$. In the latter two experiments the effective source Reynolds numbers were less than about 3500, and so the assumption of fully turbulent flow is questionable. It is interesting to note, however, that even with significantly different burners and fuels, Richardson numbers, and Reynolds numbers, the constants determined by Cetegen et al. were similar to those determined here for the fully turbulent jet flows.

The major uncertainty in the current results stems from the inaccuracy in locating the interface. Typically, the interface (and hence z) could be determined only within about 5% relative uncertainty for the cases at largest z to 10% relative uncertainty for the smallest z cases. Since the current technique measures $\dot{m}_e/\dot{m}_f$ directly, any uncertainty in measuring $\dot{m}_f$ was suppressed in the final results. Uncertainties in $\dot{m}_e/\dot{m}_f$ were much less than 5%, so that the net errors in $\dot{m}D_s/\dot{m}_f z$ and ξ were simply determined by the inaccuracies in measuring z.

Although the data presented here are limited in quantity, the measurement

technique is believed to be superior to that employed by Becker and Yamazaki (1978) and merits further study. An extensive systematic study of entrainment over a range of source Richardson number would prove valuable.

4.3 Flame Length Measurments

In addition to the entrainment measurements, visual flame length studies were performed. Several experiments on flame length of turbulent diffusion flames have been conducted. Hottel and Hawthorne (1948), Hawthorne et al. (1948), and Wohl et al. (1948) presented the first results on turbulent diffusion flames, and since that time major contributions have been made by Baev and Yasakov (1976), Baev et al. (1976), Becker and Liang (1978), and Dahm (1985).

For momentum-dominated and fully turbulent "flames" in water, the equivalent flame length has been found to be independent of Reynolds number or heat release rate, scaling only with the burner diameter (Weddell, in Hottel, 1953; Dahm, 1985). However, these results were for measurements in liquids that had little or no buoyancy effect. For all the gaseous fuel jets measured to date, none is unquestionably in the momentum-dominated regime over the whole flame length. Becker and Liang (1978) measured jets that appeared to be closest to the momentum-dominated case. For their jet flames, ξ_L, the value of ξ at the flame tip, was as low as one for some of the measurements with carbon monoxide as the fuel. For hydrogen and hydrocarbon fuels, the smallest values of ξ_L appeared to be about two. For flames in which buoyancy is not negligible, the heat addition rate and stoichiometric mixture ratio of the flame also appear to play a role (Broadwell, 1982).

In the current work, visual flame lengths were measured for hydrogen flames from a 4.25 mm nozzle burning in air. Velocities varied from 250 to 900 m/s

implying effective source Reynolds numbers, Re_s, from 18,000 to 70,000 and overall flame-zone Reynolds numbers, Re_L, from 50,000 to 130,000. The flame lengths were obtained by our measuring the top of the flame with time every 1/30 second using a video data system, and then plotting the intermittency of the flame height. This work was performed by Mr. J. Morehart. A typical intermittency curve is shown in figure (4.6), in this case for a source fuel velocity of 587 m/s. The 50% intermittency length is taken as the average flame length and the inverse of the slope of the intermittency curve at that point was defined as the fluctuation length of the flame, Δ. The flame lengths and fluctuation lengths that were measured, as well as the nondimensional quantities used to characterize these flames, are presented in Table **4.2**.

In the present experiments, the flame heights were measured by our visually observing the radiation from the hydrogen flames. The combustion zone in these flames was expected to be visible through a bluish chemilluminescence. In the current experiments, however, most of the flames had distinct yellow luminosity which we suspect was due to naturally occurring dust particles in the laboratory air. The effect that these particles have on the measurements is unclear, but it is possible that these particles could continue burning downstream from the hydrogen combustion regions, leading to erroneously long flame lengths. Keeping in mind that the measured flame height might be in error, we nonetheless compare our results to other empirical results.

In the momentum-dominated regime, the most recent flame-length estimates (Becker and Liang, 1978; Dahm et al., 1984) make predictions based on the assumption that the fuel will be completely consumed only after a stoichiometric amount of air is mixed with the fuel. Broadwell (1982) noted that the mixing must be completed on a molecular scale and that furthermore, in a fully turbulent

jet, the extent of the molecular mixing is proportional to the entrainment of ambient fluid into the jet. The works of Broadwell and Dahm et al. led to the proposal of a universal flame-length relationship for fully turbulent momentum-dominated flames

$$\frac{L}{D_s} \approx 10(1/W_1 - 1)\,, \tag{4.25}$$

where the constant was determined through correlations with their own data as well as with the data of Weddell (in Hottel, 1953). As mentioned above, these sets of data were for liquid jet flames. The extension to gaseous flame jets, however, is straightforward since the flame length, for high Reynolds numbers, is independent of the Schmidt number (Broadwell, 1982). Others (Becker and Liang, 1978; Baev and Yasakov, 1976; Hawthorne et al., 1948) have used a similar argument, neglecting any "molecular-mixing" concerns, and predicted

$$\frac{L}{D_s} \approx C_L \frac{\beta}{W_1}\,, \tag{4.26}$$

where C_L is a constant. Becker and Liang determined the constant as $C_L = 11$ by extrapolating from measurements that were not within the momentum-dominated region. Baev and Yasakov proposed a complicated flame-length model that simplified to **4.26** with $C_L = 5.6$ in the absence of buoyancy. Their determination of C_L was unclear. Finally, Hawthorne et al. predicted $C_L = 5.3$ based on correlations with a variety of fuels. However, these flames were not in the momentum-dominated regime. For momentum-dominated hydrogen flames in air, these various models predict

$$\text{Dahm et al. (1984)}: \quad L/D_s \approx 355 \tag{4.27a}$$

$$\text{Becker and Liang (1978)}: \quad L/D_s \approx 1190 \tag{4.27b}$$

$$\text{Baev and Yasakov (1976)}: \quad L/D_s \approx 610 \tag{4.27c}$$

$$\text{Hawthorne et al. (1948)}: \quad L/D_s \approx 575 \tag{4.27d}$$

current experimental results : $L/D_s \approx 460 - 630$. (4.27*e*)

The flame length for the most momentum-dominated of the current experiments was $L/D_s = 631$, which compares well with the models of Baev and Yasakov and Hawthorne et al., models which are based, at least in part, on correlations to hydrogen-air flame data. This apparent dependence on fuel suggests that flame length determination is still not well understood.

For flames that are not momentum-dominated, the most complete flame-length correlation is due to Becker and Liang (1978),

$$\frac{L}{D_s} = \frac{\beta}{W_1}\left(\frac{1}{0.18 + 0.022\mathrm{Ri}_s{}^{1/3}\frac{L}{D_s}}\right)^{3/2}, \tag{4.28}$$

and is an implicit relation. The current results were lower than the predictions of this model, as shown in figure (4.7). The current data, however, agree quite well with the rather extensive hydrogen data of Baev et al. (1976), as shown in figure (4.8).

For very buoyant plumes ($\mathrm{Ri}_s \gg 1$), **4.28** can be reduced to the form $L/D_0 \sim Q^{*2/5}$, a result found by Cetegen et al. (1984) on measurements of large buoyant diffusion flames of natural gas in air. The model developed by Cetegen et al., in correlation with their experimental measurements, underestimates the flame lengths measured by Becker and Liang by about 20 to 50%.

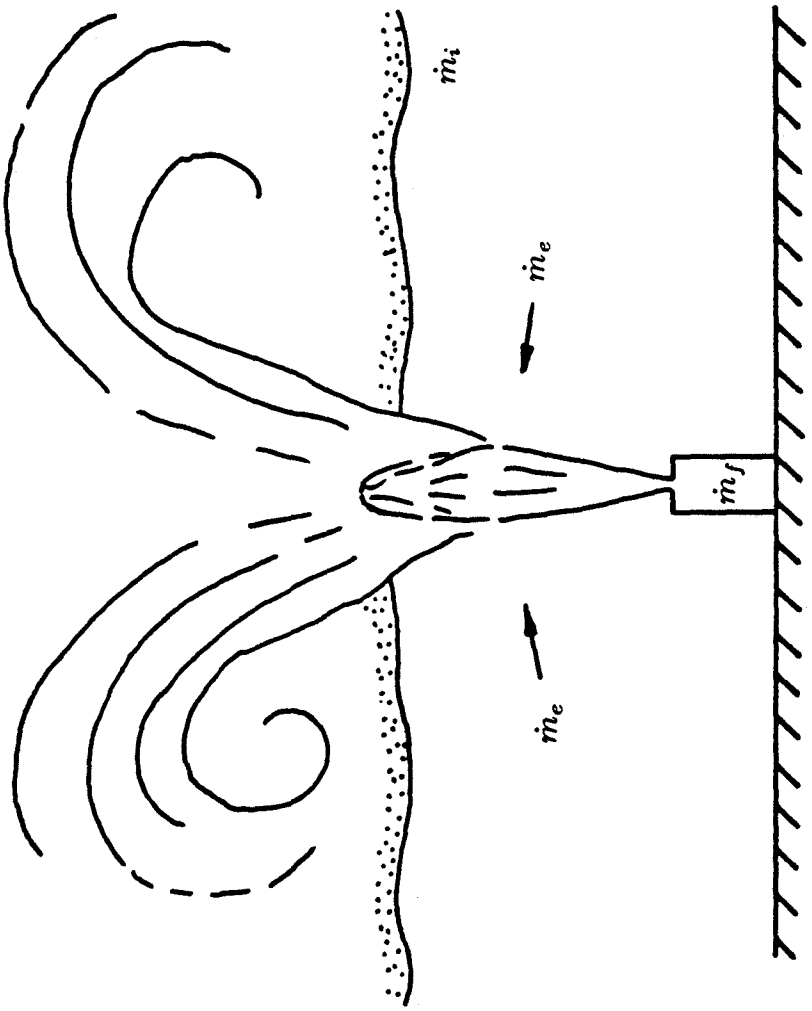

Figure (4.1) Jet flame entrainment measurement technique.

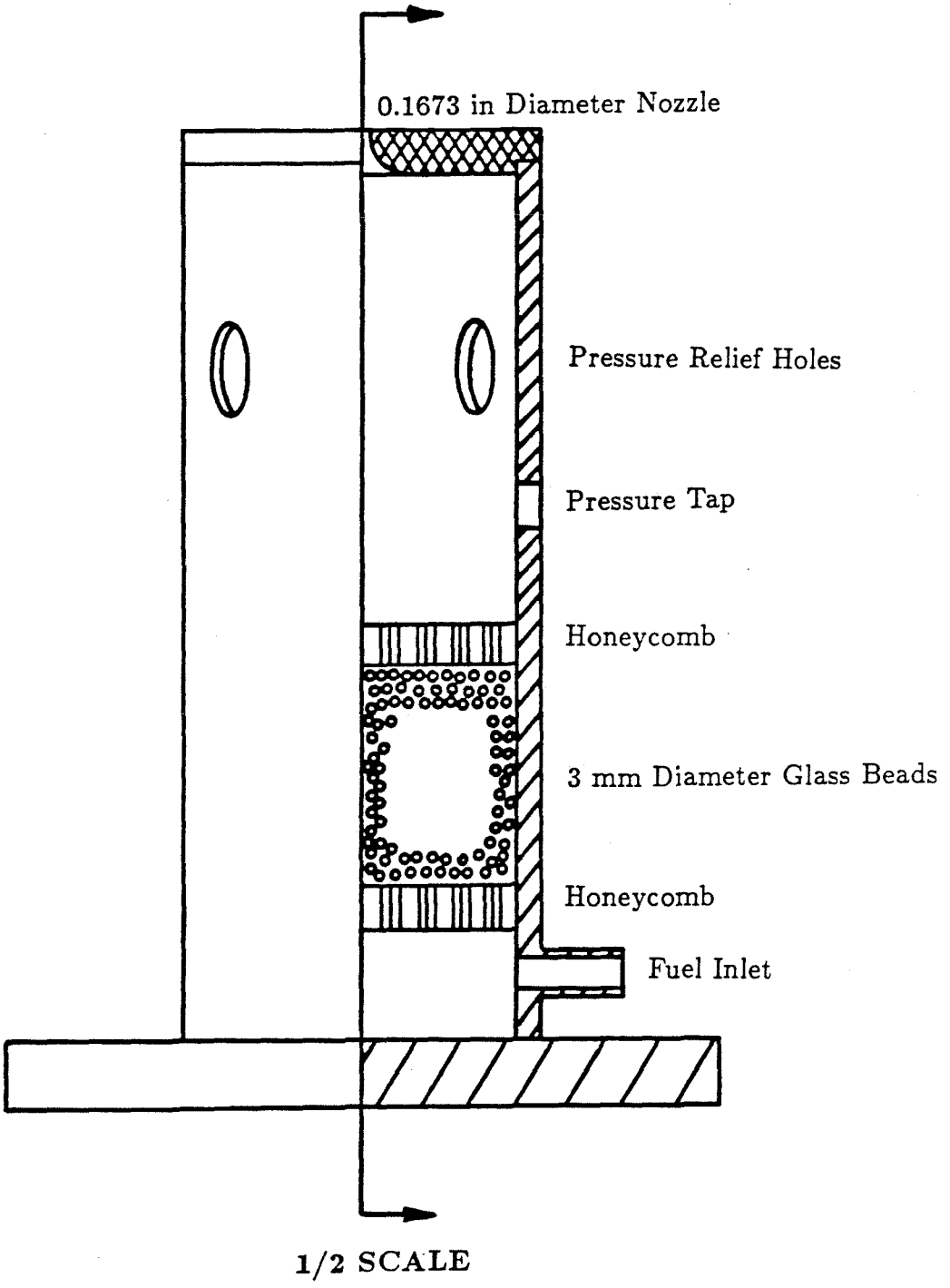

Figure (4.2) Burner geometry.

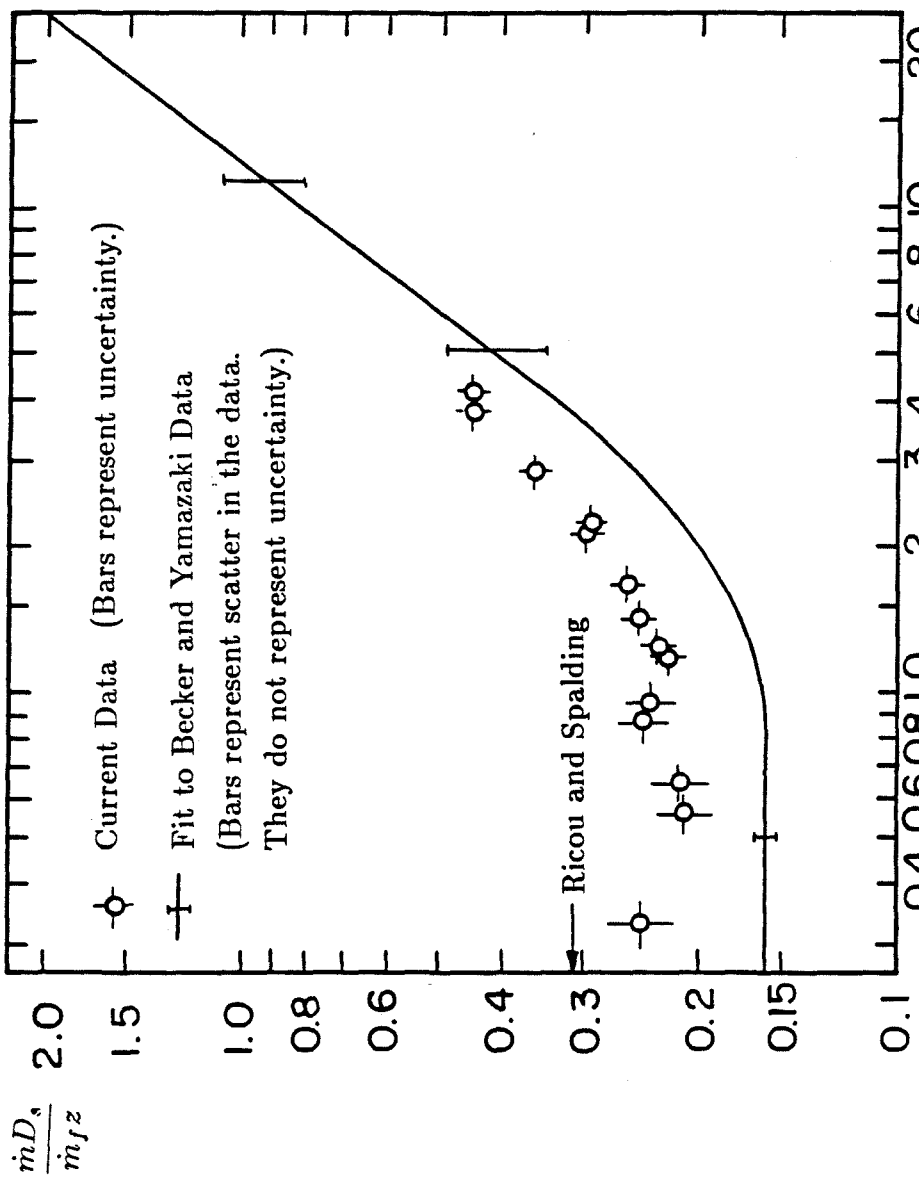

Figure (4.3) Plume mass flux data along with the data of Becker and Yamazaki (1978) and the results of Ricou and Spalding (1961).

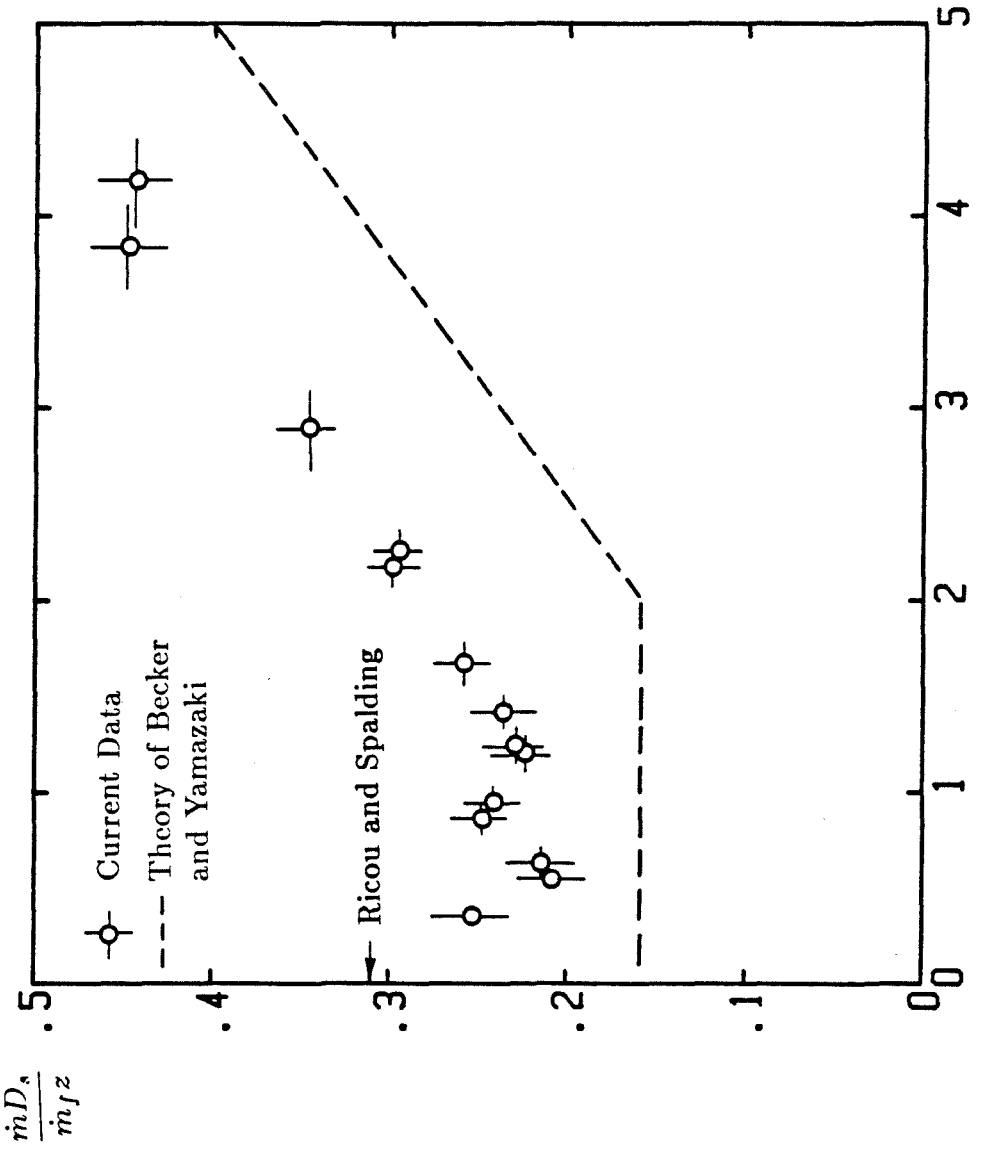

Figure (4.4) Linear representation of the plume mass flux data. Also shown are the results of Ricou and Spalding (1961) and the data-correlated theory of Becker and Yamazaki (1978).

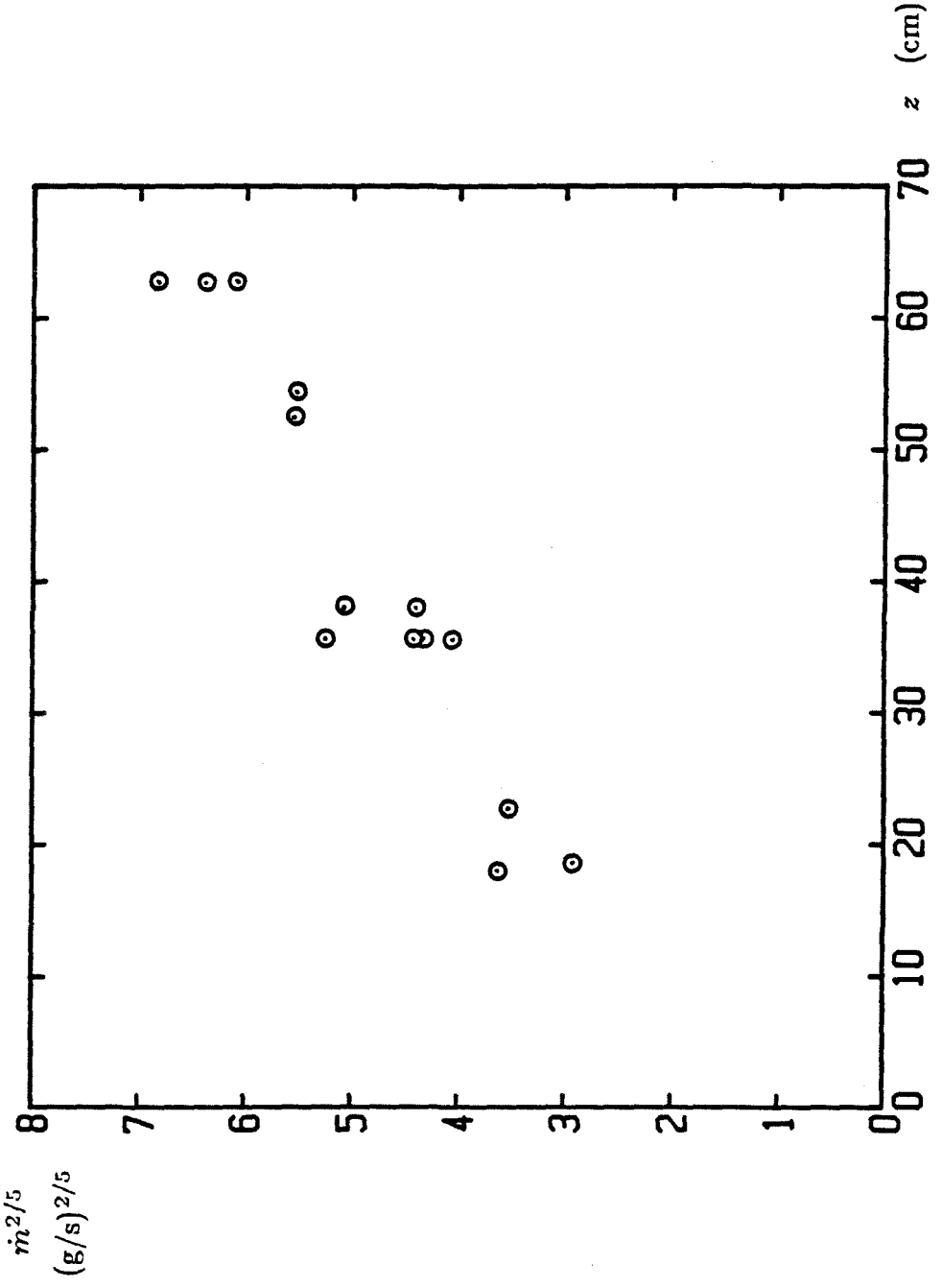

Figure (4.5) Plume mass flux as a function of height, presented in a form useful in determining a virtual origin.

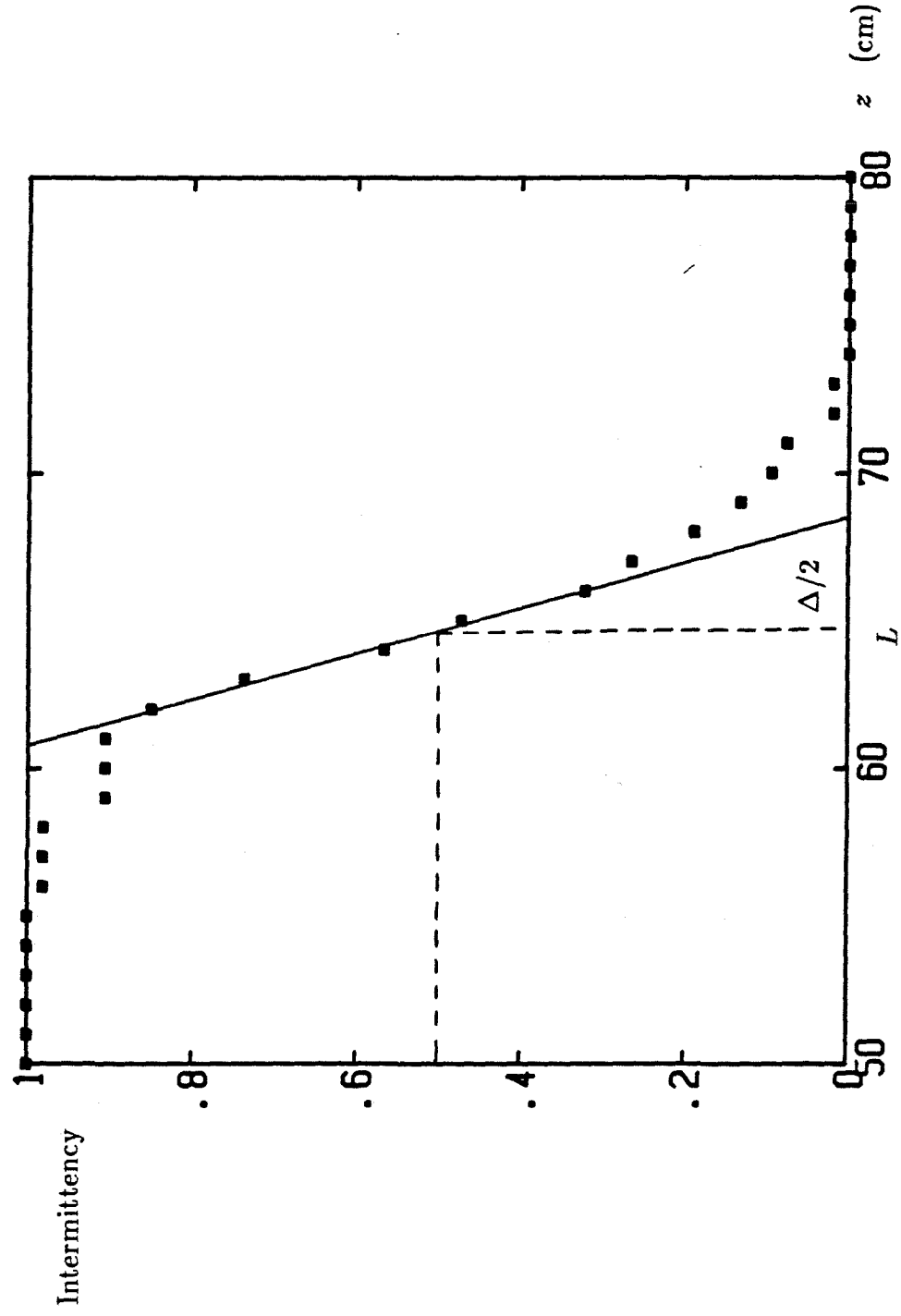

Figure (4.6) Typical flame-length intermittency data. $u_s = 587$ m/s.

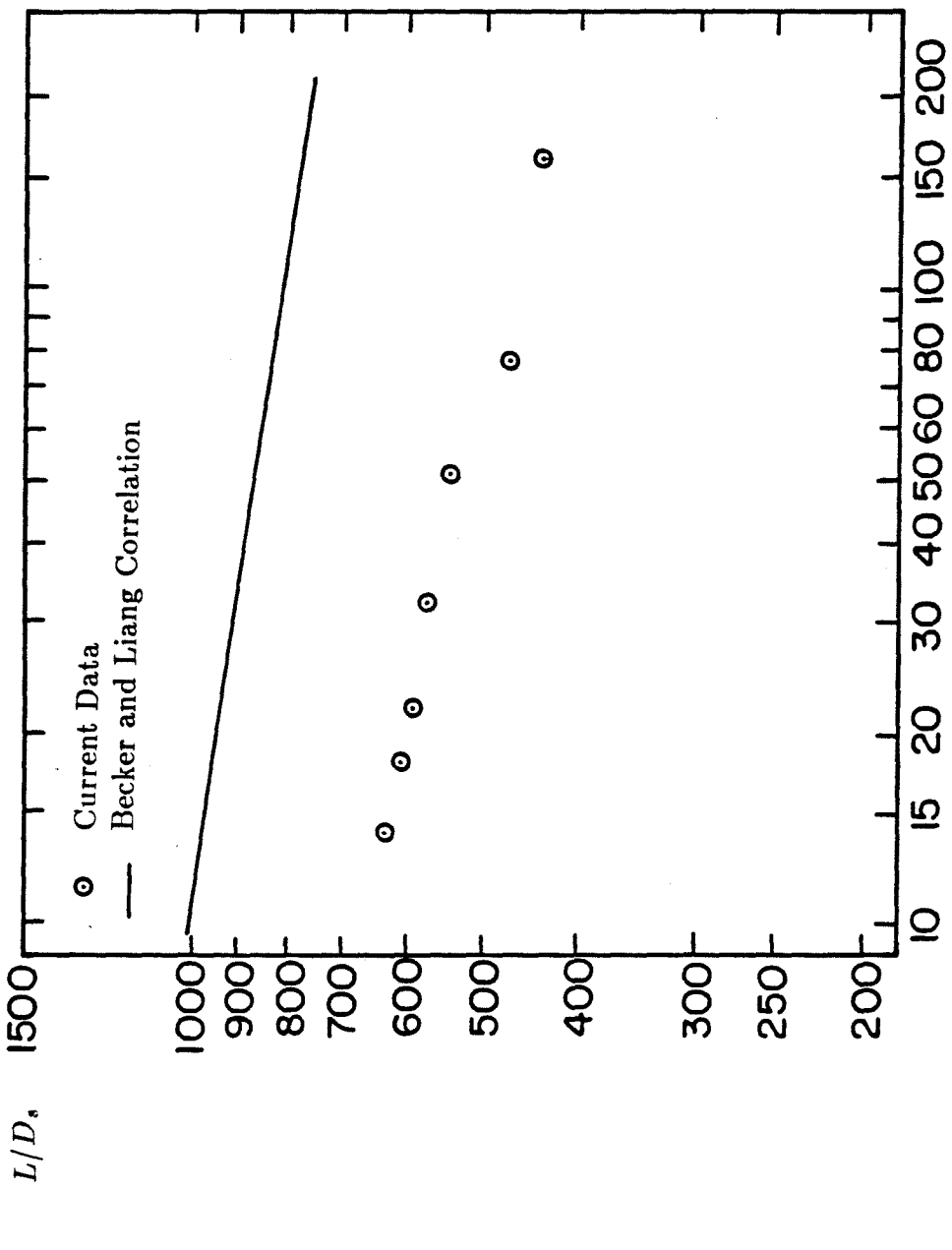

Figure (4.7) Flame length data as a function of effective source Richardson number, Ri_s. Also shown is the correlation of Becker and Liang (1978).

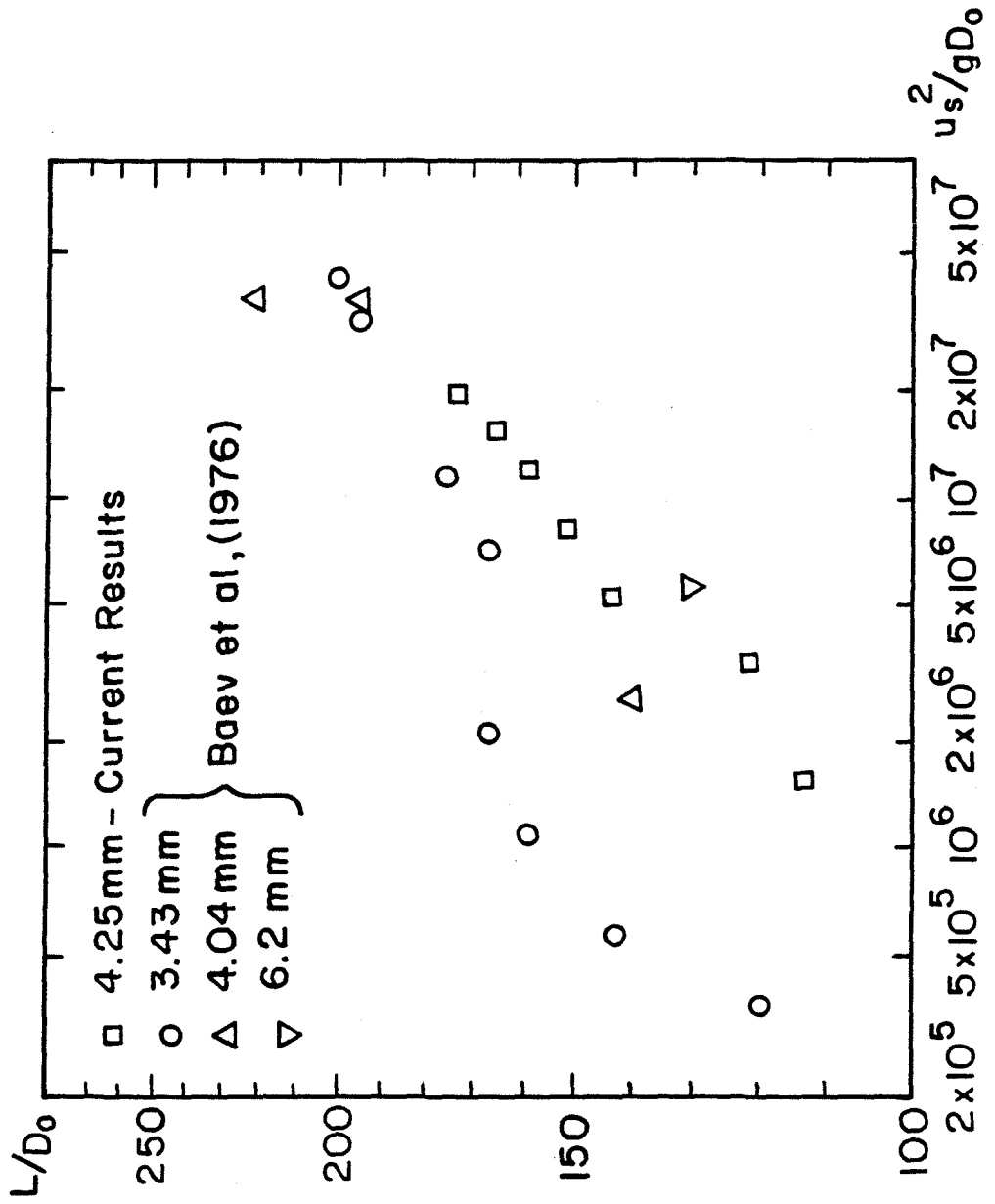

Figure (4.8) Flame length data as a function of Froude number plotted along with the data of Baev et al. (1976).

Table 4.1. Entrainment Results

u_s (m/s)	$\dot{m}_f$ (g/s)	$\dot{Q}$ (kW)	$\mathrm{Re_s}$	$10^9\mathrm{Ri_s}$	z (cm)	ξ	$\dot{m}$ (g/s)	C_4
670	0.61	86.5	48,000	25	18.5	0.478	25.3	
437	0.41	58.5	31,000	57	19.0	0.659	14.9	
579	0.53	75.9	34,000	48	23.0	0.746	23.8	
688	0.80	113	50,000	24	36.0	0.907	63.3	
694	0.71	100	50,000	23	38.5	0.967	58.0	
509	0.53	75.9	36,000	42	36.0	1.122	38.6	
486	0.55	77.6	35,000	47	36.0	1.158	40.7	
475	0.49	70.2	34,000	48	38.5	1.258	40.6	
365	0.41	57.5	26,000	82	36.0	1.408	34.1	0.153
639	0.71	101	46,000	27	63.0	1.675	119	0.132
482	0.51	73.7	34,000	47	53.0	1.715	72.7	0.124
483	0.53	75.7	34,000	47	63.0	2.034	104	0.115
302	0.32	45.9	21,000	120	55.0	2.448	72.1	0.112
338	0.37	52.6	24,000	95	63.0	2.599	93.0	0.103

Table 4.2. Flame Length Results

u_s (m/s)	$\dot{m}_f$ (g/s)	$\dot{Q}$ (kW)	$\mathrm{Re_s}$	$\mathrm{Re_L}$	$10^9\mathrm{Ri_s}$	L (cm)	ξ_L	L/D_s	Δ/L
258	0.289	41.1	18,000	50,000	160	48.3	2.39	439	0.228
376	0.426	60.6	27,000	69,000	77	51.8	1.99	471	0.124
465	0.534	75.9	33,000	74,000	51	61.3	2.03	548	0.130
587	0.686	97.6	42,000	89,000	32	64.8	1.83	574	0.144
707	0.844	120	51,000	105,000	22	67.8	1.68	595	0.141
801	0.974	138	59,000	117,000	18	70.2	1.59	610	0.210
911	1.14	162	68,000	130,000	14	73.8	1.52	631	0.169

Chapter 5

Conclusions

These experiments have investigated the entrainment of air into buoyant fire plumes in the vicinity of the source and the chemistry produced by these plumes burning in a room. In addition, entrainment in the far field of fully turbulent jet diffusion flames was studied.

5.1 Entrainment and Chemistry of Buoyant Fire Plumes

The investigation of buoyant fire plumes was conducted for unsteady, axisymmetric flames of natural gas above a 0.19 m diameter burner. An investigation over the first two diameters downstream from the burner surface characterized the entrainment in the near field of these 12 to 135 kW fires. Reynolds numbers at the burner surface varied from 150 to 1500 and the initial Richardson numbers, based on the burner diameter, were on the order of 10^{-1} to 10. A summary of the results is presented below:

1. For a given interface height, the entrained mass flux was nearly independent of the fuel flow rate. This is true for all but the smallest fires where the flame is theorized to be in a different flame regime, one in which the upper region of the flame breaks into a number of independent flamelets.

2. The entrained mass flux was a strong function of the interface height, i.e., the axial distance over which mass was entrained, and appeared to be nearly linear with this distance at distances of more than one-half diameter away from the fire source. This linear relationship falls in the middle of the various functional relationships previously proposed for the entrainment, these relationships being 3/4-power to 5/4-power functions of the interface height.

3. Nearest the burner surface, the linear dependence did not hold. In this

region, the structure of the flame was quite different than that observed farther downstream. Here, a cylindrical flame sheet pinches in periodically toward the burner centerline forming the large vortex-ring structures that dominate the downstream flowfield. As expected, the entrainment at the burner surface was nonzero.

4. After comparing the current results with previous results (Cetegen, 1982; Beyler, 1983; Lim, 1984), we find that the near-field entrainment appears to be strongly influenced by the initial buoyancy of the plume. The effect this initial buoyancy has on the development of the large, unsteady puffing structures that characterize these flames (and strongly influence the near-field entrainment) is the probable cause of the discrepancies in the near-field entrainment rates measured by different experimentors.

5. For the fires studied, the composition of the products supplied to the upper layer by the plume was a function of the equivalence ratio of the upper layer only. It was independent of the temperature of the upper layer and the residence times of the gas in the upper layer over the ranges studied.

6. For fuel-lean fires, the composition of the upper layer is modelled quite well by the chemical-equilibrium composition of the reactants. This is essentially equivalent to the fuel reacting completely and the excess air simply diluting the products of combustion.

7. For fuel-rich fires, the presence of 1 to 2% mole fractions of carbon monoxide in the upper layer with a resulting paucity of carbon dioxide implies that the oxidation of carbon monoxide was "frozen out" before completion.

8. The actual heat-release rate for these fires was inferred from the chemistry to be about 90% of that expected for complete reaction of the fuel or oxygen.

5.2 Entrainment in Turbulent Jet Diffusion Flames

Measurements on steady, axisymmetric hydrogen flames helped to characterize the entrainment by momentum-driven, fully turbulent jet diffusion flames. The jet had effective source Reynolds numbers greater than 25,000 and the source Richardson numbers varied from 10^{-8} to 10^{-7}. Compressibility effects, determined by the convective Mach number, were small. Entrainment measurements were taken from 50 to 150 diameters downstream of the 4.25 mm nozzle. In addition, visual flame heights were measured. The results are summarized below:

1. The nondimensional mass flux, $\dot{m}D_s/\dot{m}_f z$, was constant over the momentum-dominated regions of the jet, as expected from dimensional and similarity arguments. Its numerical value of 0.24 was about 50% higher than the value determined by Becker and Yamazaki (1978) by the use of point measurements. The current technique is believed to be superior to that employed by Becker and Yamazaki.

2. Measurements made in the transition region between momentum-dominated and buoyancy-dominated flows suggest that the nondimensional mass flux, $4\dot{m}/\pi\rho_\infty\sqrt{gz}z^2$, was approaching a value less than 0.1 for the buoyancy-dominated regime. However, all of the entrainment results depended on the fuel flow rate, and this result suggests that buoyancy-dominated flow was not clearly obtained in the current experiments.

3. Average flame lengths determined from a video data system compared well to the hydrogen data and hydrogen-based models of other experimentors, but did not correlate well with any of the "general" flame-length models developed using other fuels.

References

Albertson, M. L., Dai, Y. B., Jensen, R. A., and Rouse, H. (1950). Diffusion of Submerged Jets. *Trans. A.S.C.E.* **115**:639–664.

ASME (1971). *Fluid Meters: Their Theory and Application, 6th Ed.* American Society of Mechanical Engineers, NY.

Baev, V. K., Kuznetsov, P. P., Mogil'nyi, I. A., Tret'yakov, P. K., and Yasakov, V. A. (1976). Length of Diffusion Flames (translated from Russian). *Comb., Explosions, and Shock Waves* **10**:420–426.

Baev, V. K. and Yasakov, V. A. (1976). Influence of Buoyant Forces on the Length of Diffuse Flames (translated from Russian). *Comb., Explosions, and Shock Waves* **10**:752–756.

Becker, H. A. and Liang, D. (1978). Visible Lengths of Vertical Free Turbulent Diffusion Flames. *Comb. and Flame* **32**:115–137.

Becker, H. A. and Yamazaki, S. (1978). Entrainment, Momentum Flux and Temperature in Vertical Free Turbulent Diffusion Flames. *Comb. and Flame* **33**:123–149.

Beers, Y. (1957). *Introduction to the Theory of Error.* Addison-Wesley, Reading, MA.

Beyler, C. L. (1983). Development and Burning of a Layer of Products of Incomplete Combustion Generated by a Buoyant Diffusion Flame. Ph.D. Thesis, Harvard Univ., Cambridge, MA.

Beyler, C. L. (1986). Major Species Production by Diffusion Flames In a Two-layer Compartment Fire Environment. *Fire Safety J.* **10**:47–56.

Bilger, R. W. and Stårner, S. H. (1983). A Simple Model for Carbon Monoxide in Laminar and Turbulent Hydrocarbon Diffusion Flames. *Comb. and Flame* **51**:155–176.

Blinov, V. I. and Khudiakov, G. N. (1957). (In Russian). *Dokl. Akad. Nauk SSSR* **113**:1094–1097.

Broadwell, J. E. (1982). A Model of Turbulent Diffusion Flames and Nitric Oxide Production. Part I., TRW Document No. 38515-6001-UT-00, TRW, Redondo Beach, CA.

Cetegen, B. M. (1982). Entrainment and Flame Geometry of Fire Plumes. Ph.D. Thesis, California Institute of Technology, Pasadena, CA.

Cetegen, B. M., Zukoski, E. E., and Kubota, T. (1984). Entrainment in the Near and Far Field of Fire Plumes. *Comb. Sci. and Tech.* **39**:305–331.

Cooper, L. Y. (1983). A Buoyant Source in the Lower of Two, Homogeneous, Stably Stratified Layers—A Problem of Fire in an Enclosure. NBSIR83-2789, National Bureau of Standards, Dept. of Commerce, Washington, DC.

Cox, G. and Chitty, R. (1980). A Study of the Deterministic Properties of Unbounded Fire Plumes. *Comb. and Flame* **39**:191–209.

Dahm, W. J. A. (1985). Experiments on Entrainment, Mixing and Chemical Reactions in Turbulent Jets at Large Schmidt Number. Ph.D. Thesis, California Institute of Technology, Pasadena, CA.

Dahm, W. J. A., Dimotakis, P. E., and Broadwell, J. E. (1984). Non-Premixed Turbulent Flame Jets. AIAA-84-0369, Amer. Inst. Aero. and Astronautics, NY.

Dietz, W. A. (1967). Response Factors for Gas Chromatographic Analyses. *J. Gas Chrom.* **5**:68–71.

Delichatsios, M. A. and Orloff, L. (1984). Entrainment Measurements in Turbulent Buoyant Jet Flames and Implications for Modeling. *Twentieth Symposium (International) on Combustion*, The Combustion Institute, Pittsburg, PA, pp. 367–375.

Emmons, H. W. (1978). The Prediction of Fires in Buildings. *Seventeenth Symposium (International) on Combustion*, The Combustion Institute, Pittsburg, PA, pp. 1101–1111.

Glassman, I. (1977). *Combustion*, Academic Press, NY.

Hansen, R. S., Frost, R. R., and Murphy, J. A. (1964). The Thermal Conductivity of Hydrogen-Helium Mixtures. *J. Physical Chem.* **68**:2028–2029.

Hawthorne, W. R., Weddell, D. S., and Hottel, H. C. (1948). Mixing and Combustion in Turbulent Gas Jets. *Third Symposium (International) on Combustion*, The Williams and Wilkins Co., Baltimore, MD. pp. 266–288.

Hottel, H. C. (1953). Burning in Laminar and Turbulent Fuel Jets. *Fourth Symposium (International) on Combustion*, The Williams and Wilkins Co., Baltimore, MD. pp. 97–113.

Hottel, H. C. and Hawthorne, W. R. (1948). Diffusion in Laminar Flame Jets. *Third Symposium (International) on Combustion*, The Williams and Wilkins Co., Baltimore, MD. pp. 254–266.

Kee, R. J., Miller, J. A., and Jefferson, T. H. (1980). CHEMKIN: A General-Purpose, Problem-Independent, Transportable, FORTRAN Chemical Kinetics Code Package. Rept. SAND80-8003, Sandia National Laboratories, Livermore, CA.

Liew, S. K., Bray, K. N. C., and Moss, J. B. (1984). A Stretched Laminar Flamelet Model of Turbulent Nonpremixed Combustion. *Comb. and Flame* **56**:199–213.

Lim, C. (1984). Entrainment in Fire Plumes. Part 2, Engr. Thesis, California Institute of Technology, Pasadena, CA.

Lippisch, A. M. (1958). Flow Visualization. *Aero. Eng. Rev.* **17**:24–36.

Mak, R. (1985). Plume Entrainment at a Density Interface. SURF Rept., California Institute of Technology, Pasadena, CA.

McCaffrey, B. J. (1979). Purely Buoyant Diffusion Flames: Some Experimental Results. NBSIR79-1910, National Bureau of Standards, Dept. of Commerce, Washington, DC.

McCaffrey, B. J. and Cox, G. (1982). Entrainment and Heat Flux of Buoyant Diffusion Flames. NBSIR82-2473, National Bureau of Standards, Dept. of Commerce, Washington, DC.

McNair, H. M. and Bonelli, E. J. (1968). *Basic Gas Chromatography.* Varian Assoc., Palo Alto, CA.

Morton, B. R., Taylor, G. I., and Turner, J. S. (1956). Turbulent Gravitational Convection from Maintained and Instantaneous Sources. *Proc. Royal Soc.* **A234**:1–23.

Papamoschou, D. and Roshko, A. (1986). Observations of Supersonic Free Shear Layers. AIAA paper 86-0162.

Papanicalaou, P. N. (1984). Mass and Momentum Transport in a Turbulent Buoyant Vertical Axisymmetric Jet. Ph.D. Thesis, California Institute of Technology, Pasadena, CA.

Parker, J. F. and West, V. R., eds. (1973). *Bioastronautics Data Book*, NASA SP-3006. U.S. Govt. Printing Office, Washington, DC.

Peters, N. (1984). Laminar Diffusion Flamelet Models in Non-Premixed Turbulent Combustion. *Prog. Energy Combust. Sci.* **10**:319–339.

Reid, R. C., Prausnitz, J. M., and Sherwood, T. K. (1977). *The Properties of Gases and Liquids, 3rd ed.* McGraw-Hill, NY.

Reynolds, W. C. (1986). The Element Potential Method for Chemical Equilibrium Analysis; Implementation in the Interactive Program STANJAN. Rept. of the Dept. of Mech. Eng., Stanford Univ., Menlo Park, CA.

Ricou, F. P. and Spalding, D. B. (1961). Measurements of Entrainment by Axisymmetric Turbulent Jets. *J. Fluid Mech.* **11**:21–32.

Schmidt, W. (1941). Turbulente Ausbreitung eines Stromes erhitzter Luft. *Z. Angew. Math. Mech.* **21**: 265–363.

Smithsonian Inst. (1939). *Smithsonian Meteorological Tables, 5th Ed.*, Pub. 3116, Smithsonian Institution, Washington, DC.

Taylor, G. I. (1958). Flow Induced by Jets. *J. Aero/Space Sciences* **25**:464–465.

Thompson, B. (1977). *Fundamentals of Gas Analysis by Gas Chromatography.* Varian Assoc., Palo Alto, CA.

Thring, M. W., and Newby, M. P. (1952). Combustion Length of Enclosed Turbulent Jet Flames. *Fourth Symposium (International) on Combustion*, The Williams and Wilkins Co., Baltimore, MD. pp. 789–796.

Vachon, M. and Champion, M. (1986). Integral Model of a Flame with Large Buoyancy Effects. *Comb. and Flame* **63**:269–278.

Wohl, K., Gazley, C., and Kapp, N. (1948). Diffusion Flames. *Third Symposium (International) on Combustion*, The Williams and Wilkins Co., Baltimore, MD. pp. 288–300.

Zukoski, E. E. (1975). Convective Flows Associated with Room Fires. Rept. for NSF Grant #GI 31892x1, California Institute of Technology, Pasadena, CA.

Zukoski, E. E. (1978). Development of a Stratified Ceiling Layer in the Early Stages of a Closed-room Fire. *Fire and Materials* **2**:54–62.

Zukoski, E. E. (1985). Fluid Dynamic Aspects of Room Fires. *First International Symposium on Fire Safety Science*, pp. 1–30.

Appendix A

Natural Gas Data Reduction and Uncertainty Analysis

Many of the calculations referred to in the text concerning natural gas flames in air and the entire uncertainty analysis are included here in detail for completeness. The uncertainty analysis follows the standard method discussed in Beers (1957).

A.1 Water Vapor in Air

The vapor pressure of water in laboratory air was calculated as follows. A five-parameter least-squares polynomial fit to the Smithsonian saturated vapor pressure data (Smithsonian Inst., 1939) is represented as

$$p_v' = 4.53582 + 0.344087T_w + 0.010243{T_w}^2 + 0.001841{T_w}^3 + 3.47926 \times 10^{-6}{T_w}^4 , \qquad (A.1)$$

where p_v' is the saturated vapor pressure in torr and T_w is the wet-bulb temperature in degrees C. This polynomial fit has a numerical uncertainty of 0.02 torr. The vapor pressure is then corrected to atmospheric conditions using the standard formula

$$p_v = p_v' - 0.00066p(T_d - T_w)(1 + 0.00115T_w) , \qquad (A.2)$$

where p_v is the vapor pressure in air in torr, p is the barometric pressure in torr, and T_d is the dry-bulb temperature.

The uncertainty for p_v can then be represented as

$$(\delta p_v)^2 = 0.02^2 + \left(\frac{\partial p_v}{\partial p}\delta p\right)^2 + \left(\frac{\partial p_v}{\partial T_d}\delta T_d\right)^2 + \left(\frac{\partial p_v}{\partial T_w}\delta T_w\right)^2 , \qquad (A.3)$$

where in practice all of the partial derivatives were determined numerically. The mole fraction of water vapor in air and its uncertainty are then simply calculated

as

$$b_3 = p_v/p \tag{A.4}$$

$$\left(\frac{\delta b_3}{b_3}\right)^2 = \left(\frac{\delta p_v}{p_v}\right)^2 + \left(\frac{\delta p}{p}\right)^2. \tag{A.5}$$

A.2 Solution of the Conservation of Atoms Equations

A.2.1 Determination of the Coefficients

The areas of the measured peaks, A_i, and their uncertainties, δA_i, are given along with the response factors, f_i, and their uncertainties, δf_i. From **2.18**

$$y_i = \frac{f_i A_i}{f_3 A_3}, \qquad i = 1,4,5,6,9,10,11 \tag{A.6}$$

and the uncertainties are then calculated as

$$\left(\frac{\delta y_i}{y_i}\right)^2 = \left(\frac{\delta f_i}{f_i}\right)^2 + \left(\frac{\delta A_i}{A_i}\right)^2 + \left(\frac{\delta f_3}{f_3}\right)^2 + \left(\frac{\delta A_3}{A_3}\right)^2, \quad i = 1,4,5,6,9,10,11. \tag{A.7}$$

In addition, from **2.23**

$$y_2 + c_1 y_{12} = \frac{f_2 A_{2+12}}{f_3 A_3} \tag{A.8}$$

and its uncertainty is given by

$$\left(\frac{\delta(y_2 + c_1 y_{12})}{(y_2 + c_1 y_{12})}\right)^2 = \left(\frac{\delta f_2}{f_2}\right)^2 + \left(\frac{\delta A_{2+12}}{A_{2+12}}\right)^2 + \left(\frac{\delta f_3}{f_3}\right)^2 + \left(\frac{\delta A_3}{A_3}\right)^2. \tag{A.9}$$

The mole contents of natural gas, a_i, and dry air, b'_i, and their uncertainties, δa_i and $\delta b'_i$, are also easily determined and are input to the analysis. The water vapor content of air is determined above and the gross mole content of lab air, b_i, and their uncertainty, δb_i, are easily determined.

From this information the coefficients A_i, B_i, and Y_i to the set of linear equations, **2.7**, are determined from **2.8**, **2.9**, and **2.10**. The uncertainties of

each are calculated as

$$(\delta A_C)^2 = (\delta a_1)^2 + 4(\delta a_2)^2 + 9(\delta a_3)^2 + (\delta a_5)^2 \qquad (A.10a)$$

$$(\delta A_H)^2 = 4(\delta a_1)^2 + 9(\delta a_2)^2 + 16(\delta a_3)^2 \qquad (A.10b)$$

$$\delta A_O = 2\delta a_5 \qquad (A.10c)$$

$$\delta A_N = \delta a_4 \qquad (A.10d)$$

$$\delta B_C = \delta b_4 \qquad (A.11a)$$

$$\delta B_H = \delta b_3 \qquad (A.11b)$$

$$(\delta B_O)^2 = 4(\delta b_1)^2 + 4c_1^2(\delta b_5)^2 + 4b_5^2(\delta c_1)^2 + (\delta b_3)^2 + 4(\delta b_4)^2 \qquad (A.11c)$$

$$\delta B_N = \delta b_2 \qquad (A.11d)$$

$$(\delta Y_C)^2 = (\delta y_4)^2 + (\delta y_5)^2 + (\delta y_6)^2 + 4(\delta y_9)^2 + 4(\delta y_{10})^2 + 4(\delta y_{11})^2 \qquad (A.12a)$$

$$(\delta Y_H)^2 = (\delta y_1)^2 + 4(\delta y_4)^2 + (\delta y_9)^2 + 4(\delta y_{10})^2 + 9(\delta y_{11})^2 \qquad (A.12b)$$

$$(\delta Y_O)^2 = 4(\delta(y_2 + c_1 y_{12}))^2 + (\delta y_5)^2 + 4(\delta y_6)^2 \qquad (A.12c)$$

$$\delta Y_N = 0\,. \qquad (A.12d)$$

A.2.2 Solution to the Four Linear Equations

The equations, **2.7**, can be solved to determine I as

$$I = \frac{Y_N(16A_H - A_C - 16A_O) - A_N(16Y_H - Y_C - 16Y_O)}{B_N(16Y_H - Y_C - 16Y_O) - Y_N(16B_H - B_C - 16B_O)}\,. \qquad (A.13)$$

From **2.7d** x_3 is determined as

$$x_3 = (A_N + B_N I)/Y_N\,. \qquad (A.14)$$

Likewise, x_7 and x_8 are determined from **2.7c** and **2.7a** as

$$x_7 = A_O + B_O I - Y_O x_3 \qquad (A.15)$$

$$x_8 = \tfrac{1}{8}(A_C + B_C I - Y_C x_3)\,. \qquad (A.16)$$

The uncertainties can also be determined as

$$(\delta I)^2\left[B_N(16Y_H - Y_C - 16Y_O) - Y_N(16B_H - B_C - 16B_O)\right]^2 =$$

$$Y_N^2[256(\delta A_H)^2 + (\delta A_C)^2 + 256(\delta A_O)^2] + A_N^2[256(\delta Y_H)^2 + (\delta Y_C)^2 + 256(\delta Y_O)^2]$$

$$+I^2\{Y_N^2\left[256(\delta B_H)^2 + (\delta B_C)^2 + 256(\delta B_O)^2\right]$$

$$+B_N^2\left[256(\delta Y_H)^2 + (\delta Y_C)^2 + 256(\delta Y_O)^2\right]\}$$

$$+(16A_H - A_C - 16A_O)^2(\delta Y_N)^2 + (16Y_H - Y_C - 16Y_O)^2(\delta A_N)^2$$

$$+I^2\left[(16Y_H - Y_C - 16Y_O)^2(\delta B_N)^2 + (16B_H - B_C - 16B_O)^2(\delta Y_N)^2\right], \quad (A.17)$$

$$\left(\frac{\delta x_3}{x_3}\right)^2 = \left(\frac{\delta Y_N}{Y_N}\right)^2 + \left(\frac{1}{A_N + B_N I}\right)^2[(\delta A_N)^2 + I^2(\delta B_N)^2 + {B_N}^2(\delta I)^2], \quad (A.18)$$

$$(\delta x_7)^2 = (\delta A_O)^2 + I^2(\delta B_O)^2 + {B_O}^2(\delta I)^2 + {Y_O}^2(\delta x_3)^2 + {x_3}^2(\delta Y_O)^2, \quad (A.19)$$

$$(\delta x_8)^2 = \frac{1}{64}\left[(\delta A_C)^2 + {B_C}^2(\delta I)^2 + I^2(\delta B_C)^2 + {Y_C}^2(\delta x_3)^2 + {x_3}^2(\delta Y_C)^2\right]. \quad (A.20)$$

A.3 Upper-Layer Chemistry Calculations

Once x_3, x_7, and x_8 have been determined, y_7 and y_8 can be calculated as

$$y_i = \frac{x_i}{x_3} \quad (A.21)$$

$$\left(\frac{\delta y_i}{y_i}\right)^2 = \left(\frac{\delta x_3}{x_3}\right)^2 + \left(\frac{\delta x_i}{x_i}\right)^2. \quad (A.22)$$

In addition from **2.6e**

$$x_{12} = I b_5 \quad (A.23)$$

$$(\delta x_{12})^2 = I^2(\delta b_5)^2 + {b_5}^2(\delta I)^2, \quad (A.24)$$

and finally from **2.12**

$$x_2 = x_3(y_2 + c_1 y_{12}) - c_1 x_{12} \quad (A.25)$$

$$(\delta x_2)^2 = {x_3}^2(\delta(y_2 + c_1 y_{12}))^2 + (y_2 + c_1 y_{12})^2(\delta x_3)^2 + {c_1}^2(\delta x_{12})^2 + {x_{12}}^2(\delta c_1)^2. \quad (A.26)$$

Now y_2 and y_{12} and their uncertainties can be calculated from **A.21** and **A.22**.

Now that all the y_i and δy_i have been determined, the mole fractions, Y_i, can be calculated from **2.13** as

$$\mathrm{Y}_i = \frac{y_i}{\sum_{k=1}^{12} y_k} \tag{A.27}$$

and the uncertainties as

$$\left(\frac{\delta \mathrm{Y}_i}{\mathrm{Y}_i}\right)^2 = \left(\frac{\delta y_i}{y_i}\right)^2 + \frac{\sum_{k=1}^{12} (\delta y_k)^2}{\left(\sum_{k=1}^{12} y_k\right)^2} . \tag{A.28}$$

A.4 Stoichiometry Calculations

From **2.16** the stoichiometric reaction entrainment is calculated as

$$I_s = (4a_1 + 7a_2 + 10a_3)/2b_1 . \tag{A.29}$$

The uncertainty is then

$$\left(\frac{\delta I_s}{I_s}\right)^2 = \left(\frac{\delta b_1}{b_1}\right)^2 + \left(\frac{1}{2I_s b_1}\right)[16(\delta a_1)^2 + 49(\delta a_2)^2 + 100(\delta a_3)^2] . \tag{A.30}$$

Finally, the equivalence ratio is calculated from **2.17** as

$$\phi = I_s/I \tag{A.31}$$

and has uncertainty

$$\left(\frac{\delta \phi}{\phi}\right)^2 = \left(\frac{\delta I_s}{I_s}\right)^2 + \left(\frac{\delta I}{I}\right)^2 . \tag{A.32}$$

Appendix B

Tabulated Results

The results of the entrainment measurements on buoyant natural gas flames, obtained by the data reduction program, are presented here in full. All of the results should be self-explanatory with the following exceptions:

1. The sample temperature is the temperature of the upper layer measured at the sampling location.

2. The fuel inlet Reynolds number is defined as

$$\mathrm{Re_f} \equiv \frac{u_0 D_0}{\nu_f}, \qquad (B.1)$$

where u_0 is the average fuel velocity at the burner surface, D_0 is the burner diameter, and ν_f is the kinematic viscosity of the fuel.

3. The fuel inlet Richardson number is defined as

$$\mathrm{Ri_f} \equiv \frac{(\rho_\infty - \rho_f) g D_0}{\rho_f u_0^2}, \qquad (B.2)$$

where g is the acceleration of gravity, and ρ_∞ and ρ_f are the ambient and fuel densities, respectively.

4. The compositions are given in mole fractions.

* * * * * DATA REDUCTION PROGRAM OUTPUT * * * * *
RUN NUMBER 44
DATE 08/12/85 TIME 11:43

INTERFACE HEIGHT ABOVE BURNER 15.0 CM.
FIRE SIZE 12.0 KW.
SAMPLE TEMPERATURE 216 DEG. C.

FLOWRATES G/S
FUEL 0.252
AIR 15.285
TOTAL 15.537

FUEL INLET RE 147. FUEL INLET RI 1.13E+01

FUEL COMPOSITION		AIR COMPOSITION	
METHANE	0.9201	OXYGEN	0.2051
ETHANE	0.0422	NITROGEN	0.7705
PROPANE	0.0141	WATER	0.0147
NITROGEN	0.0159	CO2	0.0004
CO2	0.0076	ARGON	0.0093

FUEL VISCOSITY 108.89 MICROPOISE.
FUEL MOLECULAR WEIGHT 17.51

EQUIVALENCE RATIO 0.273 +/- 0.023

PRODUCT COMPOSITION

OXYGEN	0.1503	+/- 0.00742
NITROGEN	0.7493	+/- 0.03548
ARGON	0.0090	+/- 0.00127
CARBON DIOXIDE	0.0227	+/- 0.00112
WATER VAPOR	0.0675	+/- 0.04740
CARBON MONOXIDE	0.0006	+/- 0.00014
HYDROGEN	0.0000	+/- 0.00000
METHANE	0.0000	+/- 0.00000
ETHANE	0.0000	+/- 0.00000
ETHYLENE	0.0000	+/- 0.00000
ACETYLENE	0.0000	+/- 0.00000
SOOT (C8H)	0.0006	+/- 0.00026

HEAT OF FORMATION, FUEL -18.384
HEAT OF FORMATION, AIR -0.886
HEAT OF FORMATION, PROD. -6.054
HEAT OF FORMATION, STOICH PROD. -20.327
ACTUAL HEAT OF REACTION -178.004 KCAL/MOLE
HEAT OF STOICH. REACTION -191.722 KCAL/MOLE
RATIO HEATS OF REACTION 0.928
RATIO ACTUAL TO MAX 0.253

* * * * * DATA REDUCTION PROGRAM OUTPUT * * * * *
RUN NUMBER 45
DATE 08/12/85 TIME 13:40

INTERFACE HEIGHT ABOVE BURNER 15.0 CM.
FIRE SIZE 12.0 KW.
SAMPLE TEMPERATURE 210 DEG. C.

FLOWRATES G/S
FUEL 0.252
AIR 13.627
TOTAL 13.879

FUEL INLET RE 147. FUEL INLET RI 1.13E+01

FUEL COMPOSITION		AIR COMPOSITION	
METHANE	0.9201	OXYGEN	0.2051
ETHANE	0.0422	NITROGEN	0.7705
PROPANE	0.0141	WATER	0.0147
NITROGEN	0.0159	CO2	0.0004
CO2	0.0076	ARGON	0.0093

FUEL VISCOSITY 108.89 MICROPOISE.
FUEL MOLECULAR WEIGHT 17.51

EQUIVALENCE RATIO 0.306 +/- 0.023

PRODUCT COMPOSITION		
OXYGEN	0.1486	+/- 0.00652
NITROGEN	0.7464	+/- 0.03116
ARGON	0.0090	+/- 0.00116
CARBON DIOXIDE	0.0207	+/- 0.00091
WATER VAPOR	0.0734	+/- 0.04179
CARBON MONOXIDE	0.0007	+/- 0.00013
HYDROGEN	0.0000	+/- 0.00000
METHANE	0.0000	+/- 0.00000
ETHANE	0.0000	+/- 0.00000
ETHYLENE	0.0000	+/- 0.00000
ACETYLENE	0.0000	+/- 0.00000
SOOT (C8H)	0.0013	+/- 0.00023

HEAT OF FORMATION, FUEL -18.384
HEAT OF FORMATION, AIR -0.886
HEAT OF FORMATION, PROD. -6.206
HEAT OF FORMATION, STOICH PROD. -20.327
ACTUAL HEAT OF REACTION -162.671 KCAL/MOLE
HEAT OF STOICH. REACTION -192.137 KCAL/MOLE
RATIO HEATS OF REACTION 0.847
RATIO ACTUAL TO MAX 0.259

```
* * * * * DATA REDUCTION PROGRAM OUTPUT * * * * *
                RUN NUMBER  46
          DATE 08/12/85       TIME       14:16

INTERFACE HEIGHT ABOVE BURNER  15.0 CM.
FIRE SIZE   23.4 KW.
SAMPLE TEMPERATURE  313 DEG. C.

FLOWRATES G/S
FUEL    0.493
AIR    16.220
TOTAL  16.713

FUEL INLET RE   288.      FUEL INLET RI  2.95E+00

FUEL COMPOSITION                    AIR COMPOSITION
METHANE     0.9201                  OXYGEN      0.2051
ETHANE      0.0422                  NITROGEN    0.7705
PROPANE     0.0141                  WATER       0.0147
NITROGEN    0.0159                  CO2         0.0004
CO2         0.0076                  ARGON       0.0093

FUEL VISCOSITY  108.89 MICROPOISE.
FUEL MOLECULAR WEIGHT  17.51

EQUIVALENCE RATIO  0.504 +/-  0.022

PRODUCT COMPOSITION
OXYGEN            0.1074 +/- 0.00279
NITROGEN          0.7323 +/- 0.01628
ARGON             0.0088 +/- 0.00079
CARBON DIOXIDE    0.0399 +/- 0.00100
WATER VAPOR       0.1097 +/- 0.02230
CARBON MONOXIDE   0.0006 +/- 0.00013
HYDROGEN          0.0000 +/- 0.00000
METHANE           0.0000 +/- 0.00000
ETHANE            0.0000 +/- 0.00000
ETHYLENE          0.0000 +/- 0.00000
ACETYLENE         0.0000 +/- 0.00000
SOOT (C8H)        0.0013 +/- 0.00024

HEAT OF FORMATION, FUEL  -18.384
HEAT OF FORMATION, AIR    -0.886
HEAT OF FORMATION, PROD. -10.109
HEAT OF FORMATION, STOICH PROD. -20.327
ACTUAL HEAT OF REACTION -176.170 KCAL/MOLE
HEAT OF STOICH. REACTION -193.878 KCAL/MOLE
RATIO HEATS OF REACTION 0.909
RATIO ACTUAL TO MAX 0.458
```

* * * * * DATA REDUCTION PROGRAM OUTPUT * * * * *
RUN NUMBER 47
DATE 08/12/85 TIME 14:52

INTERFACE HEIGHT ABOVE BURNER 15.0 CM.
FIRE SIZE 36.4 KW.
SAMPLE TEMPERATURE 397 DEG. C.

FLOWRATES G/S
FUEL 0.768
AIR 18.040
TOTAL 18.808

FUEL INLET RE 449. FUEL INLET RI 1.22E+00

FUEL COMPOSITION		AIR COMPOSITION	
METHANE	0.9201	OXYGEN	0.2051
ETHANE	0.0422	NITROGEN	0.7705
PROPANE	0.0141	WATER	0.0147
NITROGEN	0.0159	CO2	0.0004
CO2	0.0076	ARGON	0.0093

FUEL VISCOSITY 108.89 MICROPOISE.
FUEL MOLECULAR WEIGHT 17.51

EQUIVALENCE RATIO 0.705 +/- 0.022

PRODUCT COMPOSITION

OXYGEN	0.0662	+/- 0.00144
NITROGEN	0.7184	+/- 0.01062
ARGON	0.0086	+/- 0.00067
CARBON DIOXIDE	0.0593	+/- 0.00106
WATER VAPOR	0.1454	+/- 0.01487
CARBON MONOXIDE	0.0009	+/- 0.00013
HYDROGEN	0.0000	+/- 0.00000
METHANE	0.0000	+/- 0.00000
ETHANE	0.0000	+/- 0.00000
ETHYLENE	0.0000	+/- 0.00000
ACETYLENE	0.0000	+/- 0.00000
SOOT (C8H)	0.0011	+/- 0.00026

HEAT OF FORMATION, FUEL -18.384
HEAT OF FORMATION, AIR -0.886
HEAT OF FORMATION, PROD. -14.008
HEAT OF FORMATION, STOICH PROD. -20.327
ACTUAL HEAT OF REACTION -183.293 KCAL/MOLE
HEAT OF STOICH. REACTION -195.621 KCAL/MOLE
RATIO HEATS OF REACTION 0.937
RATIO ACTUAL TO MAX 0.660

* * * * * DATA REDUCTION PROGRAM OUTPUT * * * * *
RUN NUMBER 48
DATE 08/12/85 TIME 15:28

INTERFACE HEIGHT ABOVE BURNER 15.0 CM.
FIRE SIZE 49.7 KW.
SAMPLE TEMPERATURE 459 DEG. C.

FLOWRATES G/S
FUEL 1.047
AIR 18.603
TOTAL 19.649

FUEL INLET RE 612. FUEL INLET RI 6.56E-01

FUEL COMPOSITION		AIR COMPOSITION	
METHANE	0.9201	OXYGEN	0.2051
ETHANE	0.0422	NITROGEN	0.7705
PROPANE	0.0141	WATER	0.0147
NITROGEN	0.0159	CO2	0.0004
CO2	0.0076	ARGON	0.0093

FUEL VISCOSITY 108.89 MICROPOISE.
FUEL MOLECULAR WEIGHT 17.51

EQUIVALENCE RATIO 0.932 +/- 0.025

PRODUCT COMPOSITION

OXYGEN	0.0246	+/- 0.00083
NITROGEN	0.7020	+/- 0.00814
ARGON	0.0084	+/- 0.00062
CARBON DIOXIDE	0.0770	+/- 0.00118
WATER VAPOR	0.1796	+/- 0.01171
CARBON MONOXIDE	0.0055	+/- 0.00015
HYDROGEN	0.0000	+/- 0.00000
METHANE	0.0021	+/- 0.00017
ETHANE	0.0000	+/- 0.00000
ETHYLENE	0.0000	+/- 0.00000
ACETYLENE	0.0000	+/- 0.00000
SOOT (C8H)	0.0006	+/- 0.00031

HEAT OF FORMATION, FUEL -18.384
HEAT OF FORMATION, AIR -0.886
HEAT OF FORMATION, PROD. -17.811
HEAT OF FORMATION, STOICH PROD. -20.327
ACTUAL HEAT OF REACTION -183.023 KCAL/MOLE
HEAT OF STOICH. REACTION -197.968 KCAL/MOLE
RATIO HEATS OF REACTION 0.925
RATIO ACTUAL TO MAX 0.862

```
* * * * * DATA REDUCTION PROGRAM OUTPUT * * * * *
                RUN NUMBER  49
          DATE 08/12/85       TIME       16:03

INTERFACE HEIGHT ABOVE BURNER  15.0 CM.
FIRE SIZE   62.3 KW.
SAMPLE TEMPERATURE  482 DEG. C.

FLOWRATES G/S
FUEL    1.314
AIR    19.260
TOTAL  20.574

FUEL INLET RE   768.      FUEL INLET RI  4.16E-01

FUEL COMPOSITION                    AIR COMPOSITION
METHANE     0.9201                  OXYGEN       0.2051
ETHANE      0.0422                  NITROGEN     0.7705
PROPANE     0.0141                  WATER        0.0147
NITROGEN    0.0159                  CO2          0.0004
CO2         0.0076                  ARGON        0.0093

FUEL VISCOSITY  108.89 MICROPOISE.
FUEL MOLECULAR WEIGHT  17.51

EQUIVALENCE RATIO  1.130 +/-  0.028

PRODUCT COMPOSITION
OXYGEN            0.0034 +/- 0.00066
NITROGEN          0.6871 +/- 0.00697
ARGON             0.0082 +/- 0.00059
CARBON DIOXIDE    0.0806 +/- 0.00115
WATER VAPOR       0.1998 +/- 0.01027
CARBON MONOXIDE   0.0124 +/- 0.00025
HYDROGEN          0.0000 +/- 0.00000
METHANE           0.0077 +/- 0.00019
ETHANE            0.0000 +/- 0.00001
ETHYLENE          0.0000 +/- 0.00002
ACETYLENE         0.0000 +/- 0.00002
SOOT (C8H)        0.0006 +/- 0.00034

HEAT OF FORMATION, FUEL  -18.384
HEAT OF FORMATION, AIR    -0.886
HEAT OF FORMATION, PROD. -19.597
HEAT OF FORMATION, STOICH PROD. -20.327
ACTUAL HEAT OF REACTION -169.452 KCAL/MOLE
HEAT OF STOICH. REACTION -200.391 KCAL/MOLE
RATIO HEATS OF REACTION 0.846
RATIO ACTUAL TO MAX 0.955
```

```
* * * * * DATA REDUCTION PROGRAM OUTPUT * * * * *
                RUN NUMBER  54
          DATE 08/13/85       TIME       14:38

INTERFACE HEIGHT ABOVE BURNER  15.0 CM.
FIRE SIZE   73.9 KW.
SAMPLE TEMPERATURE  477 DEG. C.

FLOWRATES G/S
FUEL   1.558
AIR   18.331
TOTAL 19.889

FUEL INLET RE   911.      FUEL INLET RI  2.96E-01

FUEL COMPOSITION                    AIR COMPOSITION
METHANE    0.9201                   OXYGEN      0.2052
ETHANE     0.0422                   NITROGEN    0.7708
PROPANE    0.0141                   WATER       0.0143
NITROGEN   0.0159                   CO2         0.0004
CO2        0.0076                   ARGON       0.0093

FUEL VISCOSITY  108.89 MICROPOISE.
FUEL MOLECULAR WEIGHT  17.51

EQUIVALENCE RATIO  1.407 +/-  0.034

PRODUCT COMPOSITION
OXYGEN            0.0020 +/- 0.00063
NITROGEN          0.6659 +/- 0.00649
ARGON             0.0080 +/- 0.00057
CARBON DIOXIDE    0.0793 +/- 0.00119
WATER VAPOR       0.1892 +/- 0.00974
CARBON MONOXIDE   0.0165 +/- 0.00033
HYDROGEN          0.0103 +/- 0.00115
METHANE           0.0278 +/- 0.00055
ETHANE            0.0003 +/- 0.00004
ETHYLENE          0.0002 +/- 0.00008
ACETYLENE         0.0001 +/- 0.00005
SOOT (C8H)        0.0004 +/- 0.00041

HEAT OF FORMATION, FUEL  -18.384
HEAT OF FORMATION, AIR    -0.861
HEAT OF FORMATION, PROD. -19.325
HEAT OF FORMATION, STOICH PROD. -20.312
ACTUAL HEAT OF REACTION -135.463 KCAL/MOLE
HEAT OF STOICH. REACTION -204.229 KCAL/MOLE
RATIO HEATS OF REACTION 0.663
RATIO ACTUAL TO MAX 0.933
```

```
* * * * * DATA REDUCTION PROGRAM OUTPUT * * * * *
                RUN NUMBER  55
          DATE 08/13/85       TIME       15:14

INTERFACE HEIGHT ABOVE BURNER  15.0 CM.
FIRE SIZE   87.6 KW.
SAMPLE TEMPERATURE  471 DEG. C.

FLOWRATES G/S
FUEL   1.847
AIR   18.236
TOTAL 20.083

FUEL INLET RE  1080.      FUEL INLET RI  2.11E-01

FUEL COMPOSITION                    AIR COMPOSITION
METHANE    0.9201                   OXYGEN      0.2052
ETHANE     0.0422                   NITROGEN    0.7708
PROPANE    0.0141                   WATER       0.0143
NITROGEN   0.0159                   CO2         0.0004
CO2        0.0076                   ARGON       0.0093

FUEL VISCOSITY  108.89 MICROPOISE.
FUEL MOLECULAR WEIGHT  17.51

EQUIVALENCE RATIO  1.677 +/-  0.040

PRODUCT COMPOSITION
OXYGEN           0.0004 +/- 0.00061
NITROGEN         0.6480 +/- 0.00601
ARGON            0.0078 +/- 0.00055
CARBON DIOXIDE   0.0789 +/- 0.00116
WATER VAPOR      0.1814 +/- 0.00922
CARBON MONOXIDE  0.0186 +/- 0.00037
HYDROGEN         0.0161 +/- 0.00127
METHANE          0.0470 +/- 0.00092
ETHANE           0.0004 +/- 0.00004
ETHYLENE         0.0004 +/- 0.00008
ACETYLENE        0.0009 +/- 0.00009
SOOT (C8H)       0.0000 +/- 0.00000

HEAT OF FORMATION, FUEL  -18.384
HEAT OF FORMATION, AIR    -0.861
HEAT OF FORMATION, PROD. -19.192
HEAT OF FORMATION, STOICH PROD. -20.312
ACTUAL HEAT OF REACTION -113.569 KCAL/MOLE
HEAT OF STOICH. REACTION -207.233 KCAL/MOLE
RATIO HEATS OF REACTION 0.548
RATIO ACTUAL TO MAX 0.919
```

* * * * * DATA REDUCTION PROGRAM OUTPUT * * * * *
RUN NUMBER 56
DATE 08/13/85 TIME 15:55

INTERFACE HEIGHT ABOVE BURNER 15.0 CM.
FIRE SIZE 99.4 KW.
SAMPLE TEMPERATURE 483 DEG. C.

FLOWRATES G/S
FUEL 2.094
AIR 19.459
TOTAL 21.553

FUEL INLET RE 1224. FUEL INLET RI 1.64E-01

FUEL COMPOSITION		AIR COMPOSITION	
METHANE	0.9201	OXYGEN	0.2052
ETHANE	0.0422	NITROGEN	0.7708
PROPANE	0.0141	WATER	0.0143
NITROGEN	0.0159	CO2	0.0004
CO2	0.0076	ARGON	0.0093

FUEL VISCOSITY 108.89 MICROPOISE.
FUEL MOLECULAR WEIGHT 17.51

EQUIVALENCE RATIO 1.782 +/- 0.042

PRODUCT COMPOSITION

OXYGEN	0.0005	+/- 0.00060
NITROGEN	0.6424	+/- 0.00592
ARGON	0.0077	+/- 0.00054
CARBON DIOXIDE	0.0772	+/- 0.00113
WATER VAPOR	0.1802	+/- 0.00913
CARBON MONOXIDE	0.0200	+/- 0.00040
HYDROGEN	0.0155	+/- 0.00128
METHANE	0.0543	+/- 0.00107
ETHANE	0.0006	+/- 0.00004
ETHYLENE	0.0005	+/- 0.00016
ACETYLENE	0.0011	+/- 0.00029
SOOT (C8H)	0.0000	+/- 0.00000

HEAT OF FORMATION, FUEL -18.384
HEAT OF FORMATION, AIR -0.861
HEAT OF FORMATION, PROD. -19.117
HEAT OF FORMATION, STOICH PROD. -20.312
ACTUAL HEAT OF REACTION -106.463 KCAL/MOLE
HEAT OF STOICH. REACTION -207.997 KCAL/MOLE
RATIO HEATS OF REACTION 0.512
RATIO ACTUAL TO MAX 0.912

* * * * * DATA REDUCTION PROGRAM OUTPUT * * * * *
RUN NUMBER 58
DATE 08/13/85 TIME 17:11

INTERFACE HEIGHT ABOVE BURNER 15.0 CM.
FIRE SIZE 111.3 KW.
SAMPLE TEMPERATURE 479 DEG. C.

FLOWRATES G/S
FUEL 2.347
AIR 20.264
TOTAL 22.611

FUEL INLET RE 1372. FUEL INLET RI 1.30E-01

FUEL COMPOSITION		AIR COMPOSITION	
METHANE	0.9201	OXYGEN	0.2052
ETHANE	0.0422	NITROGEN	0.7708
PROPANE	0.0141	WATER	0.0143
NITROGEN	0.0159	CO2	0.0004
CO2	0.0076	ARGON	0.0093

FUEL VISCOSITY 108.89 MICROPOISE.
FUEL MOLECULAR WEIGHT 17.51

EQUIVALENCE RATIO 1.917 +/- 0.045

PRODUCT COMPOSITION

OXYGEN	0.0004	+/- 0.00059
NITROGEN	0.6334	+/- 0.00562
ARGON	0.0076	+/- 0.00053
CARBON DIOXIDE	0.0741	+/- 0.00107
WATER VAPOR	0.1818	+/- 0.00877
CARBON MONOXIDE	0.0199	+/- 0.00039
HYDROGEN	0.0177	+/- 0.00127
METHANE	0.0618	+/- 0.00120
ETHANE	0.0006	+/- 0.00004
ETHYLENE	0.0007	+/- 0.00015
ACETYLENE	0.0014	+/- 0.00014
SOOT (C8H)	0.0005	+/- 0.00051

HEAT OF FORMATION, FUEL -18.384
HEAT OF FORMATION, AIR -0.861
HEAT OF FORMATION, PROD. -19.034
HEAT OF FORMATION, STOICH PROD. -20.312
ACTUAL HEAT OF REACTION -98.836 KCAL/MOLE
HEAT OF STOICH. REACTION -209.613 KCAL/MOLE
RATIO HEATS OF REACTION 0.472
RATIO ACTUAL TO MAX 0.904

* * * * * DATA REDUCTION PROGRAM OUTPUT * * * * *
RUN NUMBER 65
DATE 08/16/85 TIME 14:13

INTERFACE HEIGHT ABOVE BURNER 10.0 CM.
FIRE SIZE 11.8 KW.
SAMPLE TEMPERATURE 219 DEG. C.

FLOWRATES G/S
FUEL 0.249
AIR 11.129
TOTAL 11.377

FUEL INLET RE 145. FUEL INLET RI 1.16E+01

FUEL COMPOSITION		AIR COMPOSITION	
METHANE	0.9201	OXYGEN	0.2050
ETHANE	0.0422	NITROGEN	0.7699
PROPANE	0.0141	WATER	0.0155
NITROGEN	0.0159	CO2	0.0004
CO2	0.0076	ARGON	0.0093

FUEL VISCOSITY 108.89 MICROPOISE.
FUEL MOLECULAR WEIGHT 17.51

EQUIVALENCE RATIO 0.370 +/- 0.022

PRODUCT COMPOSITION

OXYGEN	0.1300	+/- 0.00454
NITROGEN	0.7418	+/- 0.02394
ARGON	0.0089	+/- 0.00097
CARBON DIOXIDE	0.0323	+/- 0.00109
WATER VAPOR	0.0864	+/- 0.03233
CARBON MONOXIDE	0.0000	+/- 0.00000
HYDROGEN	0.0000	+/- 0.00000
METHANE	0.0000	+/- 0.00000
ETHANE	0.0000	+/- 0.00000
ETHYLENE	0.0000	+/- 0.00000
ACETYLENE	0.0000	+/- 0.00000
SOOT (C8H)	0.0007	+/- 0.00025

HEAT OF FORMATION, FUEL -18.384
HEAT OF FORMATION, AIR -0.930
HEAT OF FORMATION, PROD. -8.025
HEAT OF FORMATION, STOICH PROD. -20.353
ACTUAL HEAT OF REACTION -182.492 KCAL/MOLE
HEAT OF STOICH. REACTION -192.535 KCAL/MOLE
RATIO HEATS OF REACTION 0.948
RATIO ACTUAL TO MAX 0.351

```
* * * * * DATA REDUCTION PROGRAM OUTPUT * * * * *
                RUN NUMBER  66
          DATE 08/16/85       TIME       14:46

INTERFACE HEIGHT ABOVE BURNER  10.0 CM.
FIRE SIZE   23.4 KW.
SAMPLE TEMPERATURE  326 DEG. C.

FLOWRATES G/S
FUEL   0.494
AIR   12.481
TOTAL 12.975

FUEL INLET RE   289.      FUEL INLET RI  2.94E+00

FUEL COMPOSITION                    AIR COMPOSITION
METHANE     0.9201                  OXYGEN      0.2050
ETHANE      0.0422                  NITROGEN    0.7699
PROPANE     0.0141                  WATER       0.0155
NITROGEN    0.0159                  CO2         0.0004
CO2         0.0076                  ARGON       0.0093

FUEL VISCOSITY  108.89 MICROPOISE.
FUEL MOLECULAR WEIGHT  17.51

EQUIVALENCE RATIO  0.656 +/-  0.022

PRODUCT COMPOSITION
OXYGEN            0.0716 +/- 0.00159
NITROGEN          0.7214 +/- 0.01151
ARGON             0.0087 +/- 0.00068
CARBON DIOXIDE    0.0589 +/- 0.00111
WATER VAPOR       0.1378 +/- 0.01603
CARBON MONOXIDE   0.0010 +/- 0.00013
HYDROGEN          0.0000 +/- 0.00000
METHANE           0.0000 +/- 0.00000
ETHANE            0.0000 +/- 0.00000
ETHYLENE          0.0000 +/- 0.00000
ACETYLENE         0.0000 +/- 0.00000
SOOT (C8H)        0.0006 +/- 0.00027

HEAT OF FORMATION, FUEL  -18.384
HEAT OF FORMATION, AIR    -0.930
HEAT OF FORMATION, PROD. -13.528
HEAT OF FORMATION, STOICH PROD. -20.353
ACTUAL HEAT OF REACTION -188.704 KCAL/MOLE
HEAT OF STOICH. REACTION -195.129 KCAL/MOLE
RATIO HEATS OF REACTION 0.967
RATIO ACTUAL TO MAX 0.635
```

* * * * * DATA REDUCTION PROGRAM OUTPUT * * * * *
RUN NUMBER 68
DATE 08/16/85 TIME 15:47

INTERFACE HEIGHT ABOVE BURNER 10.0 CM.
FIRE SIZE 37.0 KW.
SAMPLE TEMPERATURE 392 DEG. C.

FLOWRATES G/S
FUEL 0.779
AIR 12.820
TOTAL 13.599

FUEL INLET RE 456. FUEL INLET RI 1.18E+00

FUEL COMPOSITION		AIR COMPOSITION	
METHANE	0.9201	OXYGEN	0.2050
ETHANE	0.0422	NITROGEN	0.7699
PROPANE	0.0141	WATER	0.0155
NITROGEN	0.0159	CO2	0.0004
CO2	0.0076	ARGON	0.0093

FUEL VISCOSITY 108.89 MICROPOISE.
FUEL MOLECULAR WEIGHT 17.51

EQUIVALENCE RATIO 1.008 +/- 0.026

PRODUCT COMPOSITION

OXYGEN	0.0222	+/- 0.00079
NITROGEN	0.6960	+/- 0.00759
ARGON	0.0083	+/- 0.00060
CARBON DIOXIDE	0.0735	+/- 0.00109
WATER VAPOR	0.1884	+/- 0.01102
CARBON MONOXIDE	0.0060	+/- 0.00015
HYDROGEN	0.0000	+/- 0.00000
METHANE	0.0040	+/- 0.00017
ETHANE	0.0000	+/- 0.00000
ETHYLENE	0.0000	+/- 0.00000
ACETYLENE	0.0000	+/- 0.00000
SOOT (C8H)	0.0015	+/- 0.00030

HEAT OF FORMATION, FUEL -18.384
HEAT OF FORMATION, AIR -0.930
HEAT OF FORMATION, PROD. -18.032
HEAT OF FORMATION, STOICH PROD. -20.353
ACTUAL HEAT OF REACTION -171.630 KCAL/MOLE
HEAT OF STOICH. REACTION -198.811 KCAL/MOLE
RATIO HEATS OF REACTION 0.863
RATIO ACTUAL TO MAX 0.870

```
* * * * * DATA REDUCTION PROGRAM OUTPUT * * * * *
                RUN NUMBER  77
          DATE 08/20/85       TIME       14:08

INTERFACE HEIGHT ABOVE BURNER  10.0 CM.
FIRE SIZE   49.5 KW.
SAMPLE TEMPERATURE  410 DEG. C.

FLOWRATES G/S
FUEL   1.044
AIR   13.252
TOTAL 14.296

FUEL INLET RE   610.      FUEL INLET RI  6.59E-01

FUEL COMPOSITION                    AIR COMPOSITION
METHANE    0.9201                   OXYGEN      0.2049
ETHANE     0.0422                   NITROGEN    0.7697
PROPANE    0.0141                   WATER       0.0157
NITROGEN   0.0159                   CO2         0.0004
CO2        0.0076                   ARGON       0.0093

FUEL VISCOSITY  108.89 MICROPOISE.
FUEL MOLECULAR WEIGHT  17.51

EQUIVALENCE RATIO  1.306 +/-  0.032

PRODUCT COMPOSITION
OXYGEN           0.0083 +/- 0.00066
NITROGEN         0.6729 +/- 0.00657
ARGON            0.0081 +/- 0.00057
CARBON DIOXIDE   0.0786 +/- 0.00110
WATER VAPOR      0.1858 +/- 0.00979
CARBON MONOXIDE  0.0139 +/- 0.00023
HYDROGEN         0.0071 +/- 0.00106
METHANE          0.0240 +/- 0.00040
ETHANE           0.0003 +/- 0.00003
ETHYLENE         0.0003 +/- 0.00007
ACETYLENE        0.0007 +/- 0.00004
SOOT (C8H)       0.0001 +/- 0.00038

HEAT OF FORMATION, FUEL  -18.384
HEAT OF FORMATION, AIR    -0.944
HEAT OF FORMATION, PROD..-18.891
HEAT OF FORMATION, STOICH PROD. -20.361
ACTUAL HEAT OF REACTION -141.086 KCAL/MOLE
HEAT OF STOICH. REACTION -202.773 KCAL/MOLE
RATIO HEATS OF REACTION 0.696
RATIO ACTUAL TO MAX 0.909
```

* * * * * DATA REDUCTION PROGRAM OUTPUT * * * * *
RUN NUMBER 78
DATE 08/20/85 TIME 14:41

INTERFACE HEIGHT ABOVE BURNER 10.0 CM.
FIRE SIZE 62.0 KW.
SAMPLE TEMPERATURE 406 DEG. C.

FLOWRATES G/S
FUEL 1.306
AIR 12.611
TOTAL 13.917

FUEL INLET RE 763. FUEL INLET RI 4.21E-01

FUEL COMPOSITION		AIR COMPOSITION	
METHANE	0.9201	OXYGEN	0.2049
ETHANE	0.0422	NITROGEN	0.7697
PROPANE	0.0141	WATER	0.0157
NITROGEN	0.0159	CO2	0.0004
CO2	0.0076	ARGON	0.0093

FUEL VISCOSITY 108.89 MICROPOISE.
FUEL MOLECULAR WEIGHT 17.51

EQUIVALENCE RATIO 1.717 +/- 0.040

PRODUCT COMPOSITION

OXYGEN	0.0006	+/- 0.00060
NITROGEN	0.6455	+/- 0.00577
ARGON	0.0077	+/- 0.00054
CARBON DIOXIDE	0.0774	+/- 0.00113
WATER VAPOR	0.1847	+/- 0.00890
CARBON MONOXIDE	0.0178	+/- 0.00029
HYDROGEN	0.0144	+/- 0.00120
METHANE	0.0489	+/- 0.00078
ETHANE	0.0008	+/- 0.00004
ETHYLENE	0.0007	+/- 0.00015
ACETYLENE	0.0012	+/- 0.00005
SOOT (C8H)	0.0002	+/- 0.00046

HEAT OF FORMATION, FUEL -18.384
HEAT OF FORMATION, AIR -0.944
HEAT OF FORMATION, PROD. -19.243
HEAT OF FORMATION, STOICH PROD. -20.361
ACTUAL HEAT OF REACTION -110.875 KCAL/MOLE
HEAT OF STOICH. REACTION -207.364 KCAL/MOLE
RATIO HEATS OF REACTION 0.535
RATIO ACTUAL TO MAX 0.918

* * * * * DATA REDUCTION PROGRAM OUTPUT * * * * *
RUN NUMBER 79
DATE 08/20/85 TIME 15:15

INTERFACE HEIGHT ABOVE BURNER 10.0 CM.
FIRE SIZE 74.0 KW.
SAMPLE TEMPERATURE 407 DEG. C.

FLOWRATES G/S
FUEL 1.560
AIR 12.673
TOTAL 14.233

FUEL INLET RE 912. FUEL INLET RI 2.95E-01

FUEL COMPOSITION		AIR COMPOSITION	
METHANE	0.9201	OXYGEN	0.2049
ETHANE	0.0422	NITROGEN	0.7697
PROPANE	0.0141	WATER	0.0157
NITROGEN	0.0159	CO2	0.0004
CO2	0.0076	ARGON	0.0093

FUEL VISCOSITY 108.89 MICROPOISE.
FUEL MOLECULAR WEIGHT 17.51

EQUIVALENCE RATIO 2.041 +/- 0.047

PRODUCT COMPOSITION

OXYGEN	0.0005	+/- 0.00058
NITROGEN	0.6254	+/- 0.00545
ARGON	0.0075	+/- 0.00053
CARBON DIOXIDE	0.0754	+/- 0.00120
WATER VAPOR	0.1763	+/- 0.00860
CARBON MONOXIDE	0.0192	+/- 0.00031
HYDROGEN	0.0214	+/- 0.00139
METHANE	0.0694	+/- 0.00110
ETHANE	0.0012	+/- 0.00004
ETHYLENE	0.0012	+/- 0.00016
ACETYLENE	0.0024	+/- 0.00010
SOOT (C8H)	0.0000	+/- 0.00000

HEAT OF FORMATION, FUEL -18.384
HEAT OF FORMATION, AIR -0.944
HEAT OF FORMATION, PROD. -18.914
HEAT OF FORMATION, STOICH PROD. -20.361
ACTUAL HEAT OF REACTION -92.072 KCAL/MOLE
HEAT OF STOICH. REACTION -210.867 KCAL/MOLE
RATIO HEATS OF REACTION 0.437
RATIO ACTUAL TO MAX 0.891

* * * * * DATA REDUCTION PROGRAM OUTPUT * * * * *
RUN NUMBER 80
DATE 08/20/85 TIME 16:09

INTERFACE HEIGHT ABOVE BURNER 10.0 CM.
FIRE SIZE 37.1 KW.
SAMPLE TEMPERATURE 404 DEG. C.

FLOWRATES G/S
FUEL 0.782
AIR 12.461
TOTAL 13.243

FUEL INLET RE 457. FUEL INLET RI 1.17E+00

FUEL COMPOSITION		AIR COMPOSITION	
METHANE	0.9201	OXYGEN	0.2049
ETHANE	0.0422	NITROGEN	0.7697
PROPANE	0.0141	WATER	0.0157
NITROGEN	0.0159	CO2	0.0004
CO2	0.0076	ARGON	0.0093

FUEL VISCOSITY 108.89 MICROPOISE.
FUEL MOLECULAR WEIGHT 17.51

EQUIVALENCE RATIO 1.041 +/- 0.026

PRODUCT COMPOSITION

OXYGEN	0.0185	+/- 0.00074
NITROGEN	0.6930	+/- 0.00742
ARGON	0.0083	+/- 0.00060
CARBON DIOXIDE	0.0752	+/- 0.00110
WATER VAPOR	0.1895	+/- 0.01082
CARBON MONOXIDE	0.0074	+/- 0.00013
HYDROGEN	0.0011	+/- 0.00053
METHANE	0.0055	+/- 0.00009
ETHANE	0.0000	+/- 0.00000
ETHYLENE	0.0000	+/- 0.00000
ACETYLENE	0.0002	+/- 0.00005
SOOT (C8H)	0.0012	+/- 0.00031

HEAT OF FORMATION, FUEL -18.384
HEAT OF FORMATION, AIR -0.944
HEAT OF FORMATION, PROD. -18.311
HEAT OF FORMATION, STOICH PROD. -20.361
ACTUAL HEAT OF REACTION -169.284 KCAL/MOLE
HEAT OF STOICH. REACTION -199.344 KCAL/MOLE
RATIO HEATS OF REACTION 0.849
RATIO ACTUAL TO MAX 0.884

```
* * * * * DATA REDUCTION PROGRAM OUTPUT * * * * *
                RUN NUMBER  81
          DATE 08/20/85       TIME       16:42

INTERFACE HEIGHT ABOVE BURNER  10.0 CM.
FIRE SIZE   24.3 KW.
SAMPLE TEMPERATURE  342 DEG. C.

FLOWRATES G/S
FUEL   0.513
AIR   11.833
TOTAL 12.346

FUEL INLET RE   300.      FUEL INLET RI  2.73E+00

FUEL COMPOSITION                    AIR COMPOSITION
METHANE    0.9201                   OXYGEN      0.2049
ETHANE     0.0422                   NITROGEN    0.7697
PROPANE    0.0141                   WATER       0.0157
NITROGEN   0.0159                   CO2         0.0004
CO2        0.0076                   ARGON       0.0093

FUEL VISCOSITY  108.89 MICROPOISE.
FUEL MOLECULAR WEIGHT  17.51

EQUIVALENCE RATIO  0.718 +/-  0.022

PRODUCT COMPOSITION
OXYGEN            0.0659 +/- 0.00142
NITROGEN          0.7166 +/- 0.01041
ARGON             0.0086 +/- 0.00066
CARBON DIOXIDE    0.0581 +/- 0.00102
WATER VAPOR       0.1484 +/- 0.01462
CARBON MONOXIDE   0.0009 +/- 0.00013
HYDROGEN          0.0000 +/- 0.00000
METHANE           0.0000 +/- 0.00000
ETHANE            0.0000 +/- 0.00000
ETHYLENE          0.0000 +/- 0.00000
ACETYLENE         0.0000 +/- 0.00000
SOOT (C8H)        0.0014 +/- 0.00026

HEAT OF FORMATION, FUEL  -18.384
HEAT OF FORMATION, AIR    -0.944
HEAT OF FORMATION, PROD. -14.068
HEAT OF FORMATION, STOICH PROD. -20.361
ACTUAL HEAT OF REACTION -180.046 KCAL/MOLE
HEAT OF STOICH. REACTION -195.792 KCAL/MOLE
RATIO HEATS OF REACTION 0.920
RATIO ACTUAL TO MAX 0.661
```

* * * * * DATA REDUCTION PROGRAM OUTPUT * * * * *
RUN NUMBER 89
DATE 08/21/85 TIME 13:10

INTERFACE HEIGHT ABOVE BURNER 5.0 CM.
FIRE SIZE 12.0 KW.
SAMPLE TEMPERATURE 233 DEG. C.

FLOWRATES G/S
FUEL 0.252
AIR 7.297
TOTAL 7.549

FUEL INLET RE 147. FUEL INLET RI 1.13E+01

FUEL COMPOSITION		AIR COMPOSITION	
METHANE	0.9201	OXYGEN	0.2051
ETHANE	0.0422	NITROGEN	0.7703
PROPANE	0.0141	WATER	0.0149
NITROGEN	0.0159	CO2	0.0004
CO2	0.0076	ARGON	0.0093

FUEL VISCOSITY 108.89 MICROPOISE.
FUEL MOLECULAR WEIGHT 17.51

EQUIVALENCE RATIO 0.573 +/- 0.022

PRODUCT COMPOSITION

OXYGEN	0.0921	+/- 0.00218
NITROGEN	0.7276	+/- 0.01381
ARGON	0.0087	+/- 0.00073
CARBON DIOXIDE	0.0480	+/- 0.00106
WATER VAPOR	0.1224	+/- 0.01906
CARBON MONOXIDE	0.0000	+/- 0.00000
HYDROGEN	0.0000	+/- 0.00000
METHANE	0.0000	+/- 0.00000
ETHANE	0.0000	+/- 0.00000
ETHYLENE	0.0000	+/- 0.00000
ACETYLENE	0.0000	+/- 0.00000
SOOT (C8H)	0.0011	+/- 0.00025

HEAT OF FORMATION, FUEL -18.384
HEAT OF FORMATION, AIR -0.898
HEAT OF FORMATION, PROD. -11.589
HEAT OF FORMATION, STOICH PROD. -20.334
ACTUAL HEAT OF REACTION -181.217 KCAL/MOLE
HEAT OF STOICH. REACTION -194.387 KCAL/MOLE
RATIO HEATS OF REACTION 0.932
RATIO ACTUAL TO MAX 0.534

* * * * * DATA REDUCTION PROGRAM OUTPUT * * * * *
RUN NUMBER 90
DATE 08/21/85 TIME 14:53

INTERFACE HEIGHT ABOVE BURNER 5.0 CM.
FIRE SIZE 24.3 KW.
SAMPLE TEMPERATURE 327 DEG. C.

FLOWRATES G/S
FUEL 0.513
AIR 8.232
TOTAL 8.745

FUEL INLET RE 300. FUEL INLET RI 2.73E+00

FUEL COMPOSITION		AIR COMPOSITION	
METHANE	0.9201	OXYGEN	0.2051
ETHANE	0.0422	NITROGEN	0.7703
PROPANE	0.0141	WATER	0.0149
NITROGEN	0.0159	CO2	0.0004
CO2	0.0076	ARGON	0.0093

FUEL VISCOSITY 108.89 MICROPOISE.
FUEL MOLECULAR WEIGHT 17.51

EQUIVALENCE RATIO 1.033 +/- 0.026

PRODUCT COMPOSITION

OXYGEN	0.0239	+/- 0.00077
NITROGEN	0.6943	+/- 0.00739
ARGON	0.0083	+/- 0.00060
CARBON DIOXIDE	0.0716	+/- 0.00105
WATER VAPOR	0.1864	+/- 0.01076
CARBON MONOXIDE	0.0071	+/- 0.00016
HYDROGEN	0.0000	+/- 0.00000
METHANE	0.0063	+/- 0.00018
ETHANE	0.0001	+/- 0.00003
ETHYLENE	0.0001	+/- 0.00004
ACETYLENE	0.0005	+/- 0.00004
SOOT (C8H)	0.0015	+/- 0.00030

HEAT OF FORMATION, FUEL -18.384
HEAT OF FORMATION, AIR -0.898
HEAT OF FORMATION, PROD. -17.783
HEAT OF FORMATION, STOICH PROD. -20.334
ACTUAL HEAT OF REACTION -165.151 KCAL/MOLE
HEAT OF STOICH. REACTION -199.176 KCAL/MOLE
RATIO HEATS OF REACTION 0.829
RATIO ACTUAL TO MAX 0.856

```
* * * * * DATA REDUCTION PROGRAM OUTPUT * * * * *
                RUN NUMBER  91
          DATE 08/21/85       TIME       15:26

INTERFACE HEIGHT ABOVE BURNER    5.0 CM.
FIRE SIZE    36.7 KW.
SAMPLE TEMPERATURE  351 DEG. C.

FLOWRATES G/S
FUEL    0.774
AIR     8.964
TOTAL   9.738

FUEL INLET RE    453.      FUEL INLET RI   1.20E+00

FUEL COMPOSITION                    AIR COMPOSITION
METHANE     0.9201                  OXYGEN       0.2051
ETHANE      0.0422                  NITROGEN     0.7703
PROPANE     0.0141                  WATER        0.0149
NITROGEN    0.0159                  CO2          0.0004
CO2         0.0076                  ARGON        0.0093

FUEL VISCOSITY  108.89 MICROPOISE.
FUEL MOLECULAR WEIGHT  17.51

EQUIVALENCE RATIO  1.431 +/-  0.034

PRODUCT COMPOSITION
OXYGEN            0.0057 +/- 0.00064
NITROGEN          0.6645 +/- 0.00617
ARGON             0.0080 +/- 0.00056
CARBON DIOXIDE    0.0754 +/- 0.00103
WATER VAPOR       0.1912 +/- 0.00930
CARBON MONOXIDE   0.0148 +/- 0.00024
HYDROGEN          0.0088 +/- 0.00109
METHANE           0.0286 +/- 0.00046
ETHANE            0.0004 +/- 0.00003
ETHYLENE          0.0004 +/- 0.00011
ACETYLENE         0.0016 +/- 0.00009
SOOT (C8H)        0.0008 +/- 0.00039

HEAT OF FORMATION, FUEL  -18.384
HEAT OF FORMATION, AIR    -0.898
HEAT OF FORMATION, PROD. -18.962
HEAT OF FORMATION, STOICH PROD. -20.334
ACTUAL HEAT OF REACTION -130.027 KCAL/MOLE
HEAT OF STOICH. REACTION -204.286 KCAL/MOLE
RATIO HEATS OF REACTION 0.636
RATIO ACTUAL TO MAX 0.911
```

* * * * * DATA REDUCTION PROGRAM OUTPUT * * * * *
RUN NUMBER 92
DATE 08/21/85 TIME 15:59

INTERFACE HEIGHT ABOVE BURNER 5.0 CM.
FIRE SIZE 49.5 KW.
SAMPLE TEMPERATURE 354 DEG. C.

FLOWRATES G/S
FUEL 1.044
AIR 8.561
TOTAL 9.605

FUEL INLET RE 611. FUEL INLET RI 6.59E-01

FUEL COMPOSITION		AIR COMPOSITION	
METHANE	0.9201	OXYGEN	0.2051
ETHANE	0.0422	NITROGEN	0.7703
PROPANE	0.0141	WATER	0.0149
NITROGEN	0.0159	CO2	0.0004
CO2	0.0076	ARGON	0.0093

FUEL VISCOSITY 108.89 MICROPOISE.
FUEL MOLECULAR WEIGHT 17.51

EQUIVALENCE RATIO 2.021 +/- 0.045

PRODUCT COMPOSITION

OXYGEN	0.0005	+/- 0.00058
NITROGEN	0.6255	+/- 0.00511
ARGON	0.0075	+/- 0.00052
CARBON DIOXIDE	0.0656	+/- 0.00085
WATER VAPOR	0.1963	+/- 0.00810
CARBON MONOXIDE	0.0184	+/- 0.00029
HYDROGEN	0.0218	+/- 0.00137
METHANE	0.0574	+/- 0.00089
ETHANE	0.0010	+/- 0.00004
ETHYLENE	0.0011	+/- 0.00015
ACETYLENE	0.0021	+/- 0.00009
SOOT (C8H)	0.0028	+/- 0.00047

HEAT OF FORMATION, FUEL -18.384
HEAT OF FORMATION, AIR -0.898
HEAT OF FORMATION, PROD. -18.922
HEAT OF FORMATION, STOICH PROD. -20.334
ACTUAL HEAT OF REACTION -93.425 KCAL/MOLE
HEAT OF STOICH. REACTION -211.198 KCAL/MOLE
RATIO HEATS OF REACTION 0.442
RATIO ACTUAL TO MAX 0.894

```
* * * * * DATA REDUCTION PROGRAM OUTPUT * * * * *
                RUN NUMBER  95
          DATE 08/21/85       TIME       22:07

INTERFACE HEIGHT ABOVE BURNER    1.0 CM.
FIRE SIZE    12.0 KW.
SAMPLE TEMPERATURE  239 DEG. C.

FLOWRATES G/S
FUEL    0.253
AIR     5.605
TOTAL   5.857

FUEL INLET RE    148.      FUEL INLET RI   1.13E+01

FUEL COMPOSITION                    AIR COMPOSITION
METHANE     0.9201                  OXYGEN      0.2053
ETHANE      0.0422                  NITROGEN    0.7711
PROPANE     0.0141                  WATER       0.0139
NITROGEN    0.0159                  CO2         0.0004
CO2         0.0076                  ARGON       0.0093

FUEL VISCOSITY  108.89 MICROPOISE.
FUEL MOLECULAR WEIGHT  17.51

EQUIVALENCE RATIO  0.746 +/-  0.026

PRODUCT COMPOSITION
OXYGEN           0.0600 +/- 0.00142
NITROGEN         0.7191 +/- 0.01187
ARGON            0.0086 +/- 0.00069
CARBON DIOXIDE   0.0672 +/- 0.00135
WATER VAPOR      0.1394 +/- 0.01660
CARBON MONOXIDE  0.0032 +/- 0.00014
HYDROGEN         0.0000 +/- 0.00000
METHANE          0.0018 +/- 0.00016
ETHANE           0.0000 +/- 0.00000
ETHYLENE         0.0000 +/- 0.00000
ACETYLENE        0.0006 +/- 0.00009
SOOT (C8H)       0.0000 +/- 0.00000

HEAT OF FORMATION, FUEL  -18.384
HEAT OF FORMATION, AIR    -0.840
HEAT OF FORMATION, PROD. -14.466
HEAT OF FORMATION, STOICH PROD. -20.299
ACTUAL HEAT OF REACTION -179.423 KCAL/MOLE
HEAT OF STOICH. REACTION -195.217 KCAL/MOLE
RATIO HEATS OF REACTION 0.919
RATIO ACTUAL TO MAX 0.685
```

* * * * * DATA REDUCTION PROGRAM OUTPUT * * * * *
RUN NUMBER 96
DATE 08/21/85 TIME 22:41

INTERFACE HEIGHT ABOVE BURNER 1.0 CM.
FIRE SIZE 24.4 KW.
SAMPLE TEMPERATURE 278 DEG. C.

FLOWRATES G/S
FUEL 0.514
AIR 5.744
TOTAL 6.257

FUEL INLET RE 300. FUEL INLET RI 2.72E+00

FUEL COMPOSITION		AIR COMPOSITION	
METHANE	0.9201	OXYGEN	0.2053
ETHANE	0.0422	NITROGEN	0.7711
PROPANE	0.0141	WATER	0.0139
NITROGEN	0.0159	CO2	0.0004
CO2	0.0076	ARGON	0.0093

FUEL VISCOSITY 108.89 MICROPOISE.
FUEL MOLECULAR WEIGHT 17.51

EQUIVALENCE RATIO 1.480 +/- 0.035

PRODUCT COMPOSITION

OXYGEN	0.0086	+/- 0.00065
NITROGEN	0.6620	+/- 0.00620
ARGON	0.0079	+/- 0.00056
CARBON DIOXIDE	0.0747	+/- 0.00111
WATER VAPOR	0.1841	+/- 0.00935
CARBON MONOXIDE	0.0152	+/- 0.00025
HYDROGEN	0.0097	+/- 0.00111
METHANE	0.0346	+/- 0.00056
ETHANE	0.0005	+/- 0.00004
ETHYLENE	0.0004	+/- 0.00011
ACETYLENE	0.0018	+/- 0.00009
SOOT (C8H)	0.0004	+/- 0.00041

HEAT OF FORMATION, FUEL -18.384
HEAT OF FORMATION, AIR -0.840
HEAT OF FORMATION, PROD. -18.592
HEAT OF FORMATION, STOICH PROD. -20.299
ACTUAL HEAT OF REACTION -123.155 KCAL/MOLE
HEAT OF STOICH. REACTION -204.759 KCAL/MOLE
RATIO HEATS OF REACTION 0.601
RATIO ACTUAL TO MAX 0.890

```
* * * * * DATA REDUCTION PROGRAM OUTPUT * * * * *
                RUN NUMBER  97
          DATE 08/21/85       TIME       23:14

INTERFACE HEIGHT ABOVE BURNER    1.0 CM.
FIRE SIZE   36.8 KW.
SAMPLE TEMPERATURE  281 DEG. C.

FLOWRATES G/S
FUEL    0.775
AIR     5.775
TOTAL   6.550

FUEL INLET RE    453.      FUEL INLET RI   1.20E+00

FUEL COMPOSITION                    AIR COMPOSITION
METHANE     0.9201                  OXYGEN       0.2053
ETHANE      0.0422                  NITROGEN     0.7711
PROPANE     0.0141                  WATER        0.0139
NITROGEN    0.0159                  CO2          0.0004
CO2         0.0076                  ARGON        0.0093

FUEL VISCOSITY  108.89 MICROPOISE.
FUEL MOLECULAR WEIGHT  17.51

EQUIVALENCE RATIO  2.222 +/-  0.051

PRODUCT COMPOSITION
OXYGEN            0.0005 +/- 0.00058
NITROGEN          0.6174 +/- 0.00524
ARGON             0.0074 +/- 0.00052
CARBON DIOXIDE    0.0711 +/- 0.00112
WATER VAPOR       0.1777 +/- 0.00832
CARBON MONOXIDE   0.0207 +/- 0.00033
HYDROGEN          0.0177 +/- 0.00141
METHANE           0.0813 +/- 0.00128
ETHANE            0.0017 +/- 0.00005
ETHYLENE          0.0009 +/- 0.00026
ACETYLENE         0.0036 +/- 0.00012
SOOT (C8H)        0.0001 +/- 0.00057

HEAT OF FORMATION, FUEL  -18.384
HEAT OF FORMATION, AIR    -0.840
HEAT OF FORMATION, PROD. -18.791
HEAT OF FORMATION, STOICH PROD. -20.299
ACTUAL HEAT OF REACTION  -84.301 KCAL/MOLE
HEAT OF STOICH. REACTION -212.051 KCAL/MOLE
RATIO HEATS OF REACTION 0.398
RATIO ACTUAL TO MAX 0.883
```

* * * * * DATA REDUCTION PROGRAM OUTPUT * * * * *
RUN NUMBER 145
DATE 11/12/85 TIME 14:03

INTERFACE HEIGHT ABOVE BURNER 23.0 CM.
FIRE SIZE 61.9 KW.
SAMPLE TEMPERATURE 535 DEG. C.

FLOWRATES G/S
FUEL 1.306
AIR 28.373
TOTAL 29.679

FUEL INLET RE 761. FUEL INLET RI 4.17E-01

FUEL COMPOSITION		AIR COMPOSITION	
METHANE	0.9287	OXYGEN	0.2066
ETHANE	0.0360	NITROGEN	0.7760
PROPANE	0.0110	WATER	0.0077
NITROGEN	0.0169	CO2	0.0004
CO2	0.0074	ARGON	0.0093

FUEL VISCOSITY 109.27 MICROPOISE.
FUEL MOLECULAR WEIGHT 17.32

EQUIVALENCE RATIO 0.758 +/- 0.024

PRODUCT COMPOSITION

OXYGEN	0.0479	+/- 0.00127
NITROGEN	0.7208	+/- 0.01073
ARGON	0.0086	+/- 0.00067
CARBON DIOXIDE	0.0736	+/- 0.00138
WATER VAPOR	0.1481	+/- 0.01497
CARBON MONOXIDE	0.0009	+/- 0.00013
HYDROGEN	0.0000	+/- 0.00000
METHANE	0.0000	+/- 0.00000
ETHANE	0.0000	+/- 0.00000
ETHYLENE	0.0000	+/- 0.00000
ACETYLENE	0.0000	+/- 0.00000
SOOT (C8H)	0.0000	+/- 0.00000

HEAT OF FORMATION, FUEL -18.311
HEAT OF FORMATION, AIR -0.483
HEAT OF FORMATION, PROD. -15.507
HEAT OF FORMATION, STOICH PROD. -20.083
ACTUAL HEAT OF REACTION -193.262 KCAL/MOLE
HEAT OF STOICH. REACTION -193.682 KCAL/MOLE
RATIO HEATS OF REACTION 0.998
RATIO ACTUAL TO MAX 0.756

* * * * * DATA REDUCTION PROGRAM OUTPUT * * * * *
RUN NUMBER 146
DATE 11/12/85 TIME 14:37

INTERFACE HEIGHT ABOVE BURNER 23.0 CM.
FIRE SIZE 73.7 KW.
SAMPLE TEMPERATURE 577 DEG. C.

FLOWRATES G/S
FUEL 1.555
AIR 27.942
TOTAL 29.497

FUEL INLET RE 906. FUEL INLET RI 2.94E-01

FUEL COMPOSITION		AIR COMPOSITION	
METHANE	0.9287	OXYGEN	0.2066
ETHANE	0.0360	NITROGEN	0.7760
PROPANE	0.0110	WATER	0.0077
NITROGEN	0.0169	CO2	0.0004
CO2	0.0074	ARGON	0.0093

FUEL VISCOSITY 109.27 MICROPOISE.
FUEL MOLECULAR WEIGHT 17.32

EQUIVALENCE RATIO 0.916 +/- 0.026

PRODUCT COMPOSITION

OXYGEN	0.0189	+/- 0.00082
NITROGEN	0.7104	+/- 0.00903
ARGON	0.0085	+/- 0.00063
CARBON DIOXIDE	0.0864	+/- 0.00148
WATER VAPOR	0.1735	+/- 0.01282
CARBON MONOXIDE	0.0022	+/- 0.00013
HYDROGEN	0.0000	+/- 0.00000
METHANE	0.0000	+/- 0.00000
ETHANE	0.0000	+/- 0.00000
ETHYLENE	0.0000	+/- 0.00000
ACETYLENE	0.0000	+/- 0.00000
SOOT (C8H)	0.0000	+/- 0.00000

HEAT OF FORMATION, FUEL -18.311
HEAT OF FORMATION, AIR -0.483
HEAT OF FORMATION, PROD. -18.218
HEAT OF FORMATION, STOICH PROD. -20.083
ACTUAL HEAT OF REACTION -191.351 KCAL/MOLE
HEAT OF STOICH. REACTION -194.972 KCAL/MOLE
RATIO HEATS OF REACTION 0.981
RATIO ACTUAL TO MAX 0.899

```
* * * * * DATA REDUCTION PROGRAM OUTPUT * * * * *
                RUN NUMBER  148
          DATE 11/12/85       TIME       15:46

INTERFACE HEIGHT ABOVE BURNER  23.0 CM.
FIRE SIZE  105.0 KW.
SAMPLE TEMPERATURE  591 DEG. C.

FLOWRATES G/S
FUEL   2.214
AIR   29.291
TOTAL 31.505

FUEL INLET RE  1290.      FUEL INLET RI  1.45E-01

FUEL COMPOSITION                    AIR COMPOSITION
METHANE    0.9287                   OXYGEN      0.2066
ETHANE     0.0360                   NITROGEN    0.7760
PROPANE    0.0110                   WATER       0.0077
NITROGEN   0.0169                   CO2         0.0004
CO2        0.0074                   ARGON       0.0093

FUEL VISCOSITY  109.27 MICROPOISE.
FUEL MOLECULAR WEIGHT  17.32

EQUIVALENCE RATIO  1.244 +/-  0.031

PRODUCT COMPOSITION
OXYGEN            0.0009 +/- 0.00065
NITROGEN          0.6800 +/- 0.00675
ARGON             0.0082 +/- 0.00058
CARBON DIOXIDE    0.0840 +/- 0.00127
WATER VAPOR       0.1855 +/- 0.00999
CARBON MONOXIDE   0.0149 +/- 0.00030
HYDROGEN          0.0105 +/- 0.00042
METHANE           0.0159 +/- 0.00032
ETHANE            0.0001 +/- 0.00002
ETHYLENE          0.0001 +/- 0.00002
ACETYLENE         0.0000 +/- 0.00000
SOOT (C8H)        0.0000 +/- 0.00038

HEAT OF FORMATION, FUEL  -18.311
HEAT OF FORMATION, AIR    -0.483
HEAT OF FORMATION, PROD. -19.302
HEAT OF FORMATION, STOICH PROD. -20.083
ACTUAL HEAT OF REACTION -153.053 KCAL/MOLE
HEAT OF STOICH. REACTION -200.581 KCAL/MOLE
RATIO HEATS OF REACTION 0.763
RATIO ACTUAL TO MAX 0.949
```

```
* * * * * DATA REDUCTION PROGRAM OUTPUT * * * * *
                RUN NUMBER  149
          DATE 11/12/85       TIME       16:21

INTERFACE HEIGHT ABOVE BURNER  23.0 CM.
FIRE SIZE   90.2 KW.
SAMPLE TEMPERATURE  599 DEG. C.

FLOWRATES G/S
FUEL   1.903
AIR   30.618
TOTAL 32.521

FUEL INLET RE  1109.      FUEL INLET RI  1.96E-01

FUEL COMPOSITION                    AIR COMPOSITION
METHANE     0.9287                  OXYGEN      0.2066
ETHANE      0.0360                  NITROGEN    0.7760
PROPANE     0.0110                  WATER       0.0077
NITROGEN    0.0169                  CO2         0.0004
CO2         0.0074                  ARGON       0.0093

FUEL VISCOSITY  109.27 MICROPOISE.
FUEL MOLECULAR WEIGHT  17.32

EQUIVALENCE RATIO  1.023 +/-  0.028

PRODUCT COMPOSITION
OXYGEN           0.0053 +/- 0.00071
NITROGEN         0.7029 +/- 0.00845
ARGON            0.0084 +/- 0.00062
CARBON DIOXIDE   0.0902 +/- 0.00150
WATER VAPOR      0.1854 +/- 0.01214
CARBON MONOXIDE  0.0061 +/- 0.00015
HYDROGEN         0.0000 +/- 0.00000
METHANE          0.0016 +/- 0.00016
ETHANE           0.0000 +/- 0.00000
ETHYLENE         0.0000 +/- 0.00000
ACETYLENE        0.0000 +/- 0.00000
SOOT (C8H)       0.0000 +/- 0.00000

HEAT OF FORMATION, FUEL  -18.311
HEAT OF FORMATION, AIR    -0.483
HEAT OF FORMATION, PROD. -19.387
HEAT OF FORMATION, STOICH PROD. -20.083
ACTUAL HEAT OF REACTION -184.052 KCAL/MOLE
HEAT OF STOICH. REACTION -196.028 KCAL/MOLE
RATIO HEATS OF REACTION 0.939
RATIO ACTUAL TO MAX 0.961
```

* * * * * DATA REDUCTION PROGRAM OUTPUT * * * * *
RUN NUMBER 151
DATE 11/12/85 TIME 17:32

INTERFACE HEIGHT ABOVE BURNER 23.0 CM.
FIRE SIZE 120.2 KW.
SAMPLE TEMPERATURE 591 DEG. C.

FLOWRATES G/S
FUEL 2.535
AIR 30.283
TOTAL 32.818

FUEL INLET RE 1477. FUEL INLET RI 1.11E-01

FUEL COMPOSITION		AIR COMPOSITION	
METHANE	0.9287	OXYGEN	0.2066
ETHANE	0.0360	NITROGEN	0.7760
PROPANE	0.0110	WATER	0.0077
NITROGEN	0.0169	CO2	0.0004
CO2	0.0074	ARGON	0.0093

FUEL VISCOSITY 109.27 MICROPOISE.
FUEL MOLECULAR WEIGHT 17.32

EQUIVALENCE RATIO 1.378 +/- 0.035

PRODUCT COMPOSITION

OXYGEN	0.0019	+/- 0.00065
NITROGEN	0.6729	+/- 0.00695
ARGON	0.0081	+/- 0.00058
CARBON DIOXIDE	0.0834	+/- 0.00140
WATER VAPOR	0.1807	+/- 0.01033
CARBON MONOXIDE	0.0152	+/- 0.00031
HYDROGEN	0.0111	+/- 0.00104
METHANE	0.0260	+/- 0.00053
ETHANE	0.0003	+/- 0.00003
ETHYLENE	0.0002	+/- 0.00004
ACETYLENE	0.0003	+/- 0.00004
SOOT (C8H)	0.0000	+/- 0.00000

HEAT OF FORMATION, FUEL -18.311
HEAT OF FORMATION, AIR -0.483
HEAT OF FORMATION, PROD. -19.138
HEAT OF FORMATION, STOICH PROD. -20.083
ACTUAL HEAT OF REACTION -136.827 KCAL/MOLE
HEAT OF STOICH. REACTION -201.377 KCAL/MOLE
RATIO HEATS OF REACTION 0.679
RATIO ACTUAL TO MAX 0.936

* * * * * DATA REDUCTION PROGRAM OUTPUT * * * * *
RUN NUMBER 153
DATE 11/12/85 TIME 19:15

INTERFACE HEIGHT ABOVE BURNER 23.0 CM.
FIRE SIZE 135.5 KW.
SAMPLE TEMPERATURE 582 DEG. C.

FLOWRATES G/S
FUEL 2.858
AIR 29.401
TOTAL 32.259

FUEL INLET RE 1665. FUEL INLET RI 8.70E-02

FUEL COMPOSITION		AIR COMPOSITION	
METHANE	0.9287	OXYGEN	0.2066
ETHANE	0.0360	NITROGEN	0.7760
PROPANE	0.0110	WATER	0.0077
NITROGEN	0.0169	CO2	0.0004
CO2	0.0074	ARGON	0.0093

FUEL VISCOSITY 109.27 MICROPOISE.
FUEL MOLECULAR WEIGHT 17.32

EQUIVALENCE RATIO 1.600 +/- 0.039

PRODUCT COMPOSITION

OXYGEN	0.0003	+/- 0.00062
NITROGEN	0.6549	+/- 0.00640
ARGON	0.0078	+/- 0.00056
CARBON DIOXIDE	0.0784	+/- 0.00129
WATER VAPOR	0.1806	+/- 0.00964
CARBON MONOXIDE	0.0187	+/- 0.00038
HYDROGEN	0.0174	+/- 0.00175
METHANE	0.0393	+/- 0.00078
ETHANE	0.0005	+/- 0.00006
ETHYLENE	0.0005	+/- 0.00012
ACETYLENE	0.0015	+/- 0.00015
SOOT (C8H)	0.0001	+/- 0.00047

HEAT OF FORMATION, FUEL -18.311
HEAT OF FORMATION, AIR -0.483
HEAT OF FORMATION, PROD. -18.927
HEAT OF FORMATION, STOICH PROD. -20.083
ACTUAL HEAT OF REACTION -117.541 KCAL/MOLE
HEAT OF STOICH. REACTION -204.774 KCAL/MOLE
RATIO HEATS OF REACTION 0.574
RATIO ACTUAL TO MAX 0.918

Part 2

Laser Soot-Scattering Imaging of a Large Buoyant Diffusion Flame

Chapter 1

Introduction

The complex internal flow field produced by a large diffusion flame in the region in which rapid heat release occurs is not yet well understood. The flow can be characterized as highly unsteady and buoyancy-dominated, and the heat release regions of the resulting flames are made visible by soot formed in the combustion processes. The transition between laminar and turbulent flows and the operational distinction between unsteady laminar flows, which contain highly wrinkled laminar flames, and turbulent flows is often obscure; a body of data does not yet exist from which a convincing set of criteria can be developed to define the laminar to turbulent transition in these flames.

Visual studies of the flame luminosity have been useful in studying some phenomena, such as the flame height and the unsteady "puffing" characterizing many of these flames (Thomas et al., 1964; Zukoski et al., 1984). For flames with a height-to-source diameter ratio (L/D_0) greater than 1.0 and for which the initial momentum flux is negligible compared with the buoyancy force, the flame surface pinches in periodically toward the axis of symmetry just above the origin of the flame and produces a distinct structure in the flame. This structure has the appearance of a large irregular donut-shaped vortex ring, which rises slowly above the source and defines the top of the flame when the fuel it contains burns out. In a flame with a large height-to-source diameter ratio, several of these structures are present at any given time, and for flames with a height-to-source diameter ratio of two to three, only one structure is visible at a time. For flames with height-to-source diameter ratio less than one, the process cannot be seen in the visible flame but does appear in the shadowgraph images of the rising plume of hot combustion products.

In the present investigation, the flames had a height-to-source diameter ratio between one and three.

The puffing process has been the subject of numerous investigations and recent reviews are given in Zukoski et al. (1980) and Cetegen et al. (1984). The dominant frequency appears to scale as $\sqrt{g/D_0}$ for a wide range of diameters and fuels. Here g is the gravitational constant and D_0 is the burner diameter. The fluctuations are most apparent when the flame height-to-source diameter ratio, L/D_0, is between one and three, and the amplitude of the fluctuations decreases markedly as the initial momentum flux of the fuel increases and as L/D_0 increases from 3 to 20.

The large size of the structures and the speed at which they evolve suggest that they play an important part in fixing the entrainment and heat release in the lower part of the flame (see Part 1 of this report). Visual observations, while useful for flame height and puffing studies, do not allow visualization of the often complex flows within the fire plume, which are relevant to the entrainment rate and heat release rate in the flame, nor do they suggest a sufficiently detailed model required for calculation of radiant flux to the fuel beds.

Recently, laser lighting has been used effectively to study flows in which combustion is an important feature (Lysaght et al., 1982, for example). In these cases, particles are used as markers for the fuel, oxidizer, or products. The particles may be created or destroyed in the reaction or may be unaffected by the combustion region. These methods require either upstream seeding or auxiliary chemical reactions to produce the particles.

There have also been a number of studies of the radiation flux produced by buoyancy-controlled diffusion flames. With the exception of a technique de-

veloped by Markstein (1983), these experiments are based on absorption and emission measurements of the flame made along a line of sight through the flame and thus do not give any information concerning the structure of the interior of the flame. Markstein's technique uses a probe that had a resolution of about 60 mm.

The purpose of the current investigation was the demonstration of the laser soot-scattering technique as a useful tool in studying the structure of the flame and the location and nature of the instantaneous combustion interfaces. Since soot that is created and consumed in the flame itself is used as the scattering medium, no extraneous seeding or chemistry is required. The technique has been applied in a study of large buoyant diffusion flames with the intent of elucidating the complex internal structure of the large vortical pufflike features that dominate the heat release region of these flames. The flame studied in this investigation models liquid pool fires and related buoyant flames by a bed of glass beads with fuel supplied by the injection of natural gas.

In contrast to the probe techniques, such as the one used by Markstein (1983), the present technique is nonintrusive and can be used to give qualitative data for a cubical resolution element with a dimension of 1 to 2 mm on a side. However, it will not give the quantative data required to determine flame radiation that Markstein's intrusive probe will give.

In this report, we describe the flow visualization technique in detail and present measurements obtained using the technique to study 47.4 to 190 kW natural gas flames stabilized on a 0.5 m diameter burner. Inlet Richardson numbers, based on the burner diameter, varied from 5000 to 100,000, and inlet Reynolds numbers, also based on the burner diameter, ranged from 100 to 600.

The flow-visualization technique and the associated apparatus are described in Chapter 2. Laser light scattered off soot particles in the flame is imaged by a linear solid-state camera which is clocked at up to 586 times per second. The resulting image is a one-spatial-dimension and time "photograph" of the soot distribution. Radial measurements through the flame were made at axial distances of 0.1 to 2.0 diameters above the burner surface.

The measurements are presented and discussed in Chapter 3 for the 190 kW fire. The soot distribution within a large buoyant natural gas diffusion flame is argued to be a reasonable marker of the flame sheets. In light of this, the flame sheets are observed as highly wrinkled and convoluted surfaces distributed fairly uniformly within the instantaneous volume of the flame. Within the instantaneous flame volume, soot was found to be present about half of the time. When soot was present, it was observed as thin sheets, which became narrower in regions where the average strain was estimated to be greater.

The work described herein was accepted in July, 1986, for publication in *Combustion and Flame.*

A list of the data files for all of the measurements taken is presented in Appendix A.

Chapter 2

Experimental Technique

The basic idea for the flow visualization technique is as follows. A laser line is directed horizontally through the flame axis at a fixed location. Soot passing through the laser-line segment will scatter laser light in all directions and be "laser-illuminated" in this way. Filtering out the heat or chemically induced radiation from the flame permits viewing of only the laser-illuminated soot. The line segment is then imaged with time to give a two-dimensional (one spatial dimension plus time) picture of the soot distribution within the flame. This technique allows a view of soot at a particular location inside the flame, in contrast to visual studies in which all the luminous soot is integrated along a line of sight. As will be shown later, the soot particles mark the flame sheets in the current flames, so that in essence, the technique detects the location and structure of the flame sheets in these fires.

2.1 Burner and Fire Facility

The fuel used in the experiments was natural gas, which had a typical molar composition of 92.0% methane, 4.2% ethane, 1.0% propane, 1.6% nitrogen, 0.8% carbon dioxide, and 0.4% butanes and higher hydrocarbons. The lower heating value of the mixture was 35.3 kJ/ℓ and its molecular weight was 17.5.

The burner and exhaust facility is the same as that used by Cetegen (1982) (also in Cetegen et al., 1984). A 50 cm diameter burner was used to deliver the natural gas fuel to the flame. The fuel passed through a 4 cm deep porous bed of 2 mm spherical glass beads whose surface was made flat and flush with the outer metal edge of the burner. The sides of the burner were vertical and extended to the floor located an adjustable distance from the burner surface,

but always maintained at greater than one burner diameter distance in order to minimize ground interference. The fuel flowrate was measured with a Merriam laminar flowmeter and a Barocel differential pressure transducer connected to a Datametrics electronic manometer.

The burner was located in the center of a 2.4 m square area enclosed on the sides by a double layer of aluminum screen used to reduce the strength of flow disturbances present in the laboratory air. The screens were 2.4 m high and above them was a 2.4 m square hood, which removed the exhaust gases from the laboratory.

2.2 Dimensionless Parameters

The Reynolds and Richardson numbers were used to characterize the flow conditions at the burner exit. Due to the radiation from the the flame, the burner surface was estimated to be between 400 and 600° K.

The Reynolds number was defined as

$$\begin{aligned} \mathrm{Re_f} &\equiv \frac{\rho_f u_0 D_0}{\mu_f} \\ &\equiv \frac{4\dot{m}_f}{\pi D_0 \mu_f} \end{aligned} \tag{2.1}$$

and the Richardson number as

$$\begin{aligned} \mathrm{Ri_f} &\equiv \frac{(\rho_\infty - \rho_f) g D_0}{\rho_f u_0^2} \\ &\equiv \frac{\pi^2 (\rho_\infty - \rho_f) \rho_f g D_0^5}{16 \dot{m}_f^2} . \end{aligned} \tag{2.2}$$

The temperature of the burner surface affects the Reynolds number only through the viscosity, μ_f. For the Richardson number, inlet temperature effects are due to changes in the fuel density, ρ_f. In essence, a higher burner temperature decreases both the Reynolds and Richardson numbers.

The inlet Richardson numbers for the fuel, based on the burner diameter and assuming a fuel inlet temperature of 600° K, varied from about 100,000 at the lower heat rates to 5000 at the higher rates. The Reynolds numbers at the inlet ranged from 100 to 600, but increased downstream as the velocities increased due to buoyancy.

2.3 Optical Arrangement and Data Acquisition

2.3.1 Laser Optics

A schematic of the optical arrangement used for radial measurements is shown in Fig. (2.1). The 514.5 nm line from a 3 W Ar^{++} laser (Coherent Radiation CR-3) was passed through a steering and focusing apparatus, which was essentially a periscope with fine angular postitioning for both reflectors to allow independent accurate alignment to both the laser head's axis and the axis of the line segment in the flame that was to be imaged. The vertical length of the periscope was easily adjusted without affecting the alignment, so the imaged segment could be translated vertically with a high degree of parallelism. The output of the periscope held a long focal-length spherical lens to collimate the beam to a long thin waist within the flame and a polarization rotator to maximize the scattered intensity in the viewing direction. The r-direction is taken along the line from the periscope to the beamstop, and the z-direction is taken vertically from the face of the burner, with the center of the burner face defined as the origin.

2.3.2 Collection Optics

The collection optics for the scattered light consisted of a heat-reflecting filter, one of several narrow band interference filters, an imaging lens, and a linear solid-state camera. This camera used a 1024 element photodiode array (Reticon RL-1024G) to image the illuminated line segment up to 586 times per second.

The interference filter was used to pass only that light within a narrow band (1 to 10 nm at 514.5 nm) centered at the wavelength of the incident laser light. Given the narrow bandwidths of these filters, very little luminosity was passed through to the camera. The solid-state camera is described in detail by Koochesfahani (1984).

2.3.3 Data Acquisition System

The data acquisition system is the same as that used by Koochesfahani (1984) and described in Koochesfahani and Dimotakis (1985). It is based on a DEC PDP 11/23 CPU with a floating point accelerator, 256 kBytes of core memory, and 80 MBytes of high-speed (1 MByte per second) hard-disk storage. The photodiode array was interfaced to this system through a high-speed A/D converter, which had the capability of handling up to 10^7 8-bit conversions per second.

2.4 High-Speed Movies

Because the flow evolved significantly as it passed the radial measurement stations (i.e., relative velocities within a structure were comparable to the celerity of the structure), the distinction between an *r-t* diagram and an *r-z* "snapshot" was especially important. Both an *r-t* diagram and a "snapshot" can be viewed as a two-dimensional slice through an inherently four-dimensional object (three spatial dimensions plus time). A snapshot captures two spatial dimensions, while an *r-t* diagram captures one spatial dimension and time. The two representations offer different (reductional) views of the entire object, and only in the context of a given set of questions can either be considered superior. A movie or a two-dimensional electronic imaging time series offers a three-dimensional (two spatial plus time) view and clearly contains more information than either two-dimensional view if the spatial and temporal resolutions are comparable in

all cases. In the present investigation neither a snapshot nor any other two-dimensional imaging of the soot scattering was possible with the present illumination source (3 W Ar^{++} laser), given the high background due to the flame luminosity and due to the drop in intensity in forming a sheet of light. A much higher power laser or a pulsed laser and a fast-shuttered detector would be required to overcome this experimental difficulty.

Structures were in the process of changing dramatically as they crossed the measured line segment, so that the signature they left on an *r-t* diagram was quite distorted relative to their appearance at an instant in time. To make a correspondence between the *r-t* data and an instantaneous view, a high-speed movie camera was synchronized to photograph two perpendicular views of the flame luminosity simultaneously with the photodiode array images (117 frames per second or one movie frame for every 2.5 or 5 photodiode scans). The scattered laser radiation could not be observed consistently in the high-speed movie films, although the imaged axes could be discerned.

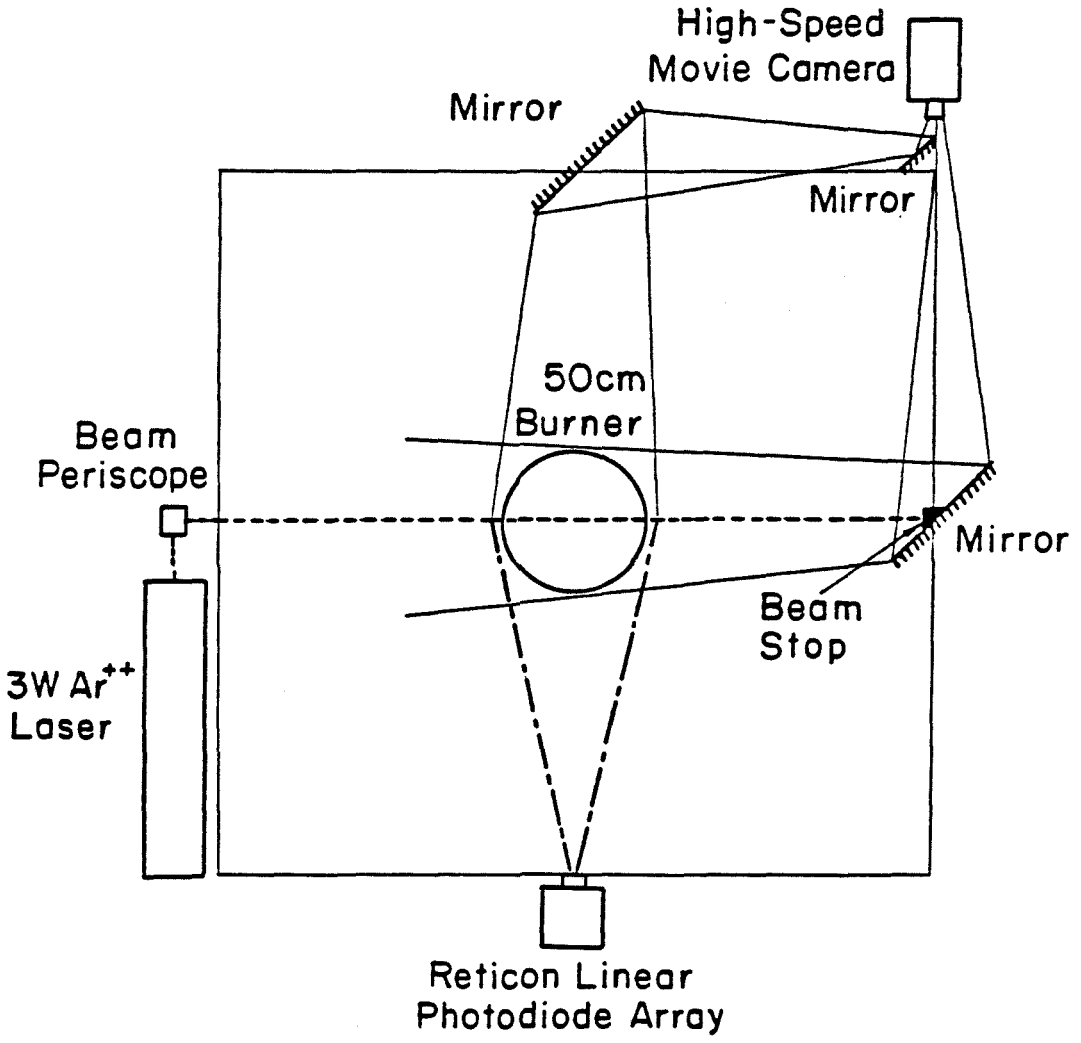

Figure (2.1) Experimental configuration.

Chapter 3

Results and Discussion

Instantaneous radial and axial profiles of soot distributions were visualized with approximately 1 mm resolution through the use of the laser soot-scattering technique in conjunction with photodiode array imaging and high-speed data acquisition. The radial measurements were analyzed in depth. A complete list of the data files and the corresponding test conditions is given in Appendix A.

3.1 Measurement Conditions

Data were collected at various z/D_0 values, from 0.1 to 2.0, and for various values of the heat releases, from 47.4 to 190 kW, as shown in Table **3.1**. Inlet Richardson numbers, Ri_0, varied from about 100,000 at the lower heat release rates to 5000 at the higher rates. The Reynolds numbers at the inlet, Re_0, ranged from 100 to 600 but increased downstream as the velocities increased due to buoyancy. For each entry in Table **3.1** marked with "x," four sets of *r-t* diagram data were collected at a 600 kHz clocking rate. One of these four data sets was collected in synchrony with the high-speed movie for each entry. For the entries marked with an asterisk, an additional data set was also collected at a 300 kHz clocking rate synchronized with the high-speed movie. The slower clocking rate allowed nearly three times more data to be collected due to computer data acquisition limitations, albeit at a lower temporal resolution. As mentioned above, a list of the data files and the corresponding test conditions is given in Appendix A.

For the 600 kHz data, core memory limited the data collection to 384 scans of 512 pixels. This amounted to 0.66 s of data collection. All 1024 pixels were read out; only the central 512 were recorded for $z/D_0 < 0.5$, while every alternate pixel (again 512 total) was recorded for $z/D_0 > 0.5$. For the 300 kHz data, core

memory was not a limitation since the data could be written directly to disk at this speed, so that 1024 (or more) scans of 512 pixels could be accommodated. Thus these data sets represent 3.5 s of data collection. Since the fire puffs at about 2 Hz, the higher clocking rate data correspond to about one puffing cycle, while the slower clocking rate data correspond to about seven cycles.

Flame lengths, L/D_0, determined from the results of Cetegen (1982) (also in Zukoski et al., 1984) for the various heat releases studied here are also shown in Table **3.1.** These flame lengths are based on 50% intermittency of the flame. The data presented in this paper correspond to the highest heat release values collected with a 300 kHz clocking rate. Except for the major difference of flame length (L/D_0) as seen in Table **3.1**, the results presented are representative of all heat release values where L/D_0 consistently reached the given axial station, i.e., $z < L$.

3.2 *r-t* Images

Figures (3.1) to (3.7) show *r-t* diagrams for a heat release of 190 kW and for z/D_0 values of 0.1, 0.2, 0.35, 0.5, 0.75, 1.0, and 2.0 taken with a 300 kHz clocking rate. The flame intermittency for the whole flame (Zukoski et al., 1984) was about 50% at $z/D_0 = 2.8$ and was nearly 100% below $z/D_0 = 1.0$. Darker regions indicate larger values of scattered intensity, although no effort has been made to interpret this intensity quantitatively, since both the particle size distribution and their number density affect the scattered intensity. The images show the first 492 of the total 1024 scans obtained for the 300 kHz tests and represent 1.7 seconds. Time is in the vertical direction with the earliest time at the top, and the horizontal direction corresponds to the measured line segment.

In figures (3.1) to (3.3), vertical lines indicate the locations of the pixels

corresponding to the center of the burner and the burner edge. In figures (3.4) to (3.7), a different optical geometry that imaged more than a full diameter of the burner was used. The two outer edges of the burner are marked for this geometry by vertical lines.

Figure (3.1) ($z/D_0 = 0.1$) demonstrates that most, if not all, of the soot is contained in thin convoluted sheets that are fairly continuous as they wind throughout the region occupied by the flame. The same general features of the soot sheets are noticeable at $z/D_0 = 0.2$, as shown in figure (3.2), although here more breaks appear in the sheet. A strong 2 Hz periodicity is evident in these two diagrams, even though individual puffs were not formed at these locations. Four sections through the image in figure (3.2) are represented by extra lines, two oriented horizontally and two vertically. These sections are plotted in figures (3.8) to (3.11). The vertical line cross sections of figure (3.2) are shown in figures (3.8) and (3.9) and are intensity-versus-time records of pixels 205 and 350 (located at $r/D_0 = 0.118$ and $r/D_0 = 0.312$), respectively, for the first 512 scans (of 1024) of the array. The horizontal lines in figure (3.2) correspond to figures (3.10) and (3.11) and are single intensity-versus-position scans of the array; figure (3.10) is scan 200, figure (3.11) is scan 350. These sections elucidate the thin sheetlike structure of the soot distribution at z/D_0 of 0.2 represented in figure (3.2).

By $z/D_0 = 0.35$, shown in figure (3.3), distinct puffs can be observed with connecting flame sheets between them. At this location the flame sheets appear thinner in the t-direction due to the increased velocity of the sheets. They are also more discontinuous than at the lower measuring locations. For figure (3.4) a different optical geometry was used and shows more than an entire burner diameter. The right edge of this figure is indistinct due to the angular cutoff of

the interference filter. The angular "window" was positioned off center to ensure that at least one edge of the flame was seen clearly. The thin contorted sheet structure is still present and the puffs are now quite clear.

The experimental resolution, which will be discussed later, begins to affect the images at $z/D_0 \approx 0.75$ as seen in figure (3.5), although the puffing character of the flame is still obvious in this diagram and in figures (3.6) (corresponding to $z/D_0 = 1.0$) and (3.7) (corresponding to $z/D_0 = 2.0$).

Figures (3.12) and (3.13) are *r-t* diagrams at $z/D_0 = 0.2$ for heat release rates of 90 kW and 45 kW, respectively. The same qualititive features of the soot distribution are observed although the overall widths of the soot-containing regions are different, as expected. Thus, as mentioned above, the data for the 190 kW flame are representative of all the heat release rates studied.

In the *r-t* diagrams and the sections shown in figures (3.8) to (3.11), it appears that the nature of the soot sheets does not depend on radial position in the flame. That is, the soot sheet thickness and curvature are qualitatively the same toward the center and toward the edges. The primary difference between the center and edges of the flame is the frequency of occurrence of soot sheets, which is greater near the center and goes to zero at the edges. The frequency of occurrence is defined as the soot intermittency, which allows a more quantitative analysis of these ideas and will be discussed below.

As previously stated, the high-speed movies offer a complementary view of the flame structure. The movie camera images the luminous soot over the whole flame, not just the soot intersecting the laser beam. Also, the movie captures most of the flame region at an instant in time, so that the flame structure can be seen directly in *r-z* space. A sequence of high-speed movie half-frames for

the z/D_0 = 0.5, 190 kW, 300 kHz data set is shown in figure (3.14). The corresponding *r-t* diagram is figure (3.4).

The puffing behavior of the flame that was evident in the *r-t* diagrams is also seen clearly in the high speed movies. The photographs in figure (3.14) show the rise of a large structure and the formation of a new one in its place. Near the burner, a strong 2 Hz periodicity is evident in the *r-t* data, although individual, separated puffs have not formed at this stage. At z/D_0 of 0.35 and beyond, distinct puffs can be observed. By integrating the *r-t* data across *r* and plotting the resulting average intensity as a function of time, the 2 Hz periodicity can be easily displayed graphically as is illustrated in figure (3.15). This type of plot clearly shows that the puffing is a quasi-periodic phenomenon, and that the period of the cyclic behavior is variable within some range. The mean frequency, f, of the puffing depends little if at all on the heat release rate and has a nondimensionalized value, $f\sqrt{D_0/g}$, of about 0.5.

The *r-t* diagrams are of interest from several points of view, not the least of which is the demonstration of the imaging soot-scattering technique as a useful probe of flame structure. The interpretation of these data is fairly straightforward, although some caveats may be in order. The first is that the interpretation of the absolute intensity of the scattered radiation has not been established. As was mentioned above, both the number density of particles and their size distribution determine the scattered intensity. Thus, without measuring or otherwise evaluating one of these parameters, there is ambiguity in the interpretation of the intensity. An unambiguous measurement would require a more sophisticated technique using either two-color or multiangle scattering at each pixel location.

The most interesting and instructive aspect of the *r-t* data is their structure. As will be argued below, this structure is reflective of the behavior of the flame

sheet surface and as such it tells much about the structure of the flame. This structure evolves with z/D_0 and is quasi-periodic in time at each z/D_0. The flame structure depends only weakly on the heat release rate (fuel flow rate) over the range studied, even though the overall length of the flame, L, does depend on the fuel flow rate (see Table **3.1**).

3.3 Soot and Flame Sheet Correspondence

The structure of the soot distribution can be tied to that of the flame sheet by several arguments. In a photographic study where the luminous soot and the laser-illuminated soot were observable simultaneously, there was no evidence of laser-illuminated soot in a region where there was no luminous soot. This is interpreted to mean that there is no appreciable cold (nonluminous) soot in the flame. This suggests that the soot is located primarily close to the hot combusting flame sheet.

Certainly, the formation of soot requires the high temperatures found near the diffusion flame. If one were to suppose that soot were to survive and move away from the flame surface, it might cool radiatively and show up as nonluminous soot — which was not observed. Further, and perhaps more significantly, soot surviving away from the burning regions would show up in the r-t diagrams, coexisting with other products in the large heated regions of the flame at larger z/D_0 stations. This is also not observed, nor is any significant amount of soot released by the flame as a whole.

From these lines of evidence, we argue that for this buoyant natural gas flame, the soot location marks approximately the flame sheet surface. The correspondence is approximate, however, since the soot is formed on the fuel side of the flame sheet before the fuel encounters oxygen and, further, the soot-bearing re-

gion is probably larger than the reaction zone (Tsuji and Yamaoka, 1970; Vandsburger et al., 1984), which here is defined as the width of the region where fuel and oxidant coexist, as shown in figure (3.16a). (This is based on the assumption that, at least locally, the flame behaves as a laminar diffusion flamelet.) Thus, the soot distribution is probably wider than the flame sheet itself in a direction normal to the flame sheet surface and is slightly displaced to the fuel side in the same direction. The wider soot distribution will not misrepresent the structure of the flame, however, if the soot burns completely before it approaches another flame sheet. That is, the soot region width must be small compared to the Kolmogorov scale, but not necessarily small compared to the flame sheet thickness, for the soot distribution to be useful as a marker of the flame sheet surface. The difference in the thickness of the two surfaces must nevertheless be kept in mind.

Thus, where there is soot, there is a flame sheet, but the converse is not necessarily true. It is possible that in an appropriate straining field, the flame temperature could drop below that required to form soot but not so low as to extinguish the flame (Glassman and Yaccarino, 1981). Alternatively, the effects of strain may be to diminish the time available for soot nucleation and growth to proceed (Kennedy, 1985). In any case, our data do not allow us to ascertain whether there is combustion without soot formation in this flame, but there are clear indications of breaks in the soot distribution for z/D_0 of 0.35 and greater. The strain rate increases with the velocity as z/D_0 increases, so this may possibly be viewed as a "straining out" of at least the soot production. Whether the entire flame is strained out at the same places is not addressed by this technique.

With the view that the soot structure and the flame sheet structure have a close correspondence, it is interesting to reconsider figures (3.1) to (3.7). Near the burner, at $z/D_0 = 0.1$ and 0.2 (figures (3.1) and (3.2)), the structure is

a continuous, convoluted surface. The soot thickness, which is presumably an upper bound for the flame sheet thickness as discussed above, is on the order of 5 mm. This estimate was obtained from the minimum widths of the soot sheets in the r-direction in the r-t images. At about $z/D_0 = 0.35$, discontinuities begin to appear (figure (3.3)) and the structures become more discontinuous with increasing z/D_0, although the spatial resolution of our measurements may be inadequate at or beyond $z/D_0 = 0.75$. The soot thickness is on the order of 2 mm at $z/D_0 = 0.35$. The spatial resolution is about 1 mm, so that as the soot thickness approaches 1 mm, it should become impossible to observe all the details of the soot structure. This is consistent with the observed lack of resolution at and beyond $z/D_0 = 0.75$.

One initially surprising feature of the soot structure is that the contorted and, for large z/D_0, broken surface does not fill a larger fraction of the space occupied by the flame. Photographs and movies of the luminous soot radiation, which integrate all luminous soot along the line-of-sight, lead one to conclude wrongly that the soot approaches a more or less uniformly volume filling distribution. In fact, the opposite is seen to be the case in the r-t diagrams, where the soot distribution is made up of flameletlike fragments that occupy the region within the outer boundaries of the flame. They are distributed approximately uniformly on average but individually are sharply localized. These observations support a model that, on a local level, the fuel and oxidant occur in alternating regions with soot (if present) along the interfaces, as shown in figure (3.16b). As more oxidant is entrained in the flame, the fuel regions shrinks until it disappears altogether. The alternating-layer theory was first proposed by Damköhler (1940), Shchelkin (1943), and Karlovitz et al. (1952) and was brought to the attention of the combustion community more recently by the work of Marble

(Carrier et al., 1975; Marble and Broadwell, 1977; Marble, 1985; Karagozian and Marble, 1986). It was then taken up by several authors, e.g., Williams (1975), in the development of the laminar diffusion flamelet theory, described recently in a review by Peters (1984).

The presence of soot on the centerline of the burner suggests that oxygen is present here. This is in agreement with the probe measurements of Gengembre et al. (1984), who found 3% oxygen on the centerline 5 cm from the surface of a 30 cm diameter burner. The presence of oxygen near the centerline should not be unexpected due to the large rates of air entrainment in the lower regions of the flame as described in Part 1 of this report.

3.4 Soot Intermittency

The laser illumination slices through the moving soot distribution, and the fraction of time that soot is present can be measured directly. The average fraction of time that soot is present at a given location is defined as the soot intermittency. Functionally, the total time that the intensity from a given region exceeds some low threshold value is divided by the total measurement time. This is plotted in figures (3.17) (lower curve) and (3.18) (lower curve) for the 300 kHz, 190 kW, $z/D_0 = 0.20$ and 0.50 cases, respectively. It can be seen that a peak value of about 0.5 to 0.6 occurs near the center and that the value decreases toward the edges of the burner. Taking into account the fact that the soot thickness is an upper bound for the flame sheet thickness, one concludes that the fraction of time that flame sheets are present might be still smaller.

Changing the threshold value used to determine the presence of soot affects the magnitude of the soot intermittency plots but not their qualitative features. The threshold value for the plots of soot intermittency was 1.5 to 2.0 times the

rms noise level of the background. If the intensity crossed that level, it was determined that soot was present. To explore the effect of the threshold value, a range of threshold values was used with the $z/D_0 = 0.2$ data. A binary series was used starting with the nominal value of 1.5 times the rms noise level and ending with 16 times this value. Figure (3.19) shows a plot of the soot intermittency using the normal threshold (upper curve) and a threshold 4 times as great (lower curve). The levels of the nominal threshold and 4 times this value are shown in figure (3.11). By raising the threshold level, the "wings" of each flamelet in the soot distribution are cut off, lowering the calculated soot intermittency. But insofar as the soot sheets are similar throughout the flame, as discussed above, the effects of raising the threshold are uniform across the flame. This argument holds at all z/D_0 values where the measurement resolution was sufficient to resolve the soot sheets.

The soot intermittency plots, in conjunction with the *r-t* diagrams, support a model of the flame in which it is made up of soot sheets (presumably following the flame sheets), which are plentiful near the center and sparser near the edges. Near the burner, the outer edges of these sheets form a complicated pseudoregular structure with an overall 2 Hz periodicity but without distinct puffs. As the observation height moves away from the burner, the scales decrease for both the width of the sheets and their radius of curvature. (The radius of curvature is on the order of the Kolmogorov length scale. The Reynolds number ranges from about 600 near the burner to about 6000 near $z/D_0 = 1.0$ based on crude estimates of the centerline velocity, the flame diameter, and the hot gas kinematic viscosity.) The overall envelope becomes a simple "puff" shape at about z/D_0 of 0.35, and this puffing occurs at the predominant 2 Hz frequency. The puffs at larger values of z/D_0 are made up of discontinuous soot sheets distributed more

or less uniformly within the confines of the puff shape.

The uniformity of the soot distribution is demonstrated in figures (3.17) and (3.18) (upper curves) where a conditional soot intermittency is plotted. This conditional soot intermittency is defined as the intermittency of the soot measured within the boundaries of the whole flame. It was calculated by first determining the horizontal edges of the soot distribution in the *r-t* data set for each time frame, using the low threshold value to distinguish the rightmost and leftmost positions at which soot was present. Then, for each pixel, the fraction of time the pixel contained soot was divided by the fraction of time that the pixel was contained between the rightmost and leftmost extents of the soot distribution (determined on a frame-by-frame basis). For the values of heat release rate and z/D_0 examined here, the conditional soot intermittency is nearly the same as the previously defined soot intermittency near the center of the flame, since the center of the flame is always well within the edges of the flame, and the flame is continually present near the center. Toward the edges, however, the flame edge moves in and out (whether there exist distinct puffs or not) and the conditional soot intermittency is substantially greater than the simple soot intermittency due to the duty cycle effect of the puffing behavior.

The conditional soot intermittency for the $z/D_0 = 0.2$ case is plotted in figure (3.17) (upper curve) and is nearly constant across the flame. There is an indication of a dip near the center as well as some residual structure farther out along the radius, but the curve lies predominantly between 45 and 55%. For $z/D_0 = 0.5$ (figure (3.18), upper curve), the conditional soot intermittency lies near 40% except near the center, where the value peaks to about 70%. Figure (3.17) is typical of all stations less than $z/D_0 = 0.35$, while figure (3.18) is typical for axial stations $z/D_0 = 0.35$ and greater. The peak in figure (3.18)

indicates that there is some difference in structure between the center and edges of the soot distribution for larger z/D_0 values, which we believe may be related to the connecting strands of soot between puffs. Nevertheless, the falling off of the simple soot intermittency toward the edges is not present in the conditional soot intermittency for any of our data.

The puff shape, then, primarily determines the simple soot intermittency curve, and the conditional soot intermittency is generally uniform within the flame edges and has a value near 40% (neglecting dips or peaks on the centerline). The flame sheets may or may not be as discontinuous as the soot sheets, but one might expect that the puff shape modulates the fraction of time that flame sheets are also encountered.

Dips in the conditional soot intermittency on the centerline were observed at the measurement stations closest to the burner surface. The paucity of soot at these locations is also seen in figures (3.1) and (3.2), and suggests that the oxidant was unable to consistantly reach the centerline of the flame close to the burner surface. The peak in the conditional soot intermittency observed near the centerline farther downstream is more difficult to explain but might be due to the connecting strands of flame observed between the large structures.

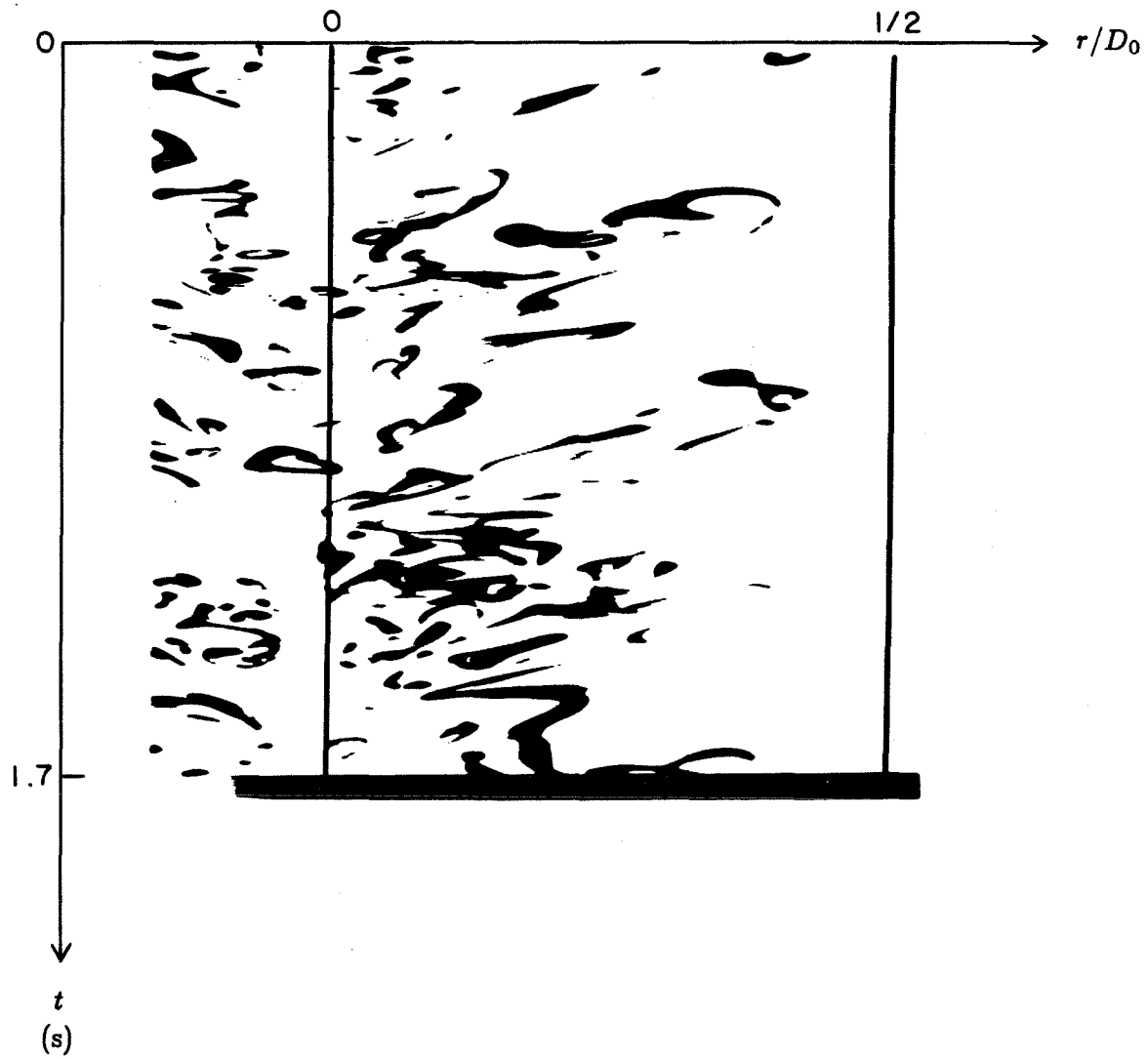

Figure (3.1) r-t diagram, 190 kW flame, $z/D_0 = 0.10$.

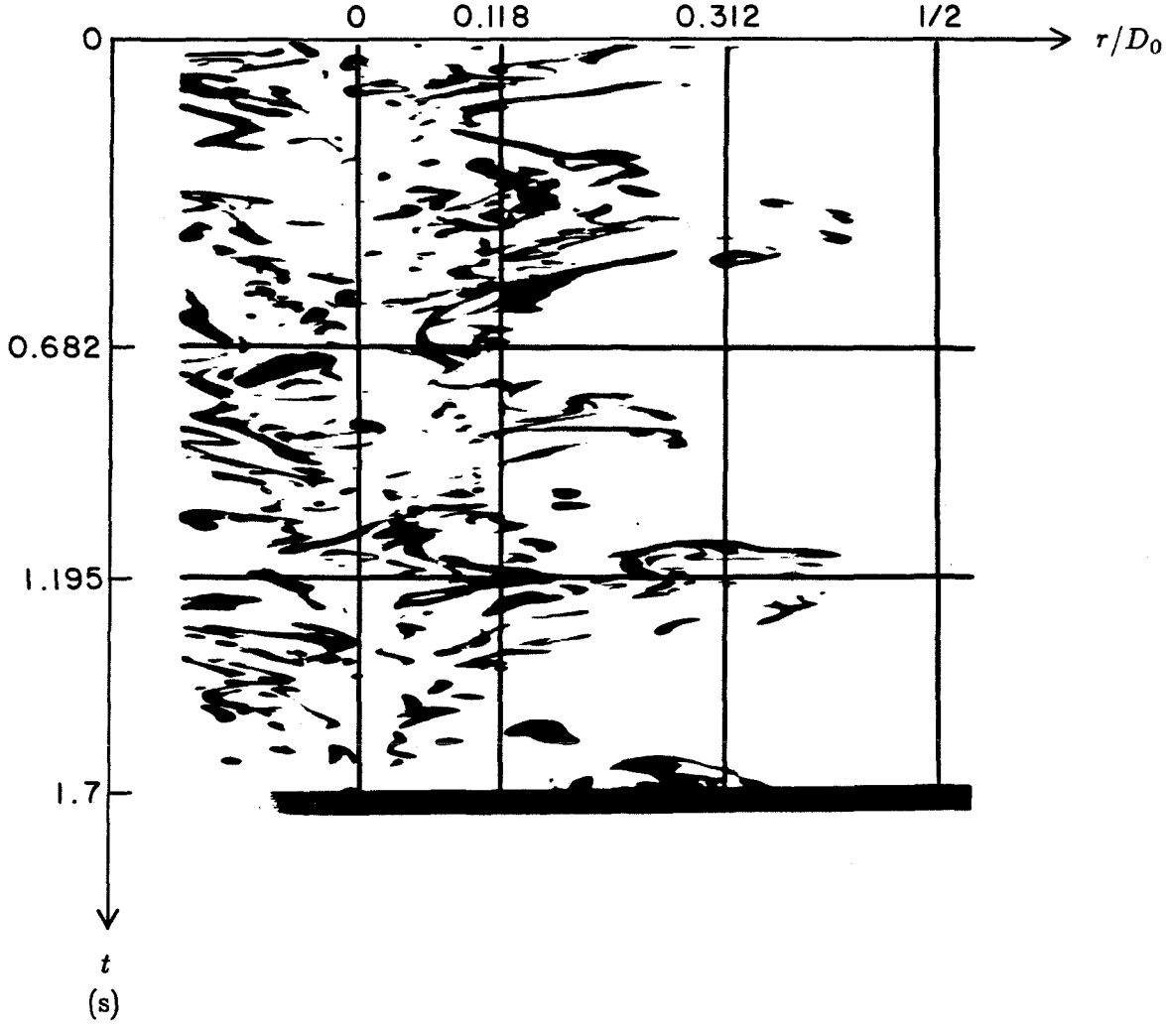

Figure (3.2) r-t diagram, 190 kW flame, $z/D_0 = 0.20$. Added lines are used for crossplots in figures (3.8) to (3.11).

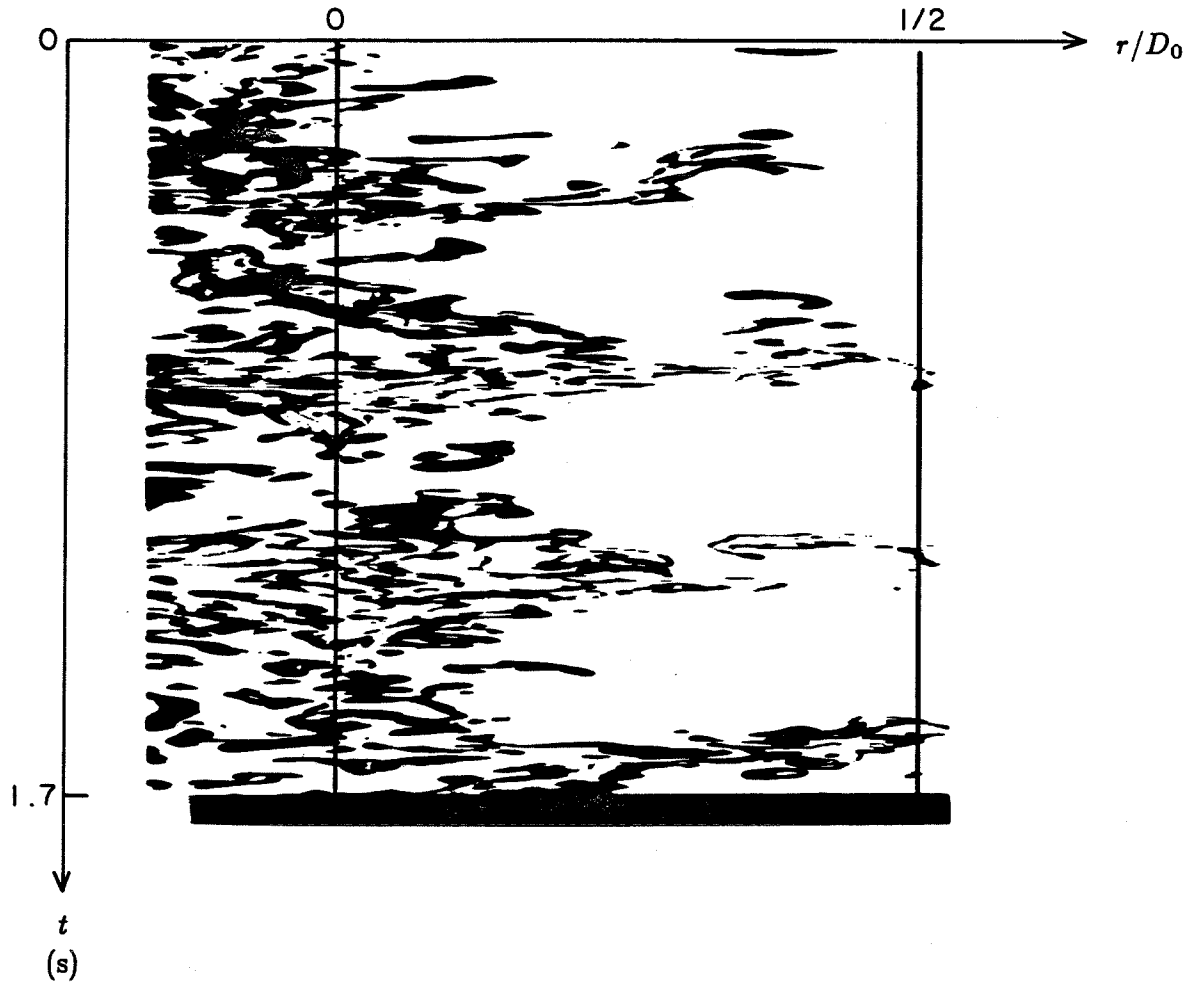

Figure (3.3) r-t diagram, 190 kW flame, $z/D_0 = 0.35$.

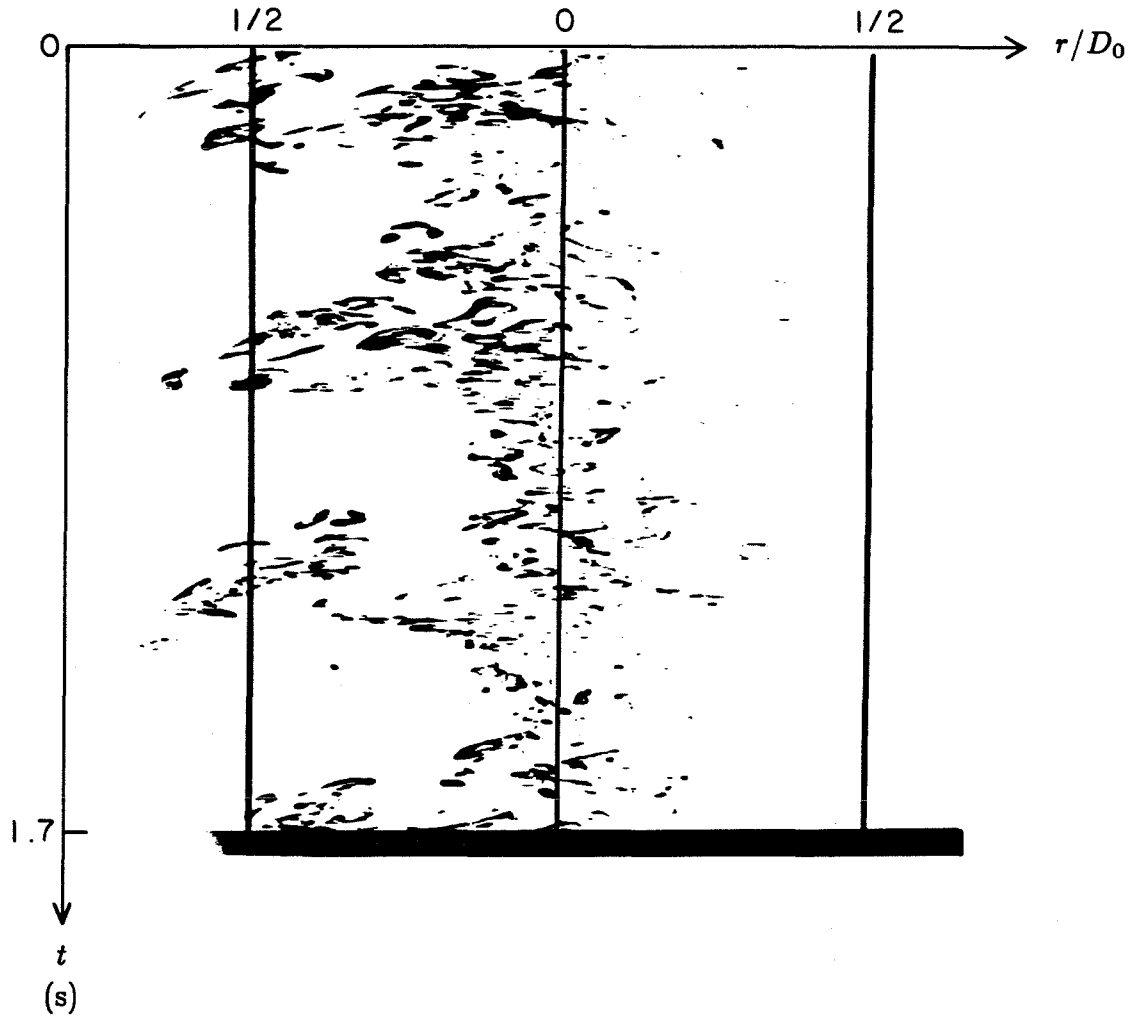

Figure (3.4) r-t diagram, 190 kW flame, $z/D_0 = 0.50$. The right edge of the figure is indistinct due to the angular cutoff of the interference filter. The angular "window" was postitioned slightly offcenter to ensure that at least one side of the flame was seen clearly.

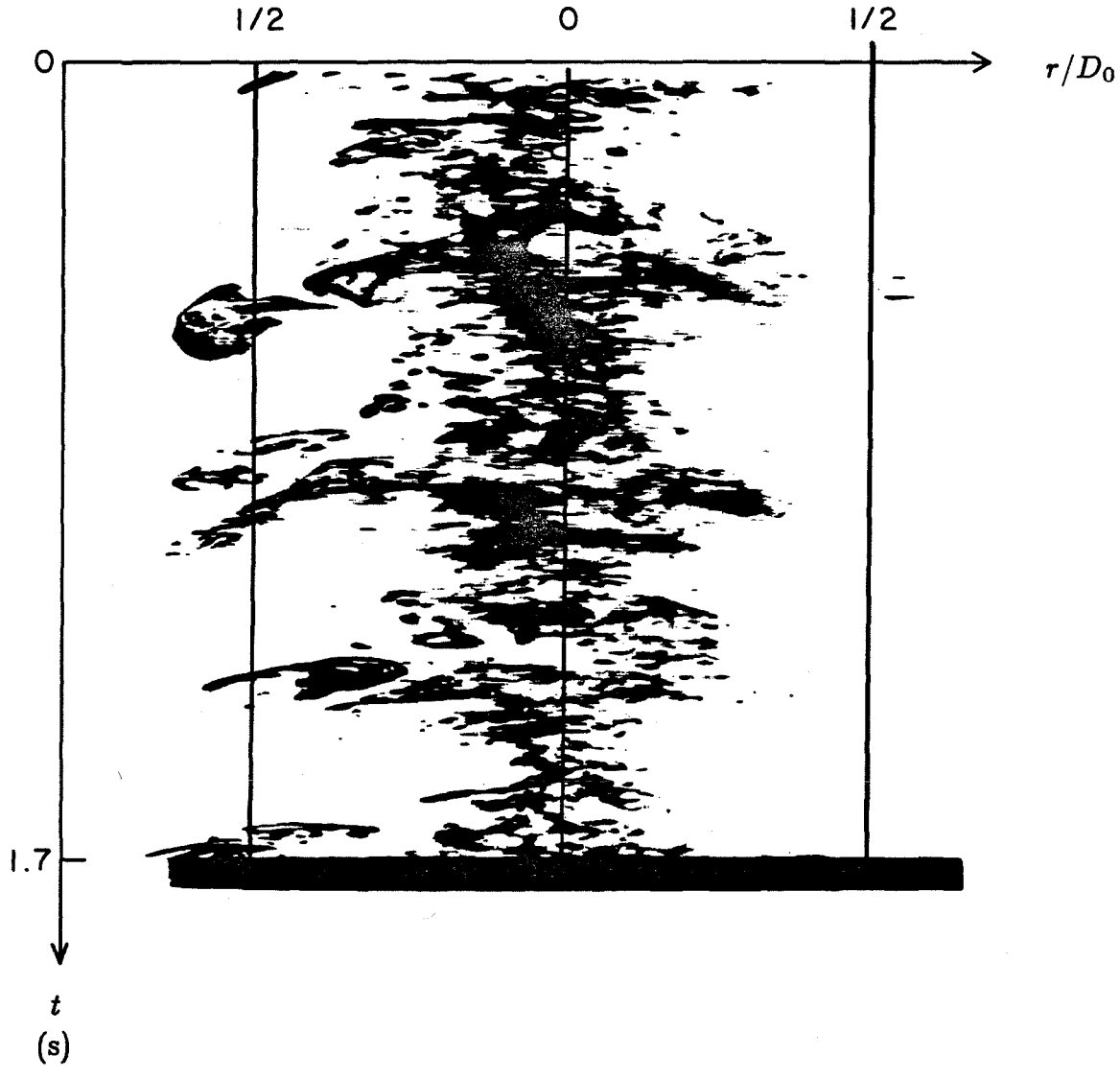

Figure (3.5) r-t diagram, 190 kW flame, $z/D_0 = 0.75$.

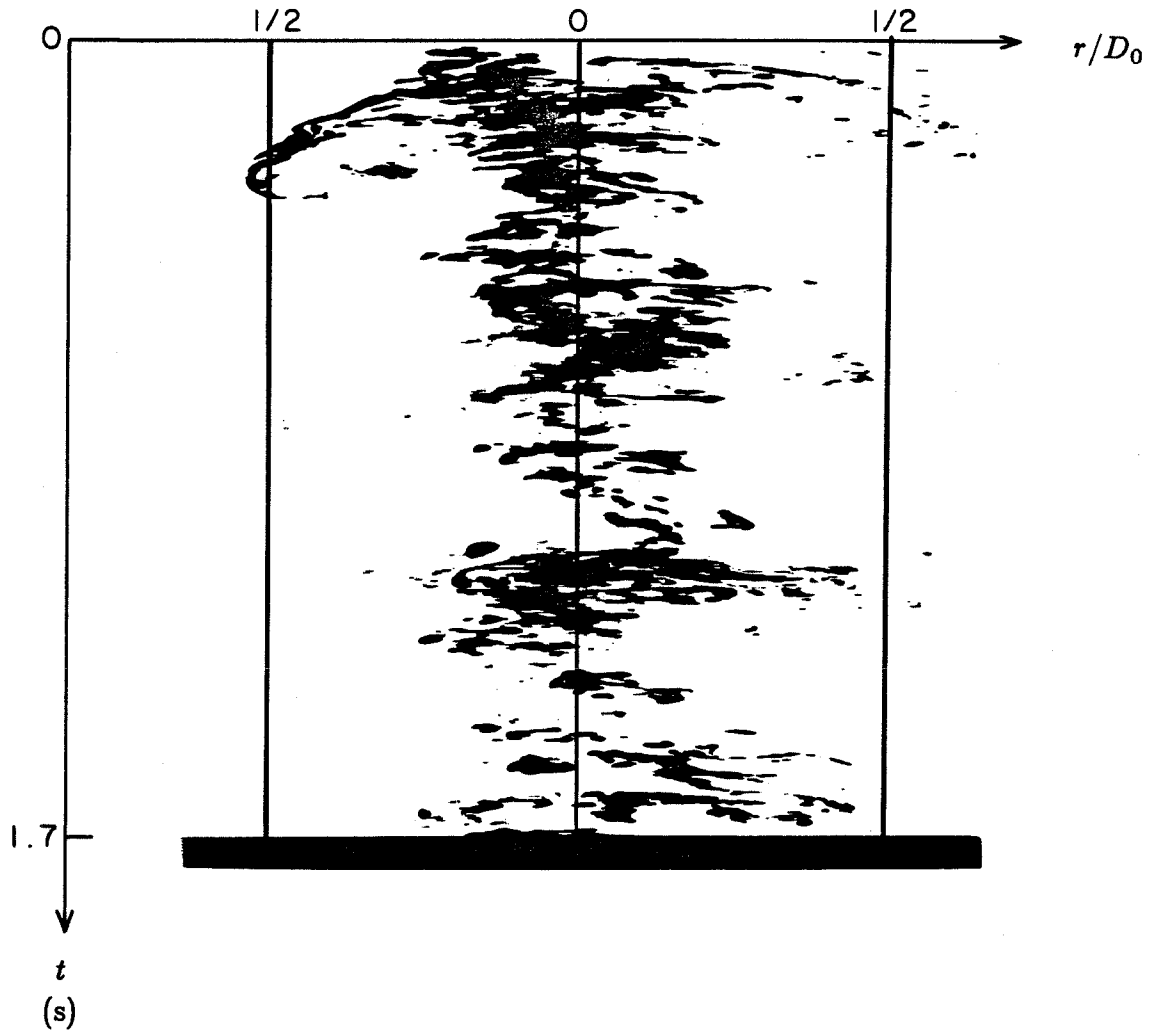

Figure (3.6) r-t diagram, 190 kW flame, $z/D_0 = 1.0$.

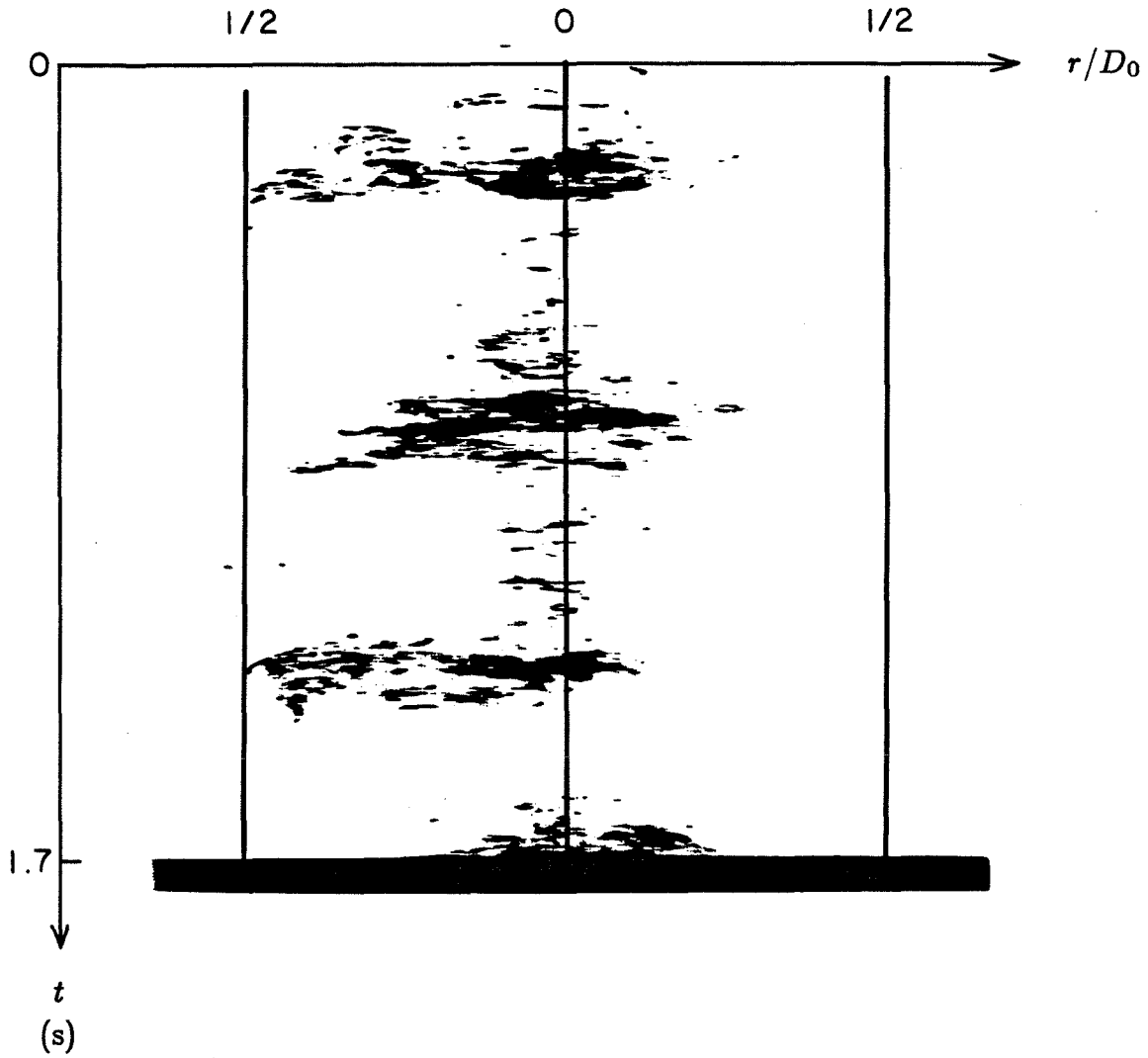

Figure (3.7) r-t diagram, 190 kW flame, $z/D_0 = 2.0$.

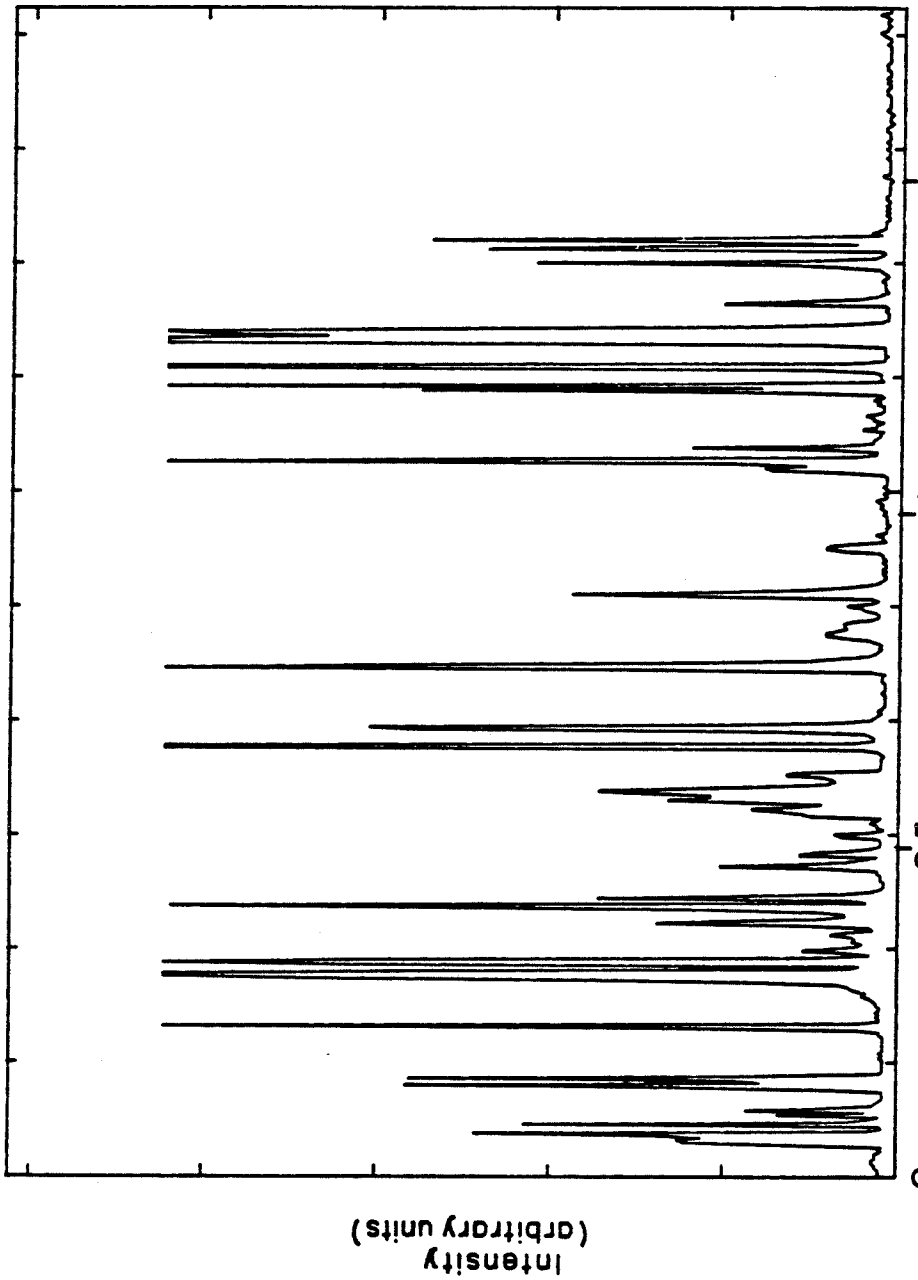

Figure (3.8) Intensity-versus-time history of pixel 205 ($r/D_0 = 0.118$), 190 kW flame, $z/D_0 = 0.2$ (see figure (3.2)).

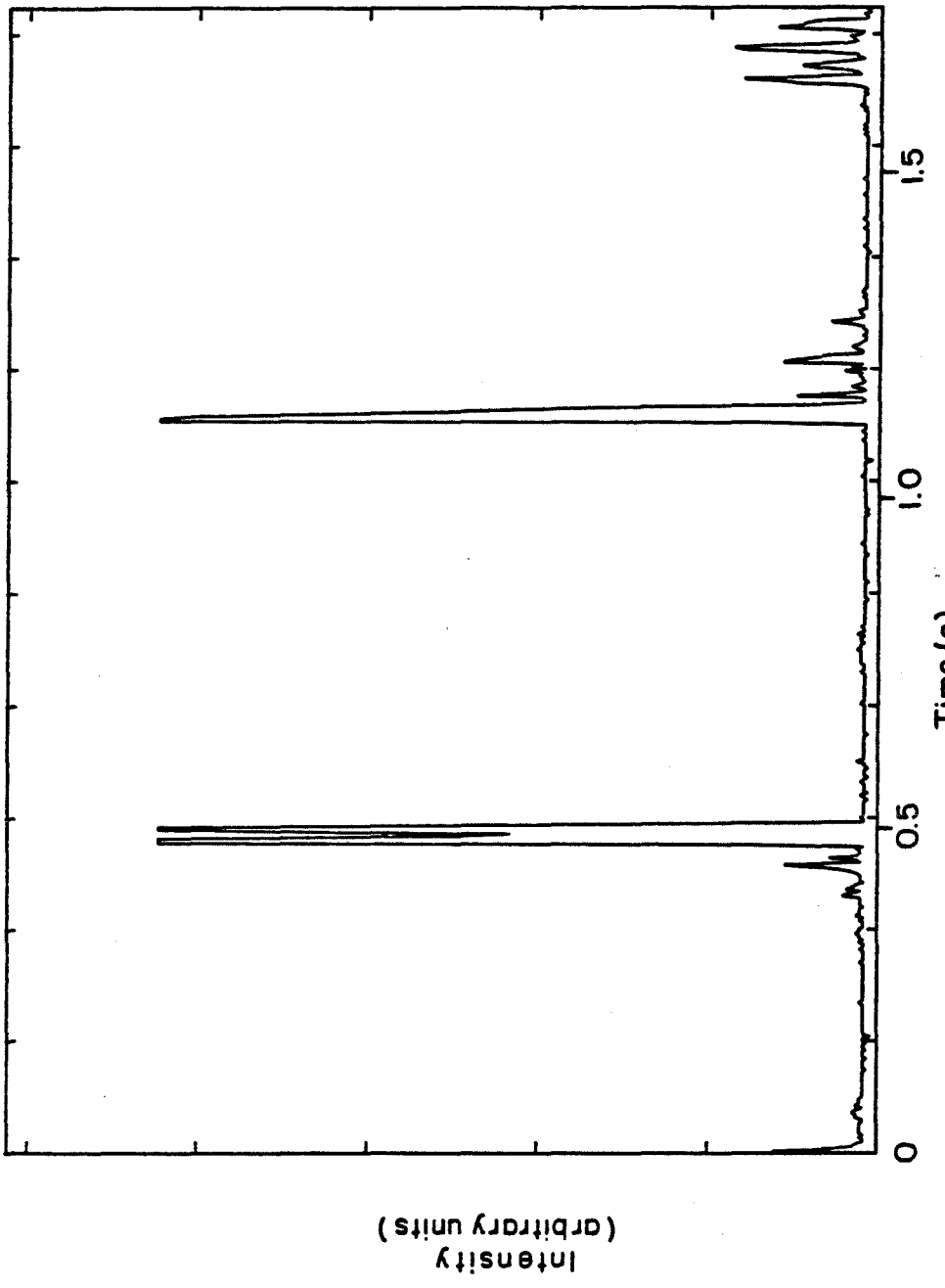

Figure (3.9) Intensity-versus-time history of pixel 350 ($r/D_0 = 0.312$), 190 kW flame, $z/D_0 = 0.2$ (see figure (3.2)).

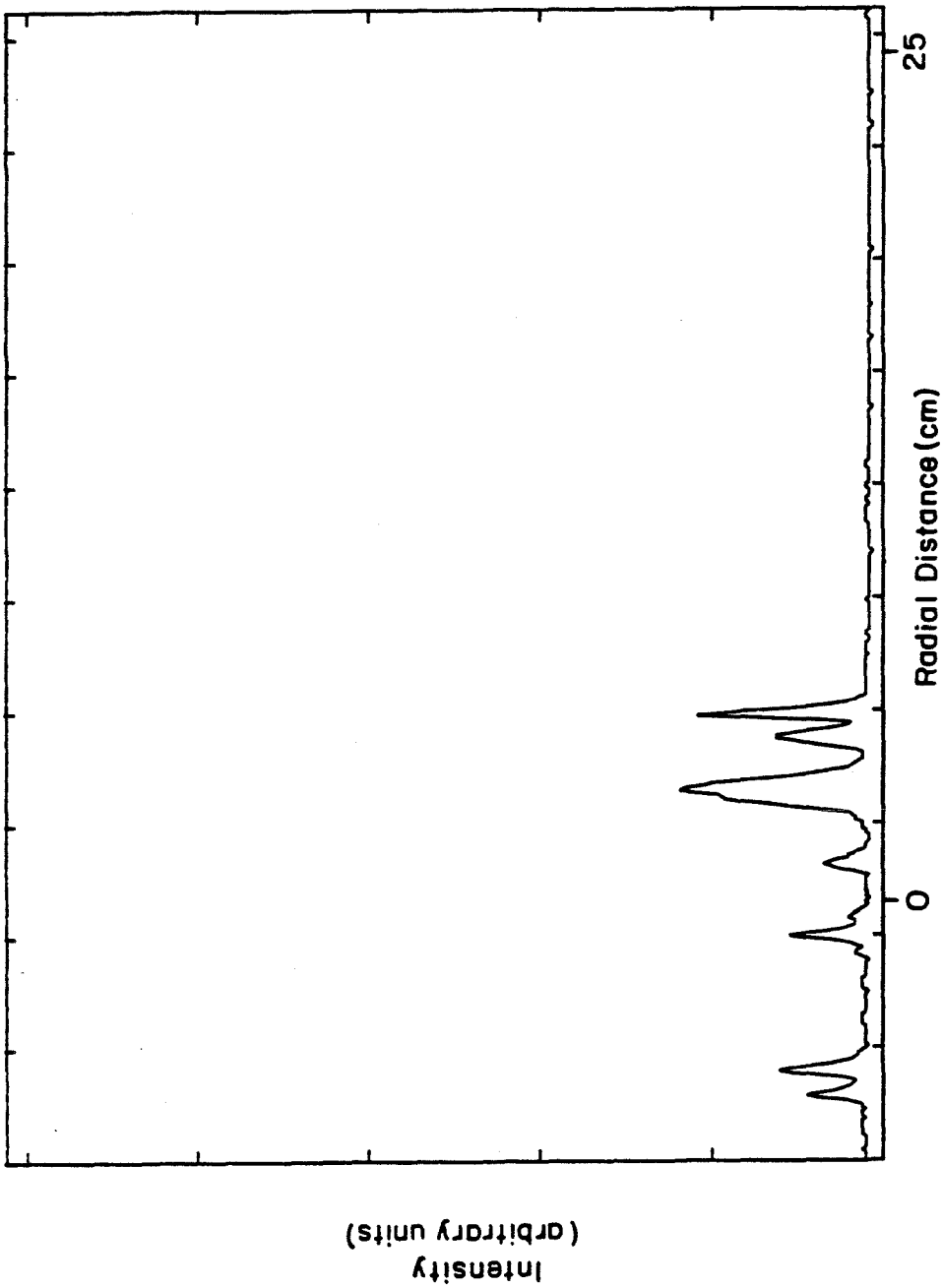

Figure (3.10) Intensity-versus-position of photodiode for scan 200 (0.682 s), 190 kW flame, $z/D_0 = 0.2$ (see figure (3.2)).

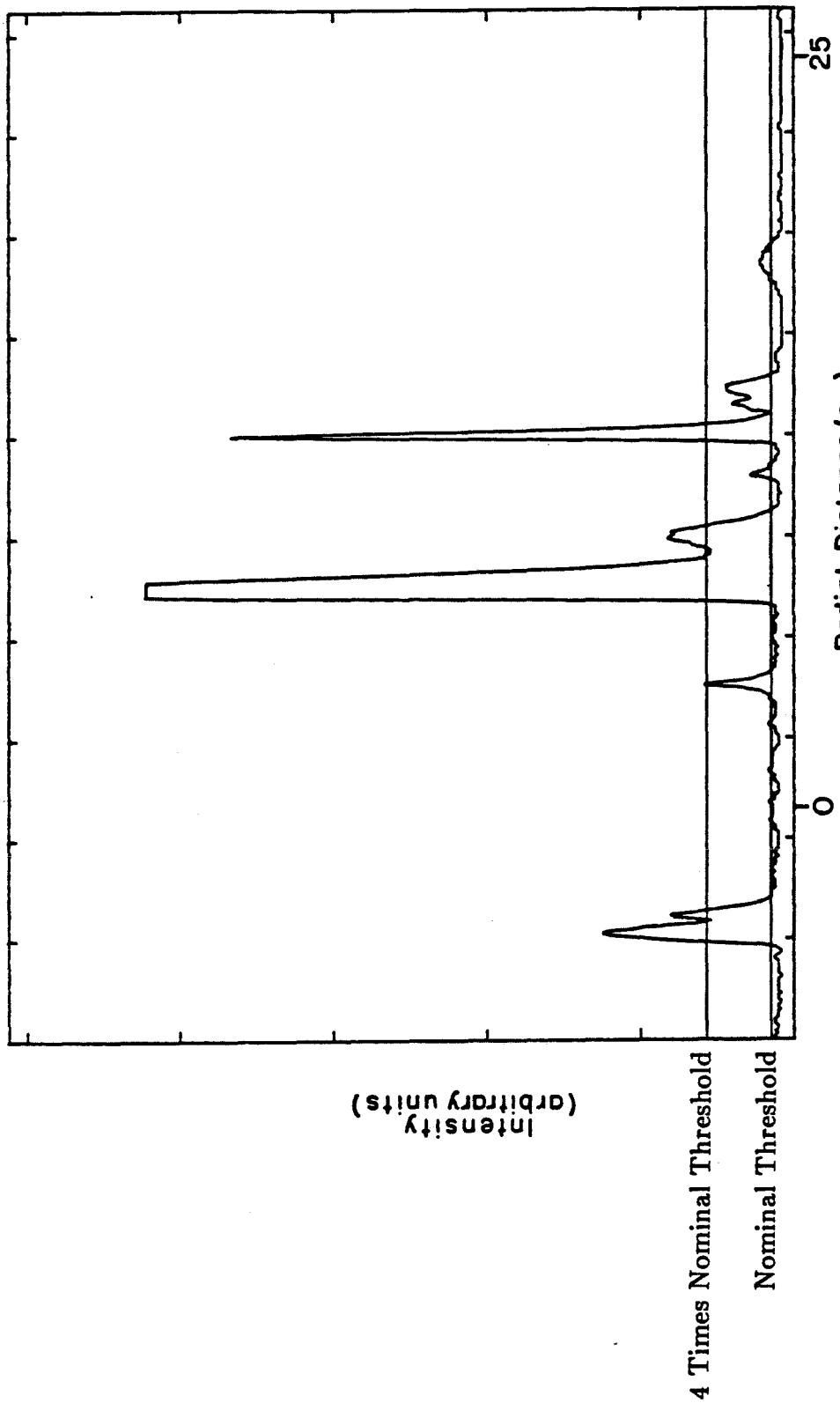

Figure (3.11) Intensity-versus-position of photodiode for scan 350 (1.195 s), 190 kW flame, $z/D_0 = 0.2$ (see figure (3.2)). The levels of the nominal threshold used in determining the presence of and a value 4 times as great are shown.

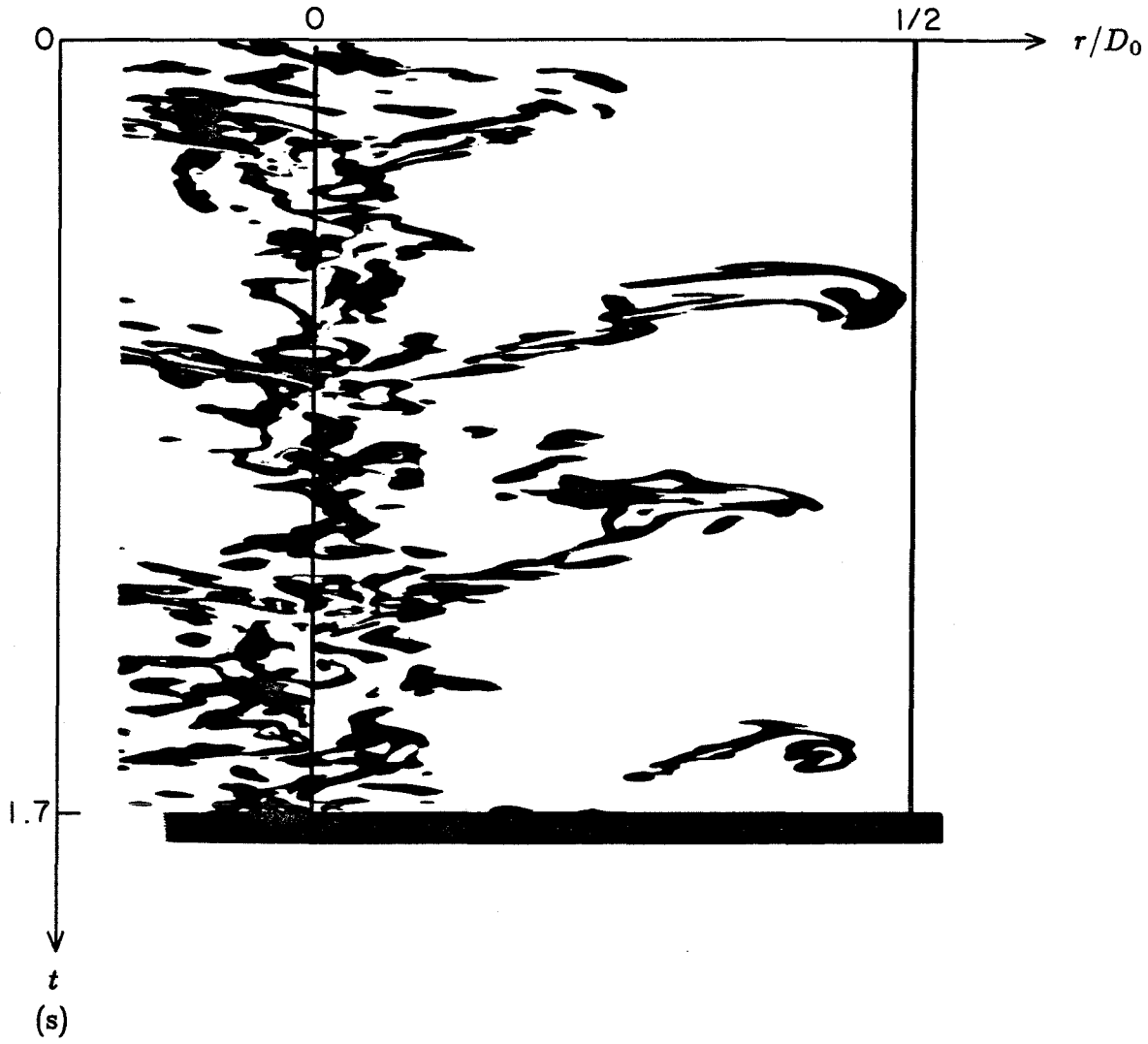

Figure (3.12) r-t diagram, 95 kW flame, $z/D_0 = 0.20$.

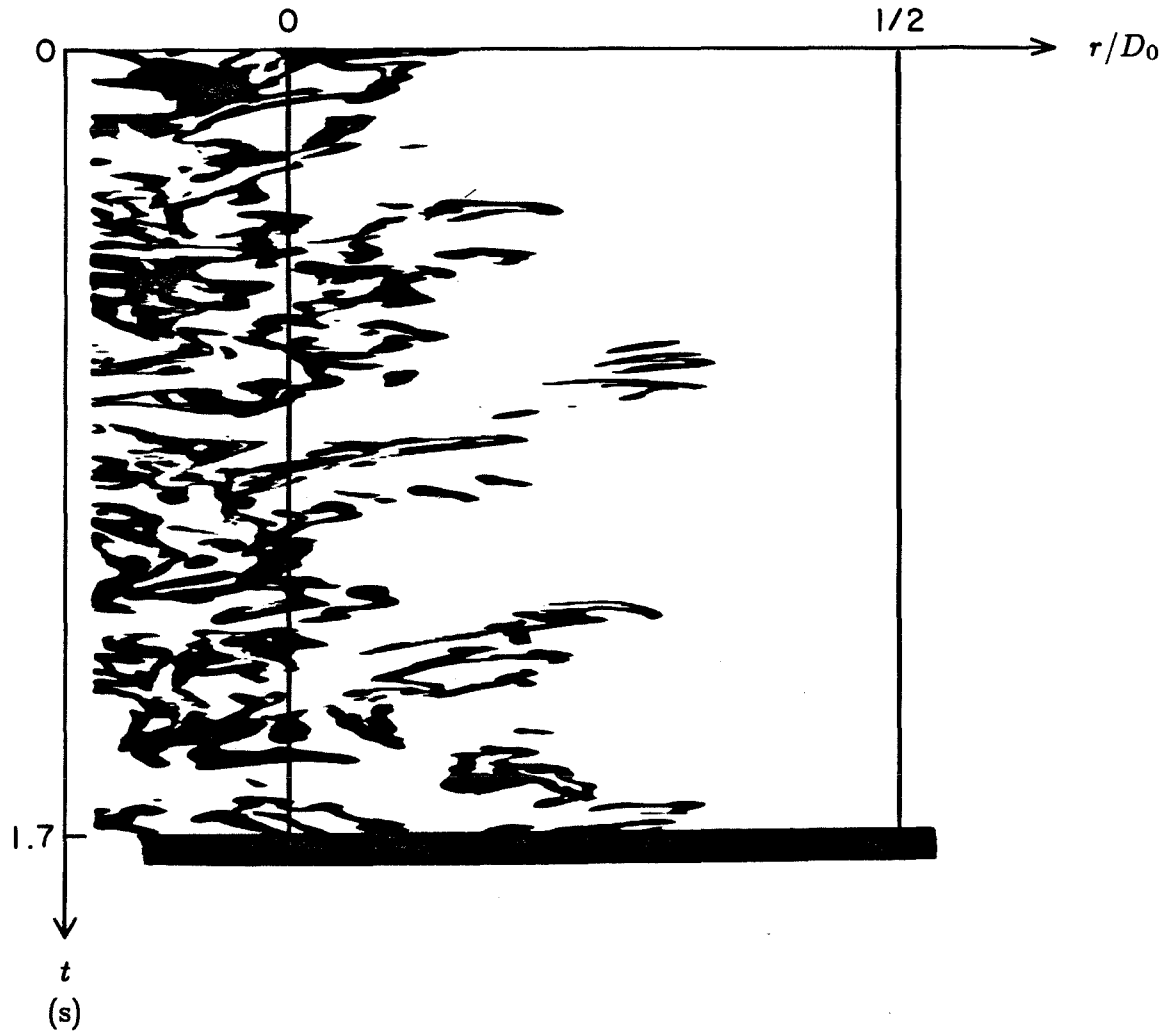

Figure (3.13) r-t diagram, 47.4 kW flame, $z/D_0 = 0.20$.

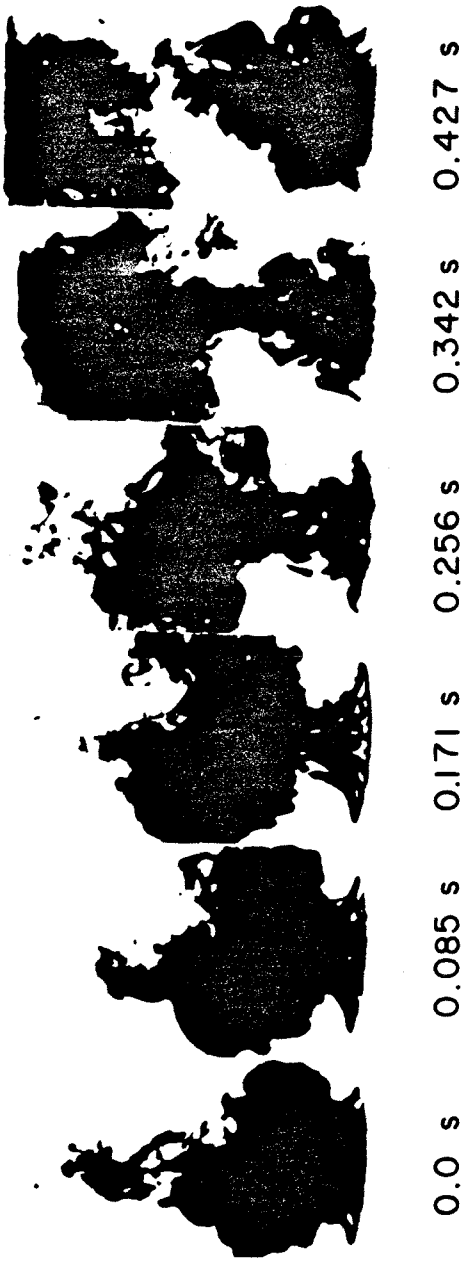

Figure (3.14) Negatives of a series of high-speed movie photographs.

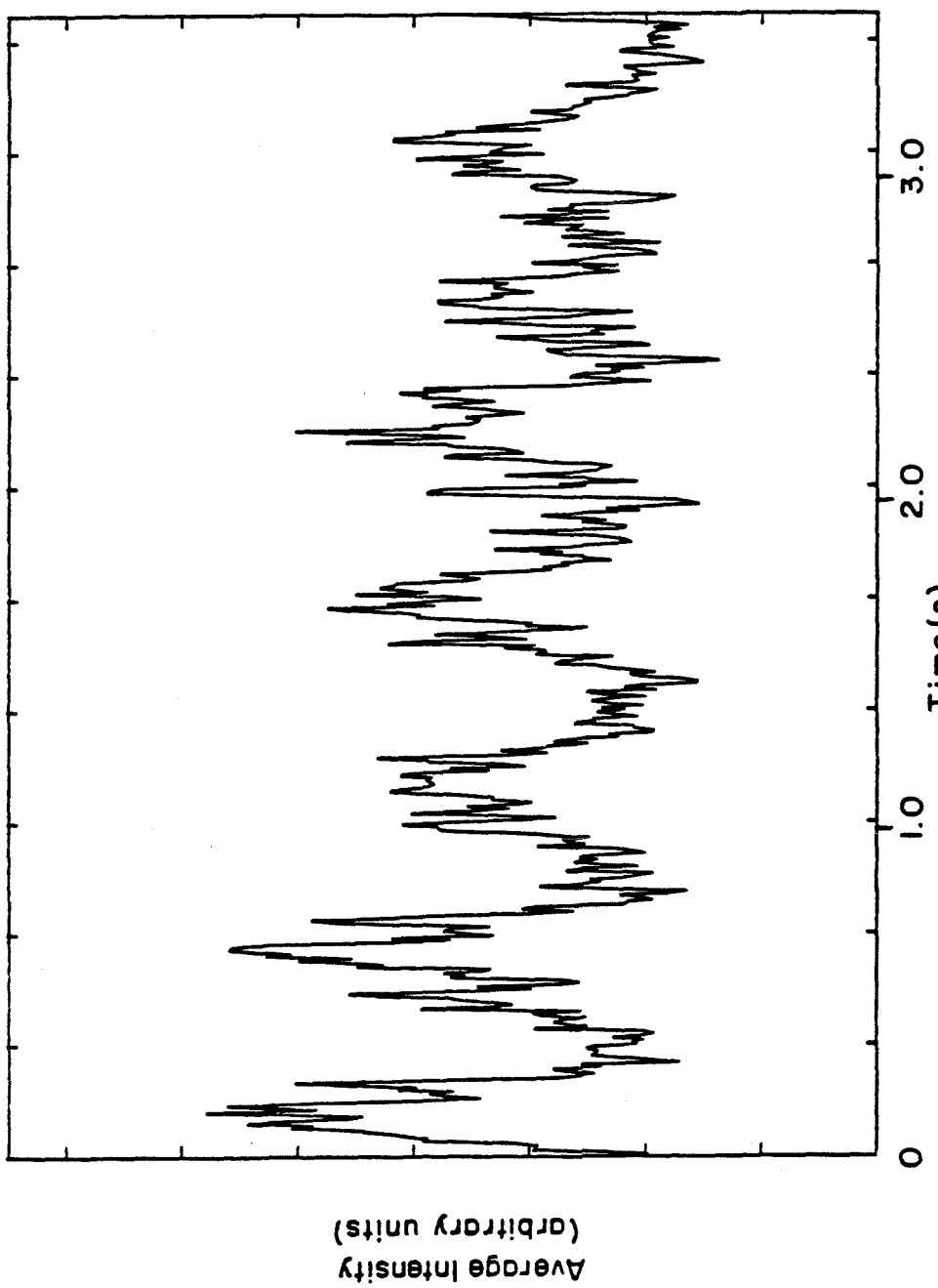

Figure (3.15) The intensity integrated along the position axis as a function of time, 190 kW flame, $z/D_0 = 0.50$.

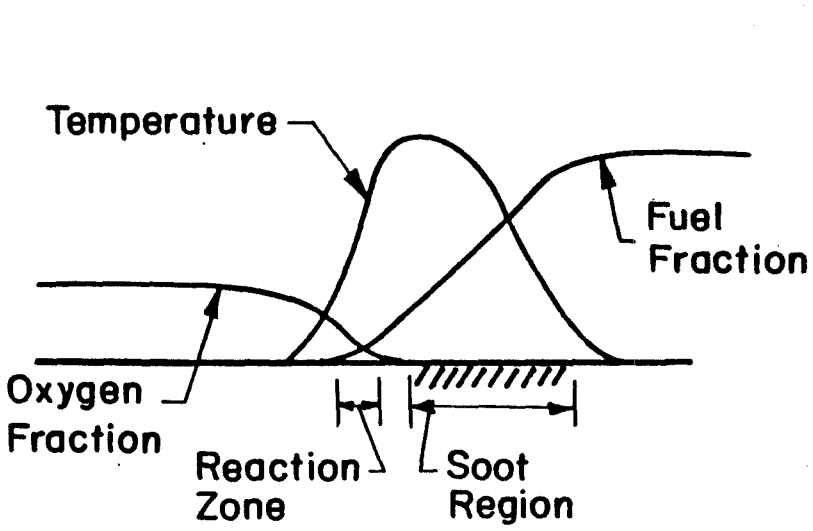

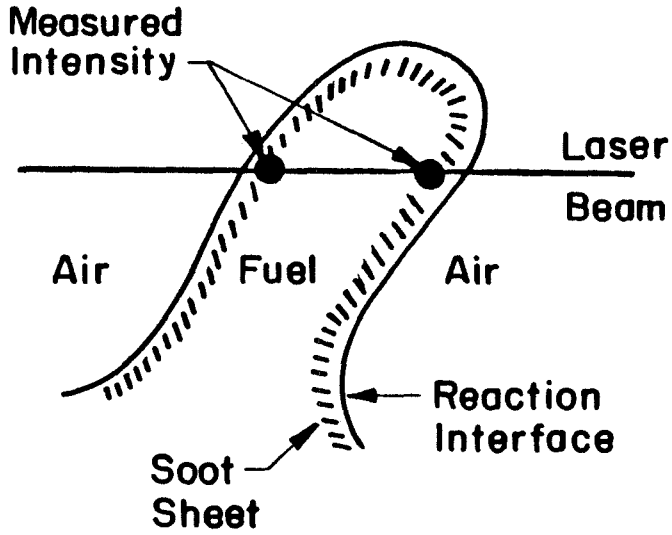

Figure (3.16) Soot location within a diffusion flame.

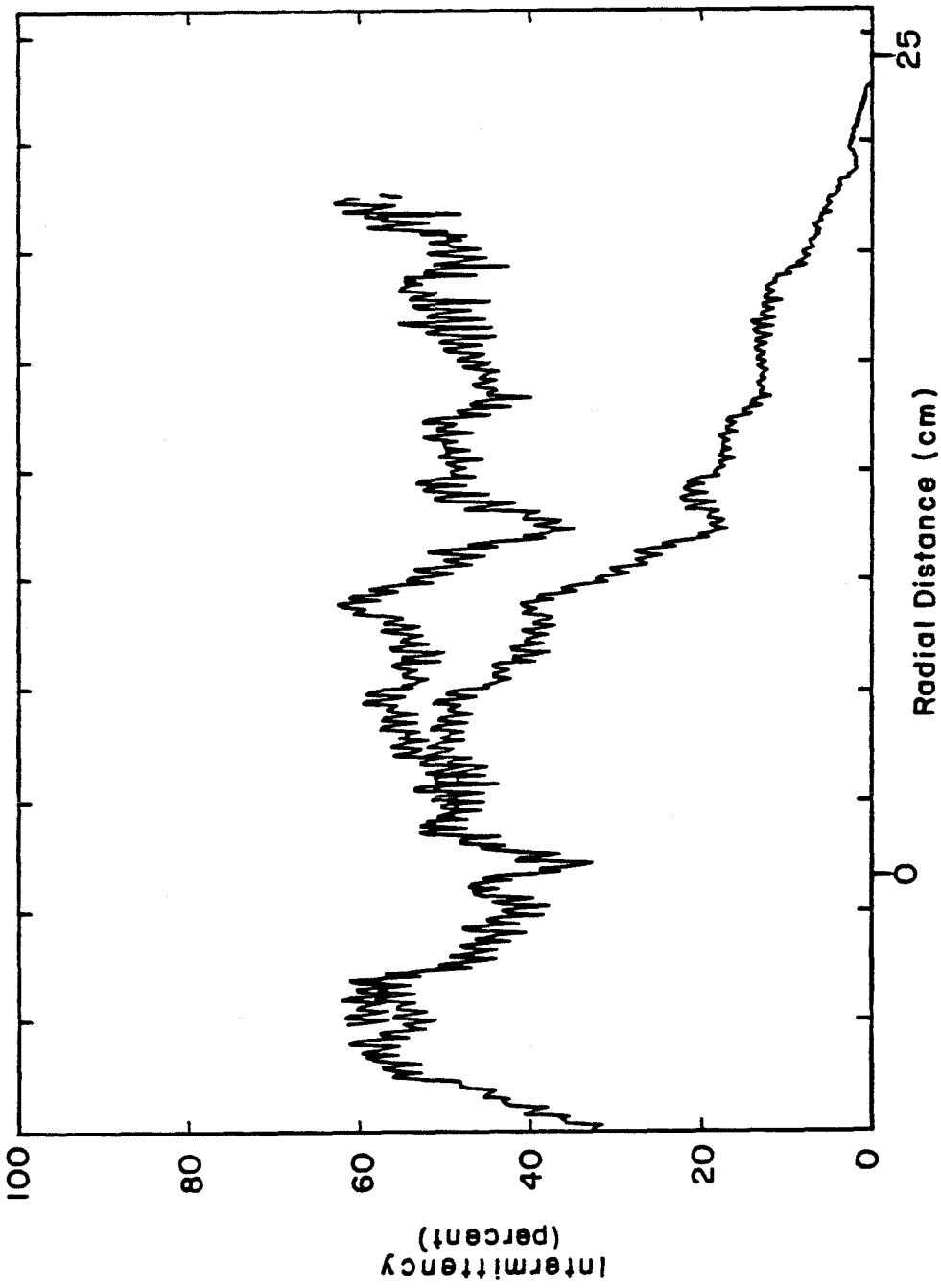

Figure (3.17) Soot intermittency (lower curve) and conditional soot intermittency (upper curve), 190 kW flame, $z/D_0 = 0.20$.

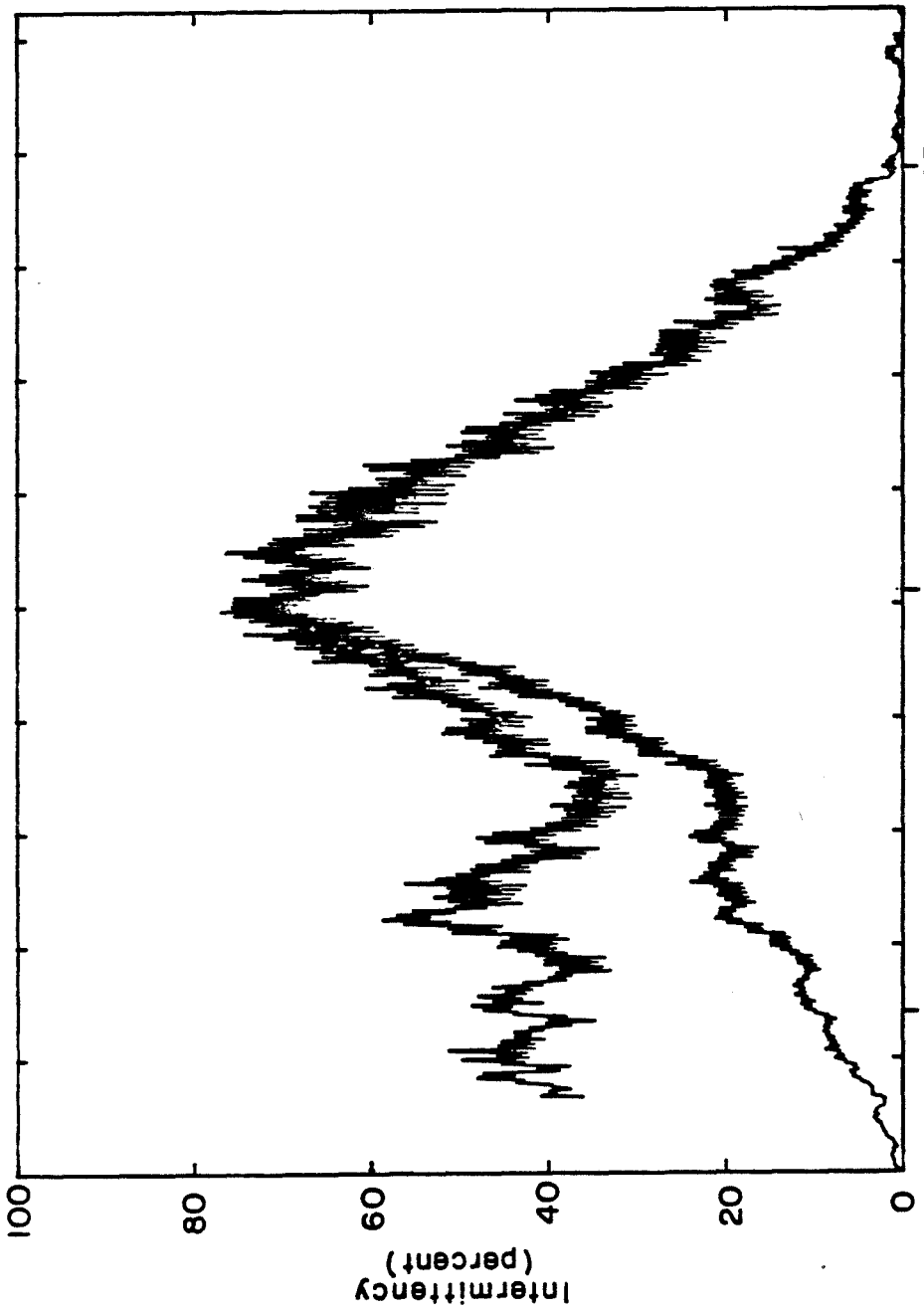

Figure (3.18) Soot intermittency (lower curve) and conditional soot intermittency (upper curve), 190 kW flame, $z/D_0 = 0.50$.

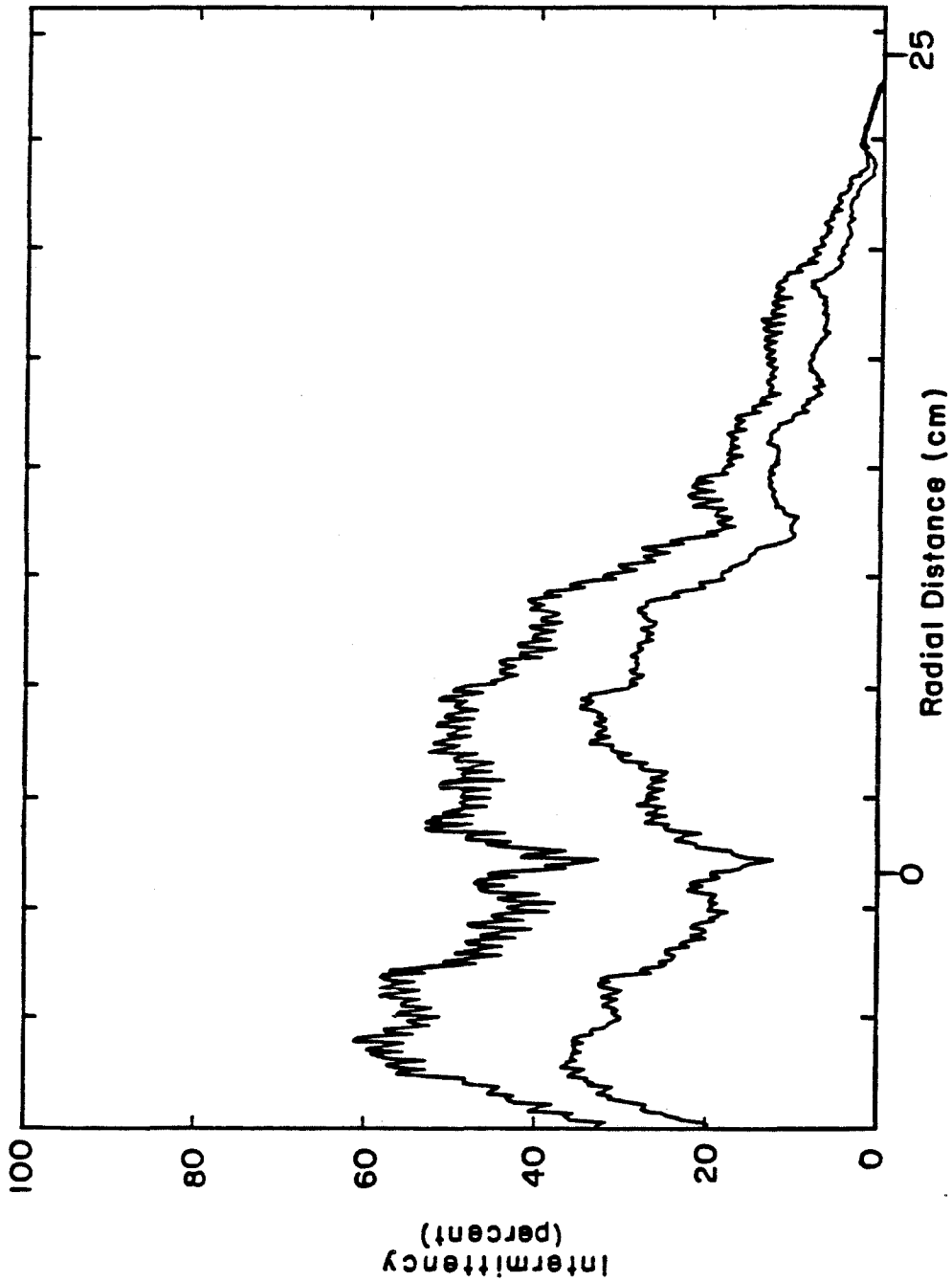

Figure (3.19) Soot intermittency using the normal threshold value (upper curve) and a value 4 times as great (lower curve), 190 kW flame, $z/D_0 = 0.50$.

Table 3.1. Flame Lengths and Axial Measurement Stations

Heat Release Rate (kW)	47.4	67.0	95.0	134	190
Flame Lengths, L/D_0	1.30	1.60	1.75	2.30	2.80
$z/D_0 = 0.10$	x^*	x	x^*	x	x^*
$z/D_0 = 0.20$	x^*	x	x^*	x	x^*
$z/D_0 = 0.35$	x^*	x	x^*	x	x^*
$z/D_0 = 0.50$	x^*	x	x^*	x	x^*
$z/D_0 = 0.75$	x^*	x	x^*	x	x^*
$z/D_0 = 1.00$	x	x	x^*	x	x^*
$z/D_0 = 2.00$				x^*	x^*

x: Four sets of r-t data were collected with a 600 kHz clocking rate. One of these was synchronized with a high-speed movie.

x^*: In addition to obtaining the data listed above, an extra set of r-t data was collected at a 300 kHz clocking rate in synchrony with a high-speed movie.

Chapter 4

Concluding Remarks

It has been shown how the scattering of laser light by soot particles may be used to determine soot distributions in diffusion flames. With some caveats, the soot, located directly adjacent to a flame sheet, can be thought of as marking flame sheets, although cases may exist where a flame sheet occurs in the absence of adjacent soot or, in other diffusion flames or with other fuels, soot may exist in the absence of a flamelet.

The technique described here was used to study the structure of large buoyant diffusion flames of natural gas. A horizontal line in the flame was scanned in time in order to obtain two-dimensional r-t diagrams of the soot structure. The results show that the flame sheets exist as a convoluted but continuous surface near the burner where strain rates are relatively small, but they appear to become discontinuous at larger distances above the burner. These soot discontinuities suggest that the strain here might be sufficient to extinguish the flame locally, or at least suppress soot formation. The decrease in the thickness of the flame sheets with increasing height above the burner is also consistent with an increase in strain rate.

The puffing character of these flames was readily apparent in the data and was found to be quasi-periodic with a frequency of about $0.5\sqrt{g/D_0}$.

Plots of soot intermittency indicate that the soot is present most frequently near the burner axis and drops to zero near the edges. By our determining the instantaneous flame boundary, the conditional soot intermittency can be analyzed. Plots of the conditional soot intermittency indicate that the soot sheets occupy about 40 to 60% of the instantaneous volume within the outer boundaries

of the flame uniformly across the flame. These data support a model of the flame made up of sheets of diffusion flames distributed approximately uniformly within the confines of the quasi-periodic pufflike structures of the flame. A necessary adjunct to this model is that regions that are oxidizer-rich and fuel-rich must alternate, on either side of the diffusion flames, uniformly within the flame surface and that the surface of the stoichiometric mixture ratio also winds throughout the flame. Thus oxidant and fuel are present even along the centerline close to the burner surface.

This study raises several questions. In the particular flames studied, the soot was found primarily in thin sheets. The entire flame was in the buoyancy-dominated range and was a (nonpremixed) diffusion flame. If one is led to surmise that the combustion in this flame is occurring on flame sheets that behave as laminar on a local scale, a supposition that perhaps must be supported by further experimentation, the question arises as to how general such a result might be. Do momentum-dominated diffusion flames also form soot sheets and does the combustion occur in laminar-type flame sheets in these flames? Greater differences might be expected with premixed combustion since a fuel/oxidizer interface does not exist and soot production is usually quite low.

To answer these questions, a means of measuring the combustion reaction interface itself must be used. Two dimensional data (r-t or r-z) must be acquired to elucidate the structure and connectivity of the reaction zones. It may be necessary to work in a nonsooting flame (such as hydrogen flames) in measuring flame sheets directly to avoid interference with the soot particles or their luminosity.

References

Carrier, G. F., Fendell, F. E., and Marble, F. E. (1975). The Effect of Strain Rate on Diffusion Flames. *SIAM J. Appl. Math.* **28**:463–500.

Cetegen, B. M. (1982). Entrainment and Flame Geometry of Fire Plumes. Ph.D. Thesis, California Institute of Technology, Pasadena, CA.

Cetegen, B. M., Zukoski, E. E., and Kubota, T. (1984). Entrainment in the Near and Far Field of Fire Plumes. *Comb. Sci. and Tech.* **39**:305–331.

Damköhler, G. (1940). Der Einfluss der Turbulenz auf die Flammengeschwindigkeit in Gasgemischen. *Z. Elektrochem.* **46**:601–626.

Gengembre, E., Cambray, P., Karmed, D., and Bellet, J. C. (1984). Turbulent Diffusion Flames with Large Buoyancy Effects. *Comb. Sci. and Tech.* **41**:55–67.

Glassman, I. and Yaccarino, P. (1981). The Temperature Effect in Sooting Diffusion Flames. *Eighteenth Symposium (International) on Combustion.* The Combustion Institute, Pittsburg, PA. pp. 1175–1183.

Karagozian, A. R., and Marble, F. E. (1986). Study of a Diffusion Flame in a Stretched Vortex. *Comb. Sci. and Tech.* **45**:65–84.

Karlovitz, B., Denniston, D. W. Jr., Knapschaefer, D. H., and Wells, F. E. (1952). Studies of Turbulent Flames. *Fourth Symposium (International) on Combustion.* Williams and Wilkins Co., Baltimore, MD. pp. 613–620.

Kennedy, I. M. (1985). Flow Field Effects on Nucleation in a Reacting Mixing Layer. *Phys. Fluids* **28**:3515–3524.

Koochesfahani, M. M. (1984). Experiments on Turbulent Mixing and Chemical Reactions in a Liquid Mixing Layer. Ph.D. Thesis, California Institute of Technology, Pasadena, CA.

Koochesfahani, M. M., and Dimotakis, P. E. (1985). Laser-Induced Fluorescence Measurements of Mixed Fluid Concentration in a Liquid Plane Shear Layer. *AIAA J.* **23**:1700–1707.

Lysaght, A. J. R., Bilger, R. W., and Kent, J. H. (1982). Visualization of Mixing in Turbulent Diffusion Flames. *Comb. and Flame* **46**:105–108.

Marble, F. E. (1985). Growth of a Diffusion Flame in the Field of a Vortex. In *Recent Advances in the Aerospace Sciences.* C. Casci, ed., Plenum Press, NY.

Marble, F. E., and Broadwell, J. E. (1977). The Coherent Flame Model for Turbulent Chemical Reactions. *Project SQUID Tech. Rept. TRW-9-PU.* TRW, Redondo Beach, CA.

Markstein, G. H. (1983). Radiant Emission and Smoke Points for Laminar Diffusion Flames of Fuel Mixture. Tech. Rept. J.I.OMON1.BU, Factory Mutual Reseach Corp., Norwood, MA.

Peters, N. (1984). Laminar Diffusion Flamelet Models in Non-Premixed Turbulent Combustion. *Prog. Energy Comb. Sci.* **10**:319–339.

Shchelkin, K. I. (1943). *J. Tech. Phys. (USSR)* **18**:520.

Thomas, P. H., Baldwin, R., and Heselden A. J. M. (1964). Buoyant Diffusion Flames: Some Measurements of Air Entrainment, Heat Transfer, and Flame Merging. *Tenth Symposium (International) on Combustion.* The Combustion Institute, Pittsburg, PA. pp. 983–996.

Tsuji, H. and Yamaoka, I. (1970). Structure Analysis of Counterflow Diffusion Flames in the Forward Stagnation Region of a Porous Cylinder. *Thirteenth Symosium (International) on Combustion.* The Combustion Institute, Pittsburg, PA. pp. 723–731.

Vandsburger, U., Kennedy, I., and Glassman, I. (1984). Sooting Counterflow Diffusion Flames with Varying Oxygen Index. *Comb. Sci. and Tech.* **39**:263–285.

Williams, F. A. (1975). Recent Advances in Theoretical Descriptions of Turbulent Diffusion Flames. In *Turbulent Mixing in Nonreactive and Reactive Flows.* S. N. B. Murthy, ed., Plenum Press, NY.

Zukoski, E. E., Cetegen, B. M., and Kubota, T. (1984). Visible Structure of Buoyant Diffusion Flames. *Twentieth Symposium (International) on Combustion.* The Combustion Institute, Pittsburg, PA. pp. 361–366.

Zukoski, E. E., Kubota, T., and Cetegen, B. (1980). Entrainment in Fire Plumes. *Fire Safety J.* **3**:107-121.

Appendix A

List of Data Files

Included here is a complete list of the data files obtained from radial measurements using the laser soot-scattering technique. All of the 300 kHz clocking rate data had a high-speed movie taken in synchrony. An asterisk (*) next to the name of the 600 kHz clocking rate data file implies that a high-speed movie was also taken for this data.

300 kHz clocking rate data

SJT080.DAT	47.4 kW	$z/D_0 = 0.10$
SJT081.DAT	95.0 kW	$z/D_0 = 0.10$
SJT082.DAT	190 kW	$z/D_0 = 0.10$
SJT110.DAT	47.4 kW	$z/D_0 = 0.20$
SJT111.DAT	95.0 kW	$z/D_0 = 0.20$
SJT112.DAT	190 kW	$z/D_0 = 0.20$
SJT140.DAT	47.4 kW	$z/D_0 = 0.35$
SJT141.DAT	95.0 kW	$z/D_0 = 0.35$
SJT142.DAT	190 kW	$z/D_0 = 0.35$
SJT170.DAT	47.4 kW	$z/D_0 = 0.50$
SJT171.DAT	95.0 kW	$z/D_0 = 0.50$
SJT172.DAT	190 kW	$z/D_0 = 0.50$
SJT200.DAT	47.4 kW	$z/D_0 = 0.75$
SJT201.DAT	95.0 kW	$z/D_0 = 0.75$
SJT202.DAT	190 kW	$z/D_0 = 0.75$
SJT230.DAT	47.4 kW	$z/D_0 = 1.0$
SJT231.DAT	95.0 kW	$z/D_0 = 1.0$
SJT232.DAT	190 kW	$z/D_0 = 1.0$
SJT258.DAT	134 kW	$z/D_0 = 2.0$
SJT259.DAT	190 kW	$z/D_0 = 2.0$
SJT280.DAT	134 kW	$z/D_0 = 2.0$
SJT281.DAT	190 kW	$z/D_0 = 2.0$

600 kHz clocking rate data

SJT060.DAT*	47.4 kW	$z/D_0 = 0.10$
SJT061.DAT	47.4 kW	$z/D_0 = 0.10$
SJT062.DAT	47.4 kW	$z/D_0 = 0.10$
SJT063.DAT	47.4 kW	$z/D_0 = 0.10$
SJT064.DAT*	67.0 kW	$z/D_0 = 0.10$
SJT065.DAT	67.0 kW	$z/D_0 = 0.10$
SJT066.DAT	67.0 kW	$z/D_0 = 0.10$
SJT067.DAT	67.0 kW	$z/D_0 = 0.10$
SJT068.DAT*	95.0 kW	$z/D_0 = 0.10$
SJT069.DAT	95.0 kW	$z/D_0 = 0.10$
SJT070.DAT	95.0 kW	$z/D_0 = 0.10$
SJT071.DAT	95.0 kW	$z/D_0 = 0.10$
SJT072.DAT*	134 kW	$z/D_0 = 0.10$
SJT073.DAT	134 kW	$z/D_0 = 0.10$
SJT074.DAT	134 kW	$z/D_0 = 0.10$
SJT075.DAT	134 kW	$z/D_0 = 0.10$
SJT076.DAT*	190 kW	$z/D_0 = 0.10$
SJT077.DAT	190 kW	$z/D_0 = 0.10$
SJT078.DAT	190 kW	$z/D_0 = 0.10$
SJT079.DAT	190 kW	$z/D_0 = 0.10$
SJT090.DAT*	47.4 kW	$z/D_0 = 0.20$
SJT091.DAT	47.4 kW	$z/D_0 = 0.20$
SJT092.DAT	47.4 kW	$z/D_0 = 0.20$
SJT093.DAT	47.4 kW	$z/D_0 = 0.20$
SJT094.DAT*	67.0 kW	$z/D_0 = 0.20$
SJT095.DAT	67.0 kW	$z/D_0 = 0.20$
SJT096.DAT	67.0 kW	$z/D_0 = 0.20$
SJT097.DAT	67.0 kW	$z/D_0 = 0.20$
SJT098.DAT*	95.0 kW	$z/D_0 = 0.20$
SJT099.DAT	95.0 kW	$z/D_0 = 0.20$
SJT100.DAT	95.0 kW	$z/D_0 = 0.20$
SJT101.DAT	95.0 kW	$z/D_0 = 0.20$
SJT102.DAT*	134 kW	$z/D_0 = 0.20$
SJT103.DAT	134 kW	$z/D_0 = 0.20$
SJT104.DAT	134 kW	$z/D_0 = 0.20$

SJT105.DAT	134 kW	$z/D_0 = 0.20$
SJT106.DAT*	190 kW	$z/D_0 = 0.20$
SJT107.DAT	190 kW	$z/D_0 = 0.20$
SJT108.DAT	190 kW	$z/D_0 = 0.20$
SJT109.DAT	190 kW	$z/D_0 = 0.20$
SJT120.DAT*	47.4 kW	$z/D_0 = 0.35$
SJT121.DAT	47.4 kW	$z/D_0 = 0.35$
SJT122.DAT	47.4 kW	$z/D_0 = 0.35$
SJT123.DAT	47.4 kW	$z/D_0 = 0.35$
SJT124.DAT*	67.0 kW	$z/D_0 = 0.35$
SJT125.DAT	67.0 kW	$z/D_0 = 0.35$
SJT126.DAT	67.0 kW	$z/D_0 = 0.35$
SJT127.DAT	67.0 kW	$z/D_0 = 0.35$
SJT128.DAT*	95.0 kW	$z/D_0 = 0.35$
SJT129.DAT	95.0 kW	$z/D_0 = 0.35$
SJT130.DAT	95.0 kW	$z/D_0 = 0.35$
SJT131.DAT	95.0 kW	$z/D_0 = 0.35$
SJT132.DAT*	134 kW	$z/D_0 = 0.35$
SJT133.DAT	134 kW	$z/D_0 = 0.35$
SJT134.DAT	134 kW	$z/D_0 = 0.35$
SJT135.DAT	134 kW	$z/D_0 = 0.35$
SJT136.DAT*	190 kW	$z/D_0 = 0.35$
SJT137.DAT	190 kW	$z/D_0 = 0.35$
SJT138.DAT	190 kW	$z/D_0 = 0.35$
SJT139.DAT	190 kW	$z/D_0 = 0.35$
SJT150.DAT*	47.4 kW	$z/D_0 = 0.50$
SJT151.DAT	47.4 kW	$z/D_0 = 0.50$
SJT152.DAT	47.4 kW	$z/D_0 = 0.50$
SJT153.DAT	47.4 kW	$z/D_0 = 0.50$
SJT154.DAT*	67.0 kW	$z/D_0 = 0.50$
SJT155.DAT	67.0 kW	$z/D_0 = 0.50$
SJT156.DAT	67.0 kW	$z/D_0 = 0.50$
SJT157.DAT	67.0 kW	$z/D_0 = 0.50$
SJT158.DAT*	95.0 kW	$z/D_0 = 0.50$
SJT159.DAT	95.0 kW	$z/D_0 = 0.50$
SJT160.DAT	95.0 kW	$z/D_0 = 0.50$
SJT161.DAT	95.0 kW	$z/D_0 = 0.50$
SJT162.DAT*	134 kW	$z/D_0 = 0.50$

SJT163.DAT	134 kW	$z/D_0 = 0.50$
SJT164.DAT	134 kW	$z/D_0 = 0.50$
SJT165.DAT	134 kW	$z/D_0 = 0.50$
SJT166.DAT*	190 kW	$z/D_0 = 0.50$
SJT167.DAT	190 kW	$z/D_0 = 0.50$
SJT168.DAT	190 kW	$z/D_0 = 0.50$
SJT169.DAT	190 kW	$z/D_0 = 0.50$
SJT180.DAT*	47.4 kW	$z/D_0 = 0.75$
SJT181.DAT	47.4 kW	$z/D_0 = 0.75$
SJT182.DAT	47.4 kW	$z/D_0 = 0.75$
SJT183.DAT	47.4 kW	$z/D_0 = 0.75$
SJT184.DAT*	67.0 kW	$z/D_0 = 0.75$
SJT185.DAT	67.0 kW	$z/D_0 = 0.75$
SJT186.DAT	67.0 kW	$z/D_0 = 0.75$
SJT187.DAT	67.0 kW	$z/D_0 = 0.75$
SJT188.DAT*	95.0 kW	$z/D_0 = 0.75$
SJT189.DAT	95.0 kW	$z/D_0 = 0.75$
SJT190.DAT	95.0 kW	$z/D_0 = 0.75$
SJT191.DAT	95.0 kW	$z/D_0 = 0.75$
SJT192.DAT*	134 kW	$z/D_0 = 0.75$
SJT193.DAT	134 kW	$z/D_0 = 0.75$
SJT194.DAT	134 kW	$z/D_0 = 0.75$
SJT195.DAT	134 kW	$z/D_0 = 0.75$
SJT196.DAT*	190 kW	$z/D_0 = 0.75$
SJT197.DAT	190 kW	$z/D_0 = 0.75$
SJT198.DAT	190 kW	$z/D_0 = 0.75$
SJT199.DAT	190 kW	$z/D_0 = 0.75$
SJT210.DAT*	47.4 kW	$z/D_0 = 1.0$
SJT211.DAT	47.4 kW	$z/D_0 = 1.0$
SJT212.DAT	47.4 kW	$z/D_0 = 1.0$
SJT213.DAT	47.4 kW	$z/D_0 = 1.0$
SJT214.DAT*	67.0 kW	$z/D_0 = 1.0$
SJT215.DAT	67.0 kW	$z/D_0 = 1.0$
SJT216.DAT	67.0 kW	$z/D_0 = 1.0$
SJT217.DAT	67.0 kW	$z/D_0 = 1.0$
SJT218.DAT*	95.0 kW	$z/D_0 = 1.0$
SJT219.DAT	95.0 kW	$z/D_0 = 1.0$
SJT220.DAT	95.0 kW	$z/D_0 = 1.0$

SJT221.DAT	95.0 kW	$z/D_0 = 1.0$
SJT222.DAT*	134 kW	$z/D_0 = 1.0$
SJT223.DAT	134 kW	$z/D_0 = 1.0$
SJT224.DAT	134 kW	$z/D_0 = 1.0$
SJT225.DAT	134 kW	$z/D_0 = 1.0$
SJT226.DAT*	190 kW	$z/D_0 = 1.0$
SJT227.DAT	190 kW	$z/D_0 = 1.0$
SJT228.DAT	190 kW	$z/D_0 = 1.0$
SJT229.DAT	190 kW	$z/D_0 = 1.0$
SJT240.DAT*	134 kW	$z/D_0 = 2.0$
SJT241.DAT	134 kW	$z/D_0 = 2.0$
SJT242.DAT	134 kW	$z/D_0 = 2.0$
SJT243.DAT	134 kW	$z/D_0 = 2.0$
SJT244.DAT*	190 kW	$z/D_0 = 2.0$
SJT245.DAT	190 kW	$z/D_0 = 2.0$
SJT246.DAT	190 kW	$z/D_0 = 2.0$
SJT247.DAT	190 kW	$z/D_0 = 2.0$
SJT250.DAT*	134 kW	$z/D_0 = 2.0$
SJT251.DAT	134 kW	$z/D_0 = 2.0$
SJT252.DAT	134 kW	$z/D_0 = 2.0$
SJT253.DAT	134 kW	$z/D_0 = 2.0$
SJT254.DAT*	190 kW	$z/D_0 = 2.0$
SJT255.DAT	190 kW	$z/D_0 = 2.0$
SJT256.DAT	190 kW	$z/D_0 = 2.0$
SJT257.DAT	190 kW	$z/D_0 = 2.0$
SJT260.DAT*	47.4 kW	$z/D_0 = 1.0$
SJT261.DAT	47.4 kW	$z/D_0 = 1.0$
SJT262.DAT	47.4 kW	$z/D_0 = 1.0$
SJT263.DAT	47.4 kW	$z/D_0 = 1.0$
SJT264.DAT*	67.0 kW	$z/D_0 = 1.0$
SJT265.DAT	67.0 kW	$z/D_0 = 1.0$
SJT266.DAT	67.0 kW	$z/D_0 = 1.0$
SJT267.DAT	67.0 kW	$z/D_0 = 1.0$
SJT268.DAT*	95.0 kW	$z/D_0 = 1.0$
SJT269.DAT	95.0 kW	$z/D_0 = 1.0$
SJT270.DAT	95.0 kW	$z/D_0 = 1.0$
SJT271.DAT	95.0 kW	$z/D_0 = 1.0$
SJT272.DAT*	134 kW	$z/D_0 = 1.0$

SJT273.DAT	134 kW	$z/D_0 = 1.0$
SJT274.DAT	134 kW	$z/D_0 = 1.0$
SJT275.DAT	134 kW	$z/D_0 = 1.0$
SJT276.DAT*	190 kW	$z/D_0 = 1.0$
SJT277.DAT	190 kW	$z/D_0 = 1.0$
SJT278.DAT	190 kW	$z/D_0 = 1.0$
SJT279.DAT	190 kW	$z/D_0 = 1.0$